

**DOE-ER-0313/55  
Distribution  
Categories  
UC-423, -424**

**FUSION MATERIALS  
SEMIANNUAL PROGRESS REPORT  
FOR THE PERIOD ENDING**

**December 31, 2013**

**Prepared for  
DOE Office of Fusion Energy Sciences  
(AT 60 20 10 0)**

**DATE PUBLISHED: March 2014**

**Prepared by  
OAK RIDGE NATIONAL LABORATORY  
Oak Ridge, Tennessee 37831  
Managed by  
UT-Battelle, LLC  
For the  
U.S. DEPARTMENT OF ENERGY**

## FOREWORD

This is the fifty-fifth in a series of semiannual technical progress reports on fusion materials science activity supported by the Fusion Energy Sciences Program of the U.S. Department of Energy. It covers the period ending December 31, 2013. This report focuses on research addressing the effects on materials properties and performance of exposure to the neutronic, thermal and chemical environments anticipated in the chambers of fusion experiments and energy systems. This research is a major element of the national effort to establish the materials knowledge base for an economically and environmentally attractive fusion energy source. Research activities on issues related to the interaction of materials with plasmas are reported separately.

The results reported are the products of a national effort involving a number of national laboratories and universities. A large fraction of this work, particularly in relation to fission reactor irradiations, is carried out collaboratively with partners in Japan, Russia, and the European Union. The purpose of this series of reports is to provide a working technical record for the use of program participants, and to provide a means of communicating the efforts of fusion materials scientists to the broader fusion community, both nationally and worldwide.

This report has been compiled under the guidance of F. W. (Bill) Wiffen and Betty Waddell, Oak Ridge National Laboratory. Their efforts, and the efforts of the many persons who made technical contributions, are gratefully acknowledged.

Peter J. Pappano  
Research Division  
Office of Fusion Energy Sciences

## TABLE OF CONTENTS

### 1. FERRITIC/MARTENSITIC STEEL DEVELOPMENT

*See also Sections 6.1, 7.5, 8.2, 8.3, 8.4, and 8.5.*

#### 1.1 Stability of MX-Type Nanoprecipitates in Fe-Base Model Alloys —

1

L. Tan, Y. Katoh, L. L. Snead (Oak Ridge National Laboratory)

The stability of MX-type nanoprecipitates TaC, TaN, and VN has been evaluated using thermal aging at 600 and 700°C for up to 5000 h, creep testing at 600°C, and Fe<sup>2+</sup> ion irradiation at 500°C and up to ~49 dpa. Transmission electron microscopy (TEM) has been primarily used to characterize the evolution of the nanoprecipitates. The results indicate different levels of stability of the nanoprecipitates under the three types of experimental conditions. Selected particle degradation modes, e.g., dissolution, growth, re-precipitation, and fragmentation, were observed on the nanoprecipitates. The results are being reported and compared to literature data in our recent papers. A parallel experiment using neutron irradiation at 300, 500, and 650°C for up to about 20 dpa has been completed recently. Post-irradiation examination (PIE) of the neutron-irradiated samples will be conducted to compare them with the Fe<sup>2+</sup> ion irradiated results.

### 2. ODS AND NANOCOMPOSITED ALLOY DEVELOPMENT

*See also Sections 6.1, 7.5, and 8.4.*

#### 2.1 Development of ODS FeCrAl for Fusion Reactor Applications —

5

D. T. Hoelzer, K. A. Unocic, S. Dryepondt, and B. A. Pint (Oak Ridge National Laboratory)

Three experimental ODS FeCrAl heats of composition Fe-12Cr-5Al were prepared by mechanical alloying with additions of Y<sub>2</sub>O<sub>3</sub>, Y<sub>2</sub>O<sub>3</sub> + ZrO<sub>2</sub> and Y<sub>2</sub>O<sub>3</sub> + HfO<sub>2</sub>. The as-extruded microstructure showed smaller grain size with the co-additions of ZrO<sub>2</sub> or HfO<sub>2</sub> and high concentrations of nano-size (<5 nm diameter) oxide particles within the grains. In the alloy with Y<sub>2</sub>O<sub>3</sub> + HfO<sub>2</sub>, either a bimodal or trimodal particle size distribution was observed. Tensile testing was performed at 25° up to 800°C and the higher oxide contents with ZrO<sub>2</sub> or HfO<sub>2</sub> resulted in higher yield and ultimate strengths but lower ductility compared to the alloy with only Y<sub>2</sub>O<sub>3</sub>.

### 3.0 CERAMIC COMPOSITE STRUCTURAL MATERIAL DEVELOPMENT

*See also Sections 8.6 and 8.7.*

## TABLE OF CONTENTS

- 3.1 Process Development and Optimization for Silicon Carbide Joining and Irradiation Studies-III — 11**  
 T. Koyanagi, J. Kiggans, C. Shih, Y. Katoh (Oak Ridge National Laboratory)
- Two robust pressureless joining methods for SiC ceramics proved to be promising. A Ti-Si-C MAX phase displacement reaction bonding using commercial bonding formula demonstrated dense microstructures and apparent shear strength of ~150 MPa. A pressureless transient eutectic-phase (TEP) process was newly developed to demonstrate promising properties. An experimental plan for the neutron irradiation effects study was developed.
- 3.2 Low Activation Joining of SiC/SiC Composites for Fusion Applications: Tape Casting TiC+Si Powders — 23**  
 C. H. Henager, Jr., R. J. Kurtz, N. L. Canfield, Y. Shin, W. G. Luscher, J. T. Mansurov, T. J. Rosendaal, and B. A. Borlaug (Pacific Northwest National Laboratory)
- The use of SiC composites in fusion environments likely requires joining two plates using reactive joining or brazing. One promising reactive joining method uses solid-state displacement reactions between Si and TiC to produce  $Ti_3SiC_2 + SiC$ . We continue to explore the processing envelope for these joints to produce optimal joints to undergo irradiation studies in the High Flux Isotope Reactor (HFIR). One noted feature of the older joints, produced with tape-calendared powders of TiC + Si, were the large, unavoidable void regions they contained. Although the joints were very strong, voids are undesirable. In addition, the tapes made for these joints were produced approximately 20 years ago and had aged. Therefore, we embarked on an effort to produce new tape-cast powders of TiC and Si that can replace our aged tape-calendared materials.
- 4. HIGH HEAT FLUX MATERIALS AND COMPONENT TESTING**
- See also Sections 8.8 and 8.9.*
- 4.1 Recent Progress in the Development of Ductile-Phase Toughened Tungsten for Plasma-Facing Materials — 29**  
 C. H. Henager, Jr., R. J. Kurtz, T. J. Rosendaal, and B. A. Borlaug (Pacific Northwest National Laboratory), G. R. Odette, K. H. Cunningham, K. Fields, D. Gragg, and F. W. Zok (University of California, Santa Barbara)
- Tungsten (W) and W-alloys are the leading candidates for plasma-facing components in nuclear fusion reactor designs because of their high melting point, strength at high temperatures, and low sputtering yield. However, tungsten is brittle and does not exhibit the required fracture toughness for nuclear applications. The ductile-brittle transition temperature (DBTT) for unirradiated W-alloys ranges from 300-1000°C and radiation hardening further elevates this range. A promising approach to increasing fracture toughness and decreasing the DBTT of a W-alloy is by ductile-phase toughening (DPT). In this method, a ductile phase is included in a brittle matrix to prevent fracture propagation by

## TABLE OF CONTENTS

crack bridging. To examine the prospect of DPT, W-Cu and W-Ni-Fe three-point bend samples were deformed at several strain rates and temperatures. Data from these tests will be used for time-dependent crack bridging studies and the calibration of a crack-bridging model that can effectively predict elevated temperature crack growth in W-composites. A study of fabricating W-wire-reinforced W-matrix composites by spark plasma sintering (SPS) was initiated. W-wires coated with Cu or tungsten carbide (WC) was consolidated in a W matrix. Characterization of these composites is ongoing.

### 4.2 Evaluation of Mechanical Properties of Tungsten After Neutron Irradiation — 40

L. L. Snead, L. M. Garrison, T. S. Byun, N. A. P. K. Kumar, and W. D. Lewis (Oak Ridge National Laboratory)

A total of 440 tungsten samples were irradiated in HFIR at temperatures from 70 to 900°C and fast neutron fluences of 0.01 to  $20 \times 10^{25}$  n/m<sup>2</sup> at E>0.1 MeV over the last year. Types of tungsten included were [110] single crystal tungsten, [100] single crystal tungsten, wrought tungsten foils, annealed tungsten foils, and tungsten-copper laminate. Samples that were irradiated at  $2 \times 10^{25}$  n/m<sup>2</sup> and below have been tensile and hardness tested at 300°C and below. The defect structure of selected low dose samples has been investigated in the TEM. The analysis of the lower dose samples is ongoing, and analysis of the higher dose samples will follow.

### 4.3 High-Heat Flux Testing of Low-Level Irradiated Materials Using Plasma Arc Lamps — 48

A. S. Sabau, E. K. Ohriner, Y. Kato, and L. L. Snead (Oak Ridge National Laboratory)

A neutron-irradiated tungsten specimen was successfully tested at ITER-relevant high-heat flux conditions using Plasma Arc Lamp at ORNL on Aug. 14, 2013, without any contamination outside the testing box, ensuring the readiness of the new facility for irradiated samples. For thin specimens, often used for studies of neutron irradiation effects, one of the main challenges to the PAL systems is the measurement of the sample temperature.

## 5. MAGNET AND DIAGNOSTIC SYSTEM MATERIALS

### 5.1 Irradiation Response of Next Generation High Temperature Superconducting Rare Earth and Nanoparticle-Doped YBa<sub>2</sub>Cu<sub>3</sub>O<sub>7-x</sub> Coated Conductors for Fusion Energy Applications — 54

K. J. Leonard, T. Aytug, Fred. A. List III, Yanwen Zhang (Oak Ridge National Laboratory), A. Perez-Bergquist, W. J. Weber (University of Tennessee), and A. Gapud (University of South Alabama)

During this semiannual reporting period, electrical characterization work was completed on the irradiated superconducting films, and two presentations were made at conferences. The first, "Irradiation Response of Next Generation High Temperature Superconductors for Fusion Energy Applications" was presented at the International Conference of Fusion

## TABLE OF CONTENTS

Reactor Materials in Beijing, China. This presentation introduced the fusion materials community to the advances that have been made in coated conductor technology and the potential for use in nuclear application. The second presentation “Irradiation of Commercial, High- $T_c$  Superconducting Tape for Potential Fusion Application: Electromagnetic Transport Properties,” was presented in November at the Southeastern Section American Physical Society Meeting in Bowling Green, KY. This detailed the electrical property characterizations of the conductors and is summarized in this report.

- 5.2 High Neutron Dose Irradiation of Dielectric Mirrors — 63**  
 K. J. Leonard, G. E. Jellison Jr., N. A. P. K. Kumar and L. L. Snead (Oak Ridge National Laboratory)
- During this semiannual reporting period, work was completed on low dose (0.001 to 0.1 dpa) examinations culminating in the presentation of data at the Radiation Effects in Insulators conference in Helsinki, Finland in July 2013. Publication of the paper “The role of microstructure on the optical performance of neutron irradiated dielectric mirrors” has been confirmed for the Journal of Nuclear Materials in 2014, volume 445, pages 281-290. The optical property characterization of the 1 and 4 dpa-irradiated mirrors has also been completed, with data presented in poster form at the International Conference of Fusion Reactor Materials in Beijing, China in October. This semiannual contribution briefly summarizes the low dose results, which are presented in more detail in the previous contributions, as well as the optical property data for the high dose samples.
- 6. FUSION CORROSION AND COMPATIBILITY SCIENCE**
- 6.1 Liquid Metal Compatibility — 67**  
 S. J. Pawel (Oak Ridge National Laboratory)
- Fabrication of the first thermal convection loop (TCL) using dispersion strengthened FeCrAl (Kanthal APMT) tubing was completed in the previous reporting period. This alloy is known for high strength and creep resistance at elevated temperature and, based on capsule testing, it is anticipated to have excellent resistance to Pb-Li. Recent accomplishments include initial refurbishment of suitable laboratory space in which to operate the TCL, acquisition and chemical analysis of the Pb-17at%Li that will be used as a working fluid, and preparation of the Kanthal APMT test coupons that will be used in the specimen chains that will be inserted into each vertical leg of the TCL.
- 7. MECHANISMS AND ANALYSIS**
- 7.1 Microstructural Stability and Mechanical Behavior of FeMnNiCr High Entropy Alloy Under Ion Irradiation — 70**  
 N. A. P. K. Kumar<sup>1,2</sup>, K. J. Leonard<sup>1</sup>, H. Bei<sup>1</sup>, Y. Zhang<sup>1,2</sup> and S. J. Zinkle<sup>1</sup> (Oak Ridge National Laboratory<sup>1</sup>, University of Tennessee<sup>2</sup>)

*Abstract of paper to be submitted.*

## TABLE OF CONTENTS

- 7.2 Effects of Ion Irradiation on BAM-11 Bulk Metallic Glass — 71**  
 A. G. Perez-Bergquist<sup>1,2</sup>, H. Bei<sup>1</sup>, Y. Zhang<sup>1,2</sup>, and S. J. Zinkle<sup>1,2</sup> (Oak Ridge National Laboratory<sup>1</sup>, University of Tennessee<sup>2</sup>)
- Bulk metallic glasses are intriguing candidates for structural applications in nuclear environments due to their good mechanical properties along with their inherent amorphous nature, but their radiation response is largely unknown due to the relatively recent nature of innovations in bulk metallic glass fabrication. Here, microstructural and mechanical property evaluations have been performed on a  $Zr_{52.5}Cu_{17.9}Ni_{14.6}Al_{10}Ti_5$  bulk metallic glass (BAM-11) irradiated with 3 MeV  $Ni^+$  ions to 0.1 and 1.0 dpa at room temperature and 200°C. Transmission electron microscopy showed no evidence of radiation damage or crystallization following ion irradiation, and changes in hardness and Young's modulus were typically <10%, with slight softening following irradiation at room temperature and no significant changes at 200°C. These results suggest that the BAM-11 bulk metallic glass may be useful for certain applications in nuclear environments.
- 7.3 Physical and Thermal Mechanical Characterization of Non-Irradiated MAX Phase Materials (Ti-Si-C and Ti-Al-C Systems) — 78**  
 C. Shih, R. Meisner, W. Porter, Y. Katoh, and S. J. Zinkle (Oak Ridge National Laboratory)
- The physical and thermo mechanical properties of two commercially available MAX phase materials have been characterized in the non-irradiated states including: density, X-ray diffraction analysis, microstructure analysis by SEM, coefficient of thermal expansion, thermal diffusivity, thermal conductivity, dynamic Young's modulus, electrical conductivity, and equibiaxial fracture strength (including Weibull modulus). The results show that the materials contain multiple phases. However, predominate phases are hexagonal MAX phases composed of Ti-SiC-C and Ti-Al-C ternary systems. High thermal and electrical conductivity, adequate Young's modulus and equibiaxial fracture strength were observed. All the properties studied agree well with data from the literature.
- 7.4 Effects of Neutron Irradiation on Ti-Si-C MAX-Phase Ceramic Microstructures — 94**  
 A. G. Perez-Bergquist<sup>1,2</sup>, Y. Katoh<sup>1</sup>, C. Shih<sup>1</sup>, N. A. P. K. Kumar<sup>1,2</sup>, and S. J. Zinkle<sup>1,2</sup> (Oak Ridge National Laboratory<sup>1</sup>, University of Tennessee<sup>2</sup>)
- MAX phase ceramics are intriguing candidates for structural applications in nuclear environments due to their unique mixture of metallic and ceramic properties. Specifically, their potential to retain adequate thermal conductivity after high levels of irradiation damage may make them an attractive alternative to SiC in fusion environments. In this study, we investigate the MAX phase ceramic  $Ti_3SiC_2$  after neutron irradiation to 3.4 dpa and 5.0 dpa at temperatures of 500 and 800°C, respectively. Initial results showed large amounts of atomic-scale radiation damage in the material, but minimal loss of strength in selected  $Ti_3SiC_2/Ti_5Si_3$  samples.

## TABLE OF CONTENTS

- 7.5 A Dual Ion Irradiation Study of Helium-DPA Interactions on Cavity Evolution in Tempered Martensitic Steels and Nanostructured Ferritic Alloys —** **100**  
 T. Yamamoto, Y. Wu, G. Robert Odette (University of California Santa Barbara),  
 K. Yabuuchi, S. Kondo, and A. Kimura (Kyoto University)
- Cavity evolutions in a normalized and tempered martensitic steel (TMS) and two nanostructured ferritic alloys (NFA) under  $\text{Fe}^{3+}$  and  $\text{He}^+$  dual ion beam irradiations (DII) at 500°C and 650°C were characterized over a wide range of dpa, He and He/dpa. Transmission electron microscopy (TEM) showed that DII of a 8Cr TMS, at 500°C to up to 60 dpa and 2100 appm He, produced a moderate density of non-uniformly distributed cavities with bimodal sizes ranging from  $\approx 1$  nm He bubbles to  $\approx 20$  nm faceted voids, and swelling  $\approx 0.44\%$ . In contrast, the same irradiation conditions produced only small  $\approx 1.3$  nm diameter bubbles and swelling of  $\approx 0.05\%$  in the NFA MA957. Similar bubble distributions were observed in MA957 and a developmental NFA DII at 650°C up to  $\approx 80$  dpa and  $\approx 3900$  appm He. These results demonstrate the outstanding He management capability of the oxide nano-features in the NFA. The various data trends are shown as a function of dpa, He, He/dpa and  $\text{He}^*\text{dpa}$ .
- 8. MODELING PROCESSES IN FUSION SYSTEM MATERIALS**
- 8.1 Modeling Concurrent Radiation Damage and Plastic Deformation —** **107**  
 T. Crosby, G. Po, N. Ghoniem (University of California, Los Angeles)
- We present here an application of a fundamentally new theoretical framework for description of the simultaneous evolution of radiation damage and plasticity that can describe both in-situ and ex-situ deformation of structural materials. The developed self-consistent framework allows for the determination of the simultaneous evolution of the dislocation microstructure, as well as the spatial distribution of vacancies, interstitials and the temperature diffusion fields. The developed theory is implemented in a new computational code that facilitates the simulation of irradiated and unirradiated materials alike in a consistent fashion. Computer simulations are presented for irradiated fcc metals that address dislocation channel formation in irradiated metals (ex-situ). The simulations, which focus on plastic flow localization in micro-pillars, show that the spatial heterogeneity in the distribution of Stacking Fault Tetrahedra (SFTs) leads to localize plastic deformation and incipient surface fracture of micropillars.
- 8.2 An Atomistic Assessment of Helium Behavior in Iron —** **110**  
 R. E. Stoller and Y. N. Osetskiy (Oak Ridge National Laboratory)
- Extended abstract – paper submitted to J. Nucl. Mater. after ICFRM-16.*

## TABLE OF CONTENTS

- 8.3 Dynamics of Helium-Loaded Grain Boundaries under Shear Deformation in  $\alpha$ -Fe — 112**  
 F. Gao, L. Yang, H. L. Heinisch and R. J. Kurtz (Pacific Northwest National Laboratory)
- Helium produced in the fusion nuclear environment will interact with microstructural features in materials, such as GBs and dislocations. At elevated temperatures helium at GBs can significantly influence creep-rupture properties by enhancing cavity formation and lowering GB cohesive energy. Grain boundary sliding can lead to stress concentrations at GB triple junctions and hard precipitates in the GB plane that may be sufficient to nucleate cavities. Here we explore the effects of helium on coupled GB migration and sliding under an applied shear stress. The  $\Sigma 3$  symmetric tilt GB with a  $\langle 110 \rangle$  rotation axis in bcc iron was selected for study. The method for exploring helium effects on GB motion involved randomly inserting different concentrations of helium atoms around the GB plane and then applying a shear stress parallel to the GB plane at 300 K. We reported previously [1] that, in the absence of helium, the critical stress to induce coupled GB migration and sliding occurred at 300 K was 1.5 GPa. The current simulations show that when helium is present the critical stress for coupled GB motion, and the GB migration velocity are both reduced. When the GB helium concentration is low, most single helium atoms and small helium clusters migrate along with the GB. However, at high helium concentrations clusters easily form that remain behind in the bulk when the GB migrates away from its original position.
- 8.4 Radiation-Induced Obstacles in Iron and Ferritic Alloys: An Atomic-Scale View — 119**  
 Y. N. Osetskiy and R. E. Stoller (Oak Ridge National Laboratory)
- Extended abstract – paper submitted to J. Nucl. Mater. after ICFRM-16, with results on 6nm obstacles added.*
- 8.5 Modeling of Irradiation Hardening of Iron After Low Dose and Low Temperature Neutron Irradiation — 121**  
 X. Hu, D. Xu, B. D. Wirth (University of Tennessee, Knoxville), and T. S. Byun (Oak Ridge National Laboratory)
- Irradiation hardening is a prominent low temperature degradation phenomena in materials. In this paper, a reaction-diffusion cluster dynamics model is used to predict the distribution of vacancy and interstitial clusters in iron subject to low temperature ( $< 373\text{K}$ ) and low dose ( $< 0.1 \text{ dpa}$ ) neutron irradiation. The predicted microstructure evolutions of high purity iron samples are compared to positron annihilation spectroscopy (PAS) and transmission electron microscopy (TEM) observations and show good agreement for neutron irradiation in this regime. The defect cluster distributions are then coupled to a dispersed barrier hardening model that assumes a strength factor,  $\alpha$ , which varies with cluster type and size to compute the yield strength increase, the results of which are compared to the values obtained from tensile tests. A reasonable agreement between modeling and experiments is achieved.

## TABLE OF CONTENTS

- 8.6 Molecular Dynamics Modeling of Atomic Displacement Cascades in 3C-SiC — 147**  
G. D. Samolyuk, Y. N. Osetskiy and R. E. Stoller (Oak Ridge National Laboratory)

*Extended abstract – paper submitted to J. Nucl. Mater. after ICFRM-16.*

- 8.7 First-Principles Calculations of Charge States and Formation Energies of Mg Transmutant in 3C-SiC — 149**

S. Y. Hu, W. Setyawan, W. Jiang, C. H. Henager, Jr. and R. J. Kurtz (Pacific Northwest National Laboratory)

We employed density functional theory to study the effect of electron potentials on charge states and the formation energies of Mg transmutant at different lattice sites in 3C-SiC. We found that  $Mg_C$ ,  $Mg_{TC}$  and  $Mg_{TSi}$  most likely have charge state +2 while  $Mg_{Si}$  prefers charge state -2. The results also show that the substitutional  $Mg_{Si}^{-2}$  has much smaller formation energy than that of  $Mg_C^{+2}$ , and interstitial  $Mg_{TC}^{+2}$  has lower formation energy than that of  $Mg_{TSi}^{+2}$ . These results imply that  $Mg_{Si}^{-2}$  is the most stable substitutional defect while  $Mg_{TC}^{+2}$  is the most stable interstitial defect in 3C-SiC. Since the quadrupole correction due to the spurious interactions between images of charged defects in periodic simulation cells was not taken into account, the calculated formation energies were overestimated. In future work we will examine the effect of quadrupole correction on the formation energies of defects. Additional studies on Al and Be transmutants in 3C-SiC are currently underway.

- 8.8 Analytical Model of Homogeneous Helium Trap-Mutation Evolution in Tungsten — 154**  
W. Setyawan, G. Nandipati, K. J. Roche, H. L. Heinisch, R. J. Kurtz (Pacific Northwest National Laboratory) and B. D. Wirth (University of Tennessee, Knoxville)

Homogeneous trap-mutation events in which helium (He) clusters above a minimum size displace tungsten (W) atoms from their lattice sites are simulated with molecular dynamics. Using a He concentration of up to 4600 appm and temperature up to 2050 K (half the absolute melting temperature), analytical models are formulated to describe the evolution of the number of trap-mutation nucleation sites ( $N_C$ ) and the number of created self-interstitial atoms ( $N_I$ ) as a function of He concentration and temperature. Consistent time scaling with respect to concentration (linear scaling) and temperature (Arrhenius scaling) is observed in the case of  $N_C$  curves. Therefore, a single analytical model can be obtained. On the other hand, while the linear time scaling still applies among the  $N_I$  curves, the Arrhenius time scaling holds only during early stages of the evolution due to the temperature-dependence of the saturation value (larger at higher temperatures). Hence, for  $N_I$ , a specific model is formulated for each temperature.

**TABLE OF CONTENTS**

- 8.9 Object Kinetic Monte Carlo Simulations of Cascade Annealing in Tungsten — 161**  
G. Nandipati, W. Setyawan, H. L. Heinisch, K. J. Roche, R. J. Kurtz (Pacific Northwest National Laboratory) and B. D. Wirth (University of Tennessee)
- We used our recently developed lattice based object kinetic Monte Carlo code; KSOME [1] to carryout simulations of annealing of individual displacement cascades in bulk tungsten that were generated using molecular dynamics (MD) simulations, at temperatures of 300, 1025 and 2050 K and PKA energies up to 100 keV. We find that at smaller PKA energies the fraction of surviving self-interstitial atoms (SIAs) and vacancies decreases with temperature, whereas at higher PKA energies the fraction of surviving defects at first decreases and then increases with temperature.
- 9. IRRADIATION METHODS, EXPERIMENTS, AND SCHEDULES**
- 9.1 Fusion Material Irradiation Test Station (FMITS) at SNS — 167**  
Mark Wendel, Phil Ferguson (Oak Ridge National Laboratory)
- Highlights of the FMITS Concept Design include safety round-table findings, advances in the mechanical design of the harness and vent-line shield block (through which FMITS utilities pass), improved remote handling procedures and tooling, and refinements of the user science envelope. Samples would be welded inside the FMITS target harness in two horizontal tubes, which project out in front of the mercury target. For these specimen locations, the back-scattering neutron flux spectra should be close to the ITER fusion spectrum. The PKA spectra at the FMITS samples were also compared to those for ITER, and the results show good agreement. Radiation damage rates would be 1.6–5.5 dpa/y for steel, with the range of helium-to-dpa production ratios starting close to those expected in D-T fusion, and increasing toward beam center locations.
- 9.2 HFIR Irradiation Experiments – December 31, 2013 — 175**  
Y. Katoh (Oak Ridge National Laboratory)

## 1.1 Stability of MX-Type Nanoprecipitates in Fe-Base Model Alloys — L. Tan, Y. Katoh, L. L. Snead (Oak Ridge National Laboratory)

### OBJECTIVE

Study the stability of MX-type nanoprecipitates in reduced-activation ferritic (RAF) steels using Fe-base model alloys under thermal, stress, and radiation conditions to help understanding the failure mechanisms of RAF steels and identify promising strengthening particles for advanced RAF steel development.

### SUMMARY

The stability of MX-type nanoprecipitates TaC, TaN, and VN has been evaluated using thermal aging at 600 and 700°C for up to 5000 h, creep testing at 600°C, and Fe<sup>2+</sup> ion irradiation at 500°C and up to ~49 dpa. Transmission electron microscopy (TEM) has been primarily used to characterize the evolution of the nanoprecipitates. The results indicate different levels of stability of the nanoprecipitates under the three types of experimental conditions. Selected particle degradation modes, e.g., dissolution, growth, re-precipitation, and fragmentation, were observed on the nanoprecipitates. The results are being reported and compared to literature data in our recent papers. A parallel experiment using neutron irradiation at 300, 500, and 650°C for up to about 20 dpa has been completed recently. Post-irradiation examination (PIE) of the neutron-irradiated samples will be conducted to compare them with the Fe<sup>2+</sup> ion irradiated results.

### PROGRESS AND STATUS

#### Introduction

MX-type precipitates have shown excellent coarsening resistance compared to Laves phase and chromium-rich M<sub>23</sub>C<sub>6</sub> in 9-12% Cr ferritic-martensitic steels as well as RAF steels. The MX-type precipitates are believed to be critical for high temperature strength of this class of steels. Recently, however, limited data have shown the instability of MX, e.g., VN, TaC, and TaN, at elevated temperatures and irradiation conditions [1-4]. Therefore, three model alloys, respectively favoring the formation of TaC, TaN, and VN nanoprecipitates, had been designed and prepared to investigate the stability of these nanoprecipitates under thermal aging, creep testing, and irradiation conditions.

#### Experimental Procedure

Samples of the TaC, TaN, and VN bearing model alloys were subjected to thermal aging at 600 and 700°C for up to 5000 h, creep testing at 600°C, and Fe<sup>2+</sup> ion irradiation at 500°C for up to ~49 dpa. The microstructures of the samples were characterized using transmission electron microscopy (TEM) in both conventional and scanning modes (STEM) on a FEI CM200 field-emission-gun TEM/STEM equipped with an EDAX energy dispersive X-ray spectroscopy (EDS) detector. TEM specimens, perpendicular to the surfaces, were lifted out and thinned to electron-transparent using focused ion beam (FIB) on a Hitachi NB5000. Specimen thickness

of the characterized regions was estimated using convergent beam electron diffraction (CBED) technique.

## Results

The thermal aging experiment exhibited different effects on the stability of the nanoprecipitates. The lower temperature aging at 600°C basically led to coarsening in different degrees, accompanied with corresponding reduction in number density. In contrast, the higher temperature aging at 700°C resulted in a bimodal phenomenon to the nanoprecipitates. Figure 1 shows an example of TaC nanoprecipitates after aging at 600 and 700°C for 5000 h. Compared to the slightly coarsened TaC particles at 600°C in the bright-field (BF) image, 700°C-aged sample in the dark-field (DF) image is predominant with ultrafine TaC particles, together with a few large particles that have size similar to the 600°C-aged sample. The high-resolution image shows lattice fringes of two large particles and one ultrafine particle pointed with a white arrow. The ultrafine particle having a different orientation from the two large particles suggests that the ultrafine particle may have been re-precipitated during the 700°C aging.

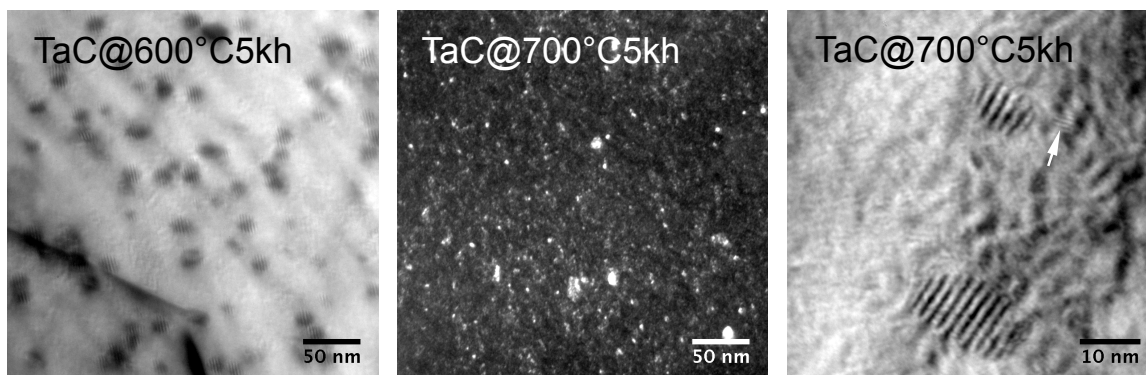


Figure 1. Effect of thermal aging at 600 and 700°C for 5000 h on the stability of TaC nanoprecipitates.

Microstructures at both the tab and gauge sections of the 600°C creep-tested samples were characterized using TEM. The tab section is assumed to be stress-free other than the stress-intensified regime at gauge section. This assumption is reasonable as the characterized results at the tab section are generally consistent with the thermal aging results at 600°C. The stress at gauge section significantly altered the geometry of TaN particles, as shown in DF images of Figure 2. The aligned plate-shaped particles were getting thinner and fragmented under the stress, which significantly reduced the size and increased the number density of the particles. Unlike TaN particles, the stress did not alter the geometry but slightly or noticeably increased the size of the TaC and VN particles.

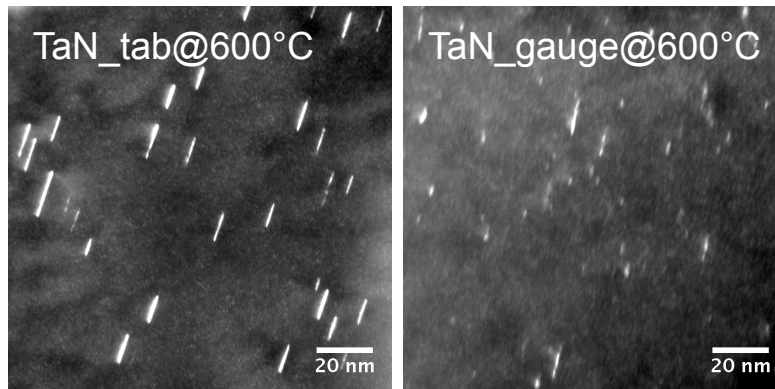


Figure 2. DF TEM images of the tab and gauges sections of the TaN sample after creep testing at 600°C and 170 MPa.

The  $\text{Fe}^{2+}$  ion irradiated samples were characterized using FIB-ed TEM specimens. Figure 3 shows an example of the VN-bearing sample from the irradiated surface on left to the matrix on right of the DF image. The irradiation damage (dpa) depth profile in the model alloy, aligned beneath the DF image, was simulated using the stopping and range of ions in matter software SRIM-2013 [5] with parameters recommended by Stoller *et al.* [6]. The length, thickness, and number density of the particles were statistically analyzed as a function of the irradiation depth as well as irradiation dose (dpa) according to the SRIM-simulated result. Similar analyses were conducted for the TaC and TaN particles.

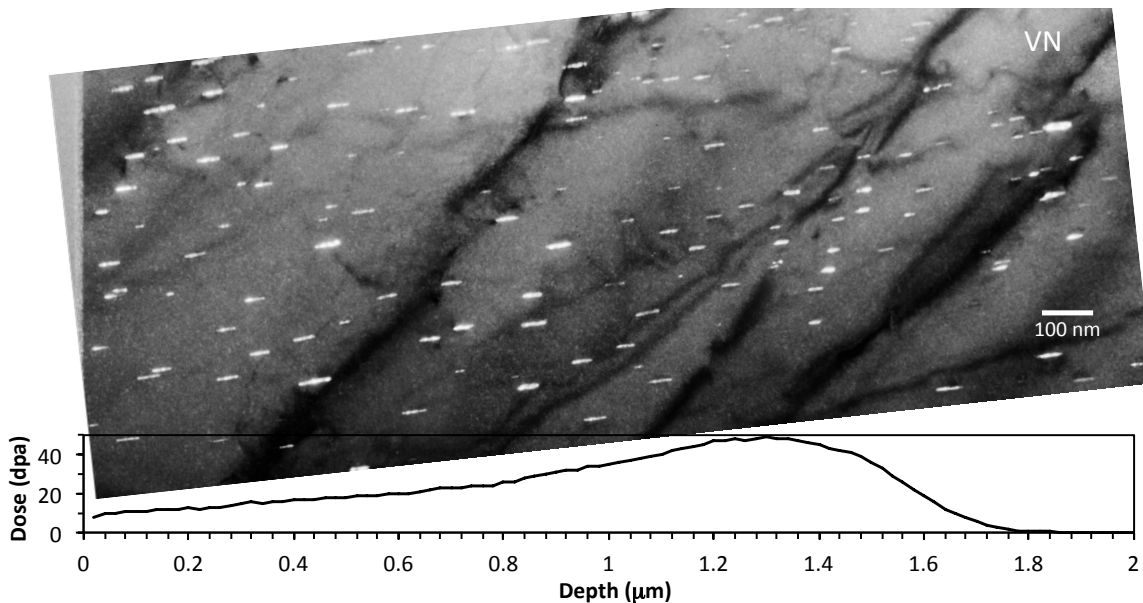


Figure 3. DF TEM image of the VN sample after  $\text{Fe}^{2+}$  irradiation at 500°C, accompanied with the simulated depth profile of irradiation dose in dpa using SRIM-2013.

Compared to the nitrides of TaN and VN, generally, TaC nanoprecipitates exhibited relatively greater stability in terms of thermal aging, creep testing, and Fe<sup>2+</sup> irradiation resistance. Both consistency and discrepancies with literature reported results are discussed in our recent papers [7,8]. Neutron irradiation experiment of the model alloy samples has been completed recently. The PIE of the samples will be conducted to compare them with the Fe<sup>2+</sup> ion irradiated results.

## REFERENCES

- [1] M. Tamura, H. Sakasegawa, A. Kohyama, H. Esaka, and K. Shinozuka, *J. Nucl. Mater.* **329** (2004) 328.
- [2] A. Kabadwal, M. Tamura, K. Shinozuka, and H. Esaka, *Metall. Mater. Trans. A* **41** (2010) 364.
- [3] H. Tanigawa, H. Sakasegawa, and R. L. Klueh, "Irradiation effects on precipitation in reduced-activation ferritic/martensitic steels," *Mater. Trans.* **46** (2005) 469-474.
- [4] H. Tanigawa, H. Sakasegawa, H. Ogiwara, H. Kishimoto, and A. Kohyama, "Radiation induced phase instability of precipitates in reduced-activation ferritic/martensitic steels," *J. Nucl. Mater.* **367-370** (2007) 132-136.
- [5] The Stopping and Range of Ions in Matter (SRIM) (<http://www.srim.org>).
- [6] R. E. Stoller, M. B. Toloczko, G. S. Was, A. G. Certain, S. Dwaraknath, and F. A. Garner, "On the use of SRIM for computing radiation damage exposure," *Nucl. Instrum. Methods Phys. Res. B* **310** (2013) 75-80.
- [7] L. Tan, Y. Kotah, and L. L. Snead, "Stability of the strengthening nanoprecipitates in reduced activation ferritic steels under Fe<sup>2+</sup> ion irradiation," *J. Nucl. Mater.* **445** (2014) 104-110.
- [8] L. Tan, T. S. Byun, Y. Kato, and L. L. Snead, "Stability of MX-type strengthening nanoprecipitates in ferritic steels under thermal aging, stress, and ion irradiation," in preparation.

## 2.1 DEVELOPMENT OF ODS FeCrAl FOR FUSION REACTOR APPLICATIONS – D. T. Hoelzer, K. A. Unocic, S. Dryepondt and B. A. Pint (Oak Ridge National Laboratory, USA)

### OBJECTIVE

The dual coolant lead-lithium (DCLL) blanket concept requires improved Pb-Li compatibility with ferritic steels in order to demonstrate viable blanket operation in a DEMO-type fusion reactor. The goal of this work is to develop an oxide dispersion strengthened (ODS) alloy with improved compatibility with Pb-Li and excellent mechanical properties. The current focus is characterizing the first batch of ODS Fe-12Cr-5Al.

### SUMMARY

Three experimental ODS FeCrAl heats of composition Fe-12Cr-5Al were prepared by mechanical alloying with additions of  $Y_2O_3$ ,  $Y_2O_3 + ZrO_2$  and  $Y_2O_3 + HfO_2$ . The as-extruded microstructure showed smaller grain size with the co-additions of  $ZrO_2$  or  $HfO_2$  and high concentrations of nano-size (<5 nm diameter) oxide particles within the grains. In the alloy with  $Y_2O_3 + HfO_2$ , either a bimodal or trimodal particle size distribution was observed. Tensile testing was performed at 25° up to 800°C and the higher oxide contents with  $ZrO_2$  or  $HfO_2$  resulted in higher yield and ultimate strengths but lower ductility compared to the alloy with only  $Y_2O_3$ .

### PROGRESS AND STATUS

#### Introduction

The DCLL blanket concept (Pb-Li and He coolants) is the leading U.S. design for a test blanket module (TBM) for ITER and for a DEMO-type fusion reactor.[1] With reduced activation ferritic-martensitic (FM) steel as the structural material, the DCLL is limited to ~475°C metal temperature because Fe and Cr readily dissolve in Pb-Li above 500°C and Eurofer 97 plugged a Pb-Li loop at 550°C.[2-3] For a higher temperature blanket for DEMO, structural materials with enhanced creep and compatibility are needed. ODS FeCrAl alloys are one possibility to meet this objective and considerable research on ODS FeCr alloys has shown an excellent combination of creep strength and radiation resistance.[4-7] However, these ODS FeCr alloys do not have adequate compatibility with Pb-based coolants, such as Pb-Bi eutectic (LBE) [8-11]. With the addition of Al, isothermal compatibility tests have shown low mass losses at up to 800°C.[12] Therefore, a materials development effort is underway, specific to this application. ODS FeCrAl was commercialized in the 1970's for its high temperature (>1000°C) creep and oxidation resistance [13] and other research groups are currently investigating new FeCrAl alloy compositions for fission and fusion applications with liquid metals.[14-16]

Previously, initial work was presented to identify composition factors such as the stability of ternary oxides and the Pb-Li compatibility of cast model FeCrAl alloys.[17,18] While previous studies found good Pb-Li compatibility for Fe-20wt.%Cr-5.5Al,[12] there is concern about thermal ageing embrittlement and the formation of  $\alpha'$  during irradiation due to the high Cr content [19]. Thus, the initial alloy fabrication focused on a base alloy composition of Fe-12Cr-5Al, as 5%Al was identified as being the minimum Al content needed for low mass change in Pb-Li at 700°C.[17] Based on the oxide stability experiments, combinations of  $Y_2O_3$  and  $ZrO_2$  or  $HfO_2$  were initially fabricated along with only  $Y_2O_3$ . A fourth alloy with  $Y_2O_3$  and  $TiO_2$  also is being processed but has not been extruded yet.

## Experimental Procedure

Three experimental ODS FeCrAl ferritic alloys were produced by mechanical alloying (MA). Powder of specified composition Fe-12.1wt.%Cr-5.0Al and particle size range ~45-150  $\mu\text{m}$  was prepared by Ar gas atomization by ATI Metal Powders. The FeCrAl powder was blended with  $\text{Y}_2\text{O}_3$  powder (17-31 nm crystallite size, produced by Nanophase, Inc.) and batches included  $\text{ZrO}_2$  and  $\text{HfO}_2$  powders (<100 nm diameter from American Elements). Three 1 kg batches of powder were prepared for ball milling with the following oxide additions: (1)  $0.3\text{Y}_2\text{O}_3$ , (2)  $0.3\text{Y}_2\text{O}_3 + 0.4\text{ZrO}_2$  and (3)  $0.3\text{Y}_2\text{O}_3 + 0.22\text{HfO}_2$ . Each batch was ball milled for 40 h in Ar gas atmosphere using the Zoz CM08 Simoloyer. After ball milling, the powders were placed in mild steel cans, degassed at  $300^\circ\text{C}$  under vacuum and sealed. The cans were equilibrated at  $950^\circ\text{C}$  for 1 h and then extruded through a rectangular shaped die. Table 1 shows the as-extruded compositions of each alloy. The alloys with additional  $\text{ZrO}_2$  and  $\text{HfO}_2$  oxide additions showed higher O contents and the Cr and Al contents were lower than the starting powder. Other typical impurities were Co, Cu, Ni and Mn at the 0.01-0.02% level and the C and N pickups from the milling process were acceptable. Tensile tests were performed using SS-3 type tensile specimens fabricated with the gage section (7.62 mm long and 0.762 mm thick) parallel to the extrusion axis of the ODS FeCrAl heats. The tensile tests were conducted in an MTS hydraulic frame at temperatures ranging from  $25^\circ\text{C}$ - $800^\circ\text{C}$  and a strain rate of  $10^{-3} \text{ s}^{-1}$ . Polished metallographic specimens were examined with a JEOL model 6500 Field Emission Gun (FEG) Scanning Electron Microscope (SEM) employing X-ray Energy Dispersive Spectroscopy (XEDS). The average grain size was obtained by the line intercept method in terms of the 95-percent confidence interval around the mean. Specimens for Transmission Electron Microscope (TEM) analysis were prepared by Focused Ion Beam (FIB, Hitachi model NB500) using the in-situ lift-out method from the polished metallographic samples of the extruded ODS FeCrAl heats. A Philips model CM200 FEG-TEM/STEM (Scanning TEM) with XEDS and EELS (Electron Energy Loss Spectroscopy) was used for analysis. Bright-Field (BF) and High Angle Annular Dark Field (HAADF) STEM and Energy Filtered TEM (EFTEM) imaging methods were used in the microstructural investigations.

## Results and Discussion

The general microstructural features of the ODS FeCrAl heats observed by BF STEM are shown in Figure 1. In the micrographs, the extrusion direction runs horizontally from left to right. The results showed variations in grain size for the three heats (Table 2); the largest grain size was observed with only  $\text{Y}_2\text{O}_3$  (Figure 1a) and the smallest grain size was observed for  $\text{Y}_2\text{O}_3 + \text{ZrO}_2$  (Figure 1b) with that of  $\text{Y}_2\text{O}_3 + \text{HfO}_2$  (Figure 1c) in between. The grain size was measured parallel and normal to the extrusion axis to determine the grain aspect ratio (GAR), which is shown in Table 2. The results showed no significant elongation of the grains parallel to the extrusion direction of the heats since the GAR values were <2 for the three heats.

Particles showing dark contrast in BF STEM images were observed in each of the three heats, but a higher number density of these particles was observed in the alloy with  $\text{Y}_2\text{O}_3 + \text{HfO}_2$  (Figure 1c). Higher

Table 1. Alloy chemical compositions (mass% or ppmw) by inductively coupled plasma analysis and combustion analysis.

Material	Fe%	Cr%	Al%	Y%	O	C	N	S	Other
Powder	82.8	12.1	5.0	<	64	31	11	<3	0.004Si
125Y	83.3	11.4	4.8	0.19	842	380	455	20	0.05W, 0.02Si, 0.01Ti
125YZ	82.8	11.5	4.9	0.18	1920	250	161	10	0.30Zr, 0.01Hf, 0.01Si
125YH	82.3	11.7	4.8	0.17	2280	220	110	10	0.68Hf, 0.01Zr, 0.01Si
PM2000	74.1	19.1	5.5	0.39	2480	14	86	8	0.48Ti, 0.02Si

< indicates below the detectability limit of <0.01%

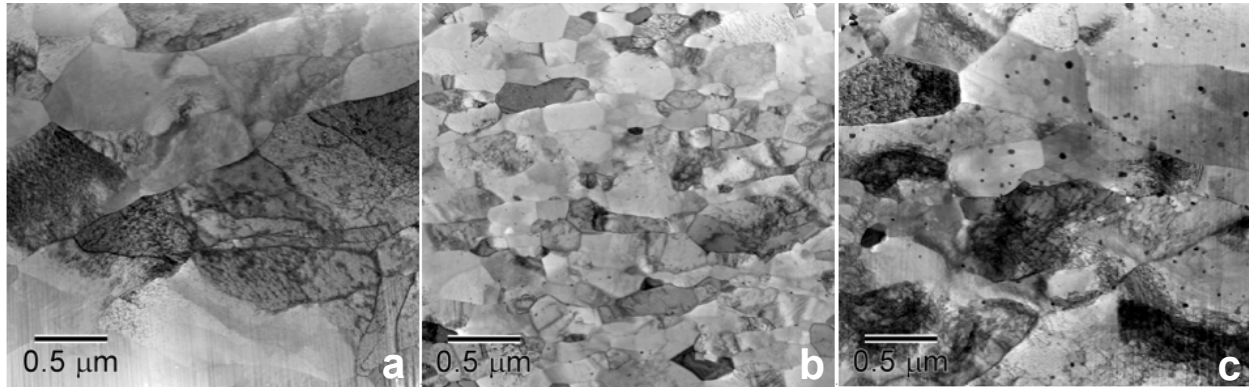


Figure 1. BF STEM micrographs showing the grain size and structure of the extruded ODS FeCrAl heats; (a) with  $Y_2O_3$ , (b)  $Y_2O_3 + ZrO_2$  and (c)  $Y_2O_3 + HfO_2$ . The extrusion axis lies horizontal from left to right.

magnification images of the oxide particle dispersions in each heat are shown in Figure 2. The microstructural analysis revealed bimodal particle sizes in the alloys with  $Y_2O_3$  and  $Y_2O_3 + ZrO_2$  and a trimodal particle size with  $Y_2O_3 + HfO_2$  based on differences in size and phase, i.e. image contrast and XEDS. The average particle size (d) determined from the bimodal and trimodal size distributions of the ODS FeCrAl heats are shown in Table 3. In general, the oxide particles observed in the bimodal size distributions with  $Y_2O_3$  and  $Y_2O_3 + ZrO_2$  showed dark contrast relative to the surrounding matrix in HAADF STEM images suggesting that they are an oxide phase. The oxygen-enriched nanoclusters observed in the advanced ODS 14YWT ferritic alloy have also been shown to exhibit darker contrast than the surrounding matrix when imaged by HAADF (commonly known as Z or atomic number contrast), since the intensity scales with  $Z^2$ . [20] The smaller particles ( $d \sim 2.5$  nm with only  $Y_2O_3$  and  $d \sim 2.9$  nm with  $Y_2O_3 + ZrO_2$ ) were present within grains and showed the highest number densities. A lower number density of larger particles ( $d \sim 7$  nm with only  $Y_2O_3$  and  $d \sim 9$  nm with  $Y_2O_3 + ZrO_2$ ) were mostly associated near grain boundaries in these heats. In the trimodal size distribution with  $Y_2O_3 + HfO_2$ , only the smallest particles ( $d \sim 3.2$  nm) showed dark contrast in HAADF STEM images as shown in Figure 3. Particles in the intermediate size range ( $d \sim 14.5$  nm) showed dark and bright contrast (indicated by arrows) while those in the largest size range ( $d \sim 28$  nm) showed bright contrast relative to the surrounding matrix, Table 3. The XEDS analysis of the largest particles showed that they were Hf-rich. The size distributions determined for the different types of particles observed in each heat are shown in Figure 4. In the counting assessment, an equal number of particles were measured in each population and are distinguished in the bar graphs with different colors. It is possible that the particles comprising the bimodal size distributions observed with only  $Y_2O_3$  (Figure 4a) and with  $Y_2O_3 + ZrO_2$  (Figure 4b) are the same phase indicating that the particles experienced different nucleation mechanisms, for example, higher solute diffusion rates near grain boundaries compared to bulk diffusion rates in the grains. For the alloy with  $Y_2O_3 + HfO_2$  (Figure 4c), the scale for particle sizes was increased to show the trimodal size distributions, which accounts for the high frequency value observed for particles below 5 nm in size. The results show three distinct particle size ranges representing the different oxide phases present in this alloy.

Table 2. Measurements of the grain size and grain aspect ratio (GAR) of the ODS FeCrAl ferritic alloys.

Alloy	Grain Size ( $\mu\text{m}$ )		GAR (Parallel/Normal)
	Parallel to Extrusion Axis	Normal to Extrusion Axis	
125Y	$0.83 \pm 0.17$	$0.56 \pm 0.09$	1.48
125YZ	$0.27 \pm 0.06$	$0.17 \pm 0.02$	1.59
125YH	$0.70 \pm 0.16$	$0.39 \pm 0.06$	1.79

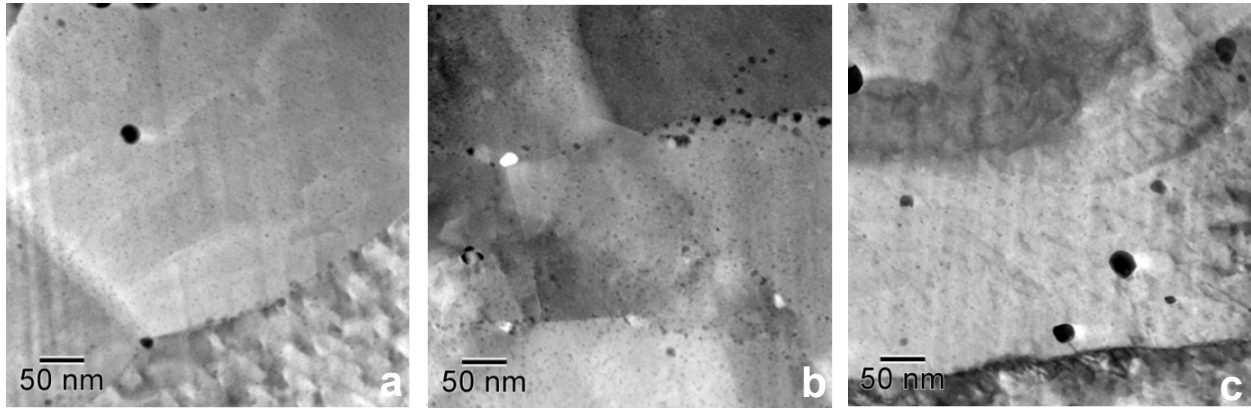


Figure 2. STEM micrographs showing the oxide particle dispersions in the extruded ODS FeCrAl heats; (a) BF STEM with  $Y_2O_3$ , (b) HAADF STEM with  $Y_2O_3 + ZrO_2$  and (c) BF STEM with  $Y_2O_3 + HfO_2$ .

Table 3. Measurements of the particle size diameters (nm) of the three Fe-12Cr-5Al heats based on the type of particle contrast in the HAADF images.

Alloy	Small dark contrast	Large dark contrast	Dark/bright contrast	Large bright contrast (Hf-rich)
125Y	$2.43 \pm 0.36$	$6.87 \pm 0.82$	–	–
125YZ	$2.91 \pm 0.32$	$8.97 \pm 0.85$	–	–
125YH	$3.18 \pm 0.51$	–	$14.58 \pm 2.18$	$27.77 \pm 3.49$

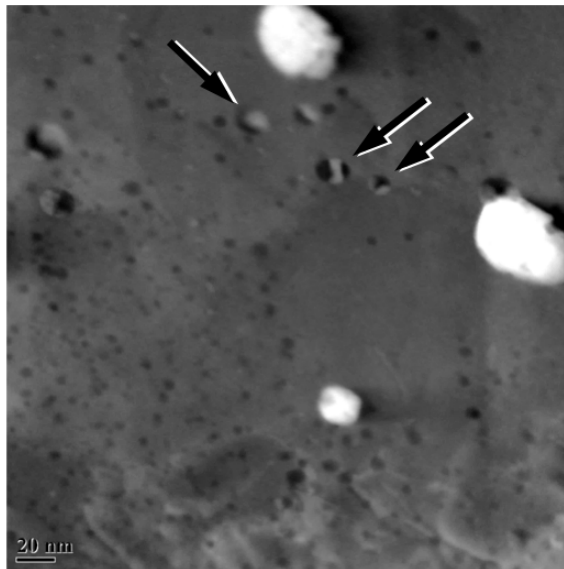


Figure 3. HAADF STEM image of the alloy with  $Y_2O_3 + HfO_2$  showing the contrast characteristics of three different particles; small dark contrast, dark/bright contrast (arrows) and large bright Hf-rich contrast.

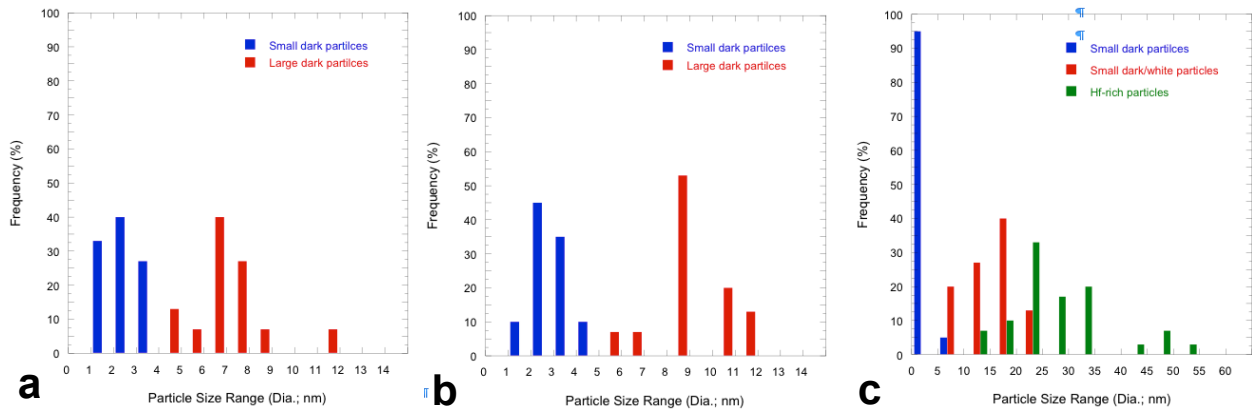


Figure 4. The size distributions measured for the different oxide particles observed in the ODS FeCrAl heats; (a) with  $Y_2O_3$ , (b)  $Y_2O_3 + ZrO_2$  and (c)  $Y_2O_3 + HfO_2$ .

The results of the tensile testing from 25°-800°C are shown in Figure 5 and are compared to data for unrecrystallized PM2000 (composition shown in Table 1). The values for yield stress ( $\sigma_{ys}$ ) and ultimate tensile strength ( $\sigma_{uts}$ ) and their temperature dependence were similar with  $Y_2O_3 + ZrO_2$  and  $Y_2O_3 + HfO_2$  (Figure 5c) and consistently higher than the values with only  $Y_2O_3$ , Figure 5a. All of the new alloys were higher than the values for PM2000. At room temperature, the  $\sigma_{ys}$  was >1200 MPa and the  $\sigma_{uts}$  was >1300 MPa for the alloys with greater oxide additions compared to  $\sigma_{ys} = 1017$  MPa and  $\sigma_{uts} = 1235$  MPa for the alloy with only  $Y_2O_3$ . Both alloys with  $Y_2O_3 + ZrO_2$  and with  $Y_2O_3 + HfO_2$  retained significant levels of strength at 800°C, with  $\sigma_{ys} = 327$  and 304 MPa and  $\sigma_{uts} = 381$  and 334 MPa, respectively. These are considerably higher than the  $\sigma_{ys} = 73$  MPa and  $\sigma_{uts} = 120$  MPa measured for PM2000 at 800°C. However, considerably different behavior was observed for the total elongation measurements in these tensile tests, Figure 5b. The elongation for PM2000 was significantly higher than any of the 12Cr-5Al alloys, especially at the higher temperatures. The large difference for PM2000 is likely related to the extrusion conditions and requires further study. Among the new alloys, both the uniform elongation and total elongation were

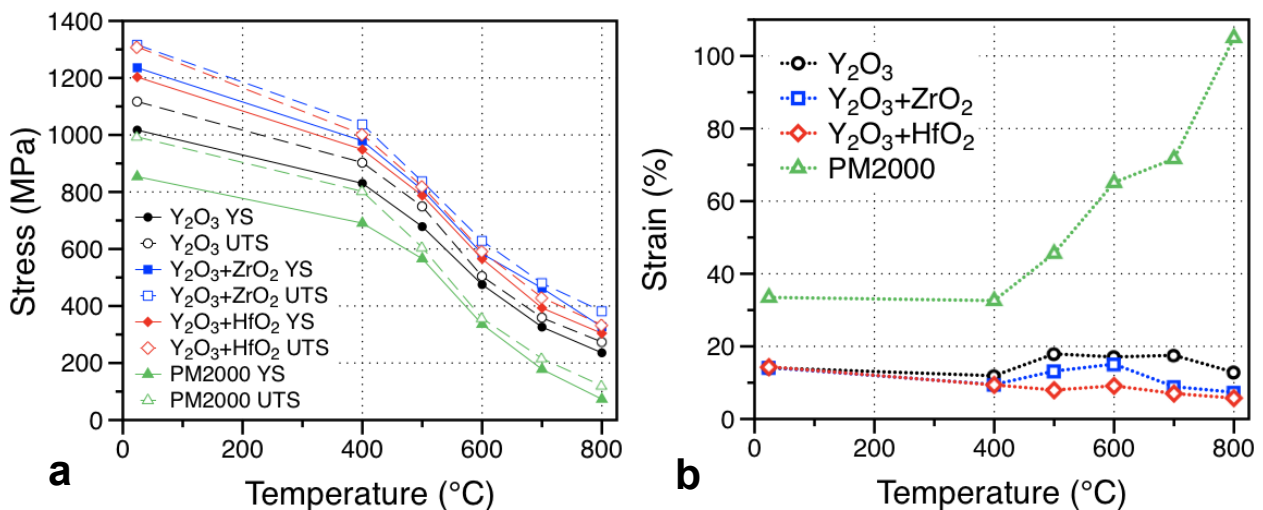


Figure 5. Tensile properties of the ODS FeCrAl heats as a function of test temperature. (a) yield stress and ultimate tensile strength and (b) total elongation.

very similar at room temperature. As the test temperature increased from 25° to 800°C, the total elongation was consistently highest for the alloy with only Y<sub>2</sub>O<sub>3</sub> compared to the other two alloys. The alloy with Y<sub>2</sub>O<sub>3</sub> + ZrO<sub>2</sub> had slightly higher ductility at 500° and 600°C. All of the new heats showed reasonable work hardening from 25° to 800°C, except for the alloy with only Y<sub>2</sub>O<sub>3</sub>, which showed very little work hardening capacity at 800°C.

## References

- [1] M. Abdou, D. Sze, C. Wong, M. Sawan, A. Ying, N. B. Morley and S. Malang, *Fus. Sci. Tech.*, 47 (2005) 475.
- [2] O. K. Chopra, D. L. Smith, P. F. Tortorelli, J. H. DeVan and D. K. Sze, *Fusion Technol.*, 8 (1985) 1956.
- [3] J. Konys, W. Krauss, J. Novotny, H. Steiner, Z. Voss and O. Wedemeyer, *J. Nucl. Mater.* 386-88 (2009) 678.
- [4] S. Ukai and M. Fujiwara, *J. Nucl. Mater.* 307 (2002) 749.
- [5] G. R. Romanowski, L. L. Snead, R. L. Klueh, D. T. Hoelzer, *J. Nucl. Mater.*, 283-287 (2000) 642.
- [6] R. L. Klueh, J. P. Shingledecker, R. W. Swindeman, D. T. Hoelzer, *J. Nucl. Mater.* 341 (2005) 103.
- [7] D. A. McClintock, M. A. Sokolov, D. T. Hoelzer and R. K. Nanstad, *J. Nucl. Mater.*, 392 (2009) 353.
- [8] T. Furukawa, G. Müller, G. Schumacher, A. Weisenburger, A. Heinzl and K. Aoto, *J. Nucl. Mater.* 335 (2004), 189.
- [9] P. Hosemann, H.T. Thau, A.L. Johnson, S.A. Maloy and N. Li, *J. Nucl. Mater.* 373 (2008) 246.
- [10] C. Schroer, J. Konys, T. Furukawa and K. Aoto, *J. Nucl. Mater.* 398 (2010) 109.
- [11] A. Weisenburger, K. Aoto, G. Müller, A. Heinzl, G. Schumacher and T. Furukawa, *J. Nucl. Mater.* 358 (2006) 69.
- [12] B. A. Pint, L. R. Walker and K. A. Unocic, *Mater. High Temp.* 29 (2012) 129.
- [13] J. D. Whittenberger, *Met. Trans.* 9A (1978) 101.
- [14] J. Lim, H.O. Nam, I.S. Hwang and J.H. Kim, *J. Nucl. Mater.* 407, (2010), 205.
- [15] A. Kimura, et al., *J. Nucl. Mater.* 417, (2011), 176.
- [16] S. Takaya, et al., *J. Nucl. Mater.* 428, (2012), 125
- [17] B. A. Pint, D. T. Hoelzer, D. Shin, J. O. Kiggans, Jr., K. A. Unocic, DOE/ER-0313/53 (2012) 10.
- [18] B. A. Pint, D. T. Hoelzer and K. A. Unocic, DOE/ER-0313/54 (2013) 27.
- [19] C. Capdevila, M.K. Miller, K.F. Russell, J. Chao, J.L. González-Carrasco, *Mater. Science and Engineering A*, 490, (2008), 277.
- [20] M.C. Brandes, L. Kovarik, M.K. Miller and M.J. Mills, *Journal of Materials Science*, 47, (2012), 3913.

**3.1 Process Development and Optimization for Silicon Carbide Joining and Irradiation Studies-III** — T. Koyanagi, J. Kiggans, C. Shih, Y. Katoh (Oak Ridge National Laboratory)

**OBJECTIVE**

The objective of this task is to develop and optimize joining processes for silicon carbide (SiC) ceramics and composites for fusion energy applications.

**SUMMARY**

Two robust pressureless joining methods for SiC ceramics proved to be promising. A Ti-Si-C MAX phase displacement reaction bonding using commercial bonding formula demonstrated dense microstructures and apparent shear strength of ~150 MPa. A pressureless transient eutectic-phase (TEP) process was newly developed to demonstrate promising properties. An experimental plan for the neutron irradiation effects study was developed.

**PROGRESS AND STATUS**

**Introduction**

Development of SiC joints that retain adequate mechanical and functional properties in fusion reactor environment is essential for use SiC and its composites as the primary structural material [1]. Requirement of external pressurization during joining process is a major factor that dictates applicability of a specific joining method to integration of components with certain geometries and dimensions. While several joining technologies for SiC ceramics and composites have proved to be neutron irradiation tolerant to low-to-intermediate fluence levels in our previous study [2], all the joining processes involved require substantial pressurization with an exception of the calcia-alumina glass-ceramic joining. The present work focuses on development of processes that are anticipated to be radiation-tolerant but do not require external pressurization for joining SiC ceramics and composites.

In the previous report [3], the optimal processing conditions for Ti and Mo foil joining have been established. In the present work, pressure-less Ti-Si-C MAX phase joining and pressure-less TEP joining were specifically prepared and evaluated. The Ti-Si-C MAX phase joining was chosen because of the previously demonstrated neutron tolerance for a similar joint, relatively low processing temperature requirement, and availability of commercial joining material. The TEP joining was considered particularly attractive because of its ability to produce SiC-based bond that anticipated leads to robust strength and irradiation tolerance.

Neutron irradiation can affect the physical and mechanical properties of the SiC joints, and the irradiation effects are of critical importance in reactor technology. This report also provides an updated technical plan for the neutron irradiation experiment in the High Flux Isotope Reactor (HFIR).

## **Experimental Procedure**

### **Materials**

For MAX phase bonding, a set of joining agent materials were purchased from Hyper-Therm High Temperature Composites, Inc. (currently Rolls-Royce High Temperature Composites, Inc., Huntington Beach, CA).  $\text{Ti}_3\text{SiC}_2$ -based joints of CVD SiC were produced at ORNL based on a pressure-less slurry process per the Hyper-Therm formula. Two types of the MAX phase joints were prepared in this work. The process conditions were same among them except for the method of slurry preparation. Details of the raw materials and the process conditions are proprietary.

The TEP joints were formed using four types of mixed powders. The mixed powders consist of SiC nano-powder (average diameters ~30 nm) or combined SiC nano- and micron-powders, and sintering additives ( $\text{Al}_2\text{O}_3$  powder and  $\text{Y}_2\text{O}_3$  powder) with or without organic agents. The total amount of the oxide additives was 6 or 10 wt.%. To form the TEP joints, SiC plates sandwiching thin mixed powder were cold-pressed at ~10 MPa and then heat-treated at 1875°C for 1 h in an argon atmosphere. Process conditions determined and the specimen ID are summarized in Table 1.

Table 1. Processing conditions, apparent shear strength, fracture behavior, and joint phases of CVD-SiC joined by MAX phase and TEP methods.

Joining method	Specimen ID	Processing Conditions				Joint Strength			Phases in joint layer
		Starting Materials	Atmosphere	Temperature (°C)	Time (h)	DNS Strength (MPa) <sup>2</sup>	Torsion shear strength (MPa) <sup>2</sup>	Fracture location	
MAX Phase	MAX-A	N.A. <sup>1</sup>	N.A.	N.A.	N.A.	141±23	152±16	Joint layer for DNS Substrate for torsion	Ti <sub>3</sub> SiC <sub>2</sub> , TiC, unknown phase
	MAX-B	N.A.	N.A.	N.A.	N.A.	44±10	142±15	Substrate and joint layer for DNS Substrate for torsion	Expected to be same as MAX-A
TEP	TEP-6A	SiC nano and micron powder, 6wt.% oxide additives, Organic agents	Ar	1875	1	113±52	N.D. <sup>3</sup>	Joint layer	SiC, oxide phases
	TEP-6B	SiC nano powder, 6wt.% oxide additives, Organic agents	Ar	1875	1	163±43	N.D.	Substrate	SiC, oxide phases
	TEP-6C	SiC nano powder, 6wt.% oxide additives,	Ar	1875	1	N.D.	N.D.	N.D.	SiC, oxide phases
	TEP-10B	SiC nano powder, 10wt.% oxide additives, Organic agents	Ar	1875	1	N.D.	N.D.	N.D.	SiC, oxide phases

<sup>1</sup> Not available due to the proprietary

<sup>2</sup> Average strength ±one standard deviation

<sup>3</sup> Not determined

Strength evaluation

Shear strength of the SiC joints were determined by double-notch shear (DNS) test [4] and torsional shear test. The DNS test has advantages for both the ease of specimen preparation and for testing. However, this test cannot provide uniform stress states at the joints, which makes an accurate evaluation of the strength difficult. The torsional shear test using an hourglass specimen is near ideal to evaluate accurate evaluation of the strength because of its ability to apply true shear loading to the joint specimens, but it is relatively difficult to machine the test specimen. Therefore, the DNS test was used for quick estimation of the shear strength and the torsion test was used for accurate strength evaluation in this work.

For DNS test specimen, distance between the notches, the notch width, and curvature radius of the notch tip were 3, 0.5, and 0.2 mm, respectively. The tip of both notches reached the joint layer. The tests were conducted at a constant cross head displacement rate of 0.6 mm/min. More than three DNS tests were conducted for each processing condition. Detailed test procedure can be found elsewhere [4].

The dimensions of the torsional test specimen were 6 mm × 6 mm × 3 mm, and diameter of the neck was 5 mm as shown in Figure 1. The torsional load was applied in a universal testing machine with a wire equipped rotating disk fixture (Figure 2). Aluminum-alloy tabs were installed at the square grip sections to obtain uniform stress distributions there. The crosshead speed was 1.0 mm/min with an estimated rotation speed of about 0.025 rad/min. Nominal shear strength values ( $\tau$ ) in this work are given by following equation,

$$\tau = 16T/\pi d^3 \tag{1}$$

where  $T$  is the applied torque and  $d$  is the specimen diameter of the neck. Number of the torsion test was more than two for each condition. Further description of details of the test method can be found elsewhere [4]. All mechanical tests were conducted at room temperature.

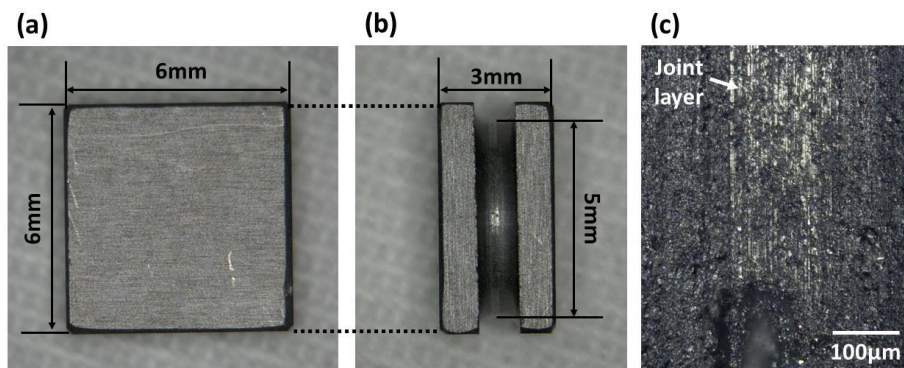


Fig. 1. Optical micrograph of torsional test specimen (MAX-B specimen): (a) Top-view image, and (b and c) side-view images.

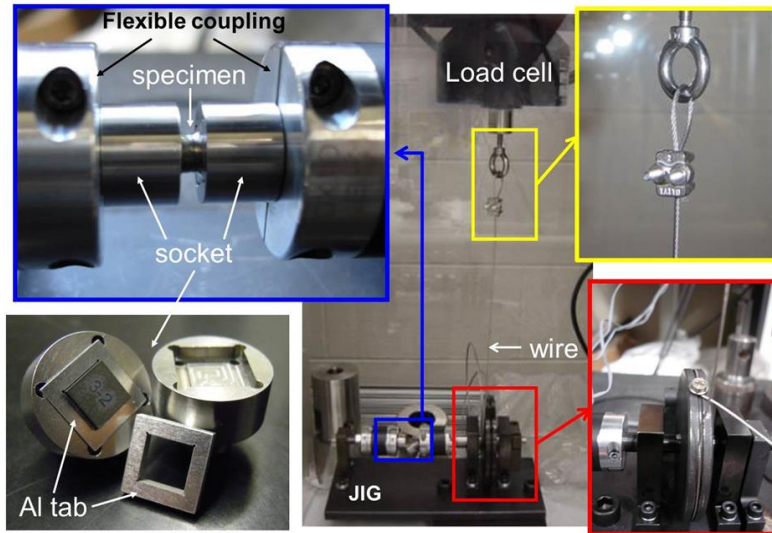


Fig. 2. Overview of the torsional testing machine.

### Metallographic examinations

Microstructures of the bonded regions were characterized using optical microscope (Keyence, VHX-1000) and field-emission scanning electron microscope (SEM, Hitachi, S4800) equipped with energy dispersive spectroscopy (EDS). The phases of the joints were determined by XRD analysis (Model Scinatang Pad V, Thermo ARL) on the fracture surface of the DNS specimens.

## **RESULTS**

### Pressureless MAX phase joining

Defects in the as-processed joints were observed using the optical microscope as shown in Figure 3. The MAX-A specimen contained high-density pores in the bonded-zone and the joint interface. By contrast, crack roughly perpendicular to the joint boundary was dominant processing defect in the MAX-B specimen.

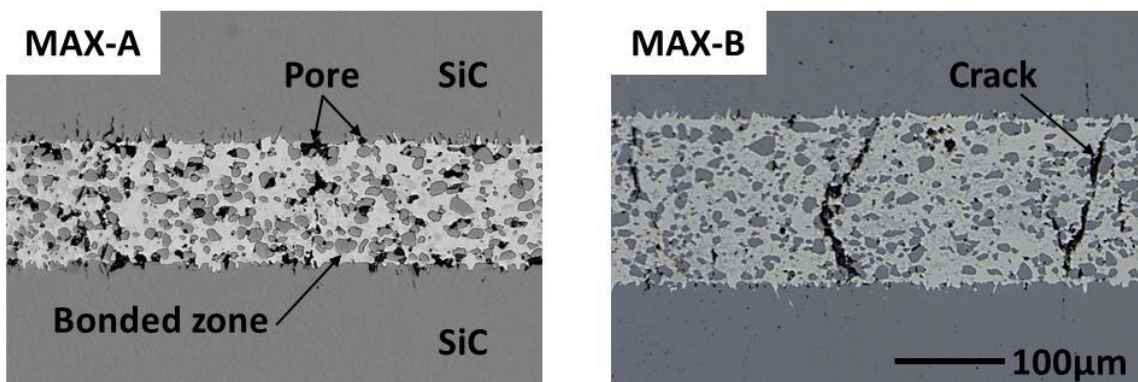


Fig. 3. Optical micrograph of MAX phase jointed SiC.

Analysis using SEM/EDS revealed that the bonded zone of the MAX-A specimen consisted of SiC grains and Ti-Si-C phase as shown in Figure 4(a). Hexagonal  $Ti_3SiC_2$  was the main phase in the Ti-Si-C phase based on SEM/EDS (Figure 4(b)) and XRD analysis. The Ti-Si-C phase also contained cubic TiC and unknown phase. The  $Ti_3SiC_2$  and TiC phases had random grain-orientation based on analysis of the XRD patterns. Note that the EDS spectrum of the point C in Figure 4(b) was affected by both  $Ti_3SiC_2$  and the unknown phase considering the spot size of the SEM. Average atomic number of the unknown phase was higher than  $Ti_3SiC_2$  judging from the backscattered electron image. Therefore, the possible candidates of that phase are TiSi,  $TiSi_2$ ,  $Ti_5Si_4$ , and  $Ti_5Si_3C_x$ , according to the phase diagram of Ti-Si-C system [4].

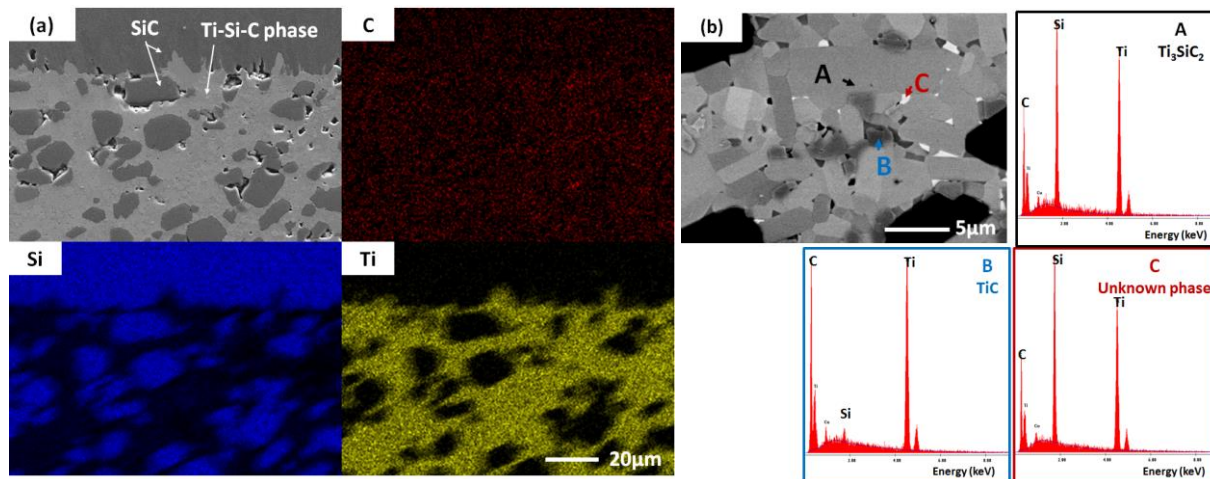


Fig. 4. SEM images and EDS spectra of the MAX-A specimen: (a) secondary electron image, and (b) backscattered electron image.

Figure 5 shows SEM images of the as-fabricated MAX phase joints. Micro-cracks along the grain boundaries were found in both specimens in addition to ~1 micron-sized pores. These cracks may be caused by the misfit strain due to differential coefficients of thermal expansion (CTE) between  $Ti_3SiC_2$  phase ( $a$ -axis  $8.6 \times 10^{-6} K^{-1}$ , and  $c$ -axes  $9.75 \times 10^{-6} K^{-1}$  at RT to  $906^\circ C$  [5]) and SiC ( $4.0 \times 10^{-6} K^{-1}$  at RT to  $1000^\circ C$  according to material property data sheet from Dow Chemical Co.).

The strong anisotropy of the thermal expansion in the  $Ti_3SiC_2$  phase was also possible cause of the micro cracking at the grain boundaries. Minor phases in Ti-Si-C layer can also affect the strain due to the CTE mismatch.

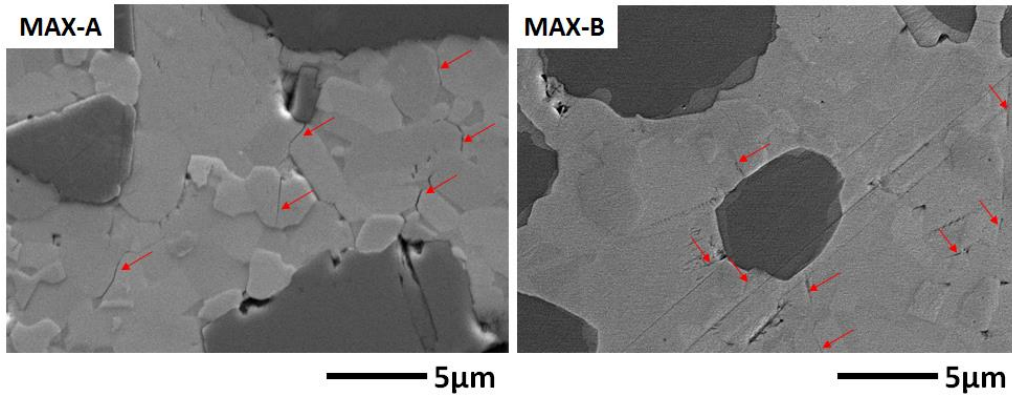
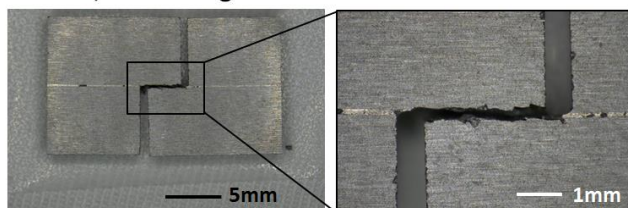


Fig. 5. Secondary electron images of as-fabricated MAX-A and MAX-B specimens. Micro-cracks are arrowed.

The apparent DNS strengths of the MAX phase joined SiC are summarized in Table 1. The average DNS strengths of the MAX-A and MAX-B joints were 141 and 44 MPa, respectively. In addition, the typical fracture appearances of the test specimens are shown in Figure 6. Notch to notch fractures were observed in both specimens. In the MAX-A specimen, the cracks propagated along the joint layer. By contrast, the cracks ran through both the SiC substrates and the joint layer in the MAX-B specimen. This differential fracture behavior may be caused by the differences of the defect shape, size, and the distribution in the bonded zone as shown in Figure 3.

MAX-A, DNS strength:141±23MPa



MAX-B, DNS strength:44±10MPa

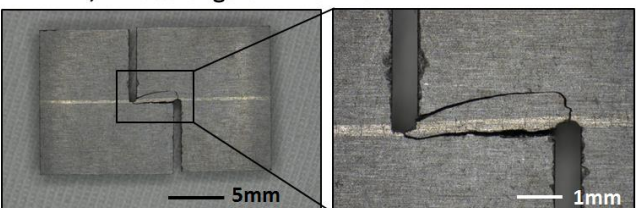


Fig. 6. Typical fracture appearances of MAX phase jointed SiC after DNS tests. The average strength and the one standard deviation are also shown.

Nominal shear strengths of ~150 MPa were demonstrated by the torsional test for both MAX phase jointed specimens. All specimens failed at the SiC substrates as shown in Figure 7, and the fracture appearance was similar between the MAX-A and MAX-B joint specimens. This base failure was typically observed in robust SiC joints determined by the torsional shear test on hourglass specimens [2]. In case of a weak bonding of SiC joints, the flat failure at the joint plane was observed, and the shear strength was typically less than ~100 MPa [2, 6]. Therefore, the torsional tests in this work indicate that both MAX phase joints had adequate shear strength. The weak DNS strength of the MAX-B specimen is not considered here, because only the torsional test can give a quantitative strength value as mentioned in the experimental section. It is difficult to identify the location of the crack initiation for the robust joints in the torsion test, because the neck part of the specimen got shattered into pieces after the test. In the torsional test, maximum stress is loaded at the surface of a neck with a minimum diameter, which corresponds to the jointed region in this study. Since machining defects on the specimen surface was more significant comparing to the process defects as shown in Figure 1(c), the fractures in the MAX phase jointed SiC might initiate from the machining defects near the joint layer.

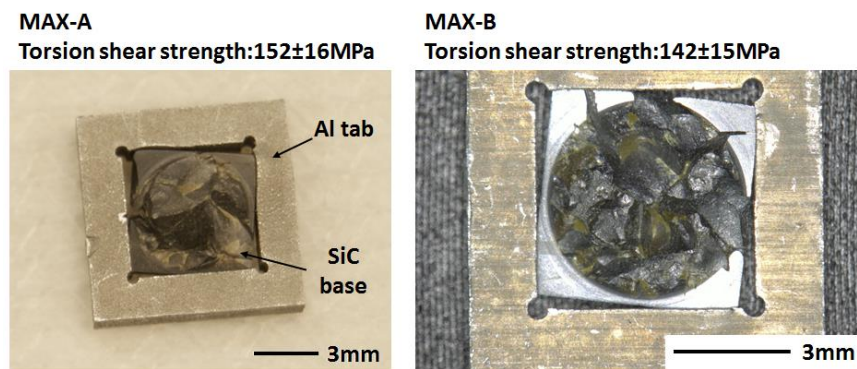


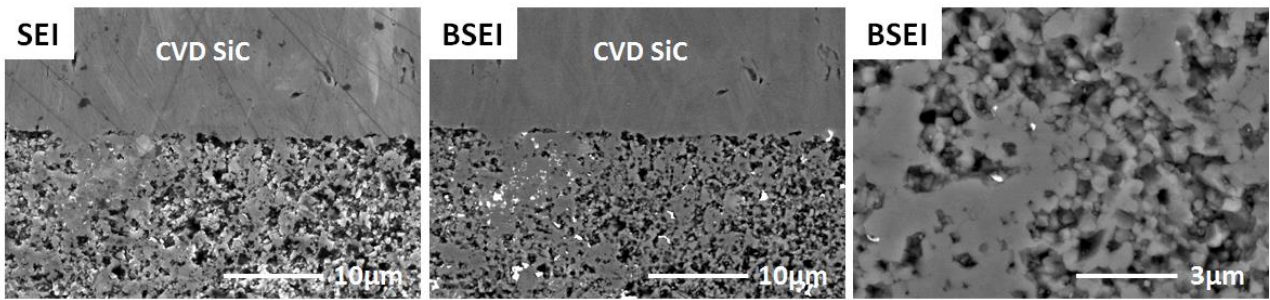
Fig. 7. Micrographs of pieces of the torsional tested specimens for the MAX-A and MAX-B. The average strength and the one standard deviation are also shown.

### Pressureless transient eutectic-phase joining

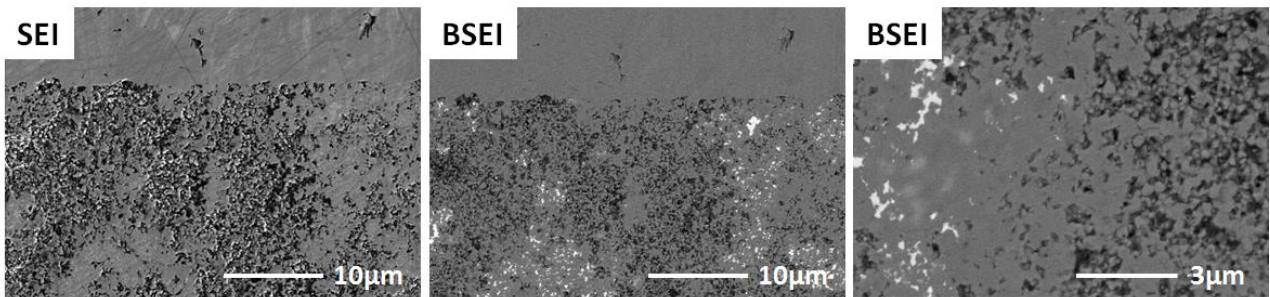
Microstructures of the as-fabricated TEP joined SiC are shown in Figure 8. It is found that the SiC-based joint layers of all specimens were composed of two different regions, where the one is well-sintered region and the other is porous region. The well-sintered regions contained secondary phases attributed to the sintering additives at the grain pockets and grain boundaries, and the secondary phases were rarely observed in the porous region. Effects of type of the starting SiC powder on the microstructures can be seen in SEM images of the TEP-6A fabricated with SiC nano- and micron-powders and TEP-6B with only the SiC nano-powder. Area ratio of the well-sintered region was not significantly different between them, but the size of the pores was smaller in the TEP-6 specimen. The effects of the use of the organic agents were clearly found in the images of the TEP-6B joint with the organic agents and TEP-6C joint without the organic agents. The large pores were observed in the bonded region of the TEP-6C joint. This result strongly indicates that the use of the organic agent was effective for improving the quality of the TEP joint.

The effects on the amount of sintering additives can be seen in the SEM images of the TEP-6B (6 wt.% of additives) joint and TEP-10B (10 wt.% of additives) joint. Reduction of the porosity was achieved by the increased use of the additives. On the other hand, the segregation of the secondary phases at the joint interface and network of the secondary phases became marked with increasing the amount of the additives. The reduction of the porosity is expected to be of advantage for the mechanical properties. The increased amount of the secondary phases possibly affects the irradiation resistance of the joint, but the effects are currently not clear, because both encouraging and negative results were reported. Excellent irradiation-resistance of the pressurized TEP joints was demonstrated following neutron irradiation at 500 and 800°C to up to 5.0 dpa [2]. On the other hand, significant degradation of the strength of monolithic SiC ceramics fabricated by the TEP method was reported following irradiation at 830 and 1270°C to ~6dpa [6]. The possible mechanism of this degradation is cracking and/or strain due to the differential swelling between SiC and the secondary phases. The effects of the secondary phases on the irradiation resistance will be determined in future HFIR irradiation experiment.

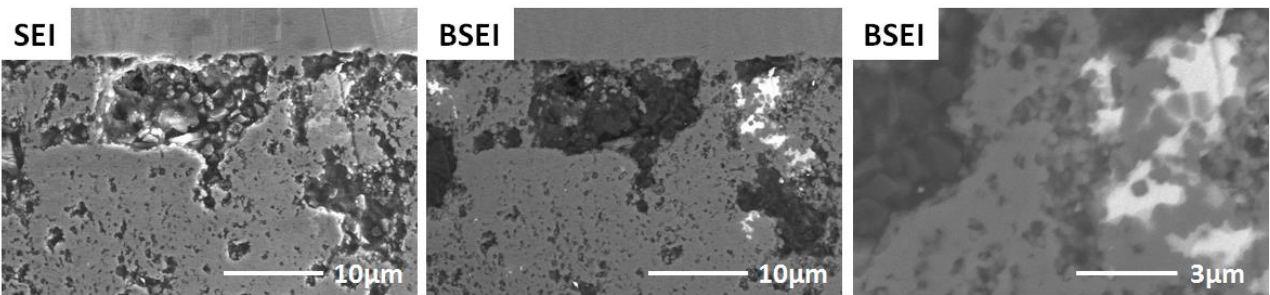
**TEP-6A**



**TEP-6B**



**TEP-6C**



**TEP-10B**

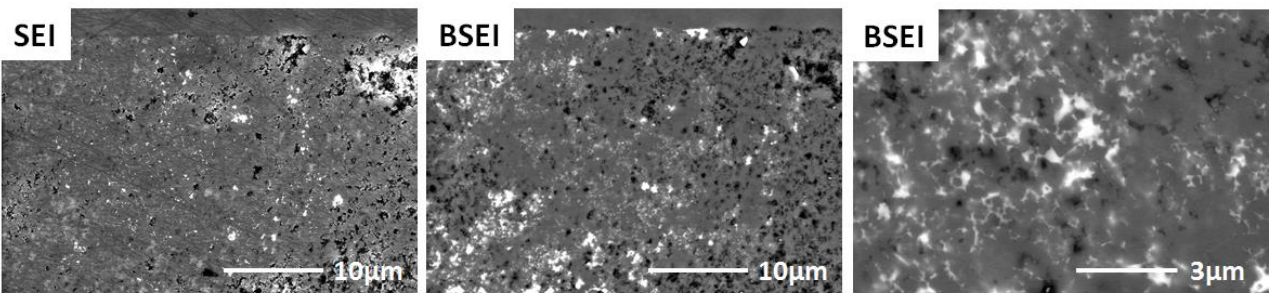


Fig. 8. Secondary electron image (SEI) and backscattered electron image (BSEI) of as-fabricated TEP jointed SiC.

The apparent DNS strengths of 113 MPa and 163 MPa were demonstrated for the TEP-6A and TEP-6B joint specimens, respectively. The one standard deviation was ~50 MPa for both joints. Though the strengths were similar to each other considering the large deviations, obvious difference of the fracture appearance was observed as shown in Figure 9. The TEP-6A joint failed at bonded zone by the DNS test. By contrast, cracks ran thorough the SiC substrates in the TEP-6B joint. The failure at the joint in the TEP-6A specimen indicates that the defects in the bonded zone affected this fracture behavior. The DNS strength of ~150 MPa with the failure at the substrates in the TEP-6B specimen is typical for very strong joints, implying absence of severe processing defect or misfit strain at the bonded zone.

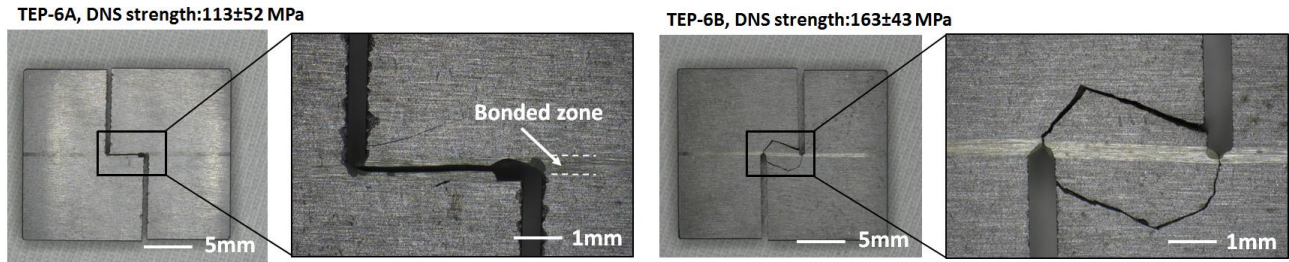


Fig. 9. Optical microscope images of the TEP-6M and TEP-6N specimen after the DNS test. The average strength and the one standard deviation are also shown.

### Irradiation test plans

It is planned that rabbit capsules containing the SiC joint specimens are irradiated in HFIR to study effects of irradiation on the shear strength. The conditions planned are irradiation at ~500°C to ~3dpa, ~500°C to >~10 dpa, and ~1000°C to ~3 dpa. The torsional test will be conducted as a post-irradiation experiment. Proven geometries of miniature torsion specimen are adopted in this experiment as shown in Figure 10 [2].

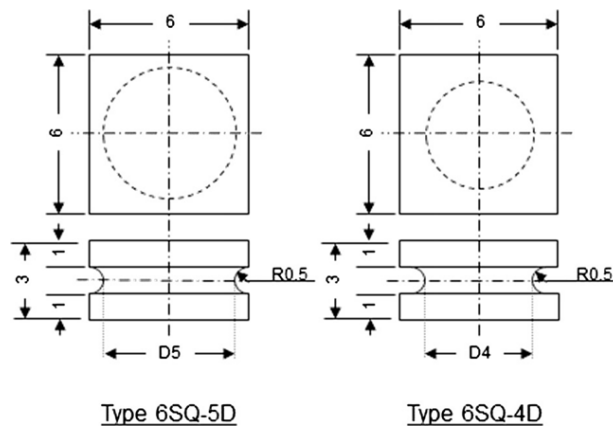


Fig. 10. Geometries of miniature torsion specimens for the irradiation study.

In the previous study conducted as a part of the ORNL and international fusion materials research and development program, several variations of SiC joints were neutron-irradiated in HFIR nominally at 500 and 800°C to the maximum dose of ~5 dpa. The joint materials included the monolithic SiC and its composites, joined by the titanium diffusion bonding, calcia-alumina (CA) glass-ceramic joining, Ti-Si-C MAX phase joining, TEP slurry joining, and TEP green tape joining. The post-irradiation examination for this experiment showed encouraging results including the retention of the pre-irradiation strength following all irradiation conditions [2]. The new experiment will evaluate irradiation tolerance of additional SiC joints prepared in this work or by collaborators. Effects of temperature and fluence on the irradiation resistance of the SiC joints will be also investigated. The joint materials that are planned to be irradiated in this campaign are listed in Table 2.

Table 2. Candidate materials for irradiation

Material description	Supplier
Rolls-Royce HTC Proprietary, Pressureless MAX-phase	Rolls-Royce HTC/ORNL
Ti Diffusion Bonding	ORNL
Mo Diffusion Bonding	ORNL
Pressureless TEP	ORNL
TEP, Slurry	Kyoto University
TEP, Green Tape	Kyoto University
Calcia-Alumina Glass-Ceramics	Politecnico di Torino
MAX-phase, Green Tape	PNNL
Spark Plasma Sintering	Queen Mary Univ.

## REFERENCES

- [1] Y. Katoh, L. L. Snead, C. H. Henager Jr, A. Hasegawa, A. Kohyama, B. Riccardi, and H. Hegeman, *J. Nucl. Mater.* **367** (2007) 659.
- [2] Y. Katoh, L. L. Snead, T. Cheng, C. Shih, W. D. Lewis, T. Koyanagi, T. Hinoki, C. H. Henager Jr., and M. Ferraris, *J. Nucl. Mater.* (2013) <http://dx.doi.org/10.1016/j.jnucmat.2013.10.002>.
- [3] T. Koyanagi, J. O. Kiggans, T. Cheng, Y. Katoh, Fusion Materials Semiannual Progress Report for Period Ending June 30, 2013, DOE/ER-0313/54, U. S. Department of Energy, 81.
- [4] W. J. J. Wakelkamp, F. J. J. van Loo, and R. Metselaar, *J. Eur. Ceram. Soc.* **8** (1991) 135.
- [5] M. W. Barsoum, T. El-Raghy, C. J. Rawn, W. D. Porter, H. Wang, E. A. Payzant, and C. R. Hubbard, *J. Phys. Chem. Solids* **60** (1999) 429.

### **3.2 Low Activation Joining of SiC/SiC Composites for Fusion Applications: Tape Casting TiC+Si Powders** — C. H. Henager, Jr., R. J. Kurtz, N. L. Canfield, Y. Shin, W. G. Luscher, J. T. Mansurov, T. J. Rosendaal, and B. A. Borlaug (Pacific Northwest National Laboratory<sup>1</sup>)

#### **OBJECTIVE**

This work discusses the latest developments in TiC + Si displacement reaction joining at PNNL based on new work to produce tape-cast powders for improved SiC-joints.

#### **SUMMARY**

The use of SiC composites in fusion environments likely requires joining two plates using reactive joining or brazing. One promising reactive joining method uses solid-state displacement reactions between Si and TiC to produce  $Ti_3SiC_2 + SiC$ . We continue to explore the processing envelope for these joints to produce optimal joints to undergo irradiation studies in the High Flux Isotope Reactor (HFIR). One noted feature of the older joints, produced with tape-calendared powders of TiC + Si, were the large, unavoidable void regions they contained. Although the joints were very strong, voids are undesirable. In addition, the tapes made for these joints were produced approximately 20 years ago and had aged. Therefore, we embarked on an effort to produce new tape-cast powders of TiC and Si that can replace our aged tape-calendared materials.

#### **PROGRESS AND STATUS**

##### **Introduction**

SiC is an excellent material for fusion reactor environments, including first wall, plasma-facing, and breeder materials. SiC is low-activation, temperature-resistant, and radiation damage-tolerant relative to most materials. In the form of woven or braided composites with high-strength SiC fibers, it has the requisite mechanical, thermal, and electrical properties to be a useful and versatile material system for fusion applications, especially since microstructural tailoring during processing allows for control over the physical properties of interest [1-6]. However, it is difficult to mechanically join large sections of SiC using conventional fasteners. As a result, the analog of welding is being pursued for these ceramic materials [2, 4-15]. This paper reports on the current status of the production of tape-cast powders to be used for strong SiC-joining materials with fewer voids than observed in previous joints made with tape-calendared powders. The status of the unirradiated strength testing and HFIR irradiation testing of the new, tape-cast joints is also discussed.

##### **Experimental Procedures**

Tapes are cast using a prepared powder, binder, solvent, and plasticizer mixture that consists of a slurry preparation and tape-casting operation using blended TiC+Si powders (all high purity and  $d < 10 \mu m$ ), ethanol and methyl ethyl ketone (MEK) as solvents, polyvinyl butyral resin (PVB) as binder, n-butyl benzyl phthalate (BBP) as a plasticizer, and EMPHOS PS-21A organophosphate ester as a dispersant. The powder loading was optimized at approximately

---

<sup>1</sup> Battelle Memorial Institute under Contract DE-AC06-76RLO 1830 operates PNNL for the U.S. Department of Energy.

55% by volume for the dry tape after casting and drying. The initial TiC+Si powders were blended with a 3:2 molar ratio. The final tape thickness was varied and joints were made from tapes that were 43  $\mu\text{m}$ , 90  $\mu\text{m}$ , and 195- $\mu\text{m}$  thick (green tape thicknesses). The tapes were smooth and easy to handle.

A single tape thickness was selected, from optical microscopy and quantitative metallographic analysis of SiC-phase content in the joints, for the production of CVD SiC miniature torsion test specimens. The CVD SiC test specimens were joined at 1708 K under 40 MPa pressure for four hours. Compared to previous processing times and temperatures, we increased the temperature by 10 K and increased the hold time at temperature and pressure to 4 h from 2 h. This was done to improve joint composition homogeneity from some preliminary high-resolution TEM results. These will be reported in a future semiannual report. Up to 20 specimens have been fabricated for unirradiated strength testing at PNNL and HFIR irradiation testing.

## Results

Table 1 shows the data for the three tapes that were produced, including tape/joint thickness and SiC-phase content. Characteristically, SiC preferentially nucleates at the Hexoloy/joint interface and complicates the quantitative metallography since the joint SiC-phase is attached to the Hexoloy SiC-phase. Difficulty in distinguishing between the SiC-phase in the joint and Hexoloy SiC make it difficult to determine the actual interface location.

**Table 1: New Tape Cast Joint Dimensions and SiC-phase Content**

Tape Designation	Tape Thickness ( $\mu\text{m}$ )	Joint Thickness ( $\mu\text{m}$ )	SiC-phase Area Fraction (%)
3TiC+2Si-5 (43)	43	22	31
3TiC+2Si-5 (90)	90	47	32
3TiC+2Si-5 (195)	195	92	33

The optical images and quantitative data of the new, tape-cast joints matched the images and data recorded from the production of a previous set of joints, made with an older, tape-calendared material. In fact, the new joints appear to be superior because the large void regions found in the old joints are not observed. These voids may have been the result of air entrapment in the tape-calendared joining material since mass loss data from the new tapes match data from the older tapes but the new tapes are much thinner. However, despite having a thinner tape, the new joints are not thinner, indicating that the total amount of binder and plasticizer (and perhaps trapped air) were reduced but the total amount of powders per unit area were not.

Joints produced from the 43- $\mu\text{m}$  tapes were exceptionally uniform. For these reasons, it was selected as the best tape to produce SiC miniature test specimens with. Hexoloy SiC specimens were initially produced to test the joining process. Figure 1 displays an optical micrograph of a Hexoloy SiC joint in its entirety, made from tape with a starting thickness of 43  $\mu\text{m}$ . After processing, the joint has an average thickness of 25.60  $\mu\text{m}$  (40.47% reduction). Figure 2 displays SEM images of the Hexoloy SiC joint at 2000x (Figure 2a) and 4000x (Figure 2b), respectively.

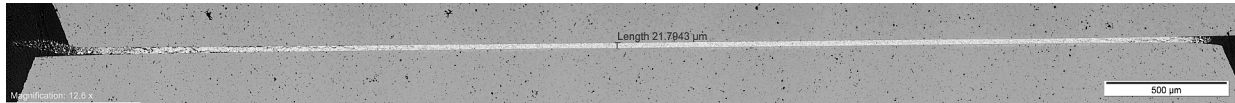
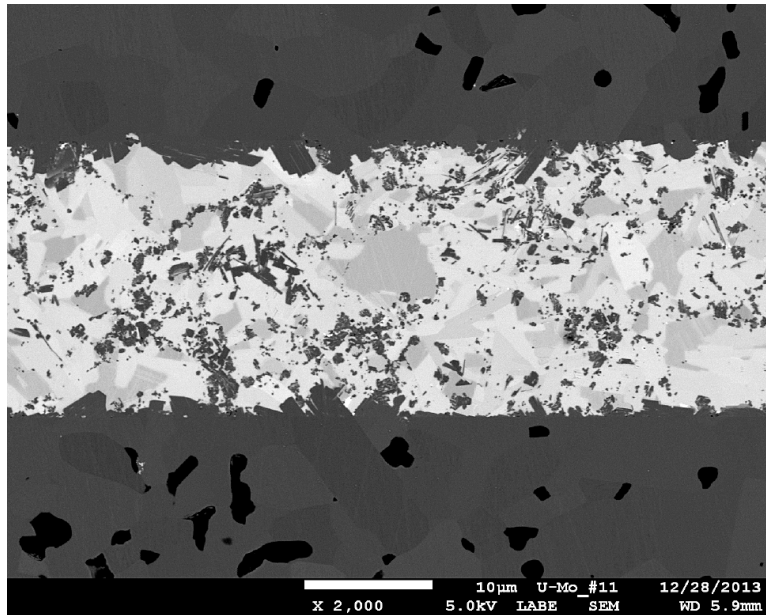
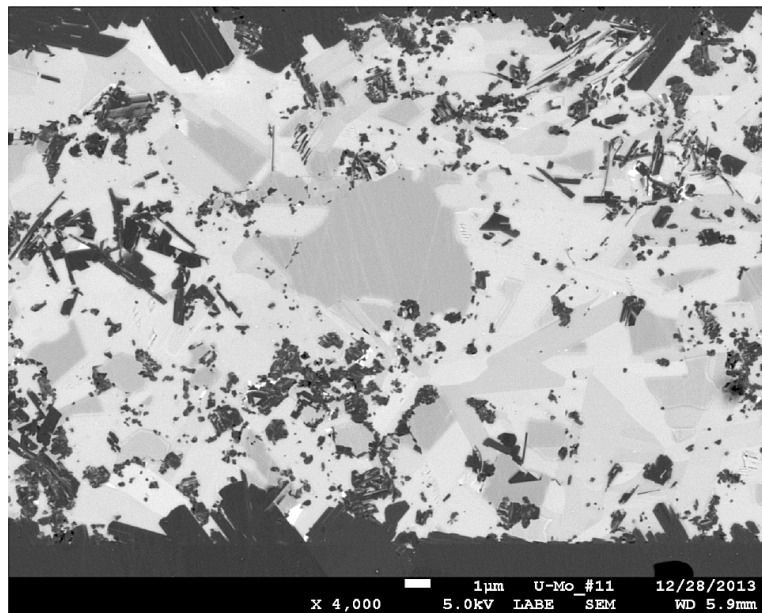


**Figure 1.** Optical micrograph with a 500- $\mu\text{m}$  dimension marker showing the full width of the Hexoloy SiC miniature test specimen produced using 43  $\mu\text{m}$  tape-cast tape. The bulk of the tape cast joint reveals a noted lack of the large pores that were a feature of previous joints. The overall joint thickness is also comparable to the previous joints.



(a)



(b)

**Figure 2.** SEM images of the joint in a Hexoloy SiC miniature test specimen produced using 43- $\mu\text{m}$  tape-cast tape. The images were taken at (a) 2000x and (b) 4000x magnification. The dark phases are SiC and the light-colored phases are  $\text{Ti}_3\text{SiC}_2$ . Note the large blocky SiC at the top and bottom surfaces of the joined regions. These SiC features are nucleated and grown in from the surface of the Hexoloy polished surfaces.

Currently, eight (8) CVD SiC miniature test specimens have been fabricated for HFIR irradiation testing at ORNL from this new tape. Future work includes mechanical testing, optical microscopy, and SEM analysis of these test specimens. The resulting data and images will be compared to that collected from the older, tape-calendared joints.

## ACKNOWLEDGEMENTS

This research was supported by Office of Fusion Energy Sciences, U.S. Department of Energy (DOE) under Contract DE-AC05-76RL01830.

## REFERENCES

- [1] Y. Katoh, L. L. Snead, C. H. Henager Jr, A. Hasegawa, A. Kohyama, B. Riccardi, and H. Hegeman, "Current status and critical issues for development of SiC composites for fusion applications," *J. Nucl. Mater.* **367-370 A**, 659-671 (2007).
- [2] C. H. J. Henager, Y. Shin, Y. Blum, L. A. Giannuzzi, B. W. Kempshall, and S. M. Schwarz, "Coatings and joining for SiC and SiC-composites for nuclear energy systems," *J. Nucl. Mater.* **367-370(1)**, 1139-43 (2007).
- [3] P. Yvon, and F. Carre, "Structural materials challenges for advanced reactor systems," *J. Nucl. Mater.* **385(2)**, 217-222 (2009).
- [4] T. Nozawa, T. Hinoki, A. Hasegawa, A. Kohyama, Y. Katoh, L. L. Snead, C. H. Henager Jr, and J. B. J. Hegeman, "Recent advances and issues in development of silicon carbide composites for fusion applications," *J. Nucl. Mater.* **386-388(C)**, 622-627 (2009).
- [5] H.-C. Jung, Y.-H. Park, J.-S. Park, T. Hinoki, and A. Kohyama, "RD of joining technology for SiC components with channel," *J. Nucl. Mater.* **386-388(C)**, 847-851 (2009).
- [6] S. Nogami, A. Hasegawa, L. L. Snead, R. H. Jones, and K. Abe. Effect of He pre-implantation and neutron irradiation on mechanical properties of SiC/SiC composite. in Proceedings of the 11th Conference on Fusion Research, December 7, 2003 - December 12, 2003. 2004. Kyoto, Japan: Elsevier.
- [7] M. Ferraris, P. Appendino, V. Casalegno, F. Smeacetto, and M. Salvo, "Joining of ceramic matrix composites for fusion application," *Adv. Sci. Tech.*, 33(10th International Ceramics Congress, 2002, Part D), 141-152 (2003).
- [8] B. Riccardi, C. A. Nannetti, T. Petrisor, and M. Sacchetti, "Low activation brazing materials and techniques for SiCf/ SiC composites," *J. Nucl. Mater.* **307-311(Pt. B)**, 1237-1241 (2002).
- [9] R. H. Jones, L. Giancarli, A. Hasegawa, Y. Katoh, A. Kohyama, B. Riccardi, L. L. Snead, and W. J. Weber, "Promise and challenges of SiC<sub>f</sub>/SiC composites for fusion energy applications," *J. Nucl. Mater.* **307-311**, 1057-1072 (2002).
- [10] R. L. Bruce, S. K. Guharay, F. Mako, W. Sherwood, and E. Lara-Curzio, "Polymer-derived SiC<sub>f</sub>/SiC<sub>m</sub> composite fabrication and microwave joining for fusion energy applications," *IEEE/NPSS Symposium on Fusion Engineering*, 1078-8891 (2002).
- [11] M. Zucchetti, M. Ferraris, and M. Salvo, "Safety aspects of joints and coatings for plasma facing components with composite structures," *Fusion Eng. Des.* **58-59**, 939-943 (2001).
- [12] A. R. Raffray, R. Jones, G. Aiello, M. Billone, L. Giancarli, H. Golfier, A. Hasegawa, Y. Katoh, A. Kohyama, S. Nishio, B. Riccardi, and M. S. Tillack, "Design and material issues for high performance SiC<sub>f</sub>/SiC-based fusion power cores," *Fusion Eng. Des.* **55(1)**, 55-95 (2001).

- [13] C. A. Lewinsohn, R. H. Jones, T. Nozawa, M. Kotani, Y. Katoh, A. Kohyama, and M. Singh, "Silicon carbide based joining materials for fusion energy and other high-temperature, structural applications," *Ceramic Engineering and Science Proceedings*, 2001, 22(4, 25th Annual Conference on Composites, Advanced Ceramics, Materials, and Structures: B, 2001), 621-625.
- [14] C. A. Lewinsohn, M. Singh, T. Shibayama, T. Hinoki, M. Ando, Y. Katoh, and A. Kohyama. *Joining of silicon carbide composites for fusion energy applications*. Colorado Springs, CO, USA: Elsevier (2000).
- [15] P. Colombo, B. Riccardi, A. Donato, and G. Scarinci, "Joining of SiC/SiC<sub>f</sub> ceramic matrix composites for fusion reactor blanket applications," *J. Nucl. Mater.* **278**(2), 127-135. (2000).

**4.1 Recent Progress in the Development of Ductile-Phase Toughened Tungsten for Plasma-Facing Materials** — C. H. Henager, Jr., R. J. Kurtz, T. J. Rosendaal, and B. A. Borlaug (Pacific Northwest National Laboratory), G. R. Odette, K. H. Cunningham, K. Fields, D. Gragg, and F. W. Zok (University of California, Santa Barbara)

**OBJECTIVE**

The objective of this study is to develop the materials science of fiber-reinforced tungsten composites as candidates for plasma-facing components in future fusion reactors.

**SUMMARY**

Tungsten (W) and W-alloys are the leading candidates for plasma-facing components in nuclear fusion reactor designs because of their high melting point, strength at high temperatures, and low sputtering yield. However, tungsten is brittle and does not exhibit the required fracture toughness for nuclear applications. The ductile-brittle transition temperature (DBTT) for unirradiated W-alloys ranges from 300-1000°C and radiation hardening further elevates this range. A promising approach to increasing fracture toughness and decreasing the DBTT of a W-alloy is by ductile-phase toughening (DPT). In this method, a ductile phase is included in a brittle matrix to prevent fracture propagation by crack bridging. To examine the prospect of DPT, W-Cu and W-Ni-Fe three-point bend samples were deformed at several strain rates and temperatures. Data from these tests will be used for time-dependent crack bridging studies and the calibration of a crack-bridging model that can effectively predict elevated temperature crack growth in W-composites. A study of fabricating W-wire-reinforced W-matrix composites by spark plasma sintering (SPS) was initiated. W-wires coated with Cu or tungsten carbide (WC) was consolidated in a W matrix. Characterization of these composites is ongoing.

**PROGRESS AND STATUS**

**Background**

Tungsten (W) and W-alloys are the solid materials of choice for the plasma-facing components (PFCs) of future fusion reactors, such as the International Thermonuclear Experimental Reactor (ITER) and Demonstration Power Plant (DEMO), due to their high melting point, strength at high temperatures, high thermal conductivity, low coefficient of thermal expansion, and low sputtering yield [1-5]. However, W and most W-alloys exhibit low fracture toughness and a high ductile-brittle transition temperature (DBTT) that would render them as brittle materials in reactor operations [1, 3, 6]. The DBTT for unirradiated W-alloys typically ranges from 573K to 1273K (300 to 1000°C) and in a reactor environment radiation hardening would further elevate this range [3, 7, 8]. Metallurgical approaches to toughen W-alloys, including rhenium (Re)-alloying and severe plastic deformation (SPD), have resulted in modest DBTT decreases [7, 9]. However, they would be difficult or impossible to implement, due to high costs and implications to irradiation hardening (Re alloys) or extremely complex processing demands (SPD) [10-12]. To prevent mechanical failure, a toughening mechanism is needed for W before it can be considered an effective plasma facing component material (PFCM). W-alloys toughened by engineered reinforcement architectures, such as ductile-phase toughening (DPT), are strong candidates for PFCMs. In DPT, a ductile phase is included in a brittle matrix to prevent fracture propagation. This is accomplished by the formation of an intact bridging zone behind the crack tip, which provides reinforcement, resulting in an increase in the remote load stress intensity for

<sup>1</sup> PNNL is operated for the U.S. Department of Energy by Battelle Memorial Institute under Contract DE-AC06-76RLO 1830.

continued crack growth with increasing crack length [13-14]. In Figure 1a, optical evidence of the crack bridging property of DPT can be seen in a W-Cu alloy.

The principles of DPT are illustrated in Figure 1b, which shows a schematic of ductile bridging ligaments stretching across an open crack in a brittle matrix material, such as W [13-14]. For a brittle material containing a suitable volume fraction of a ductile phase, a highly effective resistance curve toughening mechanism develops as the crack extends. As the crack propagates through a brittle matrix, it leaves a bridging zone of ductile ligaments over a length  $L$  behind the crack tip. As the crack extends,  $L$  increases. For small scale bridging (SSB), when the bridging zone is much smaller than the length of the crack,  $L$  reaches a steady state ( $L = L_{SSB}$ ). The ligaments act in opposition to the applied loading stress intensity factor,  $K_{Applied}$ . This reduces the crack tip stress intensity factor so that:  $K_{Tip} < K_{Applied}$ . The crack opening ( $u$ ) increases with increasing distance behind the crack-tip until the reinforcement breaks at a critical  $u^*$ .

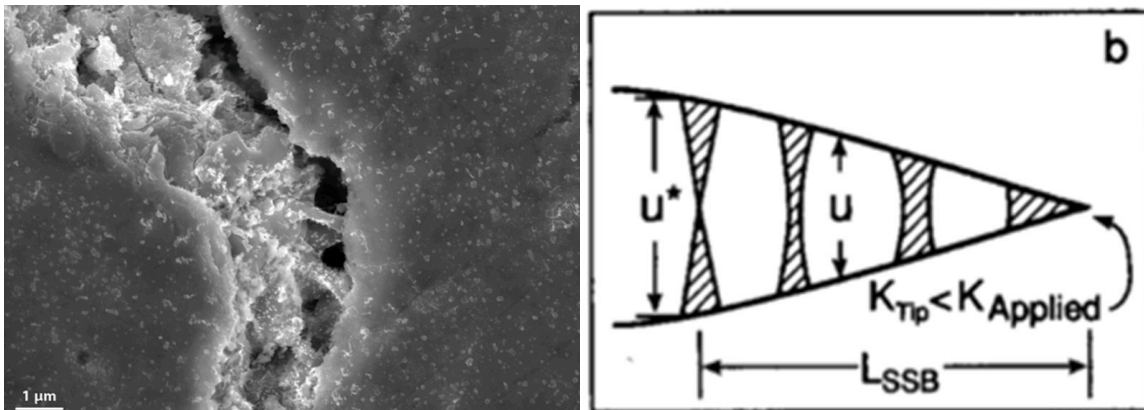


**Figure 1.** a) SEM image of W-Cu fracture where the ductile phase (Cu) is effectively bridging the crack. b) A steady-state bridging zone shown schematically in 2D [14].

## Experimental

Elevated temperature testing of notched and pre-cracked three-point bend specimens was performed in a tube furnace at  $\frac{1}{2} T_m$ ,  $\frac{2}{3} T_m$ , and room temperature, where  $T_m$  is the melting point of the reinforcement (ductile) phase. For W-Cu this is the melting point of Cu, whereas for the W-Ni-Fe material the melting point of the W-Ni-Fe phase was approximated from the phase diagram by the melting point of Ni. Displacement rates of 0.0002, 0.002, 0.02, 0.2, and 2.0 mm/min were employed. Purified Ar gas flowed through the tube furnace to prevent specimen oxidation. W-Cu and W-Ni-Fe alloys were evaluated using fracture mechanics test methods to gather quantitative data on the effects of DPT. Similar tests on monolithic W were performed to provide a baseline for comparison to these materials [15]. Tungsten matrix-tungsten wire-reinforced composites were fabricated by SPS. Copper was electrodeposited on the W-wires, while the WC coating was created by SPS packing W-wires in graphite powder.

## The W-Cu System

The W-Cu system served as a model system for the initial exploration of DPT in W-alloys [15]. Although not a plausible choice for nuclear applications due to Cu's low melting temperature, it was chosen with the goal of maximizing the plastic  $\sigma(u)$  of the Cu reinforcement. The data gathered would be used to develop a fully quantitative model of DPT in the W-Cu system that will aid in future research to develop an effective W-based PFCM. A working hypothesis for this composite material is that the fracture properties are determined by the ductile-phase mechanical properties, which in this case is the Cu phase.

The W-25% Cu (by weight) composite, Copelmet®, was purchased by UCSB and sent to PNNL in the form of 3.30mm x 1.67mm x 16.05mm bend bars for mechanical testing [15]. The bars were EDM notched to a depth ( $a_n$ ) over bar width ( $w$ ) ratio of  $a_n/w = 0.2$ . Slight variances in specimen geometry (including notch depth) were accounted for by computing the peak-load linear elastic stress intensity factor ( $K_{peak}$ ).

## The W-Ni-Fe System

W-Ni-Fe testing was conducted in order to investigate the fracture behavior of another common, W-based heavy alloy. The microstructure is comprised of a continuous network of spheroidal crystals embedded in a ductile, fcc matrix phase. Such W-composites have been studied for some time [16-26] and this report will not be able to cover the entire range of chemical, compositional, and mechanical data found in the literature. Here the focus is on determining for the future if such materials can be useful for fusion reactor applications. The overall chemical composition is 85% W, 11.7% Ni, and 3.3% Fe (by weight), where the spheroidal crystals are 99.5% W, 0.3% Ni, and 0.2% Fe, and the matrix is 56.9% Ni, 29.3% W, and 13.8% Fe. An SEM image with chemical compositional data is shown in Figure 2. The overall composition is 85-wt% W with the particles 99.5% W and the matrix 29.3% W. The balance of the matrix is Ni and Fe as indicated. Electron backscatter diffraction (EBSD) data indicated that the matrix phase was single crystal and indexed as an fcc Ni-based superalloy structure. A particle areal fraction analysis indicated that an estimate of the particle volume fraction is  $78.2\% \pm 2.3\%$ .

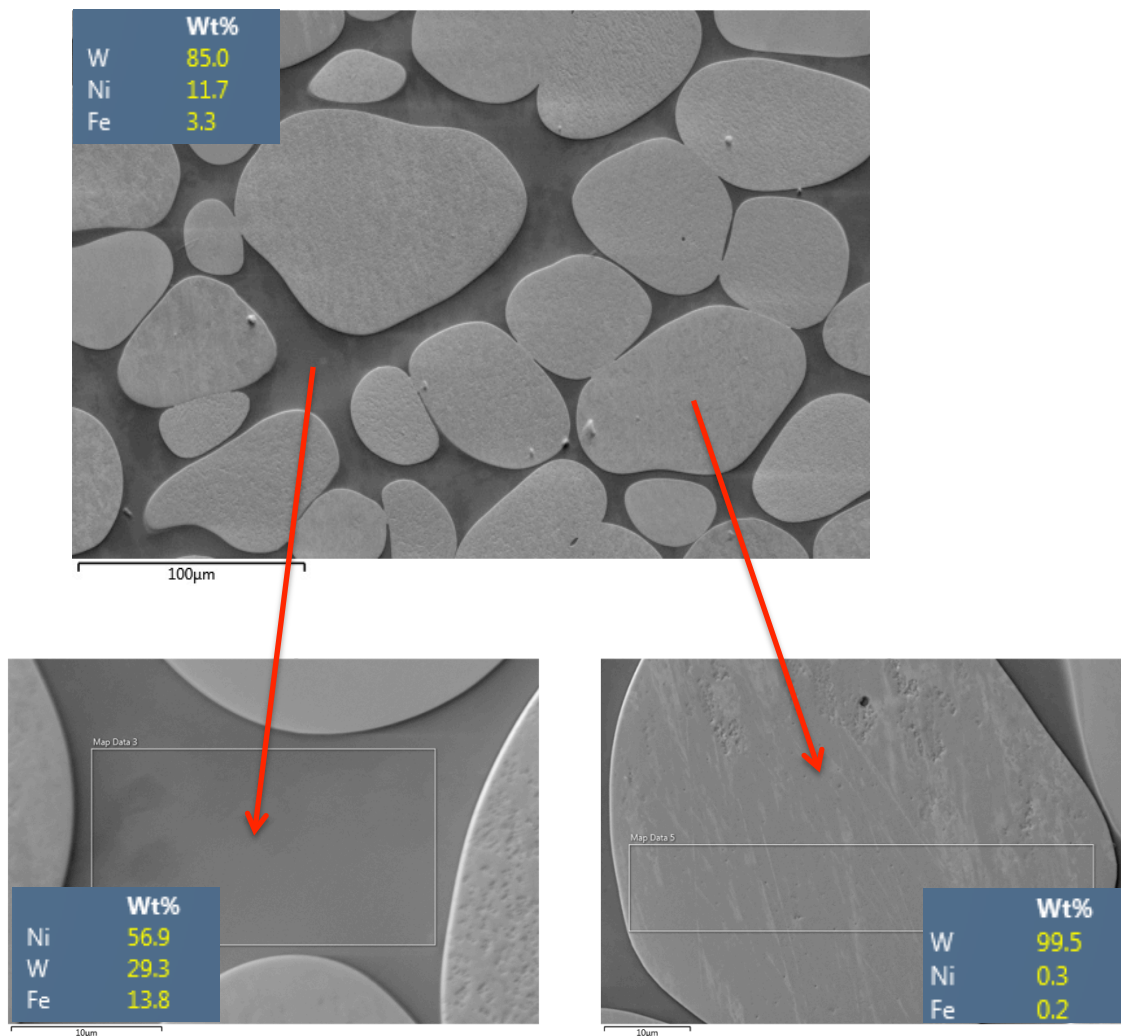


**Figure 2.** SEM images of a representative region of the W-Ni-Fe materials along with EDS composition results given in weight percent in the inset tables. The materials are liquid phase sintered from powders and these particular materials are archival materials from PNNL from prior research projects.

To test the mechanical properties of the W-Ni-Fe alloy, 4mm x 3mm x 20mm bend bars were fabricated and three-point bend tests were conducted. The bars were notched to a depth ( $a_n$ ) over bar width ( $W$ ) ratio of  $a_n/W=0.25$  and testing was performed over a range of temperatures and strain rates as for the W-Cu.

### Three-Point Bend Testing

Testing was conducted on an Instron 5582 test frame with the following parameters: 1) Test temperatures were ambient,  $\frac{1}{2} T_M$  and  $\frac{2}{3} T_M$ , and 2). Strain rates were 0.0002 to 2 mm/min covering each decade. All high temperature testing was conducted in flowing purified argon (Ar) to prevent oxidation of the sample.

### Peak Stress Intensity Calculation

Calculations of  $K_{Peak}$  were made from the 3-point SENB data using the peak load and equations A3.1 and A3.2 in ASTM-E399-12, “Standard Test Method for Linear-Elastic Plane-Strain Fracture Toughness K<sub>IC</sub> of Metallic Materials” [27]. At this stage of research,  $K_{Peak}$  provides an approximate toughness-based method for comparing the mechanical properties of the two W-alloys by accounting for differences in specimen and crack geometry. The results are not meant to be interpreted as fracture toughness data.

### The W-W Fiber-Reinforced Composite System

The interface between the two W phases is critical to the mechanical performance of the composite. A Cu coating was investigated because of its insolubility in W. WC was investigated as a potential debonding layer. Copper coatings up to 25 μm thick were electrodeposited on W wires; Twelve mm lengths of coated wire were placed in W powder in a die perpendicular to the pressing direction and subjected to SPS in the same manner as previous pure W samples (see row 1 in Table 1). Results from the first trial prompted the investigation of a different SPS route (see row 2 in Table 1) using two dwell temperatures. The intent was to consolidate the W sufficiently in the vicinity of the coated wire below the melting point of Cu, so that it would be localized at the wire-matrix interface prior to a high-temperature dwell to fully consolidate the matrix. The consolidated samples were examined using SEM and EBSD.

To carburize the W wire, 12 mm lengths of W-wire were cut and laid separately in a bed of graphite powder (2-15 μm particle size, Alfa Aesar), then pressed and heated using the SPS system (see row 3 in Table 1). Coated wires were cleaned in an ultrasonic bath to remove excess graphite particles, and then laid in W powder in the same manner above and consolidated via SPS (see row 4 in Table 1).

Table 1. Summary of process parameters for SPS system and outcomes for composite fabrication and W-wire carburization.

Materials	Pressing	Heating rate	Dwell T	Dwell t	Result
Cu-coated W wire + W	50 MPa	100 C/min	1700 C	5 min	Cu melted, found in matrix pores
Cu-coated W wire + W (2-T route)	50 50	100 100	990 1700	25 0	Cu melted, found in matrix pores
W wire + C	35 before heating, 9.5 during heating	300	1800	1	WC coating on wire ~12 μm
WC-coated W wire + W	50	100	1900	10	WC intact at interface

## RESULTS

### W-Cu

At room temperature, the peak stress intensity of W-Cu ( $\approx 20\text{-}24 \text{ MPa}\sqrt{\text{m}}$ ) is approximately three times greater than that of monolithic W ( $\approx 8 \text{ MPa}\sqrt{\text{m}}$ ) [15]. Figure 3 shows the effects of temperature and deformation rate on the peak stress intensity of W-Cu.

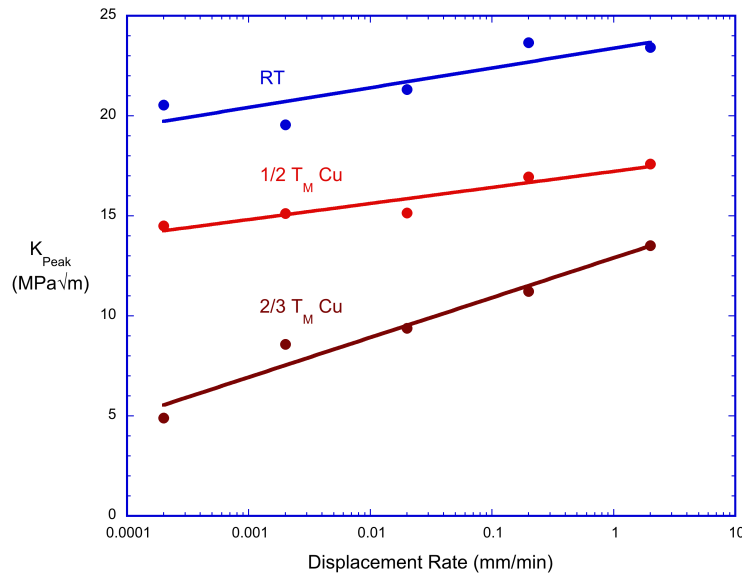


**Figure 3.** Dependence of peak stress intensity of the W-Cu composite on deformation rate and test temperature.

### W-Ni-Fe

At room temperature, the peak stress intensity of the W-Ni-Fe composite ( $\approx 32\text{-}58 \text{ MPa}\sqrt{\text{m}}$  depending on deformation rate) is approximately four to eight times greater than that of monolithic tungsten, and two to three times greater than that of the W-Cu. Figure 4 shows the effect of deformation rate on the peak stress intensity of W-Ni-Fe at room temperature.

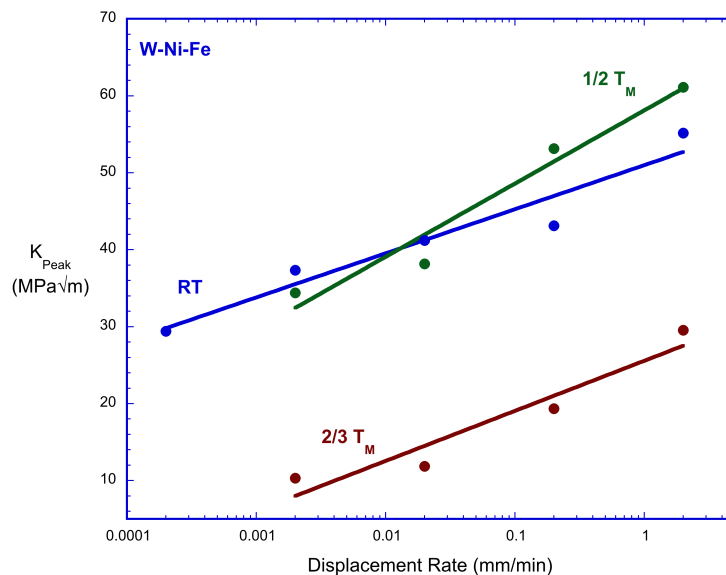


**Figure 4.** Dependence of peak stress intensity of the W-Ni-Fe composite on deformation rate and test temperature.

A graphical comparison of the W-Cu and W-Ni-Fe data at ambient temperature as a function of strain rate is shown in Figure 5. The W-Ni-Fe material is clearly much stronger and tougher but does have a much higher strain rate dependence compared to the W-Cu composite.

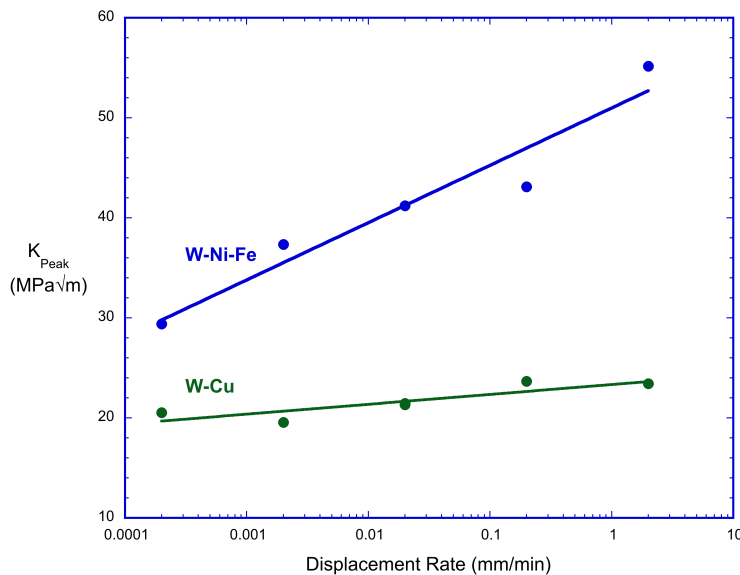


**Figure 5.** A comparison plot of peak load stress intensity as a function of displacement rate for W-Cu and W-Ni-Fe composites at ambient temperature.

### W-W Fiber-Reinforced Composite

In the case of the Cu coated wires, neither sintering method successfully maintained a Cu layer at the wire-matrix interface; rather, a small amount of wicked Cu was found to coat the walls of the matrix W-powder pores (see Figure 6). Notably, the wires maintained a fine grain size of 0.3-3  $\mu\text{m}$  with a  $\langle 110 \rangle$  axial texture after processing (see Figure 7). In contrast, the 12- $\mu\text{m}$  WC coating was intact after consolidation. Characterization of the WC-coated wire composite is ongoing.

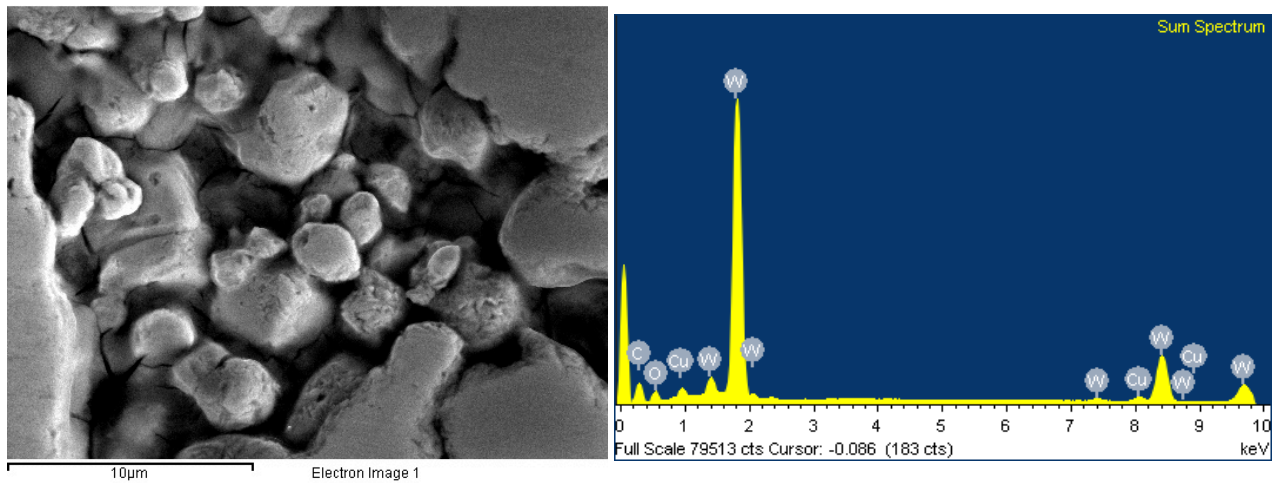


**Figure 6.** SEM image of a porous area in W matrix, scale bar 10  $\mu\text{m}$ . Sample is single-temperature SPS route for W powder consolidated around Cu-coated W wires. EDS spectrum shows Cu detected in pore. Cu was not found at the wire-matrix interface.

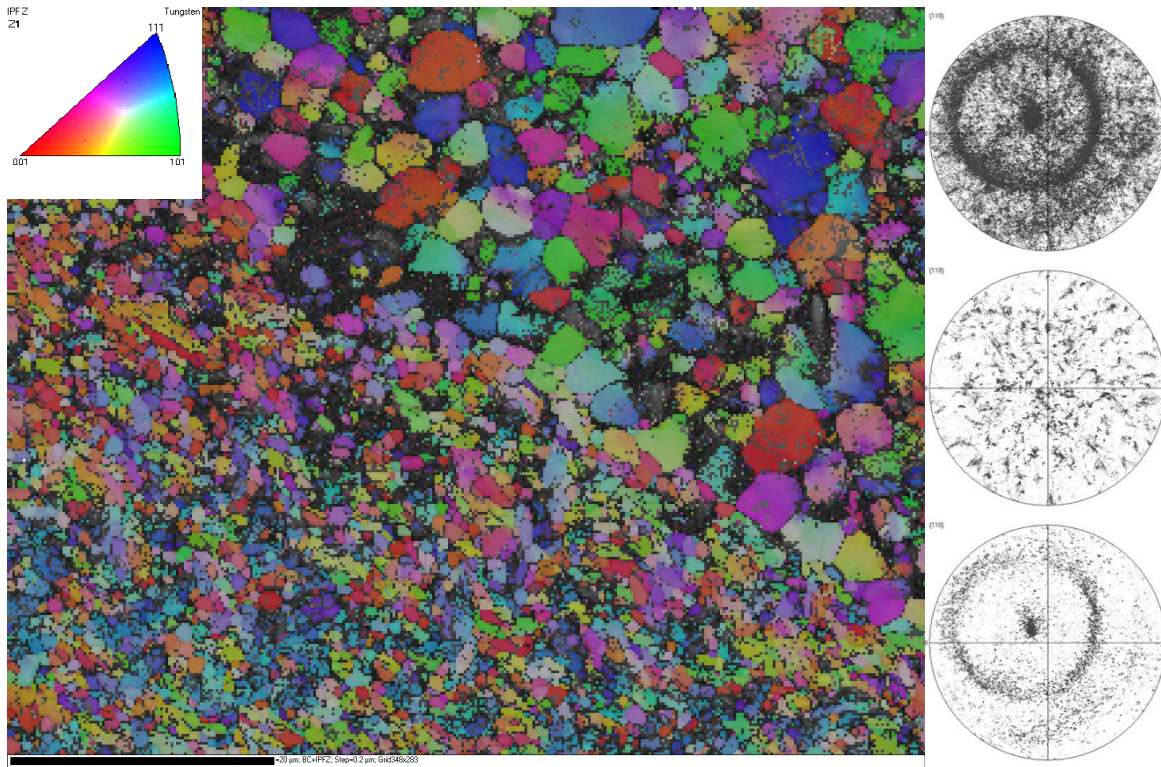


**Figure 7.** EBSD pole figures and band contrast images of the W wire adjoining showing strong  $\langle 110 \rangle$ -texturing and fine grain sizes in the Fe. From top to bottom the pole figures are 1) full frame, 2) matrix only, 3) wire only.

## FUTURE WORK

In the immediate future, testing on the W-Ni-Fe system will be concluded. A bridging model will be constructed for the W-Cu alloys and it is not apparent that such a model is suitable for the W-Ni-Fe alloys yet. The model, along with fracture data, the method and cost of synthesis, and microstructure examinations will be used to guide the future design of improved W-composites. Further characterization and mechanical testing of the W-W fiber-reinforced composites will be performed. Additional fabrication routes will be investigated, including foil-wire diffusion bonding and accumulative roll bonding. Ultimately, a clear understanding of the materials science of W-composites should be developed with relation to: a) the choice and behavior of the ductile phase; b) the synthesis, processing, and fabrication of composites; and c) the composite's microstructure as it evolves during service.

## REFERENCES

- [1] M. Rieth, J. L. Boutard, S. L. Dudarev, et al., "Review on the EFDA programme on tungsten materials technology and science," *J. Nucl. Mater.* **417**, 463-467 (2011).
- [2] R. A. Pitts, A. Kukushkin, A. Loarte, A. Martin, M. Merola, C. E. Kessel, V. Komarov, and M. Shimada, "Status and physics basis of the ITER divertor," *Phys. Scr.* **Volume T, 22009(T138)**, 014001.

- [3] P. Mertens, T. Hirai, M. Knaup, O. Neubauer, V. Philipps, J. Rapp, V. Riccardo, S. Sadakov, B. Schweer, A. Terra, I. Uytendhouwen, and U. Samm, "A bulk tungsten divertor row for the outer strike point in JET," *Fusion Eng. Des.* **84(7-11)**, 1289-93 (2009).
- [4] A. Gervash, R. Giniyatulin, T. Ihli, W. Krauss, A. Makhankov, I. Mazul, P. Norajitra, and N. Yablokov, "Fabrication of a He-cooled divertor module for DEMO reactor," *J. Nucl. Mater.* **367-370** B(SPEC. ISS.), 1472-1475 (2007).
- [5] M. Merola, W. Danner, and M. Pick, "EU RD on divertor components," *Fusion Eng. Des.* **75-79**(SUPPL.), 325-331 (2005).
- [6] P. Mertens, V. Philipps, G. Pintsuk, V. Riccardo, U. Samm, V. Thompson, and I. Uytendhouwen, "Clamping of solid tungsten components for the bulk W divertor row in JET-precautionary design for a brittle material," *Phys. Scr.* **Volume T, 2009(T138)**, 014032.
- [7] B. Gludovatz, S. Wurster, A. Hoffmann, and R. Pippan, "Fracture toughness of polycrystalline tungsten alloys," *Int. J. Refract. Metals Hard Mater.* **28**(6), 674-8 (2010).
- [8] S. J. Zinkle, and N. M. Ghoniem, "Operating temperature windows for fusion reactor structural materials," *Fusion Eng. Des.* **51-52**, 55-71 (2000).
- [9] M. Faleschini, H. Kreuzer, D. Kiener, and R. Pippan, "Fracture toughness investigations of tungsten alloys and SPD tungsten alloys," *J. Nucl. Mater.* **367-370** A(SPEC. ISS.), 800-805 (2007).
- [10] T. Tanno, A. Hasegawa, J. C. He, M. Fujiwara, M. Satou, S. Nogami, K. Abe, and T. Shishido, "Effects of transmutation elements on the microstructural evolution and electrical resistivity of neutron-irradiated tungsten," *J. Nucl. Mater.* **386-388(C)**, 218-221 (2009).
- [11] T. Tanno, A. Hasegawa, M. Fujiwara, H. Jian-Chao, S. Nogami, M. Satou, T. Shishido, and K. Abe, "Precipitation of solid transmutation elements in irradiated tungsten alloys," *Mater. Trans.* **49**(10), 2259-64 (2008).
- [12] T. Tanno, A. Hasegawa, H. Jian-Chao, M. Fujiwara, S. Nogami, M. Satou, T. Shishido, and K. Abe, "Effects of transmutation elements on neutron irradiation hardening of tungsten," *Mater. Trans.* **48**(9), 2399-402 (2007).
- [13] R. Venkateswara, G. R. Odette, and R. O. Ritchie, "Ductile-reinforcement toughening in -TiAl intermetallic-matrix composites: effects on fracture toughness and fatigue-crack propagation resistance," *Acta Metall. Mater.* **42**(3), 893-911 (1994).
- [14] G. R. Odette, B. L. Chao, J. W. Sheckherd, and G. E. Lucas, "Ductile phase toughening mechanisms in a TiAl-TiNb laminate composite," *Acta Metall. Mater.* **40**(9), 2381-9 (1992).
- [15] K. H. Cunningham, K. Fields, D. Gragg, F. W. Zok, J. C. H. Henager, R. J. Kurtz, and T. Roosendaal, Recent Progress in the Development of Ductile-Phase Toughened Tungsten for Plasma-Facing Materials, in DOE/ER-0313/54 - Volume 54, Semiannual Progress Report, June 30, 2013. 2013, US DOE: ORNL, TN.
- [16] N. Durlu, N. K. Caliskan, and S. Bor, "Effect of swaging on microstructure and tensile properties of W-Ni-Fe alloys," *Int. J. Refract. Metals Hard Mater.* **42**, 126-131 (2014).
- [17] J. Zhu, S. Cao, and H. Liu, "Fabrication of W-Ni-Fe alloys with gradient structures," *Int. J. Refract. Metals Hard Mater.* **36** 72-75 (2013).
- [18] R. Muresan, E. Riti-Mihoc, C. Prica, and M. Bodea, "Improving mechanical properties of sintered wolfram based alloy with liquid phase trough controlled cooling parameters," *Arch. Metall. Mater.* **57**(1), 87-92 (2012).
- [19] J. Das, U. R. Kiran, A. Chakraborty, and N. E. Prasad, "Hardness and tensile properties of tungsten based heavy alloys prepared by liquid phase sintering technique," *Int. J. Refract. Metals Hard Mater.* **27**(3), 577-583 (2009).

- [20] K. H. Lee, S. I. Cha, H. J. Ryu, and S. H. Hong, "Effect of two-stage sintering process on microstructure and mechanical properties of ODS tungsten heavy alloy," *Mater. Sci. Eng. A*, **458**(1-2), 323-329 (2007).
- [21] L. Woei-Shyan, L. Chi-Feng, and C. Sen-Tay, "Plastic flow of tungsten-based composite under hot compression," *J. Mater. Process. Technol.* **100**(1-3), 123-30 (2000).
- [22] Y. H. Chiou, Y. S. Zu, and S. T. Lin, "Partition of tungsten in the matrix phase for liquid phase sintered 93%W-4.9%Ni-2.1%Fe," *Scr. Mater.* **34**(1), 135-40 (1996).
- [23] R. S. Coates, and K. T. Ramesh, "Rate-dependent deformation of a tungsten heavy alloy," *Mater. Sci. Eng. A* **145**(2), 159-166 (1991).
- [24] A. Bose, D. Sims, and R. M. German, "Test temperature and strain rate effects on the properties of a tungsten heavy alloy," *Metall. Trans. A (Phys. Metall. Mater. Sci.)* **19A**(3), 487-94 (1988).
- [25] K. S. Churn and R. M. German, "Fracture behavior of W-Ni-Fe heavy alloys," *Metall. Trans. Phys. Metall. Mater. Sci.* **15A**(2), 331-8 (1984).
- [26] E. G. Zukas, E. G. and H. Sheinberg, "Sintering mechanisms in the 95% W-3.5% Ni-1.5% Fe composite," *Powder Technol.* **13**(1), 85-96 (1976).
- [27] ASTM, Standard Test Method for Linear-Elastic Plane-Strain Fracture Toughness K<sub>IC</sub> of Metallic Materials, in E399-12, 2012, ASTM International: West Conshohocken, PA.

## **4.2 Evaluation of Mechanical Properties of Tungsten After Neutron Irradiation —** L. L. Snead, L. M. Garrison, T. S. Byun, N. A. P. K. Kumar, and W. D. Lewis (Oak Ridge National Laboratory)

### **OBJECTIVE**

The objective of this work is to evaluate the effect of neutron irradiation on the mechanical properties of tungsten with selected microstructures to aid in developing plasma-facing materials for fusion reactors.

### **SUMMARY**

A total of 440 tungsten samples were irradiated in HFIR at temperatures from 70 to 900°C and fast neutron fluences of 0.01 to  $20 \times 10^{25}$  n/m<sup>2</sup> at E>0.1 MeV over the last year. Types of tungsten included were [110] single crystal tungsten, [100] single crystal tungsten, wrought tungsten foils, annealed tungsten foils, and tungsten-copper laminate. Samples that were irradiated at  $2 \times 10^{25}$  n/m<sup>2</sup> and below have been tensile and hardness tested at 300°C and below. The defect structure of selected low dose samples has been investigated in the TEM. The analysis of the lower dose samples is ongoing, and analysis of the higher dose samples will follow.

### **PROGRESS AND STATUS**

#### **Introduction**

Tungsten will be the primary divertor material in the ITER tokamak and is a leading candidate for plasma facing components in other advanced fusion reactors. Tungsten has many beneficial characteristics such as a low sputtering yield, high melting temperature, and low activation properties. However, tungsten has a ductile to brittle transition temperature between ~400-900°C [1] (the temperature depends strongly on the microstructure and test method) and can be difficult to manufacture. Additionally, there is limited data available on the behavior of tungsten under neutron irradiation. It is known that microstructure can greatly change the mechanical properties of a material. Several different microstructures of tungsten were selected for neutron irradiation and post irradiation analysis in order to form a data set on neutron-irradiated tungsten properties.

#### **Experimental Procedure**

The full list of irradiated specimens was published in the previous semi-annual report [2]. There were a total of 440 samples irradiated in HFIR at selected temperatures between 70 and 900°C and fast neutron fluences of 0.01 to  $20 \times 10^{25}$  n/m<sup>2</sup> at E>0.1 MeV over the last year. Samples of each different tungsten material--single crystal tungsten [110], single crystal tungsten [100], wrought tungsten foil, annealed tungsten foil, and tungsten-copper laminate--that received doses up to  $2 \times 10^{25}$  n/m<sup>2</sup> have been tensile tested and hardness tested. Additional tensile testing at temperatures above 300°C for the low dose samples is planned. Selected samples from each different microstructure type have been analyzed in the TEM. The higher dose samples have finished irradiation but have not been analyzed yet. Figure 1 illustrates the irradiation parameters used in the study.

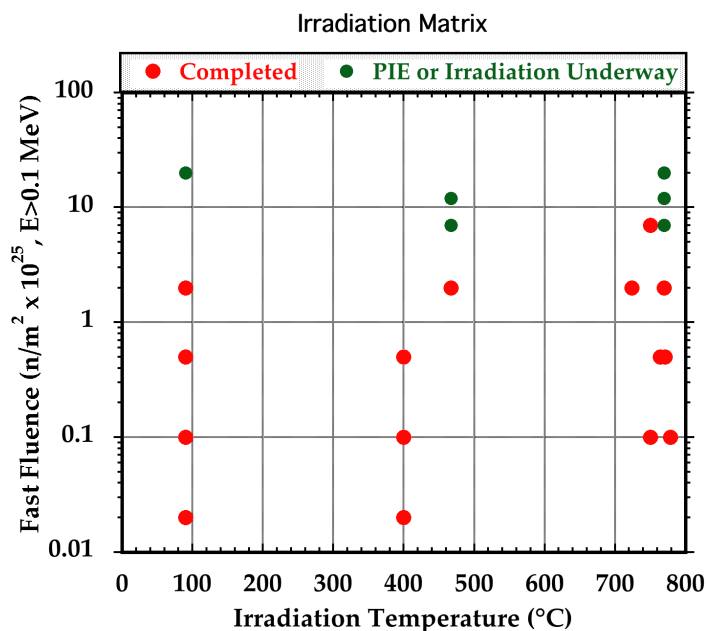


Figure 1. Irradiation matrix for the tungsten samples irradiated in HFIR in 2013.

Bar samples 0.630 X 0.157 inches (16 X 4 mm) and tensile test specimens with the same outer dimensions were used for the irradiations. The foil samples were 0.004 inches thick (0.1 mm), while the single crystal and laminate samples were 0.020 inches thick (0.5 mm). Inside the rabbits, CVD SiC pieces were used to measure the irradiation temperature. Figure 2 shows the dimensions of a tensile test sample.

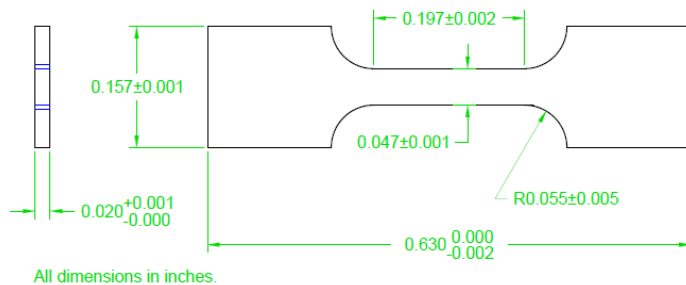


Figure 2. Tensile test specimen dimensions.

## RESULTS

### Microhardness

Single crystal tungsten samples in [100] and [110] orientations were hardness tested (Figure 3). For both orientations, hardness increased with dose, but there was not a clear trend of hardness with increasing irradiation temperature. The indentation of the hardness test induced triaxial deformation in the samples, so there was little difference between the different orientations for the hardness values.

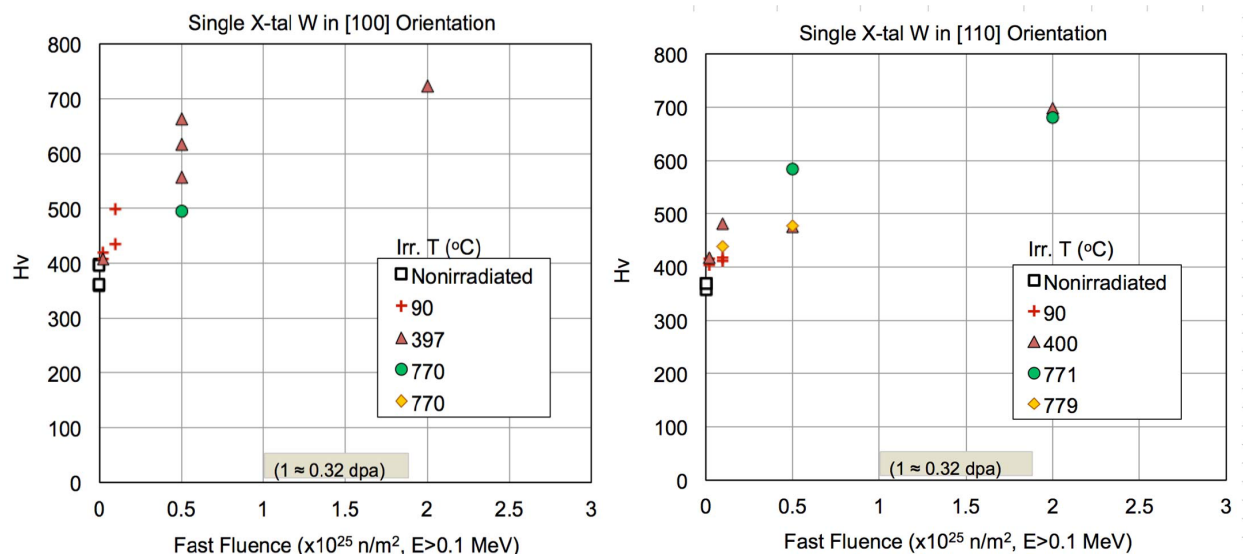


Figure 3. Hardness testing was completed for single crystal tungsten samples in orientations [110] and [100] after neutron irradiation over a range of fluences and temperatures.

### Tensile Test Results

Single crystal tungsten samples in [110] and [100] orientations were tensile tested in an unirradiated state at temperatures from room temperature up to 650°C. The results from the [110] samples are presented in Figure 4. In the unirradiated condition, both the [100] and [110] samples showed ductility starting at 300°C. Thus far, samples of [110] tungsten irradiated to two different doses have been tensile tested at room temperature, 90 and 300°C. At both doses, the [110] samples are also ductile at 300°C (Figure 4). Yield as well as fracture stress increased with irradiation dose. Additionally, total ductility started to decrease from 0.03 dpa. Samples of [100] single crystal tungsten that was irradiated to  $0.02 \times 10^{25}$  n/m<sup>2</sup> were also tensile tested at room temperature, 90, and 300°C. For the [100] orientation samples, some ductility is observed on the sample tested at 300°C. However, the overall elongation of the [100] sample at 300°C is much less than the [110] samples tested at the same temperature. Higher temperature tensile tests will be performed on irradiated specimens in 2014.

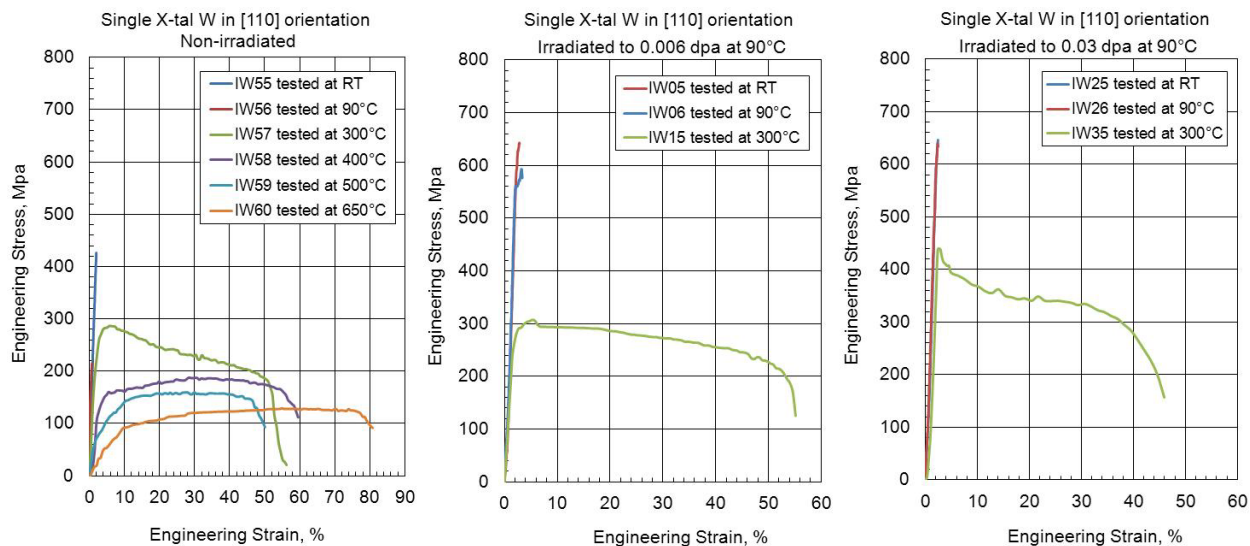


Figure 4. Tensile test results of [110] single crystal tungsten unirradiated, after 0.006 dpa, and after 0.03 dpa.

### Wrought Tungsten-Copper Laminate Material

The tungsten-copper laminate material was produced in Germany at KIT. The material consists of repeated layers of 0.1 mm tungsten and 0.1 mm copper braised together into a laminate with a total thickness of 0.5 mm. Tungsten foil of thickness 0.1 mm was found by Rieser et al. to be ductile at room temperature [3]. The motivation for the tungsten-copper laminate is to determine if a bulk material can be made that retains the ductility of the thin tungsten foils.

In the unirradiated condition, samples of wrought tungsten-copper laminate material were tensile tested at temperatures from room temperature up to 650°C (Figure 5). Both strength and ductility decreased with increasing test temperature. Embrittlement was shown at 90°C, which is consistent with the single crystal specimens.

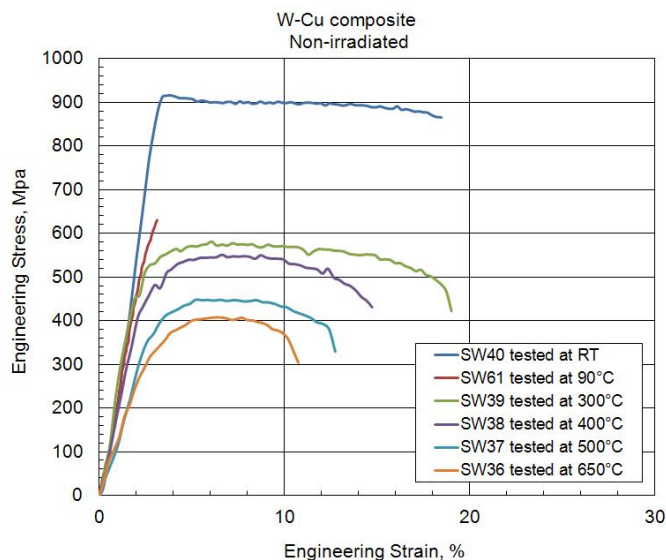


Figure 5. Tensile test results of the tungsten-copper laminate material before irradiation.

The W-Cu laminate material was irradiated at 400, 750, and 770°C and fast fluences between  $0.01$  and  $10 \times 10^{25}$   $n/m^2$ ,  $E > 0.1$  MeV. These samples were then tensile tested at room temperature (Figure 6). There is not a clear relationship between the strength of the material and the irradiated dose. As the W layer (0.1 mm thick) was heavily deformed before irradiation, additional hardening by irradiation should be limited. Therefore, the strength dependence was subjected to the statistical behavior of crack initiation and propagation in the composite. This led to the high variation in strength at different conditions. Significant ductility was retained below a fast fluence of  $0.1 \times 10^{25}$   $n/m^2$ .

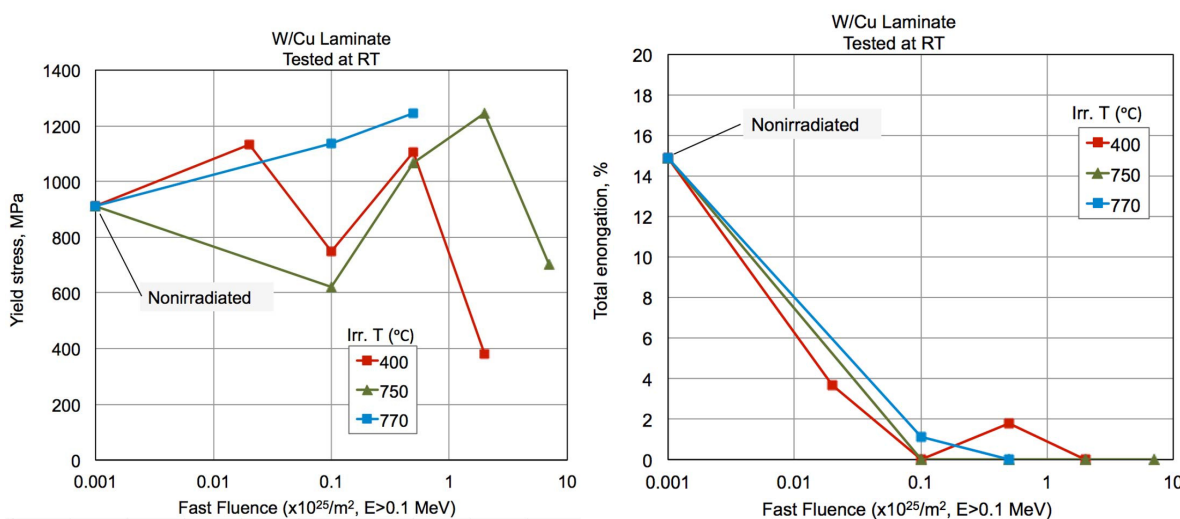


Figure 6. Yield strength and elongation of the tungsten-copper laminate material after irradiation at 400, 750, and 770°C.

### TEM Analysis of Tungsten

Thus far, TEM analysis has been completed on selected single crystal, wrought foil, and annealed foil tungsten samples. Samples were analyzed in the unirradiated state and then after fluences of  $0.1 \times 10^{25}$  n/m<sup>2</sup>,  $0.5 \times 10^{25}$  n/m<sup>2</sup>, and  $2.0 \times 10^{25}$  n/m<sup>2</sup>. A focused ion beam (FIB) system with Ga<sup>+</sup> ion beam was used to prepare TEM specimens. In order to minimize the unwanted damage caused by Ga<sup>+</sup> ions, very low energy and current (2 kV and 27 pA) was used on the TEM specimen during final thinning process. A summary of the irradiation defects is presented in Table 1, with descriptions of the different materials following. Samples of annealed foil and deformed foil samples that were irradiated at higher temperatures are currently being prepared for TEM analysis for comparison with the single crystal tungsten samples.

Table 1. Summary of dislocation loops observed in TEM analysis of single crystal, wrought foil, and annealed foil tungsten samples.

Material	Fluence in n/m <sup>2</sup> & (dpa)	Irr. Temp. in °C	Dislocation loop density ( x 10 <sup>22</sup> m <sup>-3</sup> )	Average loop diameter in nm
Single Crystal -W	$0.1 \times 10^{25}$ n/m <sup>2</sup> (0.032)	80-100	2.97	4.85
Single Crystal-W	$2 \times 10^{25}$ n/m <sup>2</sup> (0.639)	80-100	4.55	4.98
Single Crystal-W	$2 \times 10^{25}$ n/m <sup>2</sup> (0.639)	724	1.41	6.37
Single Crystal-W	$0.5 \times 10^{25}$ n/m <sup>2</sup> (0.160)	764	Low	6.56
Annealed foil-W	$0.1 \times 10^{25}$ n/m <sup>2</sup> (0.032)	80-100	3.01	4.38
Annealed foil-W	$2 \times 10^{25}$ n/m <sup>2</sup> (0.639)	80-100	4.11	4.45
Deformed foil-W	$0.1 \times 10^{25}$ n/m <sup>2</sup> (0.032)	80-100	2.59	5.07
Deformed foil-W	$2 \times 10^{25}$ n/m <sup>2</sup> (0.639)	80-100	3.55	8.08

### Deformed tungsten foil

Samples of deformed tungsten foil were analyzed in the TEM in the unirradiated state and then after irradiation at 80-100°C to fluences of  $0.1 \times 10^{25}$  n/m<sup>2</sup> and  $2.0 \times 10^{25}$  n/m<sup>2</sup>. There was a noticeable increase in damage with increased neutron dose. A high density of dislocation loops was observed for both irradiated samples. With the increase in irradiation dose, the defects appeared to coalesce, which led to a coarsening of dislocation of loops. The average loop diameter of the sample exposed to  $0.1 \times 10^{25}$  n/m<sup>2</sup> was  $\approx 5.074$  nm (average of 50 loops), while the average loop diameter of the sample exposed to  $2 \times 10^{25}$  n/m<sup>2</sup> was larger,  $\approx 8.076$  nm (average of 50 loops). The pre-existing dislocation network in the deformed specimens could be the reason for the increase in loop diameter. This observation is in agreement with previous

studies, which showed that the presence of a pre-existing, low network dislocation density would promote the decrease in loop density with simultaneous increase in loop diameter.

#### Annealed tungsten foil

Samples of annealed tungsten foil were analyzed in the TEM before and after irradiation at 80-100°C to fluences of  $0.1 \times 10^{25}$  n/m<sup>2</sup> and  $2.0 \times 10^{25}$  n/m<sup>2</sup>. While the deformed tungsten foil showed larger dislocation loops at higher fluences, the annealed foil only had a small change in dislocation loop size for the different fluences. The average loop diameter of the sample exposed to  $0.1 \times 10^{25}$  n/m<sup>2</sup> was  $\approx 4.38$  nm (average of 50 loops), and the average loop diameter of the sample exposed to  $2 \times 10^{25}$  n/m<sup>2</sup> was  $\approx 4.45$  nm (average of 50 loops). The average diameter of dislocation loops was less than the average diameter of loops found in deformed tungsten sample. An increase in defect density was observed with the increase in irradiation dose.

#### Single Crystal [110] tungsten

Four samples of neutron irradiated single crystal tungsten have been analyzed in the TEM thus far as well as a control sample in the unirradiated state. The two samples were irradiated at 80-100°C to fluences of  $0.1 \times 10^{25}$  n/m<sup>2</sup> and  $2.0 \times 10^{25}$  n/m<sup>2</sup>. Two samples were irradiated at higher temperatures before TEM analysis: one sample was irradiated at 724°C to  $2.0 \times 10^{25}$  n/m<sup>2</sup>, and another sample was irradiated at 764°C to  $0.5 \times 10^{25}$  n/m<sup>2</sup>. Dislocations were observed in all of the irradiated samples with the samples irradiated at higher temperatures having a lower dislocation density but larger dislocation loops on average than the samples irradiated at the lower temperatures. The two samples irradiated at 80-100°C did not develop voids (Figure 7), but both samples irradiated at higher temperatures did (Figure 8).

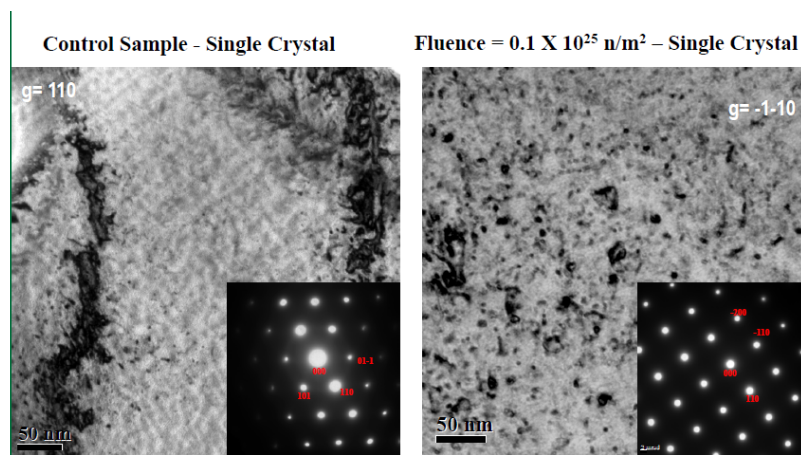


Figure 7. The single crystal tungsten unirradiated sample is shown for comparison. After irradiation to  $0.1 \times 10^{25}$  n/m<sup>2</sup> at 80-100°C dislocation loops are visible.

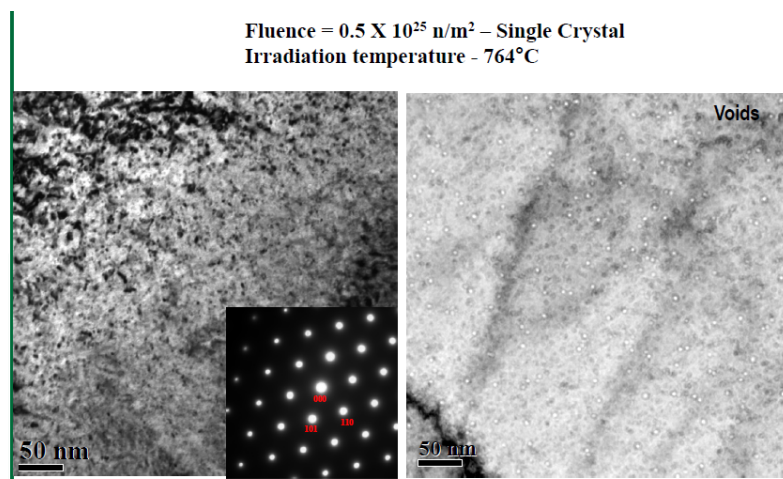


Figure 8. When irradiated at a higher temperature of 764°C, the single crystal tungsten sample developed voids in addition to dislocation loops.

## REFERENCES

- [1] M. Rieth and A. Hoffmann, *International J. Refractory Met. Hard Mater.* **28** (2010) 679-686.
- [2] Y. Katoh, and J. L. McDuffee, *Fusion Materials Semiannual Progress Report for Period Ending June 30, 2013*, DOE/ER-0313/54, 229-232.
- [3] J. Reiser, M. Rieth, B. Dafferner, and A. Hoffmann, *J. Nucl. Mater.* **423** (2012) 1-8.

**4.3 High-Heat Flux Testing of Low-Level Irradiated Materials Using Plasma Arc Lamps —**  
A. S. Sabau, E. K. Ohriner, Y. Katoh, and L. L. Snead (Oak Ridge National Laboratory)

**OBJECTIVE**

The objective of this work is testing of irradiated materials that are candidate of divertor component materials and mock-up divertor components under high-heat flux using Plasma Arc Lamps (PAL).

**SUMMARY**

A neutron-irradiated tungsten specimen was successfully tested at ITER-relevant high-heat flux conditions using Plasma Arc Lamp at ORNL on Aug. 14, 2013, without any contamination outside the testing box, ensuring the readiness of the new facility for irradiated samples. For thin specimens, often used for studies of neutron irradiation effects, one of the main challenges to the PAL systems is the measurement of the sample temperature.

**PROGRESS AND STATUS**

Effort was conducted on three main areas: (a) enhancing the RAD safety during testing of irradiated specimens, (b) enhancing the measurement accuracy of the sample temperature, and (c) conducting high-heat flux testing with non-irradiated specimens and neutron-irradiated specimens.

**Results for enhancing the RAD safety during high-heat flux testing of irradiated specimens**

The current efforts for enhancing the RAD safety during testing of irradiated specimens included:

- Design and fabrication of a new cooling rod that will enable a 3X increase in the coolant flow rate.
- Design of an additional sealed chamber enclosing the cooling rod, specimen holder, and irradiated specimen.
- Fabrication of the sealed chamber enclosing the specimen holder and irradiated specimen.
- Enhancing the automatic pressure controller – for Ar inlet and outflow - to regulate the vacuum pressure to approximately 4 psi in the test section during HHF testing to prevent the liftoff of main quartz window and escape of RAD gases.

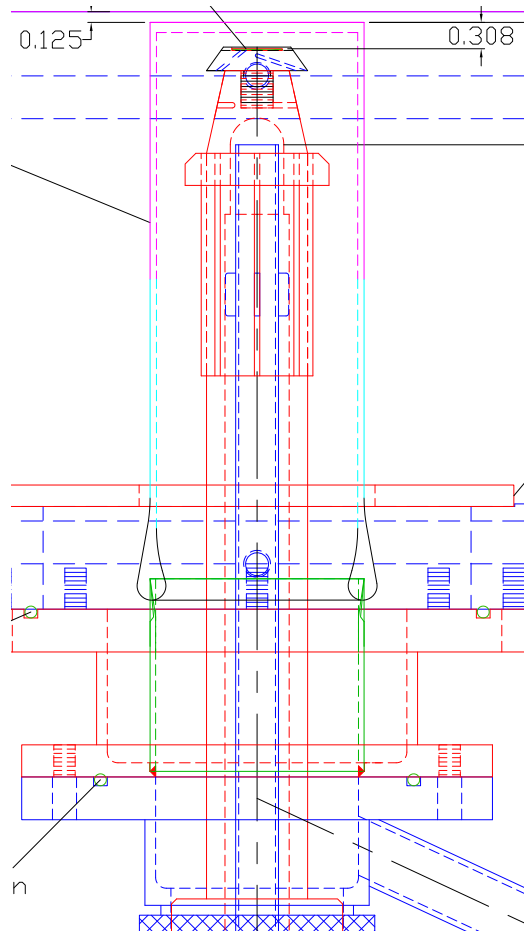


**Figure 1.** Drawing of the additional sealed chamber to confine contamination to the quartz-glass cylinder surrounding the cooling rod. The main test chamber will NOT be contaminated, lowering the maintenance and operational costs.

Color legend for the cylinder that comprises the sealed chamber:

1. **magenta** – indicate quartz cap and quartz tube surrounding the top region of the cooling rod,
2. **light blue** – graded quartz to glass region, and
3. **green** – glass region; the glass is fused on the bottom to a steel flange to insure vacuum tight conditions.

### Results for enhancing the temperature measurement

The current efforts for enhancing the temperature measurement during testing of irradiated specimens included:

- Assessment of pyrometer applicability in the actual PAL conditions.
- Use of a second generation of molybdenum specimen holder, for which the thermocouples could be installed closer to the backside surface of the specimen.
- Machining of 2G v2 Mo specimen holders with four thermocouples.
- Conduct calibration experiments in which the pyrometer was used to measure directly the temperature the W specimen surface while a thermocouple was welded on the backside of the W specimen.

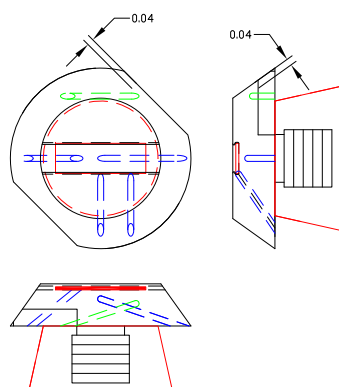


**Figure 2.** Specimen holder designed with two side thermocouples for direct measurement of the temperature of the specimen.

Using a specimen holder with two side thermocouples would enhance the evaluation of the specimen temperature during high-heat flux testing. The thermocouples that would be inserted from the side of the specimen would directly impinge onto the specimen, providing more accurate temperature data.

Clamping the specimen onto the substrate is the best option for high-heat flux testing. However, due to the large area covered by the incident heat flux from the plasma-arc lamp, the design of the clamping fixtures is not trivial as they would heat during testing, while on the other hand, there is limited cooling available to the fixtures. Due to different thermal expansion, the clamping fixture cannot be bolted to both sample and cooling rod, resulting in lack of disk cooling. In this reporting period, several attempts were made to design such fixtures in preparation for the upcoming high-heat flux testing that will be conducted in January/February 2014 at ORNL in collaboration with Dr. Kazutoshi Tokunaga for the PHENIX program.

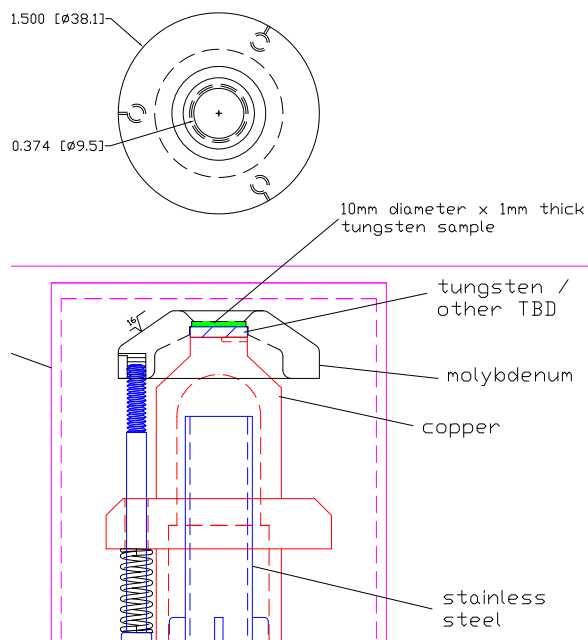


**Figure 3.** Conceptual drawing of a disk-screw clamp fixture (design phase is ongoing). The following features can be pointed out for this current design:

- Springs allow the control of the clamping force, for fixed clamping, the springs can be removed.
- Springs were placed in low temperature regions for durability and performance.
- Top disk may still absorb more energy that it can dissipate by thermal radiation.
- The top surface includes a conical area to reduce energy absorption.
- Disk cutouts (not drawn) will further minimize energy absorption.

A calibration run was first conducted when a thermocouple was welded to the backside of a non-irradiated tungsten specimen, providing direct measurement of its temperature. For this calibration run, the specimen-reflector distance was 2 cm, the incident heat flux was about 3.2 MW/m<sup>2</sup> for 30 s, while the absorbed heat flux was into the specimen was approximately 1.6 W/m<sup>2</sup> (approx. 50% of the incident heat flux). Two holes were drilled in the Mo holder for insertion of thermocouples close to the backside surface of the specimen. The placement of thermocouple tips is shown for the sake of completion to aid in data interpretation (Figure 4a). Although not shown in Figure 4a for the sake of clarity, the closed hole for the thermocouple in the center of the specimen was opened for the calibration runs. The specimen temperature is showed in Figure 4(a) with open circle symbols. This data shows an actual increase from room temperature to 1,000°C in the first 2 s. The data shown in Figure 4 indicate the following:

- 1) The pyrometer data is affected by the infrared energy from the PAL during high-energy pulses. The proof of artifact is the sharp raise and drop in pyrometer temperatures right at the onset and end of pulses. The fact that the temperature varies during the high energy indicates that the reflections from the PAL into the pyrometer, which creates the artifact at high-energies, is not dominant and thus it can be corrected.
- 2) The pyrometer data is not affected by the infrared energy during the idle period, after the end of high-energy pulses. The pyrometer temperature at idle has the similar temperature ranges as those measured by thermocouples inserted in the 1G Mo holder.

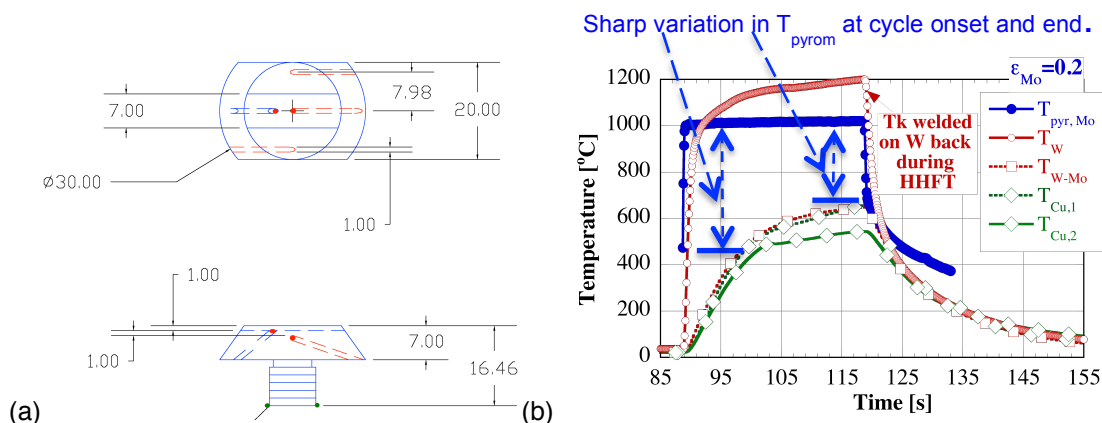


Figure 4. Data on HHFT of a non-irradiated specimen for calibration of specimen temperature: (a) 2nd generation of Mo specimen holder dimensions (thermocouple tips close to the specimen are shown with red dots) (b) Temperature measured by the pyrometer on the side surface of holder ( $T_{pyr,Mo}$ ) thermocouple welded on tungsten specimen back surface during HHFT ( $T_W$ ), thermocouple between tungsten specimen and holder ( $T_{W-Mo}$ ), and thermocouples in the cooling rod at the ends of holder thread.

From the data shown in Figure 4, it is inferred that there would be a temperature difference between that measured by the pyrometer and that by the welded thermocouple on the backside of the tungsten specimen of approximately 490 and 400°C, as estimated right when the pulse ended and 0.5 s after the pulse ended (to account for the pyrometer response time of 0.3 s), respectively. On the other hand, there would also be a temperature difference of approximately

553°C between the welded thermocouple and the thermocouple inserted in the open hole, but not welded to the specimen.

### High-heat flux experiments

Neutron-irradiated tungsten specimens were successfully tested at ITER-relevant high-heat flux conditions using Plasma Arc Lamp in August 2013 (Figure 5):

- One irradiated specimen was exposed to 81 pulses and the second one to 200 pulses at 3.3 MW/m<sup>2</sup> incident heat fluxes (1.65 MW/m<sup>2</sup> absorbed), 20 s duration, 100 s dwell time between pulses.
- No contamination was recorded outside the testing box.
- No radioactive gases leaked out of the testing box as the “negative” gauge pressure in the test enclosure was successfully maintained for the entire duration of the test of 4 h.

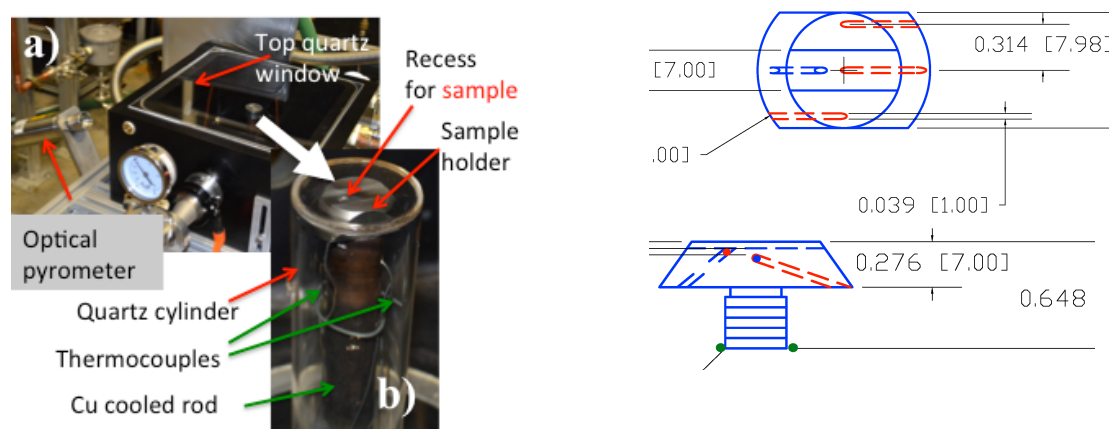


Figure 5. Experimental setup for: (a) the entire test section, (b) specimen holder and cooling rod, and (c) thermocouple placement within the sample holder.

The first irradiated tungsten specimen S1 was exposed to 80 high-heat flux cycles (Figure 6a) while the second specimen, S2, was exposed to 200 cycles. For S1, the operating parameters of the HHFT were varied for the first several cycles such that the maximum thermocouple temperatures would be limited to 700 to 800°C while allowing appropriate time for cooling (Figure 6b). According to the calibration data, this would translate to specimen temperatures of approximately 1,250 to 1,350°C (Figure 7).

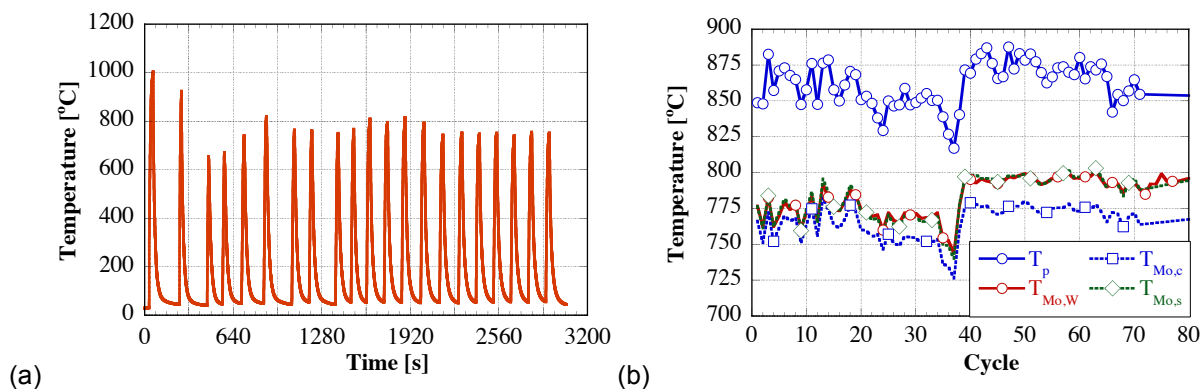


Figure 6. Measured temperatures (a) at W-Mo interface for the first 21 pulses for the first sample and (b) maximum temperature measured by the pyrometer on the side surface of Mo holder ( $T_p$ ), thermocouple on back surface of W specimen in the open hole ( $T_{Mo,W}$ ), thermocouple in the center of the sample holder ( $T_{Mo,c}$ ), and thermocouple on the side of the sample holder ( $T_{Mo,s}$ ). Sample temperature was expected to be approximately 1,200-1,300°C.

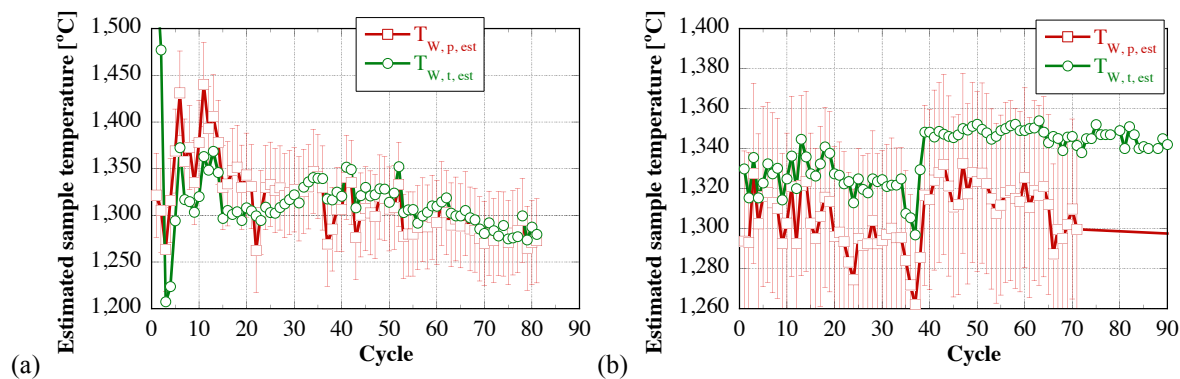


Figure 5. Estimated maximum temperature of the tungsten material for (a) specimen S1 and (b) specimen S2 (only 90 cycles out of 200 shown for the sake of clarity).

## ACKNOWLEDGMENTS

The authors would like to thank Charles Ross (Chuck) Schaich for assisting with CAD design, fabrication specifications, and assembly; Jim Kiggans for design and fabrication of the Al enclosure, Alta Marie Williams for radiation safety considerations, and David Harper for operating the PAL.

**5.1 Irradiation Response of Next Generation High Temperature Superconducting Rare Earth and Nanoparticle-Doped  $\text{YBa}_2\text{Cu}_3\text{O}_{7-x}$  Coated Conductors for Fusion Energy Applications** — K. J. Leonard, T. Aytug, Fred. A List III, Yanwen Zhang (Oak Ridge National Laboratory), A. Perez-Bergquist, W.J. Weber (University of Tennessee), and A. Gapud (University of South Alabama)

## OBJECTIVE

The goal of this work is to evaluate the irradiation response of the newest generation of coated conductors based on rare earth and nanoparticle doping of the  $\text{YBa}_2\text{Cu}_3\text{O}_{7-x}$  (YBCO) high temperature superconductors. The materials under investigation represent different methods for enhanced flux pinning for improved performance under externally applied magnetic fields. Ion beam irradiation will be used to simulate neutron damage cascades in the materials to examine the effect that radiation damage has on the different pre-existing defect structures used for flux pinning and to evaluate the superconductors capability for use in fusion reactor systems.

## SUMMARY

During this semiannual reporting period, electrical characterization work was completed on the irradiated superconducting films, and two presentations were made at conferences. The first, "Irradiation Response of Next Generation High Temperature Superconductors for Fusion Energy Applications" was presented at the International Conference of Fusion Reactor Materials in Beijing, China. This presentation introduced the fusion materials community to the advances that have been made in coated conductor technology and the potential for use in nuclear application. The second presentation "Irradiation of Commercial, High- $T_c$  Superconducting Tape for Potential Fusion Application: Electromagnetic Transport Properties," was presented in November at the Southeastern Section American Physical Society Meeting in Bowling Green, KY. This detailed the electrical property characterizations of the conductors and is summarized in this report.

## RESULTS

Thin film based coated conductors of Zr-doped  $(\text{Y,Gd})\text{Ba}_2\text{Cu}_3\text{O}_{7-x}$  (Zr-YBCO),  $(\text{Dy,Y})\text{Ba}_2\text{Cu}_3\text{O}_{7-x}$  (DyBCO) and  $\text{Gd}_2\text{Ba}_2\text{Cu}_3\text{O}_{7-x}$  (GdBCO) was irradiated by 5 MeV Ni and 25 MeV Au irradiations to fluences between  $10^{11}$  and  $10^{12}$  ions/cm<sup>2</sup>. Displacement damage was between 0.003 and 0.03 dpa depending on the type of conductor and its multi-layered architecture as determined through TRIM calculations. Differences in the nominal film thickness of each conductor types accounted for slight variations in dpa of the lower fluence 5 MeV Ni and 25 MeV irradiations and are accounted for in the following text and figures. The difference in dpa between film types for the high fluence 25 MeV Au irradiation was not as significant.

The key issue of interest of these conductors is their ability to pin the flow of magnetic flux quanta, allowing their application in high magnetic fields. In Type II superconductors as the applied magnetic field reaches the first critical field ( $H_{c1}$ ) quantized vortices begin to penetrate the superconductor. As current is applied the vortices experience Lorentz force, causing vortex flow. The vortex flow is dissipative, effectively killing the superconductivity of the material as the vortices pass through the film even if the applied field is still below the upper critical field ( $H_{c2}$ ). These latest generations of superconductors are designed to include secondary phase nanoparticles as well as defects that may be correlated to the nanoparticles as sites to trap the vortices. These defects are generally antiphase domain boundaries running in the c-axis

direction (perpendicular to the film) or intergrowths of various chemical compounds based off of variations of the standard Y123 stacking sequence of YBCO running in the *ab* direction.

Figure 1 compares the resistivity as a function of temperature for the three conductors studied following irradiation. The abrupt change from near zero resistivity is the critical temperature ( $T_c$ ). The transition point identifying the  $T_c$  is shown in greater detail within the insert of each plot. The normal state resistivity, the linear portion of the plot at temperatures above the  $T_c$ , is increased following irradiation due to the increase in scattering by added defects or impurities. The increase in normal state resistivity increases only a small amount following low fluence irradiation. The irradiation by 5 MeV Ni produces a greater increase in the normal state resistivity over the low fluence 25 MeV Au irradiations in the Zr-YBCO and DyBCO films, though the values of dpa are slightly higher ranging from 0.004 to 0.005 dpa versus 0.003 dpa for the Au irradiations. The GdBCO films show a negative curvature in the normal state resistivity with irradiation, making extrapolation of the residual resistivity ( $r_i$ ) values at 0 K difficult. For the Zr-YBCO and DyBCO conductors the normal-state is quadratic and identifiable, with the DyBCO conductor having a lower  $r_i$  than either the GdBCO or Zr-YBCO materials.

The change in resistivity versus dpa normalized to the pre-irradiated values at 100 K are compared in Figure 2 between the three conductors of this study and that of YBCO deposited on single crystal substrates [1]. The change in resistivity is significantly lower for the conductors of this study compared to the 6 MeV He and 25 MeV O irradiations of Hensel and coworkers. The electronic energy loss value for the 5 MeV Ni is similar to that of the He and O irradiations, while the 25 MeV Au is higher. However, for 120 MeV Kr irradiations the amount of damage created by the swift heavy ions is extensive with large changes in the resistivity measured.

The value of  $T_c$  decreases with dpa, though the change is relatively small in the conductors studied suggesting the presence of high-quality superconducting pathways even for the high dose 25 MeV Au irradiations. The dependence of  $T_c$  with respect to dpa, shown in Figure 3, further illustrates the reduced sensitivity of these conductors to irradiation. Reduction in  $T_c$  is a consequence of displacement reactions changing the whole carrier concentration in the Cu-O chains of the HTS structure, which are the most unstable sites due to the lightly bound oxygen atoms [2]. As oxygen-deficient and highly disordered regions are created with decreasing hole concentrations, degradation in  $T_c$  is observed. The relative changes in  $T_c$  of all three conductors, before and after the irradiation, is compared to thin YBCO films deposited on single crystal substrates. Note that except for the data of Hensel and coworkers [1] all irradiation studies were conducted near room temperature [3,4]. While increased recombination rates associated with room temperature irradiation may in part contribute to the measured stability, the  $T_c$  values of this study are still greater than those of other room temperature irradiated HTS materials. However, the higher irradiation temperatures may not necessarily influence  $T_c$  in this manner, as work by Okada and Kawakubo [5] on polycrystalline samples irradiated by neutrons at reactor temperature (360 K) showed a reduction in  $T_c$  as compared to irradiation at 20 K. The increased defect mobility at higher irradiation temperatures resulting in subsequent cascade collapse and less flux pinning in the conductor produce larger degradation in critical current density ( $J_c$ ) [6]. In contrast, the increased defect mobility at higher irradiation temperatures degrades flux pinning and  $J_c$  due to the subsequent cascade collapse.

The change in  $J_c$  and pinning force ( $F_p$ ) as a function of applied magnetic field following ion irradiation for the three conductors of this study is presented in Figure 4. The lower fluence ion irradiations have no major detrimental effect on the conductor  $J_c$  values, and in the case of DyBCO has an improvement. For the GdBCO conductor, there is a modest effect on  $J_c$  at low

fluences, though there is a 30% drop in  $F_p$  for irradiations to 0.004 dpa. However,  $J_c$  and  $F_p$  values for the conductor fall rapidly for the 0.03 dpa irradiation, despite the conductor still being superconducting. This loss is attributed to the disappearance of the  $Gd_2O_3$  nanoparticles in the microstructure and changes in the defects within the conductor following irradiation.

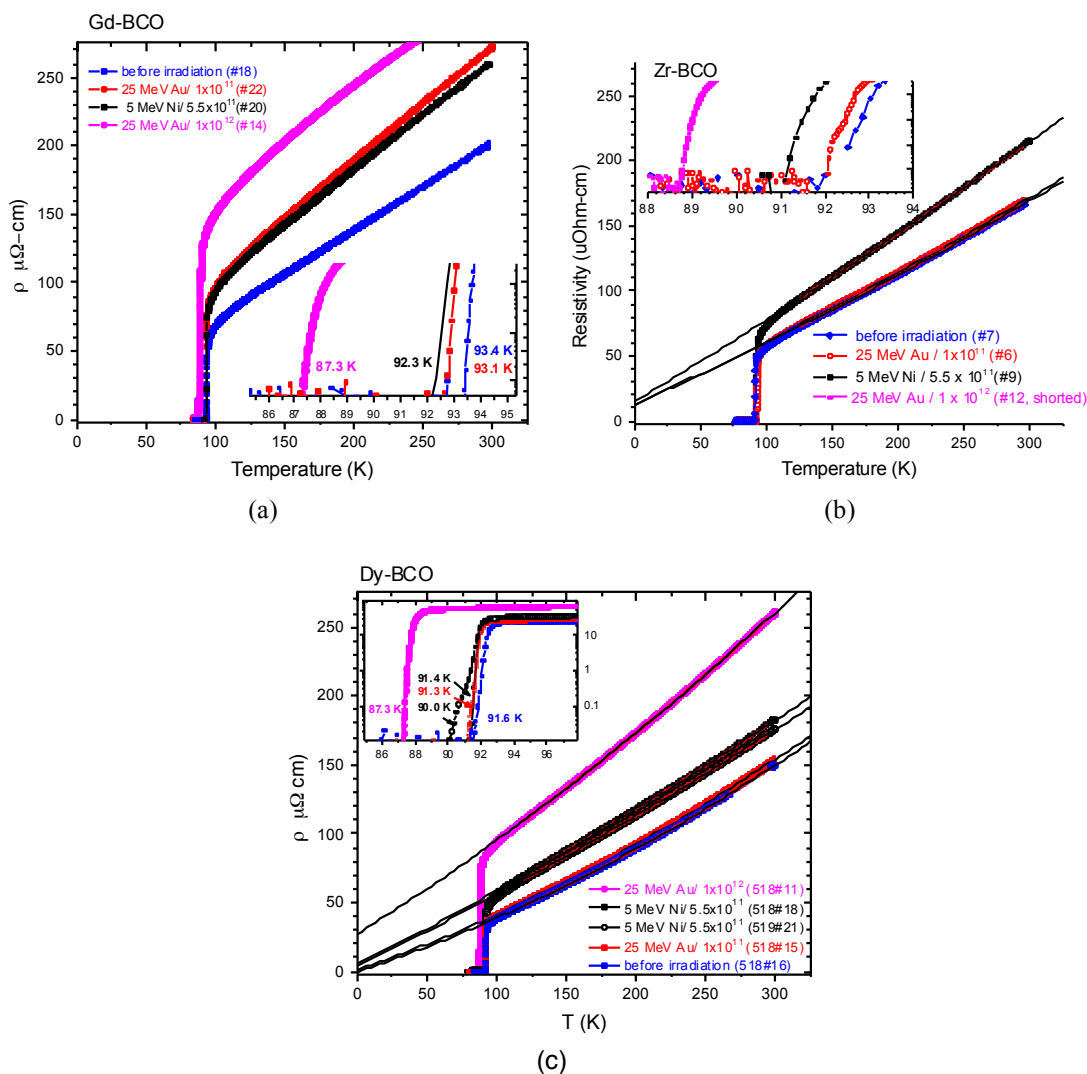


Figure 1. Transport resistivity versus temperature as a function of irradiation for the (a)  $Gd_2Ba_2Cu_3O_{7-x}$ , (b) Zr-doped  $(Y,Gd)Ba_2Cu_3O_{7-x}$ , and (c)  $(Dy,Y)Ba_2Cu_3O_{7-x}$  conductors. Insert plots for each conductor show the change in critical temperature with irradiation.

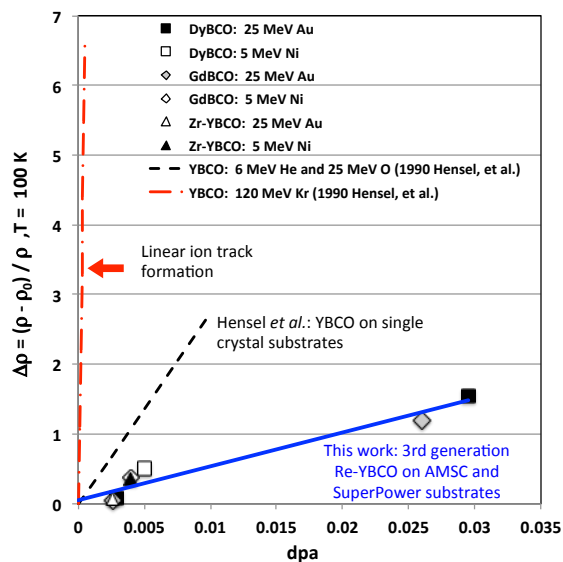


Figure 2. Change in 100 K resistivity from initial values ( $\rho_0$ ) following ion irradiation of different superconducting films based on the YBCO conductor [1].

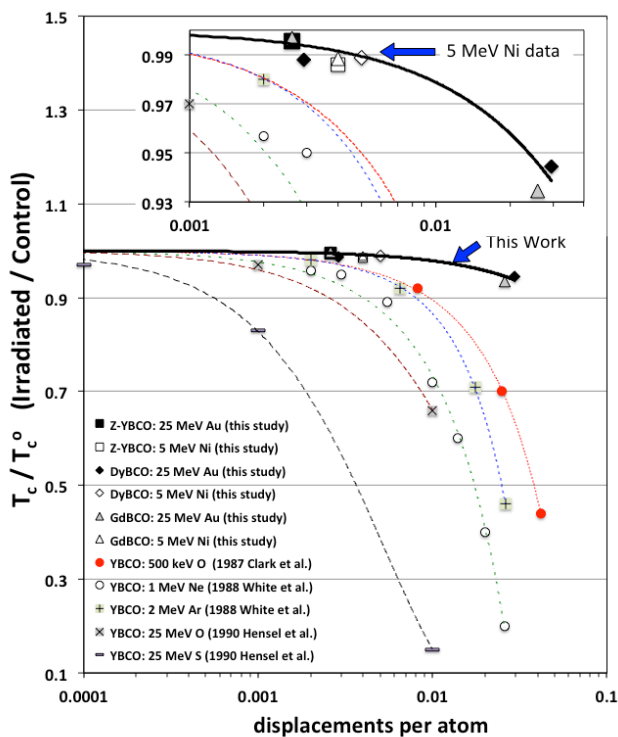


Figure 3. Change in  $T_c$  from initial values ( $T_c^0$ ) as a function of displacement dose for ion irradiated conductors of this study compared to ion irradiation data of YBCO films deposited on single crystal substrates [1,3,4].

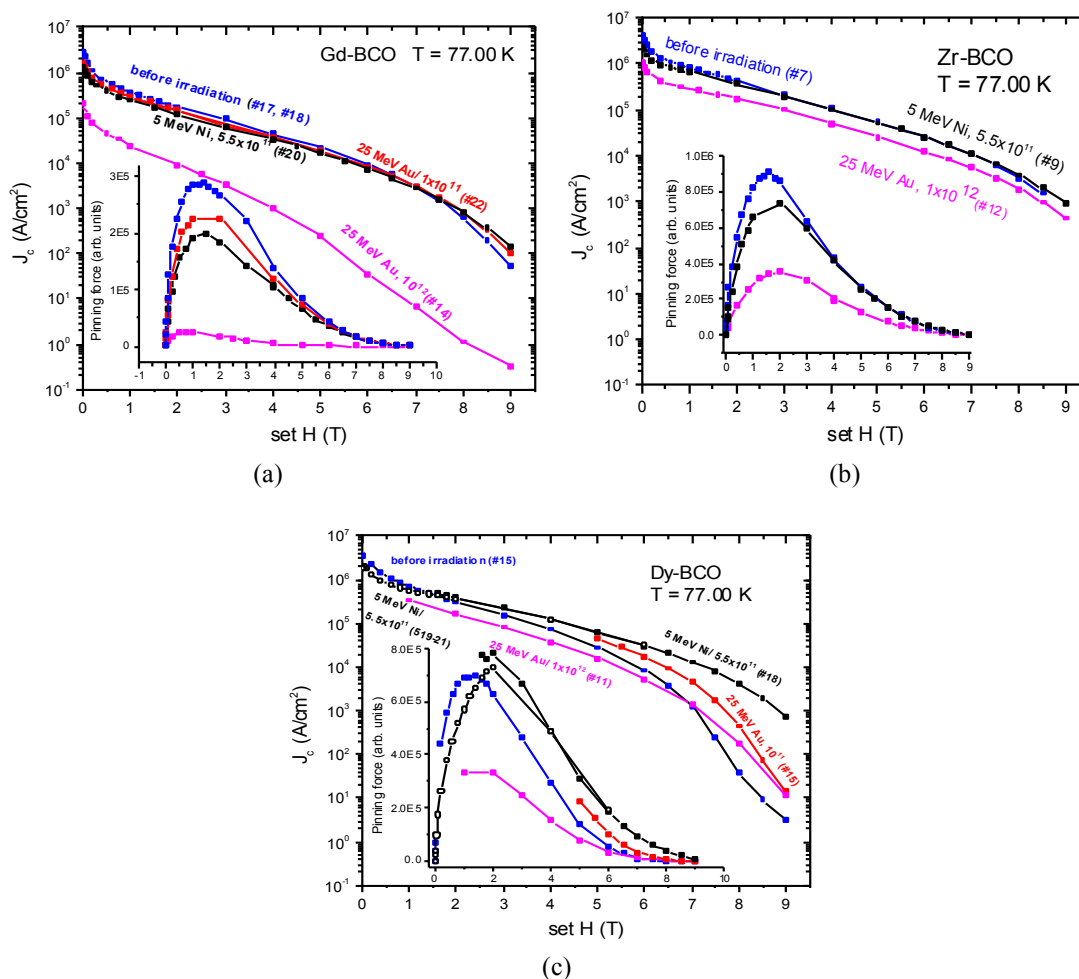


Figure 4. Transport critical current density ( $J_c$ ) and pinning force ( $F_p$ ) as a function of applied magnetic field strength for the (a)  $Gd_2Ba_2Cu_3O_{7-x}$ , (b) Zr-doped  $(Y,Gd)Ba_2Cu_3O_{7-x}$ , and (c)  $(Dy,Y)Ba_2Cu_3O_{7-x}$  conductors following ion irradiation.

Ion irradiation of the Zr-YBCO conductor results in very little change in  $J_c$  even for the 0.03 dpa condition. Losses are measured in  $F_p$  with irradiation, which was shown by microscopy to be due to the reduction in  $BaZrO_3$  (BZO) nanoparticles that are aligned in the  $c$ -axis direction within the conductor. However, this is offset by improved pinning in the  $ab$  direction by the increased amount of intergrowths generated at the interface with the BZO nanoparticles. This effect is not reflected in the results shown in Figure 4, as this data is collected in the  $H//c$  condition.

The DyBCO conductors showed a modest drop in transport properties for  $H < 2$  T, but show a very pronounced improvement at the highest field strengths. This is also reflected in the increased  $F_p$  values particularly at  $H > 3$  T. With the exception of GdBCO at 0.03 dpa, the  $J_c$  field dependence for the conductors is relatively unchanged for all test conditions for field strengths up to 6 T, above which  $J_c$  increases over the unirradiated values, and can be explained by the additional radiation induced defects in the microstructure [7,8]. The larger particles ( $Dy_2O_3$  for example) in the conductors are effective pinning centers at higher

temperatures and lower field strength [7], but at higher fields (above 6T) the additional radiation-induced defects accommodate more flux pinning resulting in enhanced transport properties. The transport measurements suggest that improved irradiation stability of the conductors in this work is obtained through the presence of nanoparticles and associated correlated defects. These defects and interfaces can either act as sinks for displacement damage or initiate the creation of additional defect structures that can in turn provide different field orientation dependencies [8]. For example, the lack of irradiation-induced change of  $J_c$  performance for the Zr-doped YBCO films along H//c is a result of columnar BZO particles absorbing irradiation-induced damage in this direction while introducing new intergrowths that improve pinning along *ab*-planes. However, an opposite behavior is observed for the DyBCO conductors and is currently under investigation.

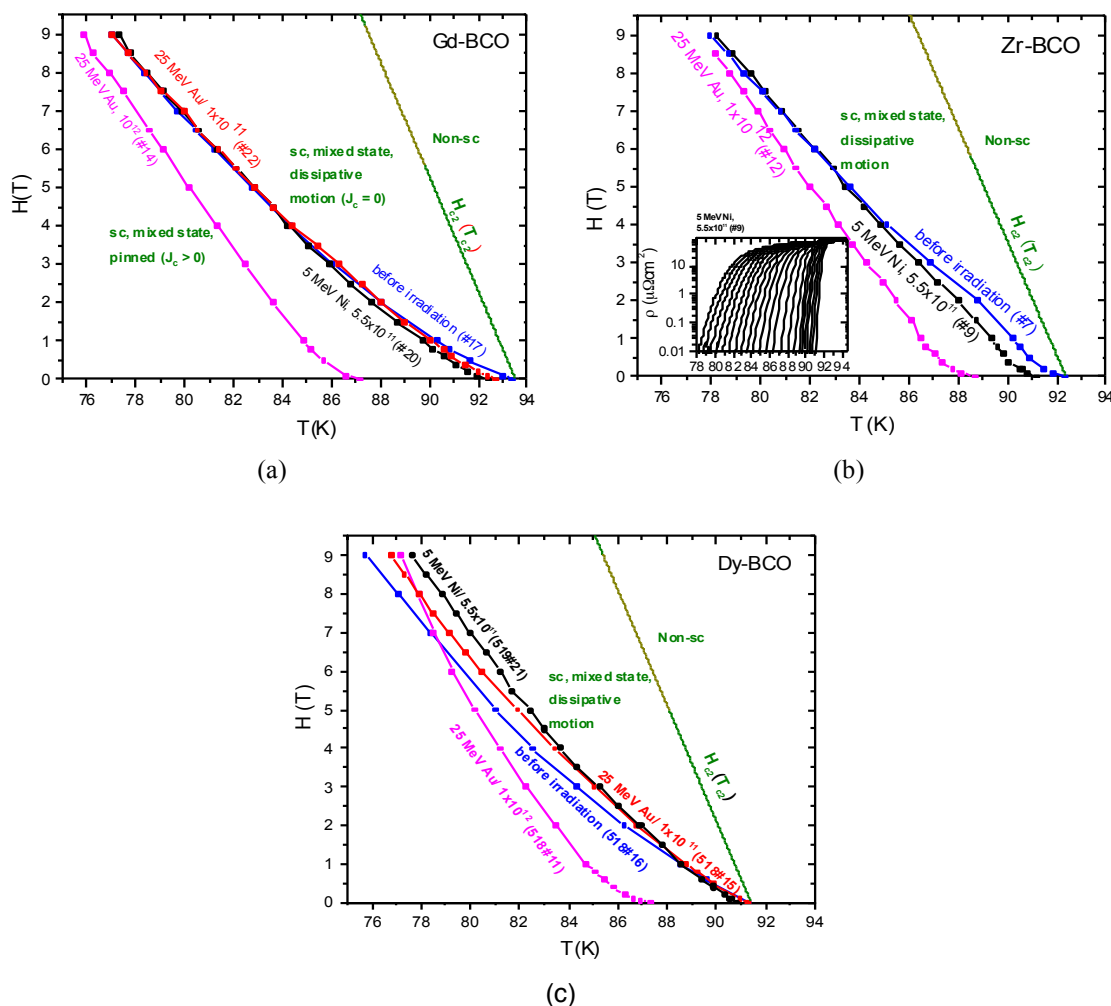


Figure 5. The irreversibility field as a function of temperature for (a)  $Gd_2Ba_2Cu_3O_{7-x}$ , (b) Zr-doped  $(Y,Gd)Ba_2Cu_3O_{7-x}$ , and (c)  $(Dy,Y)Ba_2Cu_3O_{7-x}$  conductors following ion irradiation. The boundary of the upper critical field,  $H_{C2}(T)$ , is shown for each. The irreversibility field is the boundary where critical current falls below detectable levels, whereas the  $H_{C2}(T)$  is the limit where bulk superconductivity is destroyed.

The use of YBCO conductors in large magnetic fields is limited by the characteristic irreversibility field,  $H^*(T)$ , which is lower than the upper critical field  $H_{c2}$ , and for which the values of  $J_c$  fall below detectable levels [9]. The irreversibility field, based on the effective pinning of flux-quantized line vortices by material imperfections such as point defects, grain boundaries, and secondary phases, is strongly dependent on the operating temperature and can vary from 27 Tesla at 52 K down to 5 Tesla at 80 K [9,10], where the benefit of a lower cost cryogenic cooling can be diminished by the field restrictions. The irreversibility line can be thought of as the depinning line or the boundary between pinned vortices and unpinned vortices. The changes in  $H^*(T)$  for the conductors of this study following irradiation are shown in Figure 5, and show that following irradiation to 0.005 dpa no significant decrease to the usable phase space occurs. Much of the temperature reductions for a given field strength (or the available phase space lost) occur at lower field values for the high dose irradiations with the greatest reduction observed in the GdBCO conductor and least in the Zr-YBCO material. These temperature restrictions are minimized at the higher field strengths, particularly for the DyBCO conductor that shows improvements over the unirradiated value. It is likely that a similar effect is also observed in the other conductors for field strengths in excess of 9 T due to the observed presence of small (< 2 nm) radiation-induced defects appearing in the microstructures of all the conductors following 25 MeV Au irradiation to 0.03 dpa.

From the electrical characterization performed on the samples, the vortex creep rate ( $S$ ) was determined as a function of the applied field strength. From combining the power law relationship between voltage and current with that of the Maxwell equation the creep rate is determined as  $S = -\partial \ln I / \partial \ln t$ . The lower the value of  $S$  correlates to minimizing the dissipative motion of the vortices, in which lower values are desirable to allow persistent-mode operation at the lowest voltages possible, without significant reduction in  $J_c$ . Following 5 MeV Ni irradiation the value of  $S$  shows a small increase in the GdBCO conductor, Figure 6, which converge slightly at higher fields with that of the unirradiated values. For the Zr-YBCO conductor there is little effect with irradiation to 0.004 dpa and a rise, though modest, with irradiation to 0.03 dpa. The DyBCO conductor is much more complex, in that a drop in  $S$  occurs for 0.003 – 0.004 dpa at applied fields above 2 T, and that the non-irradiated value increases to match the 0.03 dpa irradiation at higher fields. This confirms the pinning loss of the larger  $\text{Dy}_2\text{O}_3$  particles (26 nm average size) at higher fields; where smaller radiation induced defects are more efficient. The relative lack of change in the Zr-YBCO conductor is not unanticipated as the material shows a measure of resilience to irradiation damage, though some shifting in the angular field dependent properties are observed. The loss in the small (3.8 nm average size)  $\text{Gd}_2\text{O}_3$  particles with irradiation is very detrimental in the GdBCO, though radiation-induced defects may recover some properties in field strengths above 9 T.

## CONCLUSIONS

The work conducted in the past year on the three commercial high temperature superconductors has shown generally promising results in terms of radiation tolerance. The behavior of each conductor type is different and shows improved radiation tolerance over earlier generation YBCO films. For the conditions investigated, the Zr-YBCO conductor shows the least amount of degradation with irradiation, with minor and localized changes in the microstructure related to the size and defects generated from the  $\text{BaZrO}_3$  nanoparticles present within the conductor. The DyBCO conductor shows improved properties with irradiation damage to varying levels dependent on the applied magnetic field under which properties are tested. Though the GdBCO did not show as much tolerance to irradiation damage as the other conductor types, it is significantly improved over earlier generation YBCO base films.

## CURRENT AND FUTURE WORK

Work currently being engaged involves the preparation of samples and irradiation holders for the neutron irradiation of the Zr-YBCO and DyBCO conductors. This work will take place at the High Flux Isotope Reactor within the 2014 calendar year. Further work involving transmission electron microscopy characterization of the ion-irradiated samples will be performed in order to elucidate specific phenomenon identified during electrical property evaluations. This includes identification of the causes for increased c-axis pinning in the DyBCO conductor at lower ion fluences as well as the nature of the faults generated and observed in the conductors at 0.03 dpa.

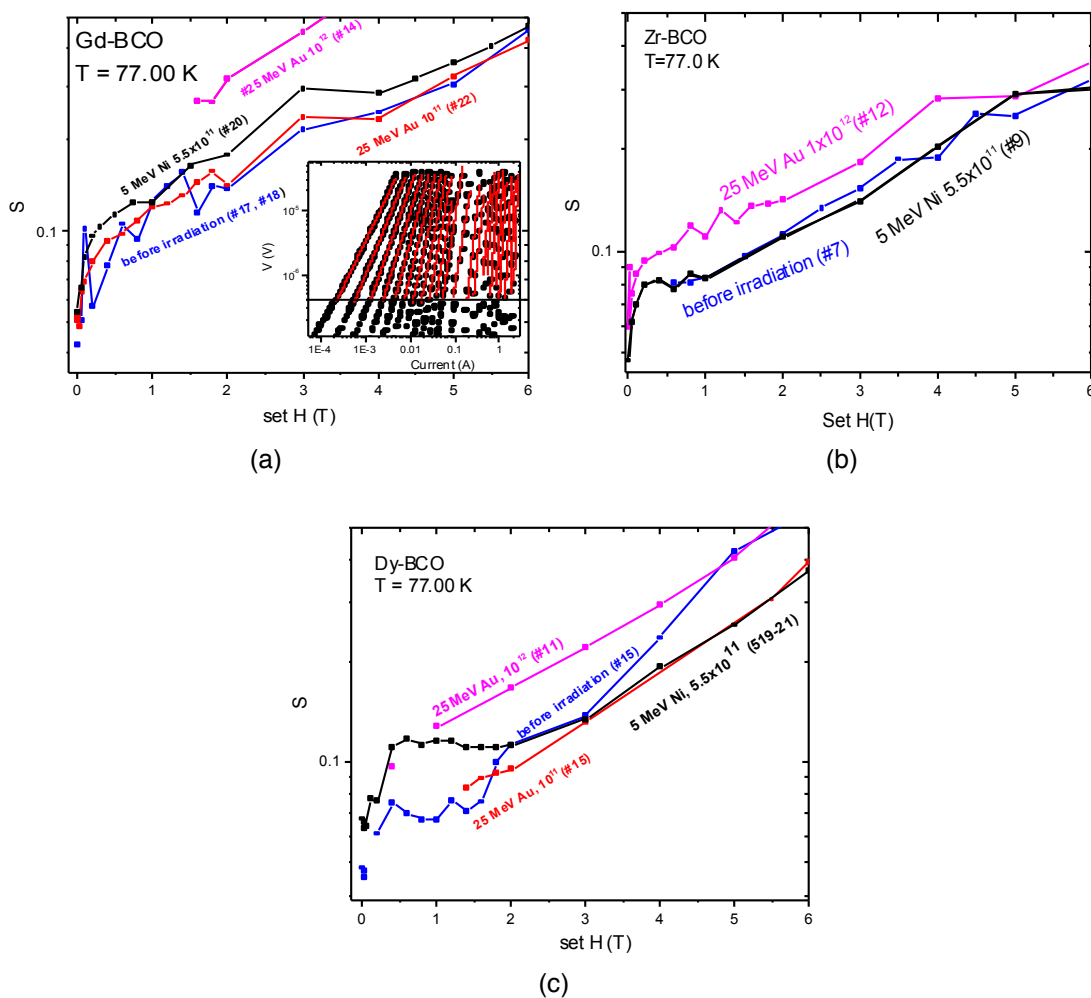


Figure 6. The vortex creep rate,  $S$ , as a function of applied magnetic field strength for (a)  $\text{Gd}_2\text{Ba}_2\text{Cu}_3\text{O}_{7-x}$ , (b) Zr-doped  $(\text{Y,Gd})\text{Ba}_2\text{Cu}_3\text{O}_{7-x}$ , and (c)  $(\text{Dy,Y})\text{Ba}_2\text{Cu}_3\text{O}_{7-x}$  conductors following ion irradiation. The insert in (a) of voltage versus current is from the data taken in determining the value of  $S$ , with the steeper slope the better.

## REFERENCES

1. B. Hensel et al., "Ion Irradiation of Epitaxial  $\text{YBa}_2\text{Cu}_3\text{O}_{7-x}$  Films: Effects of Electronic Energy Loss," *Phys. Rev. B* **42** (7), 4135 (1990).
2. D. V. Kulikov et al., "Changes in the Transition Temperature After Irradiation and Annealing in Single Crystalline  $\text{YBa}_2\text{Cu}_3\text{O}_{7-x}$ ," *Physica C* **355**, 245 (2001).
3. G. J. Clark et al., "Effects of Radiation Damage in Ion Implanted Thin Films of Metal Oxide Superconductors," *Appl. Phys. Lett.* **51**, 139 (1987).
4. A. E. White, et al., "Ion-Beam Induced Destruction of Superconducting Phase Coherency in  $\text{YBa}_2\text{Cu}_3\text{O}_{7-d}$ ," *Phys. Rev. B* **37** (7), 3755 (1988).
5. M. Okada and T. Kawakubo, "Effects of Neutron Irradiation on Superconducting Properties of Orthorhombic Y-Ba-Cu Oxides," *Rad. Eff. Defects Solids* **108**, 137 (1989).
6. M. Sawan, "Radiation Shielding Requirements for Magnets in Fusion Reactors," JAPMED-4 presentation, Cairo, Egypt, September 17-20, 2005.
7. U. Topal, L. Dorosinskii and H. Sozeri, "Effect of Neutron Irradiation on Pinning in  $\text{SmBaCuO}$  and  $\text{YBaCuO}$  Superconductors," *Physica C* **407**, 49 (2004).
8. M. Chudy et al., "Characterization of Commercial YBCO Coated Conductors After Neutron Irradiation," *IEEE Trans. Appl. Supercond.* **21** (3), 3162 (2011).
9. D. Larbalestier et al., "High  $T_c$  Superconducting Materials for Electric Power Applications," *Nature* **414**, 368 (2001).
10. R. M. Scanlan, A. P. Malozemoff, and D. C. Larbalestier, "Superconducting Materials for Large Scale Applications," *Proc. of the IEEE* **92** (10), 1639 (2004).

**5.2 High Neutron Dose Irradiation of Dielectric Mirrors** — K. J. Leonard, G. E. Jellison Jr., N. A. P. K. Kumar and L. L. Snead (Oak Ridge National Laboratory)

**OBJECTIVE**

The goal of this work is to evaluate the upper neutron irradiation dose and thermal limits of two promising dielectric mirror types, through an investigation of the radiation and thermally induced microstructural and optical property changes. While specifically of interest for use in laser control of inertial confinement fusion systems, the examination of the radiation induced structural changes in the films will be beneficial for the development of other thin-film based electronic components and sensors used in nuclear applications.

**SUMMARY**

During this semiannual reporting period, work was completed on low dose (0.001 to 0.1 dpa) examinations culminating in the presentation of data at the Radiation Effects in Insulators conference in Helsinki, Finland in July 2013. Publication of the paper “The role of microstructure on the optical performance of neutron irradiated dielectric mirrors” has been confirmed for the Journal of Nuclear Materials in 2014, volume 445, pages 281-290. The optical property characterization of the 1 and 4 dpa-irradiated mirrors has also been completed, with data presented in poster form at the International Conference of Fusion Reactor Materials in Beijing, China in October. This semiannual contribution briefly summarizes the low dose results, which are presented in more detail in the previous contributions, as well as the optical property data for the high dose samples.

**PROGRESS AND STATUS**

**Failure Mechanisms in Dielectric Mirrors**

The beginning of this semiannual period saw the completion of the low dose (0.001 to 0.1 dpa) characterization work on the  $\text{Al}_2\text{O}_3/\text{SiO}_2$  and  $\text{HfO}_2/\text{SiO}_2$  dielectric mirrors. Failure through film delamination resulting in loss in reflectance only occurred following post-irradiation annealing of the 0.1 dpa  $\text{HfO}_2/\text{SiO}_2$  mirror. However, considerable interdiffusion of Al and Si was measured across the film interfaces of the  $\text{Al}_2\text{O}_3/\text{SiO}_2$  mirror that may be related to reflectance losses at higher (1 dpa and greater) displacement damage levels.

Reflectance loss in the  $\text{HfO}_2/\text{SiO}_2$  dielectric mirror observed following 1 hr. annealing treatments at 573 and 673 K of the 0.1 dpa irradiated samples was caused by delamination of the films by defects generated at the  $\text{HfO}_2$  film/sapphire substrate interface. These defects are formed from the buckling of the first  $\text{HfO}_2$  film layer (the mirror consists of alternating  $\text{HfO}_2$  and  $\text{SiO}_2$  layers with an  $\text{HfO}_2$  being the first and last film layers in the 11 bi-layer stack) as a result of the loss of adhesion to the sapphire substrate due to the amorphization of the sapphire in the vicinity of the film interface. The defects at the interface produce a higher state of stress in the films during cooling from the annealing temperatures, which upon reaching a critical stress value can create localized delamination of the entire film stack. The loss in reflectance is greater with

increasing annealing temperature and is suspected to be the source of failure appearing temperature.

### Optical Properties of High Dose Neutron Irradiated Mirrors

A comparison of the spectral reflectance curves for the two mirror types following select irradiation and post-irradiation exposures is shown in Figure 1. Both mirrors were designed for peak reflectivity at 248 nm. For the  $\text{Al}_2\text{O}_3/\text{SiO}_2$  mirrors irradiation to 1 dpa resulted in a decrease in the working range (the width of peak reflectance shown in the curves in Figure 1) of the mirror, with a reduction in reflectance to 95% at 248 nm. Furthermore, the working range is also shifted to longer wavelengths. The change in shape of the reflectance spectra is likely due to the formation of secondary phases between the constituent film types. However, the loss in reflectance is through delamination, likely from the secondary phase particles that produce stress concentrators in the film stack. Microstructural analysis of these films is underway. Complete loss in reflectance is observed in the  $\text{Al}_2\text{O}_3/\text{SiO}_2$  mirrors following 4-dpa irradiation. Signs of film delamination could be observed visually following irradiation. Figure 2 compares the visual changes in the  $\text{Al}_2\text{O}_3/\text{SiO}_2$  mirror with increasing irradiation leading to the darkening in the optical range as well as the appearance of delaminated regions (speckling) occurring at higher levels of dpa. Similar changes in appearance are observed for the  $\text{HfO}_2/\text{SiO}_2$  mirror. The small difference in surface delamination between the 1 and 4 dpa samples suggests that failure is very rapid in this range.

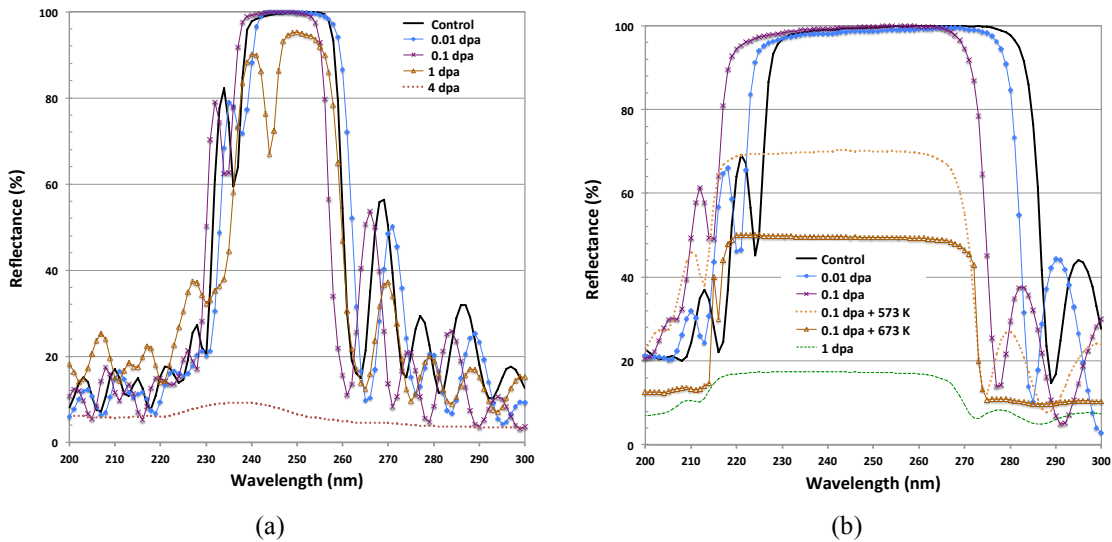


Figure 1. Photo spectrometry results of the (a)  $\text{Al}_2\text{O}_3/\text{SiO}_2$  and (b)  $\text{HfO}_2/\text{SiO}_2$  mirrors in the unirradiated and select irradiation and post-irradiation annealed conditions. The reflectivity data is normalized based on the absolute reflectivity measurements conducted through direct laser reflectance measurements.

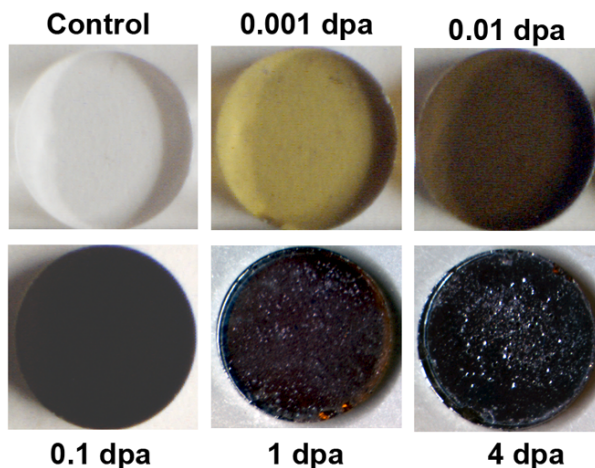


Figure 2. Visual changes in the  $\text{Al}_2\text{O}_3/\text{SiO}_2$  mirror with increasing neutron irradiation. Similar changes are observed for the  $\text{HfO}_2/\text{SiO}_2$  mirror.

The  $\text{HfO}_2/\text{SiO}_2$  mirror showed reflectance values below 20% following 1 dpa exposure (Figure 1b) and no measureable reflectance following 4 dpa. The mechanisms responsible for the losses are presumably an extension of those identified in microstructural characterization of the lower dose samples. As discussed in the previous section, partial amorphization of the sapphire near the  $\text{HfO}_2$  film interface occurs with irradiation produced a 20 nm thick layer following 0.1 dpa. It is expected that with higher displacement damage the amorphous region has further weakened the interface leading to the buckling of the  $\text{HfO}_2$  without the need for a post-irradiation anneal. Cooling from the irradiation temperature would therefore be enough to cause elevated stresses at these defects to cause delamination.

## Discussion

The work conducted in the past year on the  $\text{Al}_2\text{O}_3/\text{SiO}_2$  and  $\text{HfO}_2/\text{SiO}_2$  dielectric mirrors provided detailed insight into both the upper neutron irradiation dose and thermal exposure limits of mirrors. Thermal exposures up to 675 K produced similar changes in the materials as compared to neutron irradiation to 0.1 dpa at 448 K. It is likely that these mirrors could be capable of higher temperatures for short durations, but they are going to be very sensitive to the rate of cooling as well as the amount of accumulated damage present in the material either through thermal or displacive radiation exposure.

The  $\text{Al}_2\text{O}_3/\text{SiO}_2$  mirror shows greater stability of the two mirror types studied despite the significant interdiffusion of Al and Si between the constituent layers. The 10% loss in reflectance following 1 dpa exposure is small in comparison to losses observed in the  $\text{HfO}_2/\text{SiO}_2$  mirrors under equivalent conditions. Furthermore, our earlier work demonstrated better laser damage threshold values for the  $\text{Al}_2\text{O}_3/\text{SiO}_2$  mirror [1]. This is likely influenced by the closer matching of properties of the amorphous  $\text{Al}_2\text{O}_3$  and  $\text{SiO}_2$  layers of the mirror, as well as the near atomic level smoothness of the deposited layers

as compared to that of the HfO<sub>2</sub> layers in the other mirror. Despite some decreases in roughness with irradiation of the HfO<sub>2</sub> layers, the large microstructural changes associated with film densification, phase changes in HfO<sub>2</sub> and amorphization near the substrate/film interface would only lead to further deterioration of laser damage tolerance.

From a design perspective, the Al<sub>2</sub>O<sub>3</sub>/SiO<sub>2</sub> mirror offers a stable platform for systems in fusion applications where laser based diagnostic devices are used. The peak reflectance for the mirror can be tuned to different wavelengths by varying the thickness of the constituent films. There may be some limitation if substantially thick layers are required and ion-beam assisted vapor deposition can no longer maintain an amorphous, smooth and defect free films. Due to the large difference in refractive indices of the constituent layers the HfO<sub>2</sub>/SiO<sub>2</sub> mirror offers increased working range of the mirror with fewer number of bi-layers required (better control of defects) for high reflectance. However, the lack of radiation stability of the HfO<sub>2</sub> layer makes this mirror less attractive for nuclear applications. Other materials with large refractive index values compared to SiO<sub>2</sub>, such as TiO<sub>2</sub> and ZrO<sub>2</sub> also suffer from similar radiation-induced phase changes as HfO<sub>2</sub>.

The evaluation of other film layer combinations may lead to some improvements over the Al<sub>2</sub>O<sub>3</sub>/SiO<sub>2</sub> mirror, though these improvements are likely to be small. However, the Al<sub>2</sub>O<sub>3</sub>/SiO<sub>2</sub> mirror maintained  $\geq 95\%$  reflectance up to 1 dpa neutron exposure, which is two orders of magnitude greater than for the laser control systems of the inertial confinement fusion system that this study was initially intended to examine. The outcomes of this work definitively showed the link between microstructural changes in the mirrors to that of its optical properties and identified the mechanisms leading to delamination of film layers.

### **Current and Future Work**

Work on the 1 and 4 dpa mirrors is completing with the examination of the microstructures through transmission electron microscopy. The key issues that will be examined in these samples are 1.) If secondary phase development occurred at the Al<sub>2</sub>O<sub>3</sub>/SiO<sub>2</sub> film interfaces and, 2.) If the delamination mechanisms in the HfO<sub>2</sub>/SiO<sub>2</sub> mirror following 1 and 4 dpa are the same as that observed in the 0.1-dpa mirrors following post-irradiation annealing.

Further work on optical properties of diagnostic system based materials will be applied to the identification of needed areas of examination or clarifications related to materials behavior in fusion environments. The purpose of which is to identify possible areas in which the US Fusion Materials Program could be situated in order to provide greater international leadership in the area of diagnostic systems.

### **REFERENCES**

- [1] L. L. Snead, K. J. Leonard, G. E. Jellison Jr., M. Sawan and T. Lehecka, *Fusion Sci. Technol.* **56** (2), 1069 (2009).

## 6.1 Liquid Metal Compatibility — S. J. Pawel (Oak Ridge National Laboratory)

### OBJECTIVE

The objective of this task is to identify potential structural materials having sufficient compatibility with flowing Pb-Li eutectic that the maximum metal temperature for operation can be increased to improve overall system efficiency.

### SUMMARY

Fabrication of the first thermal convection loop (TCL) using dispersion strengthened FeCrAl (Kanthal APMT) tubing was completed in the previous reporting period. This alloy is known for high strength and creep resistance at elevated temperature and, based on capsule testing, it is anticipated to have excellent resistance to Pb-Li. Recent accomplishments include initial refurbishment of suitable laboratory space in which to operate the TCL, acquisition and chemical analysis of the Pb-17at%Li that will be used as a working fluid, and preparation of the Kanthal APMT test coupons that will be used in the specimen chains that will be inserted into each vertical leg of the TCL.

### PROGRESS AND STATUS

#### Introduction

Currently, the maximum allowable wall temperature for the dual coolant lead-lithium (DCLL) blanket concept is set at 475°C based primarily on corrosion limitations of the structural containment materials. To increase overall system efficiency, potential structural materials are being sought with a combination of high strength and creep resistance with simultaneous resistance to dissolution in eutectic Pb-Li at temperatures > 500°C. Preliminary research using static capsule exposures has indicated that dispersion strengthened FeCrAl (Kanthal APMT) may be resistant to dissolution in eutectic Pb-Li at temperatures in the range of 600-800°C, at least in part due to the stability of an Al-rich oxide film. However, corrosion data in a flowing system must be generated to analyze the potential for issues associated with thermal gradient mass transfer – relatively high dissolution in hotter portions of the flow system with concomitant deposition in the colder portions – which has been known to disrupt heat transfer and even plug flow paths completely in some temperature gradient – material combinations.

Thus, thermal convection flow loops (TCLs) are being incorporated as the follow-on step to capsule testing for evaluation of liquid metal compatibility. The initial laboratory testing associated with this effort will utilize a monometallic TCL fabricated of Kanthal APMT with APMT specimens inserted within each of the hot leg and cold leg of the TCL for use in post-exposure evaluation. Fabrication of the first such TCL utilizing APMT tubing (26.7 mm OD, 3.1 mm wall), which evaluated welding and heat treatment procedures to be used in subsequent TCL construction with this alloy, was successfully completed near the end of FY13. Preparations for loop operation and corrosion testing are now underway.

#### Results

Figure 1 shows a schematic of the APMT loop, as it will appear in assembled form. The loop is about 1 m tall and 0.5 m wide in the flow path. Heating on one side of the loop (the “hot” leg) will cause the density of the liquid Pb-Li material to decrease relative to the liquid in the

unheated leg; the density difference drives flow (down on cooled side, up on heated side) once a steady temperature gradient is established. [In Figure 1, the liquid metal flow direction would be counterclockwise.] This loop will contain two specimen chains – one in each vertical leg of the loop. Test coupons of APMT have been prepared in the form of miniature tensile specimens, and will be strung together with APMT wire (see Figure 2 for an example from a previous TCL experiment in this laboratory). Most of the APMT test specimens received the same high temperature oxidation treatment afforded the loop itself, but a few of the specimens remain in the as-machined (no oxide) condition to permit ready comparison of compatibility with Pb-Li as a function of temperature around the loop. In addition to APMT coupons, a few small rectangular specimens of commercially pure tungsten have been prepared for incorporation at the bottom of each specimen chain to act as a “sinker” to keep the relatively low-density specimen chains from floating in the Pb-Li test fluid.

Completion of laboratory space preparation and the loop test stand has been delayed somewhat by lack of space availability and limited craft resources to finish electrical wiring and ventilation cabinet construction. At present, it is expected that these activities will be completed in time to permit loop operation to commence in mid-to-late March 2014.

Independent compositional analyses of the Pb-Li alloy that will be used for these experiments (purchased from a commercial supplier in Europe) was completed; results from a range of positions within several units of material (ingots shown in Figure 3) uniformly yielded 83.0 at% Pb and 17.0 at% Li with about 1200 ppm oxygen and 240 ppm carbon and all other elements below the detectability limit (~ 1-5 ppm).

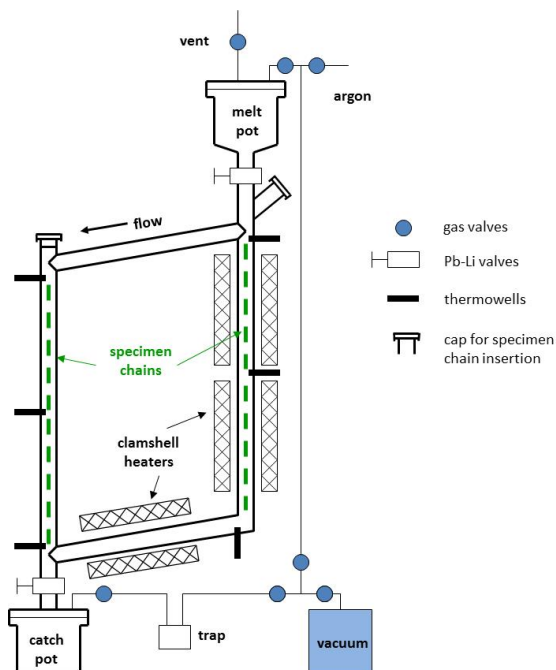


Figure 1. Schematic of the thermal convection loop for Pb-Li experiments. Actual dimensions are approximately 1 m x 0.5 m in the liquid metal flow path around the loop.

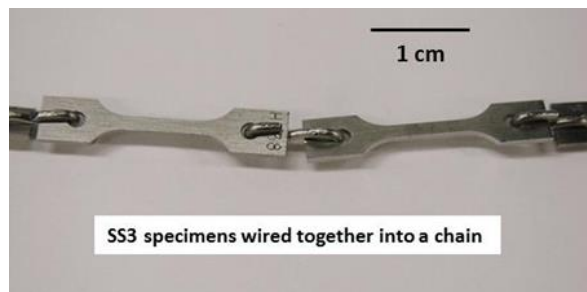


Figure 2. Representative example of miniature tensile specimens (“SS3” design) wired together as part of a specimen chain for a thermal convection loop experiment. The SS3 specimens are about 25 mm long, 5 mm wide, and 1 mm thick.



Figure 3. Ingots of Pb-17at%Li just prior to shipment to USA. Each ingot is approximately 4.5kg of high purity eutectic alloy.

**7.1 Microstructural Stability and Mechanical Behavior of FeMnNiCr High Entropy Alloy Under Ion Irradiation** — N. A. P. K. Kumar<sup>1,2</sup>, K. J. Leonard<sup>1</sup>, H. Bei<sup>1</sup>, Y. Zhang<sup>1,2</sup> and S. J. Zinkle<sup>1</sup> (*Oak Ridge National Laboratory<sup>1</sup>, University of Tennessee<sup>2</sup>*)

**ABSTRACT** - to be submitted to the Journal of Nuclear Materials

In recent years, high entropy alloys (HEAs) have attracted significant attention due to their excellent mechanical properties and good corrosion resistance, making them potential candidates for high temperature fusion structural applications. However, there is practically nothing known about their radiation resistance. In the present study, a high entropy alloy of composition 27%Fe-27%Mn-28%Ni-18%Cr, manufactured at ORNL, is ion irradiated at room temperature and at 500°C to doses ranging from 0.1 dpa to 10 dpa. Transmission electron microscopy (TEM), scanning transmission microscopy with energy diffraction spectrometry (STEM/EDX) and X-ray diffraction (XRD) were used to examine the radiation defects and microstructural changes. Irradiation at 500°C showed evidence of significant solute segregation at grain boundaries and discrete precipitates were observed; precipitation was not observed in the room temperature irradiated samples. Voids were not observed for any irradiation condition. Nano-indentation tests on the specimens showed a rapid increase in hardness ~40% higher than the unirradiated value at 0.1 dpa and to approximately double the unirradiated hardness at 1 dpa with the irradiation at room temperature. The irradiation hardness was less pronounced for 500°C irradiations. The present study provides insight of the fundamental irradiation behavior of HEA material.

**7.2 EFFECTS OF ION IRRADIATION ON BAM-11 BULK METALLIC GLASS —**  
A. G. Perez-Bergquist<sup>1,2</sup>, H. Bei<sup>1</sup>, Y. Zhang<sup>1,2</sup>, and S. J. Zinkle<sup>1,2</sup> (Oak Ridge National  
Laboratory<sup>1</sup>, University of Tennessee<sup>2</sup>)

**OBJECTIVE**

The goal of this study is to investigate the radiation behavior of the bulk metallic glass BAM-11 and to determine if it is a viable candidate for high-radiation structural applications in fusion applications.

**SUMMARY**

Bulk metallic glasses are intriguing candidates for structural applications in nuclear environments due to their good mechanical properties along with their inherent amorphous nature, but their radiation response is largely unknown due to the relatively recent nature of innovations in bulk metallic glass fabrication. Here, microstructural and mechanical property evaluations have been performed on a  $Zr_{52.5}Cu_{17.9}Ni_{14.6}Al_{10}Ti_5$  bulk metallic glass (BAM-11) irradiated with 3 MeV  $Ni^+$  ions to 0.1 and 1.0 dpa at room temperature and 200°C. Transmission electron microscopy showed no evidence of radiation damage or crystallization following ion irradiation, and changes in hardness and Young's modulus were typically <10%, with slight softening following irradiation at room temperature and no significant changes at 200°C. These results suggest that the BAM-11 bulk metallic glass may be useful for certain applications in nuclear environments.

**PROGRESS AND STATUS**

**Introduction**

Amorphous metallic glasses were first synthesized in the 1960s [1] and have since received considerable scientific attention due to their appealing properties, including their good thermal conductivity, high strength, good ductility, and corrosion resistance [2-4]. In particular, metallic glasses are an intriguing candidate for use in radiation environments due to their lack of crystalline structure, which prohibits the formation of conventional radiation defects such as vacancy-interstitial Frenkel pairs and dislocation loops that occur in crystalline solids. Although particle irradiation can produce point defects and macroscopic changes in amorphous materials in a manner somewhat analogous to what happens in crystalline materials, there is some evidence that the amount of retained displacement damage can be significantly less in amorphous materials [5]. In addition, metallic glasses may possess high helium permeabilities due to their large free atomic volumes and lack of grain boundaries that can act as helium traps [5]. In fact, recent studies show that metallic glasses may be resistant to cavity swelling, and hence possibly tritium retention, as compared to crystalline materials, which would make them appealing for fusion energy applications [6].

Though metallic glasses could initially only be fabricated as thin sheets due to the extremely high cooling rates required to quench the material in the amorphous phase, pronounced advances have been made over the past few decades in metallic glass fabrication that now allow for the creation of high-performance structural glasses in bulk

form, thus vastly increasing their usefulness for structural applications [7,8]. To date, however, little data exists on the effects of displacement irradiation on these highly engineered metallic glasses. Different studies have reported crystallization of metallic glasses under irradiation [9-13] while others have not [6, 14-18], but tests have been performed on different amorphous alloys under different ion irradiation conditions and at varying temperatures (see Table 1). Though irradiation-induced softening has been reported in several studies [15, 18-20], and hardening has also been reported in at least one [11], mechanical properties of irradiated bulk metallic alloys are still largely unknown, as is the microstructural evolution of irradiated bulk metallic glasses as a function of irradiation dose and temperature.

**Table 1.** Summary of ion irradiation studies in bulk metallic glass, organized by incident ion fluence.

Material	Ion Species	Ion Energy (keV)	Ion Fluence (cm <sup>-2</sup> )	Temp.	Crystallization (Y/N)	Source
Zr <sub>50</sub> Cu <sub>40</sub> Al <sub>10</sub>	Al <sup>+</sup> , Xe <sup>+</sup>	5000, 200000	1 x 10 <sup>12</sup> - 3 x 10 <sup>14</sup>	RT	N	[17,18]
Zr <sub>55</sub> Cu <sub>30</sub> Al <sub>10</sub> Ni <sub>5</sub>	Ga <sup>+</sup>	30	7 x 10 <sup>14</sup> - 7 x 10 <sup>15</sup>	RT	N	[16]
Ti <sub>40</sub> Zr <sub>25</sub> Be <sub>30</sub> Cr <sub>5</sub>	C <sup>+</sup> , Cl <sup>+</sup>	2500	1 x 10 <sup>15</sup> - 8 x 10 <sup>15</sup>	LN	N	[15]
Zr <sub>61.5</sub> Cu <sub>21.5</sub> Fe <sub>5</sub> Al <sub>12</sub>	Ar <sup>+</sup>	300	3 x 10 <sup>15</sup> - 3 x 10 <sup>16</sup>	RT	Y	[12]
Ni <sub>52.5</sub> Nb <sub>10</sub> Zr <sub>15</sub> Ti <sub>15</sub> Pt <sub>7.5</sub>	Ni <sup>+</sup>	1000	1 x 10 <sup>16</sup>	RT	Y	[13]
Zr <sub>55</sub> Cu <sub>30</sub> Ni <sub>5</sub> Al <sub>10</sub>	Co <sup>+</sup>	40	7 x 10 <sup>16</sup>	140°C	N	[14]
Fe <sub>81</sub> B <sub>13.5</sub> Si <sub>3.5</sub> C <sub>2</sub>	He <sup>+</sup>	2800	1 x 10 <sup>16</sup> - 1 x 10 <sup>17</sup>	RT	Y	[9]
Cu <sub>50</sub> Zr <sub>45</sub> Ti <sub>5</sub>	He <sup>+</sup>	140	1.7 x 10 <sup>17</sup>	RT	Y	[10]
Zr <sub>55</sub> Cu <sub>30</sub> Al <sub>10</sub> Ni <sub>5</sub>	Ar <sup>+</sup>	10	2.7 x 10 <sup>17</sup>	RT	Y	[11]
Cu <sub>47</sub> Zr <sub>45</sub> Al <sub>8</sub> Y <sub>1.5</sub>	He <sup>+</sup>	500	2 x 10 <sup>17</sup> - 2 x 10 <sup>18</sup>	-	N	[6]

### Experimental Procedures

A Zr<sub>52.5</sub>Cu<sub>17.9</sub>Ni<sub>14.6</sub>Al<sub>10</sub>Ti<sub>5</sub> alloy (BAM-11) was fabricated by arc melting in an argon atmosphere using a mixture of base metals with the following purities: 99.5% Zr, 99.99% Cu, 99.99% Ni, 99.99% Al, and 99.99% Ti [21]. The alloy was then remelted and drop cast into a cylindrical copper mold of 7 mm in diameter in a Zr-gettered helium atmosphere. Sections of the drop cast rod were evaluated via x-ray diffraction (XRD) and differential scanning calorimetry, which both confirmed the material to be fully in the amorphous state. The rod was then cut into sections of 8 by 3 by 1 mm and mechanically polished to a mirror finish.

After fabrication, BAM-11 specimens were ion irradiated using 3 MeV Ni<sup>+</sup> ions at perpendicular incidence. Samples were implanted to fluences of 4.2 x 10<sup>13</sup> and 4.2 x 10<sup>14</sup> ions/cm<sup>2</sup>, or peak damage levels of 0.1 and 1.0 dpa, respectively, at both room temperature and elevated temperature (200°C) at the University of Tennessee/ORNL Ion

Beam Materials Laboratory (IBML). Ion range and damage event profiles were used to determine the fluence to dpa conversion and were generated by the SRIM software using average displacement energy of 40 eV [22]. The mode of the ion range was calculated to be 1.36  $\mu\text{m}$ , with implanted Ni concentrations reaching  $5.5 \times 10^{18}$  atoms/ $\text{cm}^3$  at this depth. Damage levels at the sample surface were calculated to be about 40% of peak levels. Elevated temperature irradiations were performed at 200°C to keep the metallic glass far below its glass transition temperature of 393°C [21].

Post-irradiation microstructural characterizations of the irradiated bulk metallic glass specimens were performed via transmission electron microscopy (TEM). TEM foils were fabricated using an FEI Quanta Dual-beam focused ion beam (FIB)/SEM with a final thinning step of 2kV  $\text{Ga}^+$  ions at a glancing angle of about 4° in order to minimize ion beam milling damage. Samples were then analyzed in a Phillips CM 200 TEM operating at 200 kV using the techniques of bright field (BF) imaging, selected area electron diffraction (SAED), high resolution TEM (HRTEM), and x-ray energy dispersive spectroscopy (EDS) performed in scanning TEM (STEM) mode.

Mechanical properties were examined via microindentation using an MTS XP nanoindenter, with the indentations performed normal to the mechanically polished control and irradiated surfaces. All tests were performed using a Berkovitch diamond indenter (3 sided pyramidal tip) in continuous stiffness measurement mode at a constant indentation rate of 0.05/s with a maximum applied load of 200 mN [23]. For statistical purposes, each sample was indented a total of 16 times and the averages of those results are reported within this manuscript. Hardness and elastic modulus were measured as a function of depth from the point of contact of the nanoindenter with the surface to a depth of about 1200 nm. Data generated within the first ~100 nm of the surface was discarded due to large scatter associated with surface roughness.

### **Mechanical Properties**

Hardness and elastic modulus data generated through nanoindentation tests were reported upon in the previous semiannual progress report (DOE/ER-0313/54 - Volume 54). However, due to concerns over surface finish of the tested samples, those measurements were retaken. Results of those experiments are shown in Figures 1 and 2.

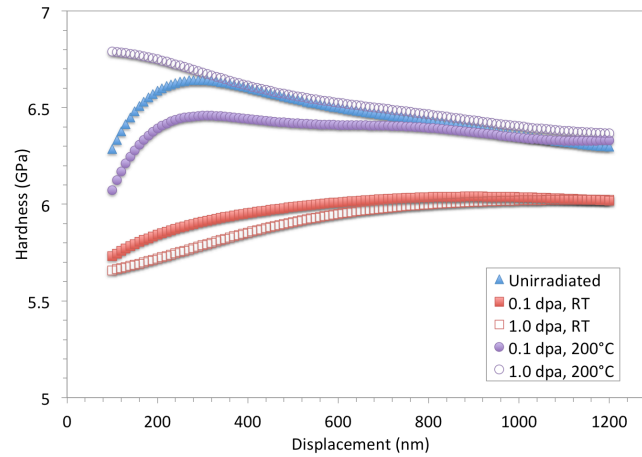


**Figure 1.** Hardness as a function of indenter depth in the unirradiated and irradiated BAM-11 specimens.

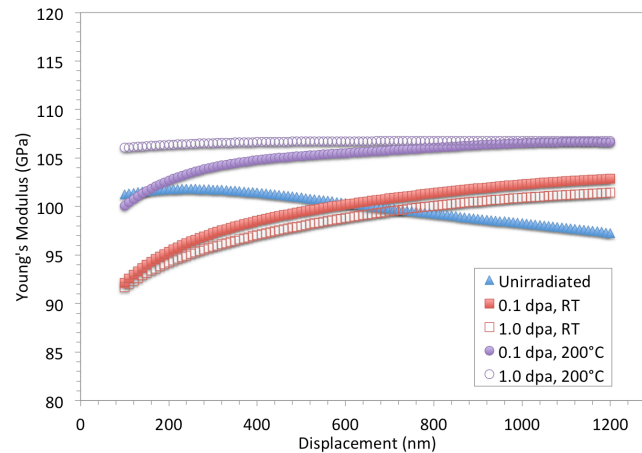


**Figure 2.** Elastic modulus as a function of indenter depth in the unirradiated and irradiated BAM-11 specimens.

Hardness and elastic modulus both dropped slightly for the specimens irradiated at room temperature as compared to the sample in the unirradiated condition. Hardness decreased about 12% from 6.6 GPa in the unirradiated state to 5.8 and 5.7 GPa in samples irradiated to 0.1 and 1.0 dpa at room temperature. Similarly, elastic modulus decreased about 7% from 101.8 GPa to 95.3 and 94.3 GPa, respectively.

In the samples irradiated at 200°C, the change in mechanical properties due to irradiation was even smaller than in the room temperature irradiations. Hardness in the samples irradiated at elevated temperature was relatively unchanged, with samples irradiated to 0.1 and 1.0 dpa exhibiting hardness values of 6.4 and 6.7 GPa. In addition, elastic modulus was seen to increase about 1-4% from 101.8 GPa in the unirradiated condition to 102.7 and 106.4 GPa in the samples irradiated to 0.1 and 1.0 dpa, respectively. Though data set variance was slightly higher for the samples irradiated at 200°C, the results

nonetheless seem to indicate a slightly better radiation tolerance of the bulk metallic glass at elevated temperature. Hardness remains unchanged at 200°C, likely due to somewhat enhanced self-annealing effects, and an increase in the Young's modulus, which is largely a function of interatomic bonding distance, suggests a slight densification of the BAM-11 alloy following irradiation.

### **Microstructure**

Microstructural data derived via TEM, including BF imagery, SAED patterns, and HRTEM, was reported upon in detail in the previous semiannual progress report (DOE/ER-0313/54 - Volume 54) and will not be reiterated here. However, additional analysis has since been performed upon diffractograms of the HRTEM images taken from each specimen.

Fast Fourier transforms, also known as diffractograms, can provide insight into the atomic spacing of amorphous alloys. When a diffractogram is created from an image of an amorphous material, the result is a concentric ring pattern such as the one shown in Figure 3. The ratio of the distance between the primary circle at the center of the pattern and the surrounding rings can provide information as to the spacing of atoms in a material, and since a diffractogram is a representation of an image in reciprocal space, an expansion of diffractogram rings indicates material densification and vice versa. For our irradiated materials, diffractograms were created from images taken at a magnification of 135kx. Distances from the center of the diffractograms to the center circle edge, first ring edge, and second ring edge were plotted. These data points were then used to produce the ratio from the ring edges to the central circle edge, which are shown in Table 2. As seen in Table 2, the ratio increases with irradiation dose, both for the samples irradiated at room temperature and those irradiated at 200°C, indicating densification of the BAM-11 alloy with ion irradiation. This observation matches up well with the slight increase in Young's modulus observed in the samples irradiated at 200°C but is at odds with the slight decrease in Young's modulus observed in the room temperature samples.

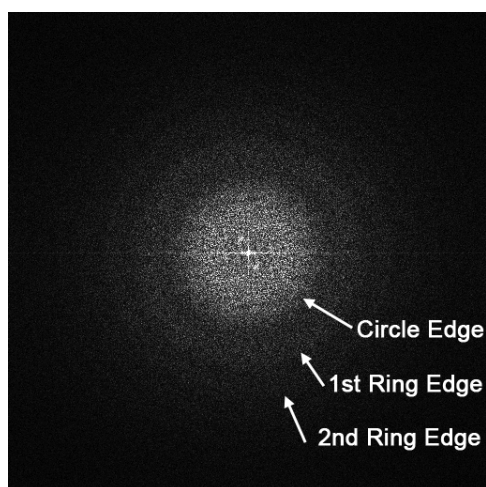


**Figure 3.** Diffractogram of the BAM-11 specimen irradiated to 1.0 dpa at 200°C. Circle, first ring, and second ring edges are shown.

**Table 2.** Summary of diffractogram measurements on unirradiated and irradiated BAM-11 specimens.

	Ratio from 1st Ring Edge to Circle Edge	Ratio from 2nd Ring Edge to Circle Edge
Unirradiated	1.54	1.94
0.1 dpa, RT	1.62	2.15
1.0 dpa, RT	1.76	2.24
0.1 dpa, 200C	1.55	2.01
1.0 dpa, 200C	1.65	2.10

## CONCLUSIONS

After irradiation with 3 MeV Ni<sup>+</sup> ions to dose levels of 0.1 and 1.0 dpa at room temperature and 200°C, amorphous BAM-11 bulk metallic glass specimens were found to exhibit no observable changes in microstructure and only minor (less than ~10%) changes in mechanical properties. A slight degree of sample densification following irradiation, as seen via changes in Young's modulus and diffractogram data, was also observed.

Overall, the favorable constitutive response of BAM-11 following irradiation to low fluence levels indicates that the alloy may have applications as a structural material in nuclear applications, albeit only in low temperature scenarios where the alloy stays below its glassy transition temperature. However, studies of bulk metallic glasses in general seem to show a strong correlation between total dose and irradiation-induced crystallization, as shown in Table 1. For many fusion applications, bulk metallic glasses would likely undergo neutron irradiation to levels of 10-100 dpa. Therefore, further work is needed to understand the response of BAM-11 to very high fluence levels, and neutron-irradiation studies are also needed to help understand how the material would behave in a nuclear environment.

## REFERENCES

- [1] W. Klement, R. H. Wilens, and P. Duwez, *Nature* **187** (1960) 869-870.
- [2] R. W. Cahn, *Nature* **341** (1989) 183-184.
- [3] P. Chaudhari and D. Turnbull, *Science* **199** (1978) 11-21.
- [4] A. L. Greer, *Science* **267** (1995) 1947-1953.
- [5] W. J. Weber, R. C. Ewing, C. A. Angell, G. W. Arnold, A. N. Cormack, J. M. Delaye, D. L. Griscom, L. W. Hobbs, A. Navrotsky, D. L. Price, A. M. Stoneham, and M. C. Weinberg, *J. Mater. Res.* **12** (1997) 1946-1978.
- [6] X. Mei, B. Wang, C. Dong, F. Gong, Y. Wang, and Z. Wang, *Nucl. Instrum. Methods Phys. Res. B* **307** (2013) 11-15.
- [7] A. Inoue, *Acta Mater.* **48** (2000) 279-306.
- [8] W. L. Johnson, *MRS Bulletin* **24** (1999) 42-56.
- [9] M. Sorescu, *J. Alloys Compd.* **284** (1999) 232-236.

- [10] J. Carter, E. G. Fu, G. Bassiri, B. M. Dvorak, N. D. Theodore, G. Xie, D. A. Lucca, M. Martin, M. Hollander, X. Zhang, and L. Shao, *Nucl. Instrum. Methods Phys. Res. B* **267** (2009) 1518-1521.
- [11] M. Iqbal, J. I. Akhter, Z. Q. Hu, H. F. Zhang, A. Qayyum, and W. S. Sun, *J. Non-Cryst. Solids* **353** (2007) 2452-2458.
- [12] W. D. Luo, B. Yang, and G. L. Chen, *Scripta Mater.* **64** (2011) 625-628.
- [13] M. Myers, E. G. Fu, M. Myers, H. Wang, G. Xie, X. Wang, W.-K. Chu, and L. Shao, *Scripta Mater.* **63** (2010) 1045-1048.
- [14] Y. Z. Yang, P. J. Tao, G. Q. Li, Z. X. Mu, Q. Ru, Z. W. Xie, and X. C. Chen, *Intermetallics* **17** (2009) 722-726.
- [15] Z. Hu, Z. Zhao, Y. Hu, J. Xing, T. Lu, and B. Wei, *Mater. Res.* **15** (2012) 713-717.
- [16] N. Kawasegi, N. Morita, S. Yamada, N. Takano, T. Oyama, K. Ashida, J. Taniguchi, I. Miyamoto, S. Momota, and H. Ofune, *Appl. Phys. Lett.* **89** (2006) 143115.
- [17] Y. Fukumoto, A. Ishii, A. Iwase, Y. Yokoyama, and F. Hori, *J. Phys.: Conf. Ser.* **225** (2010) 012010.
- [18] N. Onodera, A. Ishii, Y. Fukumoto, A. Iwase, Y. Yokoyama, and F. Hori, *Nucl. Instrum. Methods Phys. Res. B* **282** (2012) 1-3.
- [19] R. Raghavan, K. Boopathy, R. Ghisleni, M. A. Pouchon, U. Ramamurty, and J. Michler, *Scripta Mater.* **62** (2010) 462-465.
- [20] R. Raghavan, B. Kombaiah, M. Dobeli, R. Erni, U. Ramamurty, and J. Michler, *Mater. Sci. Eng. A* **532** (2012) 407-413.
- [21] C. T. Liu, L. Heatherly, D. S. Easton, C. A. Carmichael, J. H. Schneibel, C. H. Chen, J. L. Wright, M. H. Yoo, J. A. Horton, and A. Inoue, *Metall. Mater. Trans. A* **29A** (1998) 1811-1820.
- [22] J. F. Ziegler, J. P. Biersack, and U. Littmark. The Stopping and Range of Ions in Solids, Pergamon Press, New York (1985). Also see: <http://www.srim.org>.

### **7.3 Physical and Thermal Mechanical Characterization of Non-Irradiated MAX Phase Materials (Ti-Si-C and Ti-Al-C Systems) — C. Shih, R. Meisner, W. Porter, Y. Katoh, and S. J. Zinkle (Oak Ridge National Laboratory)**

#### **OBJECTIVE**

The main objective of this work is to investigate the physical and thermal mechanical properties of two commercially available MAX phase materials, nominally  $Ti_3SiC_2$  and  $Ti_2AlC$ , at non-irradiated states.

#### **SUMMARY**

The physical and thermo mechanical properties of two commercially available MAX phase materials have been characterized in the non-irradiated states including: density, X-ray diffraction analysis, microstructure analysis by SEM, coefficient of thermal expansion, thermal diffusivity, thermal conductivity, dynamic Young's modulus, electrical conductivity, and equibiaxial fracture strength (including Weibull modulus). The results show that the materials contain multiple phases. However, predominate phases are hexagonal MAX phases composed of Ti-Si-C and Ti-Al-C ternary systems. High thermal and electrical conductivity, adequate Young's modulus and equibiaxial fracture strength were observed. All the properties studied agree well with data from the literature.

#### **PROGRESS AND STATUS**

##### **Introduction**

MAX phase materials are ternary compounds with the general formula of  $M_{n+1}AX_n$  ( $n = 1, 2, \text{ or } 3$ ) where M is an early transition metal, A is an A-group element and X is C or N. These materials have hexagonal lattice structures with unique properties that "bring together some of the best attributes of ceramics and metals" [1]. Like ceramics, they are oxidation, creep and fatigue resistant. They show reasonable mechanical properties at high temperatures [2]. On the other hand, they possess metal-like properties, including high electrical and thermal conductivity, excellent machinability, and damage tolerance in certain conditions. Because of their unique properties, the MAX phase materials have seen a lot of research activities in the past few decades. They are considered promising materials for applications where high temperature strength and corrosion resistance are required.

The unique properties of MAX phase materials have also attracted attention from the nuclear research community [3-8]. Proposed nuclear applications include: oxidation barrier coating for the fuel cladding systems in the light water reactors and core components for advanced reactor concepts including the gas fast reactors [4]. Moreover, these ceramics are being studied for fundamental irradiation responses in the US fusion materials program as novel materials that potentially possess radiation tolerance or bring on new scientific insight toward future development of innovative radiation resistant materials. The primary objective of present study is to characterize some of the MAX phase ceramics, which have been subjected to a fundamental neutron irradiation effects study in the High Flux Isotope Reactor, in a non-irradiated condition.

## **Experimental**

### **Materials**

Nominally  $Ti_3SiC_2$  and  $Ti_2AlC$  blocks (150 × 44 × 35 mm) were purchased from 3-ONE-2, LLC (Willow Grove, PA). According to the vendor, the materials are fabricated by cold isostatic pressing of pre-reacted ternary carbide powders followed by pressureless sintering. The materials were machined into different shapes for individual characterization method.

### **Density**

The nominally 25 × 2 × 1.5 mm multi-purpose rectangular samples and nominally 6 mm diameter, 1.5 mm thick thermal diffusivity discs were used to determine the density by measuring the mass and bulk volume. The mass of each sample was determined by a Sartorius Genius lab balance to an accuracy of 0.01 mg. The dimensions of the samples were measured by a Mitutoyo micrometer to an accuracy of 1 mm. The volume is calculated using the measured dimensions. The bulk density is simply calculated as the measured mass divided by the bulk volume.

### **XRD**

Continuous  $\theta$ - $2\theta$  scans were performed on the Panalytical Xpert diffractometer from nominally 10 to 60°  $2\theta$  in 60 min scans using MoK $\alpha$  radiation ( $\lambda=0.709319 \text{ \AA}$ ) or CuK $\alpha$  radiation ( $\lambda=1.540598 \text{ \AA}$ ) and the X'Celerator detector. All scans used  $\frac{1}{4}^\circ$  fixed slits and  $\frac{1}{2}^\circ$  anti-scatter slit. A search match was conducted using the "Jade" and/or High Score software and the ICDD database.

### **Scanning electron microscopy (SEM)**

The samples were mounted in epoxy and polished with a series of diamond suspension to obtain a mirror finish. Microstructure of the polished samples was examined using either a Hitachi S4700 or a Hitachi S4800 field emission gun SEM.

### **Coefficient of thermal expansion (CTE)**

The samples used for CTE measurement have dimensions of 25 × 2 × 1.5 mm. A NETZSCH DIL 402 CD Thermal Expansion Dilatometer was used to measure the CTE of the samples in vacuum for temperatures from ~25 °C to 1000 °C at a temperature ramp rate of 3 °C per minute.

### **Thermal diffusivity and thermal conductivity**

The samples used for thermal diffusivity, and heat capacity measurements are cylindrical discs with a diameter of 6 mm and a thickness of 1.5 mm. Thermal diffusivity was measured following the guidelines of ASTM E1461 using a NETZSCH LFA 457 Micro Flash Laser Flash Thermal Diffusivity Apparatus. The thermal conductivity is calculated using the measured thermal diffusivity, heat capacity and density according to equation 1

$$k = \alpha \cdot \rho \cdot C_p \quad (1)$$

where  $k$  is the thermal conductivity,  $\alpha$  the thermal diffusivity,  $\rho$  the density, and  $C_p$  the heat capacity. Measurements were done at room temperature and from 100°C to 1000°C with

100°C intervals in flowing ultra-high purity argon gas. The temperature ramp rate was 10°C per minutes or less and a dwell time of 30 minutes were used before each measurement to ensure the equilibrium temperature was reached.

### **Dynamic Young's modulus**

The dynamic Young's modulus (sonic elastic modulus) was measured by the impulse excitation and vibration method following the guidelines of ASTM C1259-08 using a GrindoSonic Mk5 Industrial Non-Destructive Elastic Property Measurement System. The specimen size was 25 × 2 × 1.5 mm. Ten measurements were recorded for each specimen and the average was reported.

### **Electrical conductivity**

The electrical conductivity was measured using the four-point probe method following the guidelines of ASTM C611-98 with a sample dimension of 25 × 2 × 1.5 mm. A probe distance of 10 mm and a cross sample current of 10 mA were used. The current was generated using a KEITHLEY 2400 Source Meter and the voltage drop across the two probes was measured using a KEITHLEY 2192A Nonovoltmeter. Sixteen measurements were conducted on each sample using different geometry combinations. All the measurements were conducted at room temperature.

### **Equibiaxial fracture strength and Weibull modulus**

The room temperature equibiaxial (ring on ring) fracture strength was measured following the guidelines of ASTM C1499-09 with a sample dimension of 6 × 6 × 0.5 mm. This test method is chosen to evaluate the mechanical properties of the materials because of several advantages including: ease of operation, small sample volume compatible, which is important for irradiation studies, and high temperature testing compatible. From our past experience with graphite materials, this test method has shown to generate data with decent quality and statistical distribution. For each material, 30 samples were tested in order to obtain a representative average fracture strength and Weibull modulus.

The  $Ti_3SiC_2$  and  $Ti_2AlC$  are expected to have a ductile to brittle transition temperature (DBTT) between 900 to 1200°C. In order to determine this DBTT and any change in DBTT following irradiation, a high temperature equibiaxial fracture fixture has been designed and is now under machining as of December of 2013.

## **Results and Discussion**

### **Density**

Bulk densities of the disc and rectangular bar samples are summarized in Table 1. For both materials, there is no notable difference between samples of the same shape and between two difference sample shapes. The data scattering is very low with coefficient of variation around 0.5%, indicating both good machining quality and material homogeneity. The obtained density agrees well with the reported theoretical density in the open literature [2, 9], but appears to be about 3-4% smaller, suggesting the presence of micro porosity and/or impurity phases in the microstructure.

Table 1. Density, electrical resistivity, Young’s modulus, and flexural strength of the non-irradiated materials.

	# of samples	Ti-Si-C	Ti-Al-C
density, disc specimens (g/cm <sup>3</sup> )	22	4.390 (0.021)	3.964 (0.035)
density, bar specimens (g/cm <sup>3</sup> )	13	4.360 (0.023)	3.923 (0.024)
Electrical resistivity (ohm-m)	13	2.85×10 <sup>-7</sup> (5.39×10 <sup>-9</sup> )	4.67×10 <sup>-7</sup> (1.87×10 <sup>-8</sup> )
Young’s modulus (GPa)	13	313.4 (6.2)	250.8 (6.5)
Flexural strength (MPa)	30	445 (29)	308 (16)

Numbers in the parenthesis represent one standard deviation to the mean

**XRD profiles of non-irradiated samples**

The XRD profile of the Ti-Si-C sample is presented in Figure 1 where identified peaks are labeled. The software calculated phase composition of this sample is 70.4 wt. % Ti<sub>3</sub>SiC<sub>2</sub>, 23.8 wt. % TiC, and 5.7 wt. % TiSi<sub>2</sub>. Very similar XRD calculated phase composition for Ti<sub>3</sub>SiC<sub>2</sub> blocks purchased from the same company has been reported by Nappe et al [7]. It is worth mentioning that some of the peaks in the XRD are not identified.

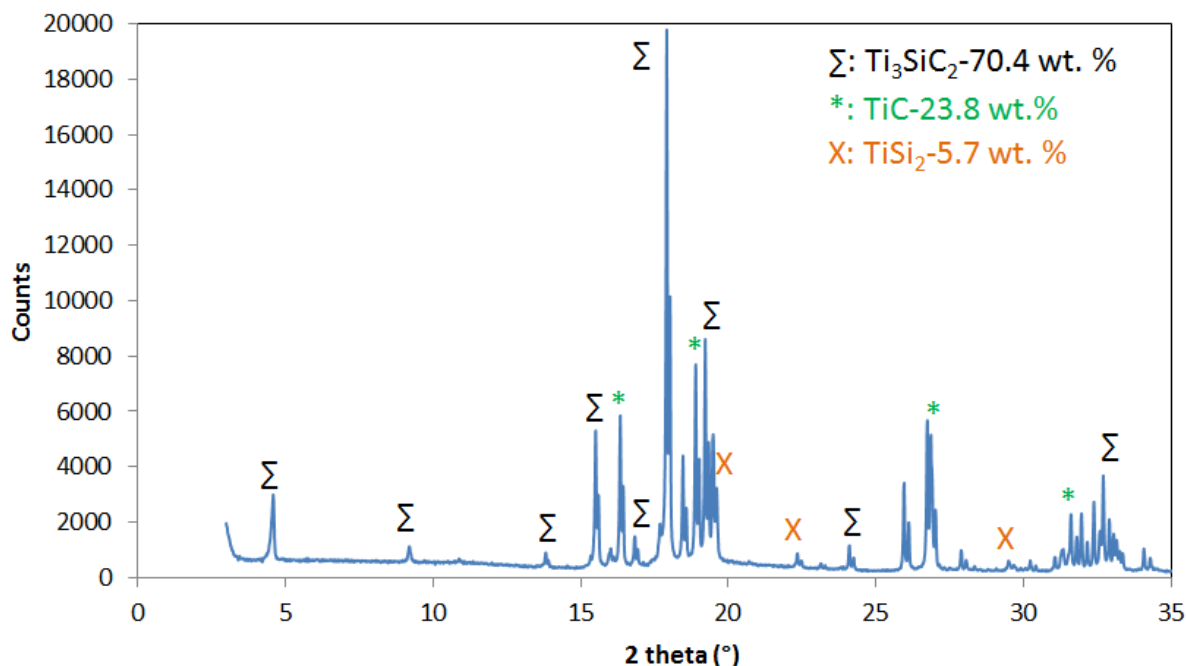
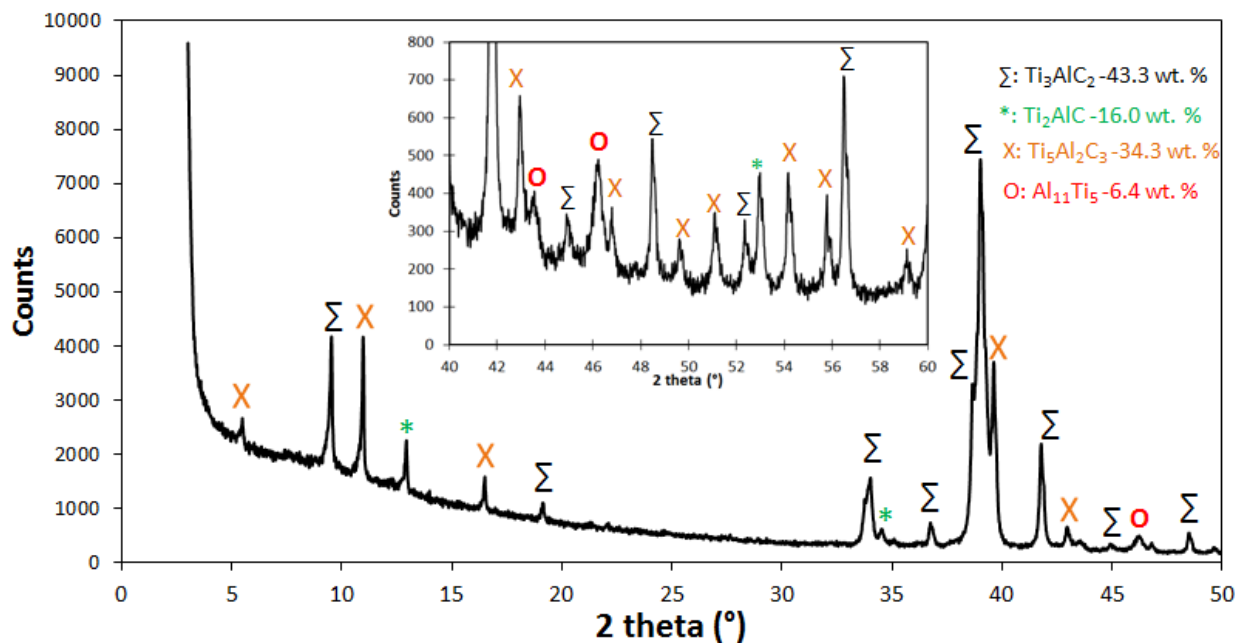


Figure 1. XRD profile of  $\text{Ti}_3\text{SiC}_2$ .

The XRD profile of the Ti-Al-C sample is shown in Figure 2 where identified peaks are labeled. The software calculated phase composition of this sample is 43.3 wt. %  $\text{Ti}_3\text{AlC}_2$ , 16.0 wt. %  $\text{Ti}_2\text{AlC}$ , 34.3 wt. %  $\text{Ti}_5\text{Al}_2\text{C}_3$  and 6.4 wt. %  $\text{Al}_{11}\text{Ti}_5$ . This results suggest that the nominally  $\text{Ti}_2\text{AlC}$  block actually contains mostly  $\text{Ti}_3\text{AlC}_2$  and  $\text{Ti}_5\text{Al}_2\text{C}_3$  phases. The  $\text{Ti}_5\text{Al}_2\text{C}_3$  phase has been synthesized and characterized in bulk only recently [1, 10]. The lattice structure can be described as alternating layers of  $\text{Ti}_2\text{AlC}$  and  $\text{Ti}_3\text{AlC}_2$ . For this reason, the major physical properties of  $\text{Ti}_5\text{Al}_2\text{C}_3$ , including density, electrical conductivity, thermal conductivity, coefficient of thermal expansion, and elastic properties, are believed and have been reported [1] to be very similar to those of  $\text{Ti}_2\text{AlC}$  and  $\text{Ti}_3\text{AlC}_2$ .

In the paper that characterized the structure of  $\text{Ti}_5\text{Al}_2\text{C}_3$  [10], the material is synthesized from heating  $\text{Ti}_2\text{AlC}$  powders (from the same vendor as this study) under flowing argon to 1500 °C. The fact that our nominally  $\text{Ti}_2\text{AlC}$  material contains other phases indicates that there might be some processing errors, presumably from heat treatment temperatures, caused further phase transformation from  $\text{Ti}_2\text{AlC}$  to  $\text{Ti}_3\text{AlC}_2$ ,  $\text{Ti}_5\text{Al}_2\text{C}_3$ , and  $\text{Al}_{11}\text{Ti}_5$ . It should be noted that predominate phases are all hexagonal MAX phases composed of Ti, Al, and C ternary system.

Since the nominally  $\text{Ti}_3\text{SiC}_2$  and  $\text{Ti}_2\text{AlC}$  samples contain other phases, hereafter they are referred as Ti-Si-C and Ti-Al-C, respectively, in this report.

Figure 2. XRD profile of Ti<sub>2</sub>AlC.

## SEM

Secondary and back-scattered SEM images of the polished Ti-Si-C sample are shown in Figure 3. The very bright areas in the secondary electron images (Figure 3a and c) are identified as pores. The material is not 100% dense and the observed pores correspond to the lowered density as discussed previously. Those pores have a dimension of smaller than 4 mm and are located at grain boundaries. A closer look at the microstructures revealed three distinct contrasts: the elongated grain that appears in bright contrast, the more round shaped dark grain and the island-like grains with ragged boundaries, which are indicated with white arrows in Figure 3d. By cross-referencing the energy dispersive x-ray spectroscopy (EDS) element composition results and the XRD phase composition results, the elongated bright grains are identified as Ti<sub>3</sub>SiC<sub>2</sub>, the round dark grain are identified as TiC, and the ragged island grains are identified as TiSi<sub>2</sub>. The percent weight composition observed by the SEM images corresponds well with that calculated from the XRD profiles.

SEM images of the polished Ti-Al-C sample are shown in Figure 4. The areas with very bright edges in Figure 4a are identified as pores. Ti-Al-C sample appears to have slightly less porosity than Ti-Si-C. Three phases are identified and labeled in Figure 4d as bright grains, dark grains and background matrix. Both bright and dark grains showed elongated shapes with width in the range of 4 to 10 mm and length of over 50 mm. The aspect ratio of the grains in Ti-Al-C sample appears to be larger than those seen in Ti-Si-C sample.

In the back-scattered electron (BSE) image in Figure 4d, the brightness differences between different elongated grains are minor, suggesting similar average atomic weight. However, the matrix appears to be significantly darker, suggesting a much-lowered average atomic weight. Cross-referencing between the BSE images, the EDS element composition results and the XRD phase composition results suggest that the elongated grains are Ti<sub>2</sub>AlC, Ti<sub>3</sub>AlC<sub>2</sub>, and Ti<sub>5</sub>Al<sub>2</sub>C<sub>3</sub>.

Since all three MAX phase compounds have similar average atomic weight and similar theoretical density, the brightness difference of those phases from the BSE image is expected to be minor. If we further consider that the crystal orientation of each grain affects its brightness, we can conclude that it is difficult to unambiguously assign a phase to each grain unless rigorous EDS analysis is conducted. The dark matrix is likely the  $Al_{11}Ti_5$  phase, which has a tetragonal structure with space group  $I4/mmm$ . Even though  $Al_{11}Ti_5$  also has a similar average atomic weight to the other MAX phases in the sample, it has a significantly lower theoretical density of  $3.5 \text{ g/cm}^3$  while the three MAX phases all have a theoretical density of  $\sim 4.2 \text{ g/cm}^3$ . This lower density explains the lower brightness of  $Al_{11}Ti_5$  grains in the BSE image.

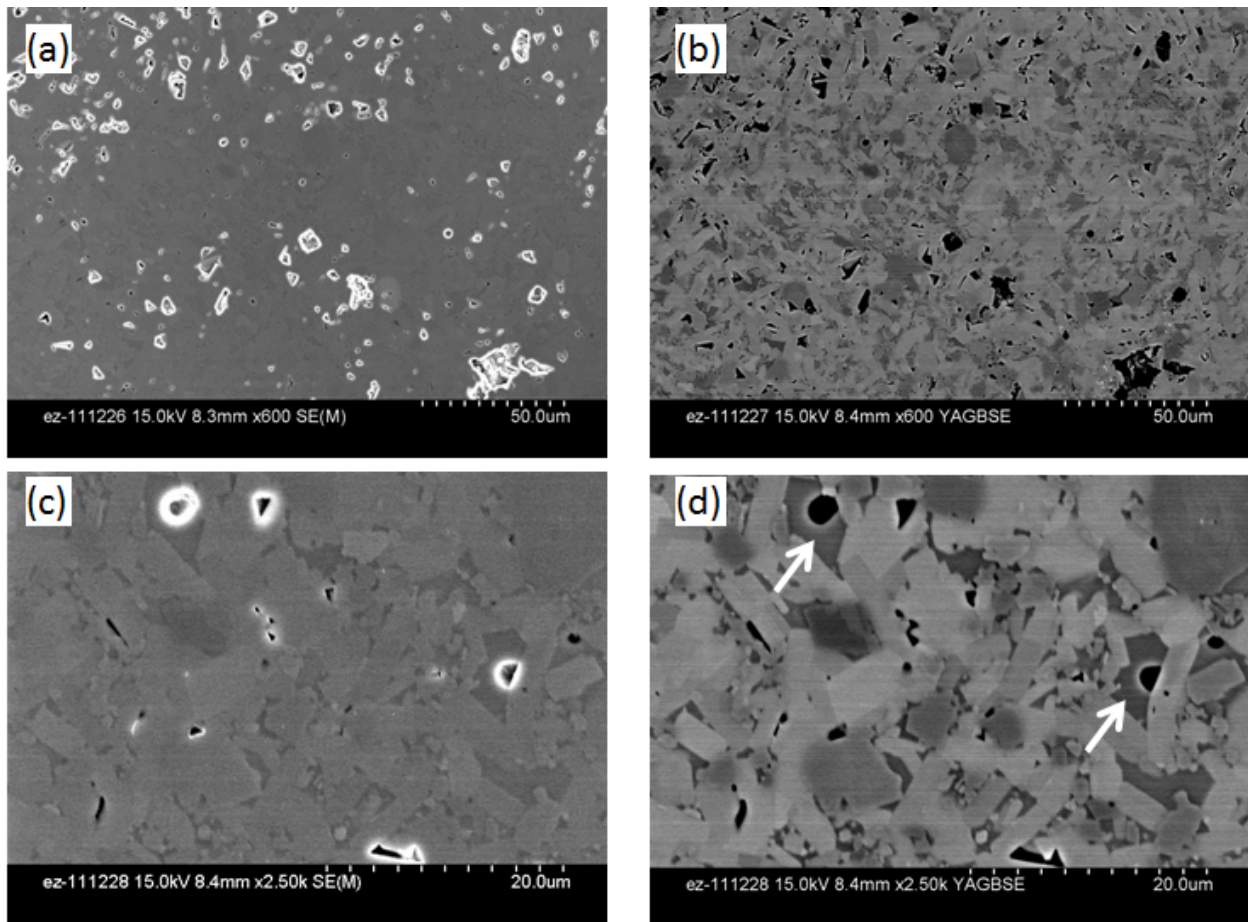


Figure 3. SEM images of (nominally)  $Ti_3SiC_2$  sample. (a) and (c): secondary electron images; (b) and (d): back scattered electron images.

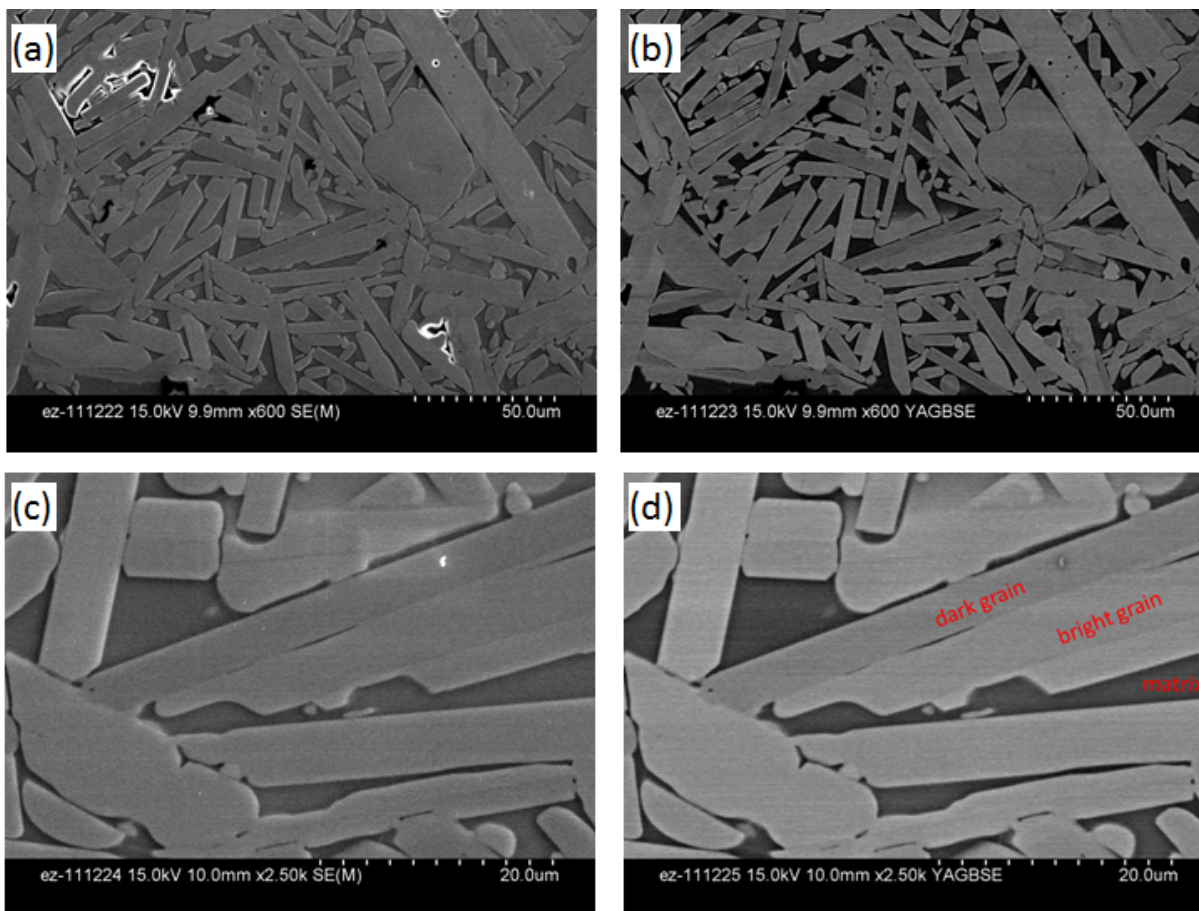


Figure 4. SEM images of (nominally)  $\text{Ti}_2\text{AlC}$  sample. (a) and (c): secondary electron images; (b) and (d): back scattered electron images.

### **Coefficient of thermal expansion (CTE)**

The CTE of Ti-Si-C and Ti-Al-C is shown in Figure 5. Ti-Si-C has a CTE of  $\sim 7\text{-}9 \times 10^{-6} \text{ K}^{-1}$ , while Ti-Al-C showed a CTE of  $8\text{-}10 \times 10^{-6} \text{ K}^{-1}$ . CTE of both materials increases with increasing temperature. If we use beta CVD SiC as a reference material, which has a CTE of  $\sim 4.5 \times 10^{-6}$  per  $^\circ\text{C}$  at this temperature range, the MAX phase materials in this study showed higher CTE values. They also showed higher CTE values than Zircaloy-4 cladding tubes in the circumferential direction ( $4.4 \times 10^{-6} \text{ K}^{-1}$  at room temperature).

The measured CTE of Ti-Si-C is similar to the reported value ( $10 \times 10^{-6}$  per  $^\circ\text{C}$ ) for hot isotactic pressed  $\text{Ti}_3\text{SiC}_2$  [9]. Moreover, the measured CTE of Ti-Al-C corresponds well with the reported CTE of  $\text{Ti}_2\text{AlC}$  and  $\text{Ti}_3\text{AlC}_2$  [11], which is in the range of  $8\text{-}9 \times 10^{-6}$  per  $^\circ\text{C}$ .

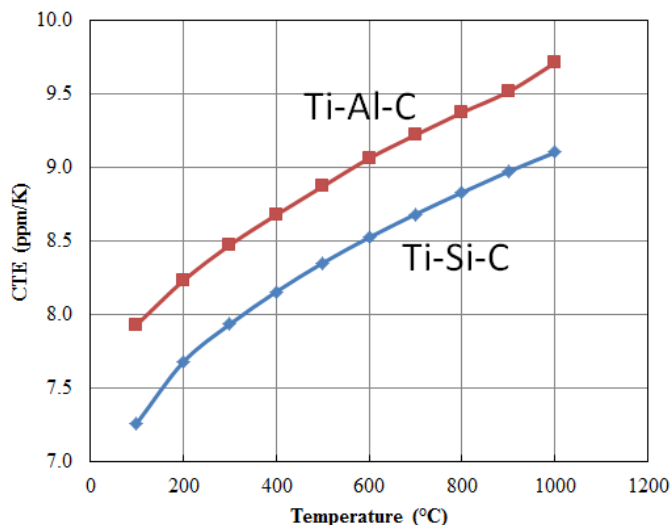


Figure 5. Coefficient of thermal expansion referenced to room temperature for Ti-Si-C and Ti-Al-C.

### Thermal diffusivity and thermal conductivity

The heat capacity ( $C_p$ ) of the two materials is shown in Figure 6 as a function of temperature. Ti-Si-C showed a higher heat capacity than Ti-Al-C at all temperatures. Heat capacity ( $C_p$ ) of Ti-Si-C in this report is higher than  $C_p$  of  $Ti_3SiC_2$  reported in the literature, which is about 0.56 to 0.59 J/g·K [14, 15] at room temperature. Large specimen-to-specimen variation is also observed. TiC is a main impurity in the Ti-Si-C samples. However, its  $C_p$  is not particularly higher than  $Ti_3SiC_2$  and thus cannot explain the higher  $C_p$  in the Ti-Si-C samples. It's likely that the higher  $C_p$  in this study is caused by measurement errors because of the small specimen size. This measurement error might be the reason of the sharp  $C_p$  increase at 1000°C.

Even though the Ti-Al-C sample in this study is actually composed of  $Ti_2AlC$ ,  $Ti_3AlC_2$ , and  $Ti_5Al_2C_3$  phases, the  $C_p$  of these phases has been reported to be similar [16, 17] to each other. For this reason, the  $C_p$  is compared only with  $Ti_2AlC$  data in the literature [16], which was reported to be similar to those in this report in the temperature range of 25°C to 600°C. At temperatures above 600°C, a sharp increase in  $C_p$  is observed in our measurements while decrease in  $C_p$  was reported [16] and was attributed to the loss of aluminum atoms. The reason for sharp increase of  $C_p$  for  $Ti_2AlC$  at higher temperatures (> 800°C) is unclear, but might be related to the small sample size, which causes errors in the measurements. Another potential reason is the oxidation from residual oxygen in the Ar gas. The rather large data scattering for the three Ti-Si-C samples and the three Ti-Al-C samples used in this study also suggest large errors associated with the  $C_p$  measurements.

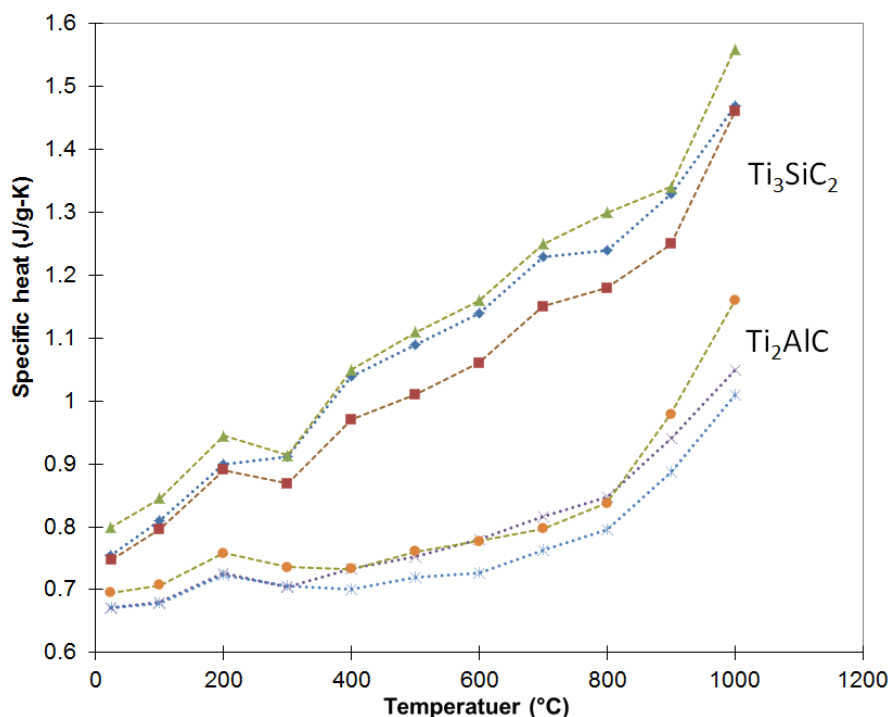


Figure 6. Measured specific heat of Ti-Si-C and Ti-Al-C (3 samples for each material).

The measured thermal diffusivity and calculated thermal conductivity are shown in Figure 7 and Figure 8, respectively. Ti-Si-C showed higher thermal diffusivity and conductivity than Ti-Al-C at all temperatures. Diffusivity of both materials decreases with increasing temperature.

Thermal diffusivity of relatively pure Ti<sub>3</sub>SiC<sub>2</sub> has been reported to be ~15 mm<sup>2</sup>/s at room temperature by two different research groups [14, 15], which is close to our measurement of ~14 mm<sup>2</sup>/s, regardless of the higher fraction of impurity phases in this study. This indicates that the common impurity phases (mostly TiC) in the nominally Ti<sub>3</sub>SiC<sub>2</sub> material has little effect in the overall thermal diffusivity of the material at non-irradiated state. The thermal conductivity is calculated from the product of measured density, measured C<sub>p</sub>, and measured thermal diffusivity. The measured thermal conductivity of Ti-Si-C is higher than the values reported in the literature [9, 14] mainly because of higher measured C<sub>p</sub>. The higher thermal conductivity and large increase of thermal conductivity at higher temperatures (above 800°C) is considered artifact caused by the measurement errors of C<sub>p</sub>.

Thermal diffusivity and conductivity of  $Ti_2AlC$  has been reported by Barsoum *et al.* [12] and Bai *et al.* [18]. However, there is a large difference (46.0 W/m-K vs. 27.0 W/m-K at room temperature) between the two. In the former paper, the higher thermal conductivity is attributed to the phonon contribution, which is suggested to be much lower in the latter paper. The reason for the lower phonon thermal conductivity contribution in the  $Ti_2AlC$  in the latter paper is suggested to be related to the fine-grain microstructure and nonstoichiometry of the material, which both caused larger phonon scattering. In this report, the thermal diffusivity and conductivity are closer to the latter paper by Bei *et al.* [18]. Since the nominally  $Ti_2AlC$  in this study are mainly composed of other phases, a lower thermal conductivity can be expected.

Overall, both materials in this study have high thermal conductivities at non-irradiated states. However, neutron irradiation is known to reduce the thermal conductivity of materials. Hence the emphasis should be put on the thermal conductivities following neutron irradiation.

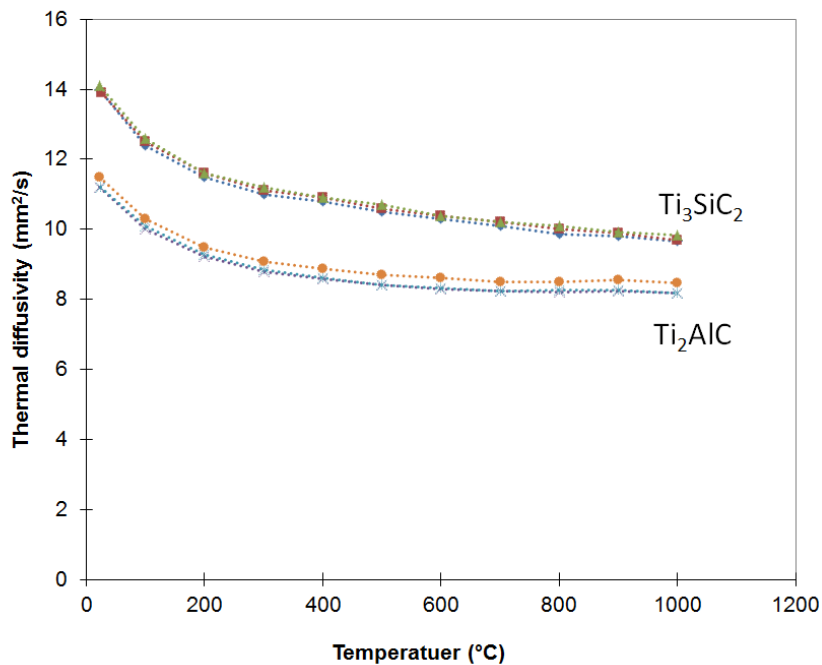


Figure 7. Measured thermal diffusivity of  $Ti_3SiC_2$  and  $Ti_2AlC$  (3 samples for each material).

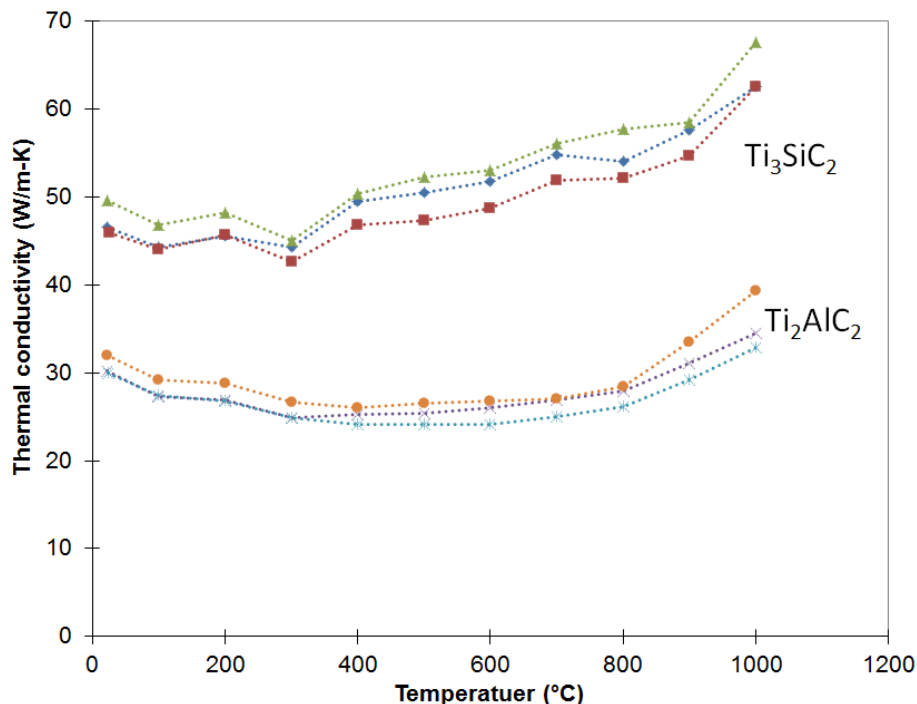


Figure 8. Calculated thermal conductivity of  $Ti_3SiC_2$  and  $Ti_2AlC_2$  (3 samples for each material).

### Dynamic Young's modulus

Average dynamic Young's moduli of Ti-Si-C and Ti-Al-C are listed in Table 1. At least 13 samples were measured for each material. Ti-Si-C showed an average Dynamic Young's modulus of 313 GPa with a coefficient of variation of 6.2%. This measured modulus is in line with the reported Young's modulus from the literature (322-333 GPa) [9]. It should be noted that TiC is an impurity in  $Ti_3SiC_2$  that are difficult to eliminate because the structure similarity of TiC with  $Ti_3SiC_2$ . The amount of TiC in the nominally  $Ti_3SiC_2$  material will affect the modulus.

Ti-Al-C showed a dynamic Young's modulus of 251 GPa with a coefficient of variation of 6.4%. The Young's moduli of  $Ti_2AlC_2$  and  $Ti_3AlC_2$  have been summarized in reference [11] and are in the range of 267 to 306 GPa and 298 to 309 GPa, respectively. The Young's modulus for Ti-Al-C in this study appears to be slightly lower than the literature value.

### Electrical resistivity

The average electrical resistivity of the nominally Ti-Si-C and Ti-Al-C are reported in Table 1. Ti-Si-C and Ti-Al-C have room temperature electrical resistivity of 0.285 and 0.467 mΩ-m, respectively. The coefficient of variation is in the range of 2 to 4%. Those materials are highly electrical conductive and have resistivity values comparable to some metals like iron, lead and titanium.

The electrical conductivity of  $\text{Ti}_3\text{SiC}_2$  has been studied using *ab initio* calculations [19], which suggest that the conduction bands are provided almost entirely by the Ti 3d states. The measured electrical resistivity of 0.285 m $\Omega$ -m for Ti-Si-C is comparable with the literature values of 0.1 to 0.23 m $\Omega$ -m [9, 15]. The difference in the electrical conductivity can be attributed to the different microstructures and impurity phases of the materials used.

Theoretical work has shown that the high electrical conductivity of  $\text{Ti}_2\text{AlC}$  and  $\text{Ti}_3\text{AlC}_2$  is related to the large  $N(E_F)$ , which is dominated by the Ti d-orbitals [11]. The electrical resistivity of Ti-Al-C in this study is consistent with the values reported in the literature for  $\text{Ti}_2\text{AlC}$  [18] and  $\text{Ti}_3\text{AlC}_2$  [20].

### **Equibiaxial fracture strength and Weibull modulus**

The average fracture strength and standard deviation of the two materials are listed in Table 1. The Weibull plots of Ti-Si-C and Ti-Al-C are shown in Fig. 9 and Fig. 10, respectively. Ti-Si-C showed a Weibull characteristic strength of 458 MPa with a Weibull modulus of ~17. The average fracture strength of 445 MPa agrees well with the literature value of 450 MPa [9], indicating that the material is of good quality and that the equibiaxial fracture test with small specimens is a reliable and comparable test method.

The Weibull modulus of  $\text{Ti}_3\text{SiC}_2$  from three-point bend fracture strength was reported to be 28.1 using the same statistical method [21]. The reason for the difference in modulus is unclear but is likely related to the different microstructure and different strength test methods.

Ti-Al-C showed a Weibull characteristic strength of 315 MPa with a Weibull modulus of ~22. The average fracture strength value is close to the reported fracture strength of  $\text{Ti}_2\text{AlC}$  and  $\text{Ti}_3\text{AlC}_2$  [11], which are in the range of 275 to 375 MPa.

When comparing the Weibull modulus of the two materials with monolithic SiC, which shows Weibull modulus between 2 and 12 [22], it is obvious that MAX phase materials have a much larger Weibull modulus, thus a better reliability performance, at the non-irradiated state.

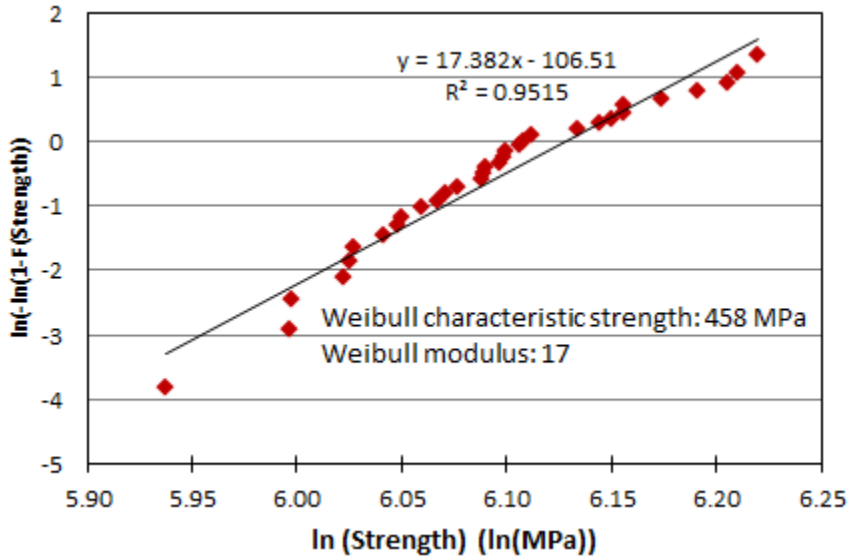


Figure 9. Weibull plot of  $\text{Ti}_3\text{SiC}_2$ .

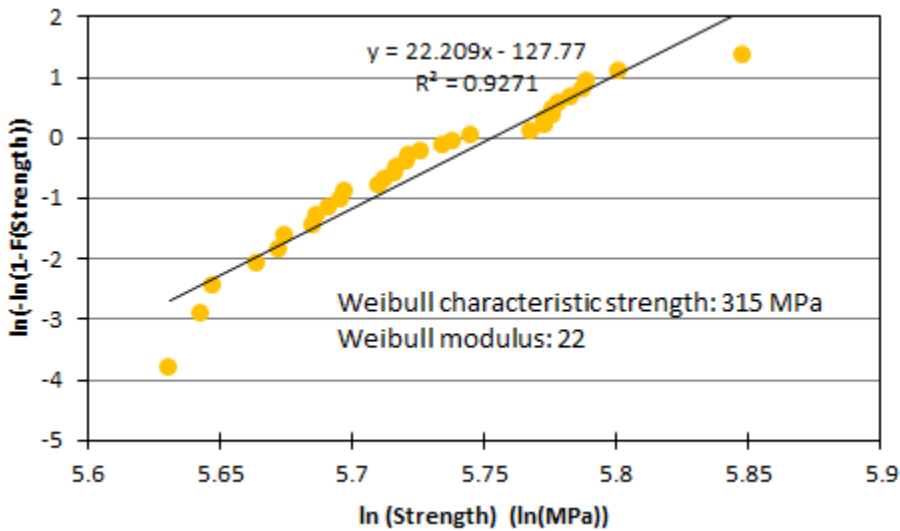


Figure 10. Weibull plot of  $\text{Ti}_2\text{AlC}$ .

## CONCLUSIONS

This report summarized the physical and thermal mechanical properties of two commercially available MAX phase materials, normally  $\text{Ti}_3\text{SiC}_2$  and  $\text{Ti}_2\text{AlC}$ , at non-irradiated states. The reported properties include: density, XRD analysis, microstructure analysis by SEM, CTE,

thermal diffusivity, thermal conductivity, dynamic Young's modulus, electrical conductivity, and equibiaxial fracture strength (including Weibull modulus). These properties are compared with existing data from the literature and good agreement is observed for all the properties studied.

The characterization of the non-irradiated MAX phase materials shows that these materials contain MAX phases of different stoichiometry and other non-MAX phase grains. The effect of radiation on the two materials likely will not represent that of pure phase materials. For this reason, the radiation effect will need to be examined carefully. However, techniques that characterize properties within one single grain would likely obtain representative information for a particular phase, assuming that phase and structure of the grain being studied is identified. Examples of such characterization techniques include transmission electron microscope analysis and nano-indentation.

## REFERENCES

- [1] N. J. Lane, S. C. Vogel, E. N. Caspi, and M. W. Barsoum, *J. Appl. Phys.* **113** (2013).
- [2] M. W. Barsoum, *Prog. Solid State Chem.* **28** (2000) 201-281.
- [3] E. N. Hoffman, D. W. Vinson, R. L. Sindelar, D. J. Tallman, G. Kohse, and M. W. Barsoum, *Nucl. Eng. Des.* **244** (2012) 17-24.
- [4] X. M. Liu, M. Le Flem, J. L. Bechade, F. Onimus, T. Cozzika, and I. Monnet, *Nucl. Instrum. Methods Phys. Res. Sect. B-Beam Interact. Mater. Atoms* **268** (2010) 506-512.
- [5] J. C. Nappé, P. Grosseau, F. Audubert, B. Guilhot, M. Beauvy, M. Benabdesselam, and I. Monnet, *J. Nucl. Mater.* **385** (2009) 304-307.
- [6] J. C. Nappé, C. Maurice, P. Grosseau, F. Audubert, L. Thomé, B. Guilhot, M. Beauvy, and M. Benabdesselam, *J. Eur. Ceram. Soc.* **31** (2011) 1503-1511.
- [7] J. C. Nappé, I. Monnet, F. Audubert, P. Grosseau, M. Beauvy, and M. Benabdesselam, *Nucl. Instrum. Methods Phys. Res. Sect. B-Beam Interact. Mater. Atoms* **270** (2012) 36-43.
- [8] J. C. Nappé, I. Monnet, P. Grosseau, F. Audubert, B. Guilhot, M. Beauvy, M. Benabdesselam, and L. Thome, *J. Nucl. Mater.* **409** (2011) 53-61.
- [9] H. B. Zhang, Y. W. Bao, and Y. C. Zhou, *J. Mater. Sci. Technol.* **25** (2009) 1-38.
- [10] N. J. Lane, M. Naguib, J. Lu, L. Hultman, and M. W. Barsoum, *J. Eur. Ceram. Soc.* **32** (2012) 3485-3491.
- [11] X. H. Wang and Y.C. Zhou, *J. Mater. Sci. Technol.* **26** (2010) 385-416.
- [12] M. W. Barsoum, M. Ali, and T. El-Raghy, *Metall. Mater. Trans. A-Phys. Metall. Mater. Sci.* **31** (2000) 1857-1865.
- [13] B. Manoun, F. X. Zhang, S. K. Saxena, T. El-Raghy, and M. W. Barsoum, *J. Phys. Chem. Solids* **67** (2006) 2091-2094.
- [14] M. W. Barsoum, T. El-Raghy, C. J. Rawn, W. D. Porter, H. Wang, E. A. Payzant, and C. R. Hubbard, *J. Phys. Chem. Solids* **60** (1999) 429-439.
- [15] Z. M. Sun, H. Hashimoto, Z. F. Zhang, S. L. Yang, and S. Tada, *Mater. Trans.* **47** (2006) 170-174.
- [16] M. W. Barsoum, I. Salama, T. El-Raghy, J. Golczewski, W. D. Porter, H. Wang, H. J. Seifert, and F. Aldinger, *Metall. Mater. Trans. A-Phys. Metall. Mater. Sci.* **33** (2002) 2775-2779.
- [17] A. Togo, L. Chaput, I. Tanaka, and G. Hug, *Phys. Rev. B* **81** (2010).
- [18] Y. L. Bai, X. D. He, C. C. Zhu, and G. Q. Chen, *J. Am. Ceram. Soc.* **95** (2012) 358-364.
- [19] Y. C. Zhou, Z. M. Sun, X. H. Wang, and S. Q. Chen, *J. Phys Condens. Matter* **13** (2001) 10001-10010.
- [20] N. V. Tzenov and M. W. Barsoum, *J. Am. Ceram. Soc.* **83** (2000) 1551-1551.
- [21] Y. W. Bao, Y. C. Zhou, and H. B. Zhang, *J. Mater. Sci.* **42** (2007) 4470-4475.

- [22] L. L. Snead, T. Nozawa, Y. Katoh, T. S. Byun, S. Kondo, and D. A. Petti, *J. Nucl. Mater.* **371** (2007) 329-377.

**7.4 Effects of Neutron Irradiation on Ti-Si-C MAX-Phase Ceramic Microstructures —**  
A. G. Perez-Bergquist<sup>1,2</sup>, Y. Katoh<sup>1</sup>, C. Shih<sup>1</sup>, N. A. P. K. Kumar<sup>1,2</sup>, and S. J. Zinkle<sup>1,2</sup> (Oak Ridge National Laboratory<sup>1</sup>, University of Tennessee<sup>2</sup>)

**OBJECTIVE**

The goal of this study is to investigate the neutron irradiation behavior of the MAX-phase ceramic  $Ti_3SiC_2$  and to determine if it is a viable candidate for high-radiation structural applications in fusion applications.

**SUMMARY**

MAX phase ceramics are intriguing candidates for structural applications in nuclear environments due to their unique mixture of metallic and ceramic properties. Specifically, their potential to retain adequate thermal conductivity after high levels of irradiation damage may make them an attractive alternative to SiC in fusion environments. In this study, we investigate the MAX phase ceramic  $Ti_3SiC_2$  after neutron irradiation to 3.4 dpa and 5.0 dpa at temperatures of 500 and 800°C, respectively. Initial results showed large amounts of atomic-scale radiation damage in the material, but minimal loss of strength in selected  $Ti_3SiC_2/Ti_5Si_3$  samples.

**PROGRESS AND STATUS**

**Introduction**

MAX phase ceramics are defined as a family of ternary compounds with the general composition of  $M_{n+1}AX_n$  where  $n = 1, 2, \text{ or } 3$ ,  $M$  is early transition metal,  $A$  is a Group A element, and  $X$  is carbon, nitrogen, or both. They have a hexagonal crystal structure with the primary lattice consisting of  $M$  and  $A$  atoms and the sublattice consisting of  $X$  atoms in the interstitial spots (Figure 1). Though these unique carbide and nitride ceramics were first discovered in the 1960s [1], interest in them was minor until the mid 1990's, when Barsoum and El-Raghy first synthesized relatively phase-pure samples of  $Ti_3SiC_2$  and elucidated upon some of the material's unique mixture of metallic and ceramic properties [2]. Since then, interest in MAX phase materials has magnified greatly, with various MAX phase ceramics being reported to exhibit high modulus, low specific gravity, adequate machinability (as comparable to graphite), outstanding tolerance against oxidation and thermal shock, good thermal conductivity, moderate ductility, and the capacity to maintain strength up to about 1300°C [2-6]. For potential fusion applications, it is also important to note that many of the compositions for MAX phase ceramics qualify as low activation materials [7].

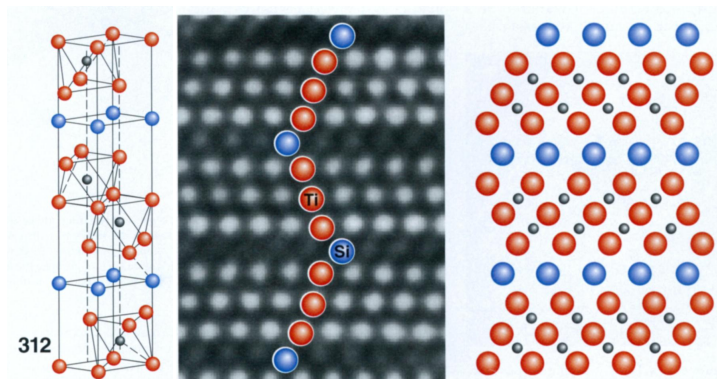


**Figure 1.** Crystal structure of a 312 MAX phase material (left), along with a HRTEM image of Ti<sub>3</sub>SiC<sub>2</sub> (middle) and a diagram showing atomic configurations (right). Ti atoms are red, Si atoms blue, and C atoms grey [5].

By far, the most extensively studied MAX phase ceramic thus far has been Ti<sub>3</sub>SiC<sub>2</sub>, a member of the 312 family of MAX phases. Ti<sub>3</sub>SiC<sub>2</sub> has been shown to exhibit high compressive strength (560-1000 MPa at room temperature, 200-260 MPa at 1200-1300°C) and tensile strength (200 to 300 MPa at room temperature), which is better than most monolithic ceramics, as well as fracture toughness comparable to or slightly higher than most ceramics (5 to 16 MPa-m<sup>1/2</sup> at room temperature) [3,4,8]. Ti<sub>3</sub>SiC<sub>2</sub> also happens to possess a thermal conductivity comparable or superior to many engineering structural alloys (37 to 32 W/m-K as temperature is increased from room temperature to 1200°C), with the conductivity predominantly due to electronic conduction [9].

Perhaps the most promising aspect among the anticipated irradiation resistance of MAX phase ceramics, such as Ti<sub>3</sub>SiC<sub>2</sub>, is their potential to retain adequate thermal conductivity. Silicon carbide (SiC), which is otherwise a nearly perfectly irradiation resistant ceramic material, suffers a large decrease in thermal conductivity during irradiation due to the production of a very high density of radiation defects in the matrix, which are very effective in scattering the phonons that are predominantly responsible for heat conduction in silicon carbide [10,11]. Conversely, the thermal conductivity of MAX phase ceramics such as Ti<sub>3</sub>SiC<sub>2</sub> is predominantly due to electronic conduction [8], which is only weakly affected by the presence of radiation defects [12,13].

Over the past several years, a number of new ion irradiation studies have been performed on Ti<sub>3</sub>SiC<sub>2</sub> and Ti<sub>3</sub>AlC<sub>2</sub>, investigating damage tolerance, microstructural changes, mechanical properties, and thermal stability, among other properties [14-24]. Here, we investigate the effects of neutron irradiation upon the MAX phase ceramic Ti<sub>3</sub>SiC<sub>2</sub>.

## Experimental Procedures

MAX phase Ti<sub>3</sub>SiC<sub>2</sub> was fabricated in the seams of joined SiC plates via two different methods. In one set of samples, a 20 μm pure titanium foil was used to diffusion bond the SiC plates. The bond was formed by inserting the foil between the plates and hot pressing at 1170°C at 20 MPa for 3 hours in an argon atmosphere, producing Ti<sub>3</sub>SiC<sub>2</sub>/Ti<sub>5</sub>Si<sub>3</sub> in the joints. In the second set of samples, a tape calendaring process using organic binders and a mixture of TiC and Si powders (99.99% purity, TiC:Si ratio of 3:2) were used. Two hundred μm thick calendared tapes were pressed and heated between two SiC plates at 1425°C at 30 to 40 MPa applied pressure for 2

hours, producing  $Ti_3SiC_2/SiC$  in the joints. Samples were then neutron irradiated at the Flux Trap Facility in the High Flux Isotope Reactor (HFIR) at Oak Ridge National Laboratory to 3.4 dpa and 5.0 dpa at temperatures of 500 and 800°C, respectively.

Post-irradiation examination was carried out in the Low Activation Materials Development and Analysis (LAMDA) laboratory at ORNL. Detailed examination in LAMDA included torsional shear strength evaluation and cross-sectional microstructural and micro-chemical analyses. Details of the shear strength test procedure are given in reference [25]. Scanning electron microscope (SEM) examinations and analyses were performed using field-emission-gun SEM Hitachi Models S4700 and S4800 equipped with energy dispersive X-ray spectroscopy (EDS) systems. Transmission electron microscopy (TEM) foils were fabricated using an FEI Quanta Dual-beam focused ion beam (FIB)/SEM with a final thinning step of 2kV  $Ga^+$  ions at a glancing angle of about 4° in order to minimize ion beam milling damage. Samples were then analyzed in a Phillips CM 200 TEM operating at 200 kV using the techniques of bright field (BF) imaging, selected area electron diffraction (SAED), high resolution TEM (HRTEM), and EDS performed in scanning TEM (STEM) mode.

### Mechanical Properties

The failure modes of primary interest in ceramic joints are shear and tension, and of these, shear is the more common mode of failure. While numerous methods can be used for shear strength determination of ceramic composite joints, only torsional tests are capable of producing true shear loading and are appropriate for testing lap-joined small specimens.

Therefore, torsional tests were chosen for determining joint shear strength in this study. In this document, nominal shear strength values ( $t_{th}$ ) are reported as  $t_{th} = 16T/\pi d^3$ , where T = applied torque and d = specimen (fillet) diameter at the joint plane. Overall,  $Ti_3SiC_2/Ti_5Si_3$  joints retained full strength after neutron irradiation, while  $Ti_3SiC_2/SiC$  joints saw a 16% drop in strength and a shift from basal failure to failure in the joint following irradiation. Full results are shown in Table 1.

**Table 1.** Torsional test (shear strength) results.

Joint	Strength, Unirradiated (MPa)	Failure Location, Unirradiated	Irradiation Condition	Strength, Irradiated (MPa)	Failure Location, Irradiated
$Ti_3SiC_2/Ti_5Si_3$	124 (23)	Joint (Full/Partial)	500°C, 3.4 dpa	125 (36)	Joint (Full/Partial)
$Ti_3SiC_2/SiC$	117 (10)	Basal Plane	800°C, 5.0 dpa	98 (22)	Joint (Full)

### Microstructure

SEM analysis of the unirradiated material revealed some major cracking through the thickness of the bonding layer as well as some porosity at the bond interface in the  $Ti_3SiC_2/Ti_5Si_3$  sample. In the unirradiated  $Ti_3SiC_2/SiC$  sample, no cracking or porosity was observed. After irradiation, both samples exhibited increased microcracking throughout. A much more extensive

microstructural analysis than that provided here, including figures of the samples in question, has recently been published and is available in reference [26].

TEM analysis is currently in progress and has been partially completed on the  $\text{Ti}_3\text{SiC}_2/\text{Ti}_5\text{Si}_3$  sample irradiated to 3.4 dpa at 500°C. Microcracking seen in initial SEM analyses was found to be primarily transgranular, though some cracking along  $\text{Ti}_5\text{Si}_3$  grain boundaries was observed. No cracking was found along  $\text{Ti}_3\text{SiC}_2/\text{Ti}_5\text{Si}_3$  grain boundaries, but due to the nature of the FIB sample, the sample size of observable  $\text{Ti}_3\text{SiC}_2$  grains was very small. A composite image of the microcracks is shown in Figure 1.

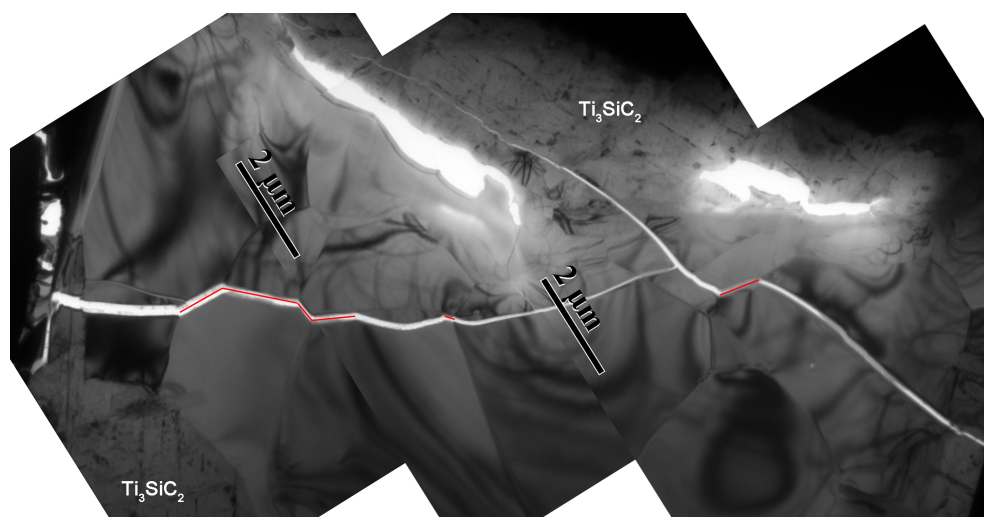


**Figure 1.** Microcracks in the  $\text{Ti}_3\text{SiC}_2/\text{Ti}_5\text{Si}_3$  sample irradiated to 3.4 dpa at 500°C. Cracking along grain boundaries is marked in red.  $\text{Ti}_3\text{SiC}_2$  grains are labeled. All other grains are  $\text{Ti}_5\text{Si}_3$ .

TEM also revealed extensive radiation-induced defect formation in the  $\text{Ti}_3\text{SiC}_2$  MAX phase grains following irradiation, as shown in Figure 2. Figure 2a displays an unirradiated  $\text{Ti}_3\text{SiC}_2$  grain that exhibits thickness fringes due to variations in sample thickness but exhibits no visible microstructural damage or defects. Figure 2b shows a  $\text{Ti}_3\text{SiC}_2$  grain after irradiation, displaying numerous planar defects that are suspected to be stacking faults. Figure 3b then shows the same area as Figure 2b but at a diffraction condition where irradiation-induced dislocations and black spot damage are visible, and the damage is so dense as to turn the image of the sample nearly black. Surprisingly, the  $\text{Ti}_5\text{Si}_3$  grains did not show any evidence of irradiation-induced defects of any kind, merely displaying thickness fringes as shown in Figure 1. Continued analysis of the  $\text{Ti}_3\text{SiC}_2$  grains is ongoing, with compositional analysis and detailed analysis of defect structures upcoming.

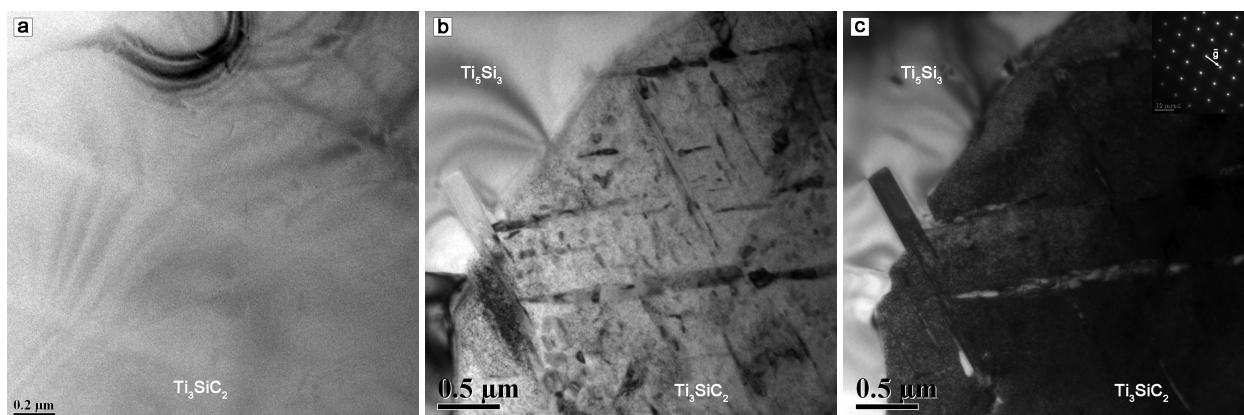


**Figure 2.** Bright field TEM images of a) unirradiated  $\text{Ti}_3\text{SiC}_2$  and b,c)  $\text{Ti}_3\text{SiC}_2$  irradiated to 3.4 dpa at  $500^\circ\text{C}$ . b) Numerous planar defects are visible at an arbitrary diffraction condition. c) Heavy dislocation damage is visible under 2-beam conditions.

### Conclusions and Future Work

Mechanical property evaluations showed loss of strength in  $\text{Ti}_3\text{SiC}_2/\text{SiC}$  joints after neutron irradiation but not in  $\text{Ti}_3\text{SiC}_2/\text{Ti}_5\text{Si}_3$  joints.  $\text{Ti}_3\text{SiC}_2/\text{Ti}_5\text{Si}_3$  joints showed greater strength overall, both before and after irradiation. From a microstructural standpoint, extensive radiation damage was visible in  $\text{Ti}_3\text{SiC}_2$  grains following neutron irradiation to 3.4 dpa at  $500^\circ\text{C}$ .  $\text{Ti}_5\text{Si}_3$  grains, however, showed no evidence of irradiation damage.

While the sheer magnitude of irradiation-induced defects in the irradiated  $\text{Ti}_3\text{SiC}_2$  grains is visually striking, density of defects is not necessarily indicative of poor radiation performance. As such, further microstructural analysis of  $\text{Ti}_3\text{SiC}_2$ , both in  $\text{Ti}_3\text{SiC}_2/\text{Ti}_5\text{Si}_3$  and  $\text{Ti}_3\text{SiC}_2/\text{SiC}$  joints, is needed before the viability of  $\text{Ti}_3\text{SiC}_2$  as a fusion material can be assessed.

Future work for this project includes additional TEM analysis, specifically on the  $\text{Ti}_3\text{SiC}_2/\text{SiC}$  joined specimen, as well as analysis of bulk  $\text{Ti}_3\text{SiC}_2$  and  $\text{Ti}_2\text{AlC}$  currently being neutron irradiated to 2-10 dpa at  $400\text{-}1000^\circ\text{C}$  in HFIR.

### REFERENCES

- [1] W. Jeitschk and H. Nowotny, *Monatsh. Chem.* **98** (1967) 329-337.
- [2] M. W. Barsoum and T. El-Raghy, *J. Am. Ceram. Soc.* **79** (1996) 1953-1956.
- [3] M. W. Barsoum, *Prog. Solid State Chem.* **28** (2000) 201-281.
- [4] N. Tzenov and M. W. Barsoum, *J. Am. Ceram. Soc.* **83** (2000) 825-832.
- [5] M. W. Barsoum and T. El-Raghy, *American Scientist* **89** (2001) 334-343.
- [6] P. Eklund, M. Beckers, U. Jansson, H. Hogberg, and L. Hultman, *Thin Solid Films* **518** (2010) 1851-1878.
- [7] E. N. Hoffman, D. W. Vinson, R. L. Sindelar, D. J. Tallman, G. Kohse, and M. W. Barsoum, *Nucl. Eng. Des.* **244** (2012) 17-24.
- [8] M. W. Barsoum and M. Radovic, *Annu. Rev. Mater. Res.* **41** (2011) 195-227.
- [9] M. W. Barsoum, T. El-Raghy, C. J. Rawn, W. D. Porter, H. Wang, E. A. Payzant, and C. R. Hubbard, *J. Phys. Chem. Sol.* **60** (1999) 429-439.
- [10] L. L. Snead, *J. Nucl. Mater.* **329-333** (2004) 524-529.

- [11] L. L. Snead, S. J. Zinkle, and D. P. White, *J. Nucl. Mater.* **340** (2005) 187-202.
- [12] S. J. Zinkle, *J. Phys. F: Met. Phys.* **18** (1988) 377-391.
- [13] S. J. Zinkle and S. A. Fabritsiev, *At. Plasma-Mater. Interact. Data Fusion* **5** (1994) 163-192.
- [14] J. C. Nappe, Ph. Grosseau, F. Audubert, B. Guilhot, M. Beauvy, M. Benabdesselam, and I. Monnet, *J. Nucl. Mater.* **385** (2009) 304-307.
- [15] M. Le Flem, X. Liu, S. Doriot, T. Cozzika, and I. Monnet, *Int. J. Appl. Ceram. Technol.* **7** (2010) 766-775.
- [16] X. Liu, M. Le Flem, J.-L. Bechade, F. Onimus, T. Cozzika, and I. Monnet, *Nucl. Instrum. Methods Phys. Res. B* **268** (2010) 506-512.
- [17] X. M. Liu, M. Le Flem, J. L. Bechade, and I Monnet, *J. Nucl. Mater.* **401** (2010) 149-153.
- [18] K. R. Whittle, M. G. Blackford, R. D. Aughterson, S. Moricca, G. R. Lumpkin, D. P. Riley, and N. J. Zaluzec, *Acta Mater.* **58** (2010) 4362-4368.
- [19] J. C. Nappe, C. Maurice, Ph. Grosseau, F. Audubert, L. Thome, B. Guilhot, M. Beauvy, and M. Benabdesselam, *J. Eur. Ceram. Soc.* **31** (2011) 1503-1511.
- [20] J. C. Nappe, I. Monnet, Ph. Grosseau, F. Audubert, B. Guilhot, M. Beauvy, M. Benabdesselam, and L. Thome, *J. Nucl. Mater.* **409** (2011) 53-61.
- [21] L. Zhang, Q. Qi, L. Q. Shi, D. J. O'Conner, B. V. King, E. H. Kisi, and D. K. Venkatachalam, *Appl. Surf. Sci.* **258** (2012) 6281-6287.
- [22] L. F. Marion and I. Monnet, *J. Nucl. Mater.* **433** (2013) 534-537.
- [23] C. Liu, L. Shi, Q. Qi, D. J. O'Conner, B. V. King, E. H. Kisi, X. B. Qing, and B. Y. Wang, *Nucl. Instrum. Methods Phys. Res. B* **307** (2013) 536-540.
- [24] C. Wang, T. Yang, S. Kong, J. Xiao, J. Xue, Q. Wang, C. hu, Q. Huang, and Y. Wang, *J. Nucl. Mater.* **440** (2013) 606-611.
- [25] M. Ferraris, M. Salvo, V. Casalegno, A. Ventrella, and M. Avalle, *Int. J. Ceram. Appl. Technol.* **9** (2012) 795-807.
- [26] Y. Katoh, L. L. Snead, T. Cheng, C. Shih, W. D. Lewis, T. Koyanagi, T. Hinoki, C. H. Henager, and M. Ferraris, *J. Nucl. Mater.* (in press), <http://dx.doi.org/10.1016/j.jnucmat.2013.10.002>.

**7.5 A Dual Ion Irradiation Study of Helium-DPA Interactions on Cavity Evolution in Tempered Martensitic Steels and Nanostructured Ferritic Alloys** — T. Yamamoto, Y. Wu, G. Robert Odette (University of California Santa Barbara), K. Yabuuchi, S. Kondo, and A. Kimura (Kyoto University)

**OBJECTIVE**

The objective of the research is to find how cavity and other evolutions are influenced by the starting microstructure and irradiation variables, including, displacements per atom (dpa), dpa rate, He/dpa ratio. This particular report is to give an extended summary of our recently accepted publication in Journal of Nuclear Materials.

**SUMMARY**

Cavity evolutions in a normalized and tempered martensitic steel (TMS) and two nanostructured ferritic alloys (NFA) under  $\text{Fe}^{3+}$  and  $\text{He}^+$  dual ion beam irradiations (DII) at 500°C and 650°C were characterized over a wide range of dpa, He and He/dpa. Transmission electron microscopy (TEM) showed that DII of a 8Cr TMS, at 500°C to up to 60 dpa and 2100 appm He, produced a moderate density of non-uniformly distributed cavities with bimodal sizes ranging from  $\approx 1$  nm He bubbles to  $\approx 20$  nm faceted voids, and swelling  $\approx 0.44\%$ . In contrast, the same irradiation conditions produced only small  $\approx 1.3$  nm diameter bubbles and swelling of  $\approx 0.05\%$  in the NFA MA957. Similar bubble distributions were observed in MA957 and a developmental NFA DII at 650°C up to  $\approx 80$  dpa and  $\approx 3900$  appm He. These results demonstrate the outstanding He management capability of the oxide nano-features in the NFA. The various data trends are shown as a function of dpa, He, He/dpa and He\*dpa.

**BACKGROUND**

Predicting and mitigating the effects of a combination of large levels of transmutant He and displacement damage (dpa), produced by high energy neutrons, on the dimensional stability and mechanical properties of structural materials is one of the key challenges in the development of fusion energy [1]. The fundamental overriding questions about He and dpa effects and their synergisms include: a) what are the basic interacting mechanisms controlling He and displacement defect transport, fate and consequences; b) how are the resulting cavity and other evolutions are influenced by the starting microstructure and irradiation variables, including, displacements per atom (dpa), dpa rate, He/dpa ratio and irradiation temperature; and, c) how can the detrimental effects of He-dpa synergisms be mitigated and managed by proper microstructural designs?

We have previously demonstrated that in situ He implantation (ISHI) in mixed spectrum fission reactor irradiations provides a very attractive approach to assessing the effects of He-dpa synergisms, while avoiding most of the confounding effects associated with Ni- or B-alloy doping type experiments [1-8]. Another approach is to use dual ion beam irradiations (DII) to simultaneously implant He and create displacement damage [1,9-12]. Note, the two techniques are complementary but manifest many differences that, in the case of DII, include: a) much higher dpa rates; b) non-uniform spatial distributions of dpa and He; and, c) the proximity of a free surface. Here we focus on DII encompassing a wide

range of dpa, He and He/dpa that naturally arise from varying profiles of these damage parameters with depth from the specimen surface. Comparisons of DII and ISHI experiments will be the subject of future publications.

### Experimental Procedure

The alloys studied here were TMS F82H mod.3 and two NFAs, MA957 and developmental variant 14YWT-PM2 (hereafter referred to as PM2). The mod.3 variant adjusted the base composition of a large program heat F82H-IEA (nominal in wt.%, 7.5Cr 2W 0.2V 0.1C 0.1Si 0.02Ta, 60ppm N, bal. Fe) by reducing the N and Ti to 14 ppm and 0.001%, respectively, while increasing Ta to 0.1% [13]. MA957 is a widely studied representative reference variant of NFA that was first produced by INCO in the late 1970s [5]. The composition of the MA957 heat studied here is 13.6Cr, 0.30Mo, 0.98Ti, 0.26Y<sub>2</sub>O<sub>3</sub>, balance trace impurities and Fe. NFA are of growing interest due to their radiation damage resistance, and especially their transformational He management capabilities [3,5,6,14]. The average grain size ( $d_g$ ) in MA 957 is about 0.6 and 1.5 mm in the transverse and axial directions, respectively. Prototypic number densities (N) and average diameter ( $\langle d \rangle$ ) of the oxide NFs in MA957 are  $\approx 5.6 \times 10^{23}/\text{m}^3$  and 2.7 nm, respectively [15]. The corresponding dislocation densities ( $\rho$ ) are  $\approx 0.8 \times 10^{15}/\text{m}^2$ . The nominal composition of PM2 is Fe-14%Cr, 3%W, 0.35%Ti, 0.3%Y<sub>2</sub>O<sub>3</sub> wt.%, bal. trace impurities and Fe). PM2 was processed at ORNL by D. Hoelzer, as part of a LANL-ORNL-UCSB collaboration to develop larger quantities of best practice NFA [16]. The N,  $\langle d \rangle$ ,  $d_g$  and  $\rho$  in PM2 are  $\approx 8.6 \times 10^{23}/\text{m}^3$ , 2.1 nm, 424 nm and  $1.2 \times 10^{15}/\text{m}^2$ , respectively [16]. More details about these materials, including processing paths, micro-nanostructures and properties, are given elsewhere [5,13-19].

In the case of the 500°C studies, DII were carried out on 3 mm diameter disks, mechanically ground to a nominal thickness of 200 mm prior to electro-polishing; the corresponding specimens used in the 650°C study were 500 mm thick 4x8 mm<sup>2</sup> electro-polished coupons. The DII were performed in DuET facility located at the Institute of Advanced Energy, Kyoto University in Japan. Here, Fe<sup>3+</sup> and He<sup>+</sup> ions are accelerated to 6.4MeV and 1MeV, respectively [20]. The two 500°C irradiations targeted nominal damage levels of 10 dpa/480 appm He and 26 dpa/1200 appm He, respectively, at a reference point 600 nm from the specimen surface. The 650°C irradiation targeted a corresponding 600 nm depth nominal damage level of 48 dpa/2200 appm. Taking advantages of spatial distributions of damage and He concentration produced by the ion irradiations, we analyzed microstructures of the specimens at various He – dpa conditions as shown in Figure 1. The damage calculations are based on the Kinchin-Pease damage energy model, with a displacement energy of 40 eV for Fe and Cr, as recommended in ASTM E521-96 (2009) [21,22]. DuET irradiations provide a basis to evaluate the effects of a wide range of irradiation variables, including high dpa with no He, as well as undamaged regions. Figure 1 shows a corresponding He-dpa map. Damage region in the analyses were selected avoiding the effects of surface proximity and injected self-interstitials. TEM was performed on the FEI 200 keV Technai T20 and 300 KeV Titan instruments in the UCSB Microstructure and Microanalysis Facility. Through focus bright field imaging was used to characterize the cavities.

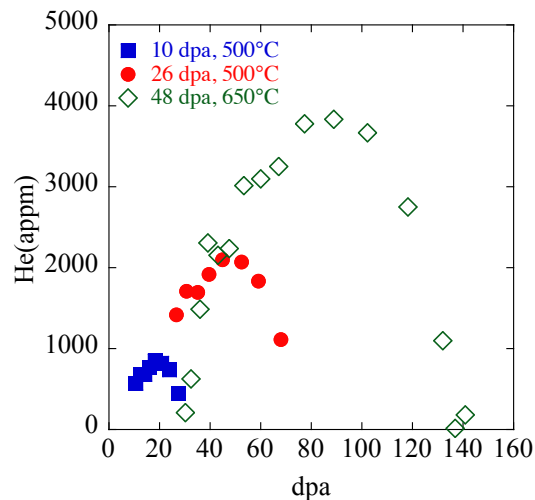


Figure 1. dpa-He conditions in the discrete depth sections where quantitative analyses were carried out.

### Key Results

Table 1 briefly summarizes the observed trends in the number density ( $N$ ), average diameter ( $\langle d \rangle$ ) and the volume fraction ( $f$ ) of cavities in F82H mod.3 (note, trying to describe these complex trends in words quickly becomes very confusing). Some key observations include:

- None of the damage parameters is, in itself, sufficient to represent the data.
- A significant amount of the apparent scatter is also associated with differences in the local alloy microstructure.
- $N$  depends only weakly on, or is independent of, all the damage parameters within the observed scatter.
- $\langle d \rangle$  systematically increases with He, dpa (with possible peaks) and  $\text{He}^*\text{dpa}$  for a given irradiation condition.
- $\langle d \rangle$  also increases between the lower and higher dpa condition.
- $f$  systematically increases with He, dpa (with possible peaks) and  $\text{He}^*\text{dpa}$  for a given irradiation condition.
- $f$  also increases between the lower and higher dpa condition.
- The  $\text{He}^*\text{dpa}$  damage parameter provides the most effective correlation with the  $f$  trends.

Note, there is no special physical significance to the use of the  $\text{He}^*\text{dpa}$  damage parameter, except that both He and dpa are needed for void formation. However, to some extent this parameter captures the critical bubble to void conversion mechanism leading to an incubation dose in void swelling [1,26,27]. This is illustrated in Figure 2a plotting the volume fraction of cavities larger than 4 nm as a function of dpa for various He/dpa ratios. Figure 2b shows the corresponding variation in the number density of the larger cavities. While the absolute swelling and swelling rates are still low, it is important to emphasize that it is likely that the cavity volume fraction will continue to increase in F82H mod.3, and even accelerate at higher dpa, perhaps reaching the nominal 0.2%/dpa proposed by Garner [28].

**Table 1. Summary of cavity parameters trends with irradiation variables**

N, <d>, f	He	dpa	He/dpa	He*dpa
N	Weak decrease especially at higher dpa	Weak increase at higher dpa	No significant systematic trend	No significant systematic trend
<d>	Systematic increase	Increases with possible peaks at both dpa ranges	No significant systematic trend - or weak drop in going from the lower to higher dpa range	Systematic increase
f	Systematic and scattered increase	Systematic and scattered increase or peak following possible threshold	No significant systematic trend - or weak drop in going from the lower to higher dpa range	Systematic increase after possible threshold

In MA957, the trends are very different than in the F82H3. The <d> are remarkably constant, while the N and f actually appear to decrease slightly with increasing He, dpa and He\*dpa. The later trend may reflect sample variations, rather than a real physical trend. The N in MA957 are much higher and the <d> much smaller than in F82H. As described in more detail elsewhere [29], the bubbles are essentially all associated with NFs. These results clearly indicate the ability of NFs in NFA to manage high concentrations of He.

Figure 3 summarizes and cross-compares plots of N, <d> and f versus He\*dpa for the different alloys and irradiation conditions. Key observations include:

- At 500°C the trends in the TMS F82H mod.3 are markedly different than in the NFA MA957. F82H mod.3 has fewer and larger void cavities that produce more swelling than in the NFA.
- Except for NFA PM2, the N are generally weakly dependent on He\*dpa after an initial rise. This PM2 trend is likely a visibility effect.
- The N in NFA is similar to, or slightly larger than, the number density of NFs, as reflected in the larger N (and f) in PM2 versus MA957.
- The <d> are essentially constant for both NFA and both irradiation conditions, while <d> systematically increases in F82H mod.3.
- A corresponding systematic increase in f void (swelling) begins in the TMS beyond He\*dpa  $\approx 5 \times 10^4$  appm He-dpa due to the presence of growing voids, as signaled by the trend in <d>.
- The bubble f in the NFA gradually increase with He\*dpa at 650°C and are higher than at 500°C.

These results clearly demonstrate the superior He management capability of the NFA compared to TMS, which experience swelling at sufficiently high He and dpa.

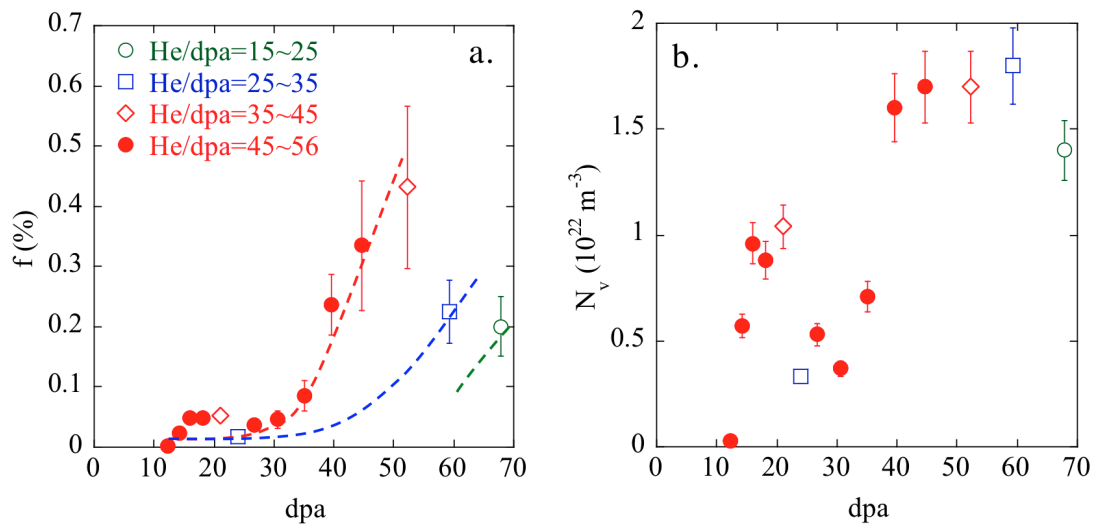


Figure 2. a) The volume fraction,  $f$ , and b) number density,  $N$ , of cavities larger than 4 nm as a function of the dpa at levels of He/dpa in F82H mod.3 irradiated at 500°C.

**SUMMARY**

We have summarized the cavity evolutions observed in a TMS and two NFA under  $Fe^{3+}$  and  $He^+$  DII performed at 500°C (F82H mod.3 and MA957) and 650°C (MA957 and PM2), to nominal dpa and He levels of  $\approx 10$  to 48 dpa and  $\approx 480$  to 2200 appm, respectively. The TMS F82H mod.3 irradiated at 500°C contains a moderate density of non-uniformly distributed cavities with sizes ranging from  $\approx 1$  nm (bubbles) up to  $\approx 20$  nm (voids). In contrast, the MA957 only contains a uniform distribution of small  $\approx 1.3$  nm diameter bubbles. Notably, qualitatively similar bubble distributions are observed up to  $\approx 80$  dpa and  $\approx 3900$  appm He at 650°C, demonstrating the outstanding He management capability of nm-scale features in NFA MA957 and PM2. The observed bubbles are more numerous and the bubble swelling is larger at 650°C compared to 500°C. The total swelling in F82H at 500°C reaches  $\approx 0.44\%$  at  $\approx 50$  dpa, due to a well-established population of voids.

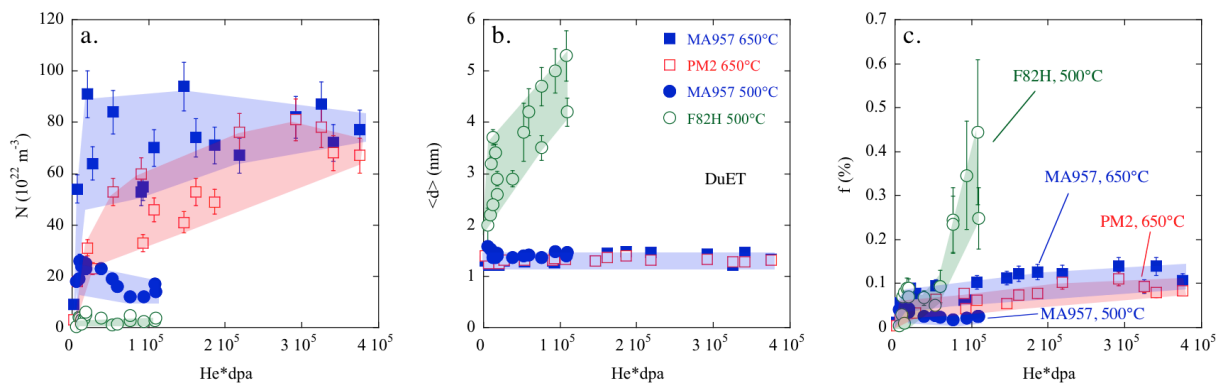


Figure 3. Comparison of all the dual ion beam irradiation results for  $N$ ,  $\langle d \rangle$  and  $f$  as a function of  $He \cdot dpa$ .

## ACKNOWLEDGEMENTS

The dual ion-beam irradiations were initially conducted in the TITAN program for US DOE-Japan MEXT collaboration for fusion energy research and continued under the support of the “Joint Research Program on Zero-Emission Energy Research,” Institute of Advanced Energy, Kyoto University (ZE24A-13 and 23B-3). The work performed at UCSB was supported by the U. S. Department of Energy, Office of Fusion Energy Sciences, under contract DE-FG03-94ER54275. We acknowledge the contributions of the NSF sponsored UCSB Microstructure and Microanalysis Facility. We are also grateful for generous support of research materials, F82H mod.3 from Dr. K. Shiba, (JAEA, Japan), MA957 from Dr. R. J. Kurtz (PNNL) and 14YWT-PM2 from Dr. D. T. Hoelzer (ORNL).

## REFERENCES

- [1] Y. Dai, G. R. Odette, and T. Yamamoto, “The Effects of helium on irradiated structural alloys,” in *Comprehensive Nuclear Materials*, R. Konings, T. R. Allen, R. E. Stoller, and S. Yamanaka, Eds. (2012) Elsevier.
- [2] T. Yamamoto, G. R. Odette, L. R. Greenwood, Fusion Materials Semiannual Report 1/1 to 6/30/2005 DOE/ER-313/38 (2005) 95.
- [3] T. Yamamoto, G. R. Odette, P. Miao, D. T. Hoelzer, J. Bentley, N. Hashimoto, H. Tanigawa, R. J. Kurtz, *J. Nucl. Mater.* **367-370** (2007) 399.
- [4] R. J. Kurtz, G. R. Odette, T. Yamamoto, D. S. Gelles, P. Miao, and B. M. Oliver, *J. Nucl. Mater.* **367-370** (2007) 417.
- [5] G. R. Odette, M. J. Alinger, and B. D. Wirth, *Annu. Rev. Mater. Res.* **38** (2008) 471.
- [6] T. Yamamoto, G. R. Odette, P. Miao, D. J. Edwards, and R. J. Kurtz., *J. Nucl. Mater.* **386-388** (2009) 338.
- [7] D. J. Edwards, R. J. Kurtz, G. R. Odette, and T. Yamamoto, *Fusion Materials Semiannual Report 12/31/2009* DOE/ER-313/47 (2010) 59.
- [8] G. R. Odette, P. Miao, D. J. Edwards, T. Yamamoto, R. J. Kurtz, and Y. Tanigawa, *J. Nucl. Mater.* **417** (2011) 1001.
- [9] E. H. Lee, J. D. Hunn, T. S. Byun and L. K. Mansur, *J. Nucl. Mater.* **280** (2000) 18.
- [10] H. Kishimoto, K. Yutani, R. Kasada, and A. Kimura, *Fusion Eng. Des.* **81** (2006) 1045.
- [11] R. Kasada, H. Takahashi, H. Kishimoto, K. Yutani, A. Kimura, *Mater. Sci. Forum* **654-656** (2010) 2791 ([doi:10.4028/www.scientific.net/MSF.654-656.2791](https://doi.org/10.4028/www.scientific.net/MSF.654-656.2791)).
- [12] T. Yamamoto, Y. Wu, G. R. Odette, K. Yabuchi, and A. Kimura, *Fusion Materials Semiannual Report 12/31/2010* DOE/ER-313/49 (2011) 1.
- [13] K. Shiba, M. Enoeda, and S. Jitsukawa, *J. Nucl. Mater.* **329-333** (2004) 243.
- [14] G. R. Odette and D. T. Hoelzer, *JOM* **62** (2010) 84.
- [15] N. J. Cunningham, Y. Wu, G. R. Odette, D. T. Hoelzer, S. A. Maloy, Fusion Materials Semiannual Report 6/30/2013 DOE/ER-313/54 (2013) 15.
- [16] N. J. Cunningham, Y. Wu, G. R. Odette, D. Gragg, K. Fields, D. T. Hoelzer, S. A. Maloy, Fusion Materials Semiannual Report 12/31/2012 DOE/ER-313/53 (2013) 20.
- [17] M. L. Hamillton, D. S. Gelles, R. J. Lobsinger, M. M. Paxton, and W. F. Brown, “Fabrication Technology for ODS Alloy MA957,” PNL-13165, Pacific Northwest Laboratory (2000).
- [18] J. H. Kim, T. S. Byun, D. T. Hoelzer, S.-W. Kim, and B. H. Lee, *Mater. Sci. Eng. A* **559** (2013) 101.

- [19] Y. Wu, E. M. Haney, N. J. Cunningham, and G. R. Odette, *Acta Meta.* **60** (2012) 3456.
- [20] A. Kohyama, Y. Katoh, M. Ando, and K. Jimbo, *Fusion Eng. Des.* **51-52** (2000) 789.
- [21] ASTM E521-96 (2009), ASTM
- [22] R. E. Stoller, M. B. Toloczko, G. S. Was, A. G. Certain, S. Dwaraknath, and F. A. Garner, *Nucl. Instr. Methods Phys. Res. B* **310** (2013) 75.
- [23] E. H. Lee, L. K. Mansur, and M. H. Yoo, *J. Nucl. Mater.* **85-86** (1979) 577.
- [24] F. A. Garner, *J. Nucl. Mater.* **117** (1983) 177.
- [25] A. D. Brailsford and L. K. Mansur, *J. Nucl. Mater.* **71** (1977) 110.
- [26] R. E. Stoller and G. R. Odette, *J. Nucl. Mater.* **131** (1985) 118.
- [27] W. A. Coughlan and L. K. Mansur, *J. Nucl. Mater.* **122-123** (1984) 495.
- [28] F. A. Garner, M. B. Toloczko, and B. H. Sencer, *J. Nucl. Mater.* **276** (2000) 123.
- [29] Y. Wu, T. Yamamoto, N. Cunningham, G. R. Odette, S. Kondo, and A. Kimura, Fusion Materials Semiannual Report 6/30/2013 DOE/ER-0313/54 (2013) 42.

## 8.1 Modeling Concurrent Radiation Damage and Plastic Deformation<sup>1</sup> — T. Crosby, G. Po, N. Ghoniem (University of California, Los Angeles)

### OBJECTIVE

This work has as an objective the modeling of concurrent radiation damage and plastic deformation in irradiated materials using a newly developed dislocation dynamics.

### SUMMARY

We present here an application of a fundamentally new theoretical framework for description of the simultaneous evolution of radiation damage and plasticity that can describe both in-situ and ex-situ deformation of structural materials. The developed self-consistent framework allows for the determination of the simultaneous evolution of the dislocation microstructure, as well as the spatial distribution of vacancies, interstitials and the temperature diffusion fields. The developed theory is implemented in a new computational code that facilitates the simulation of irradiated and unirradiated materials alike in a consistent fashion. Computer simulations are presented for irradiated fcc metals that address dislocation channel formation in irradiated metals (ex-situ). The simulations, which focus on plastic flow localization in micro-pillars, show that the spatial heterogeneity in the distribution of Stacking Fault Tetrahedra (SFTs) leads to localize plastic deformation and incipient surface fracture of micropillars.

### PROGRESS AND STATUS

#### Introduction

Irradiation of metals with high-energy particles, such as neutrons and ions, induces changes in the material microstructure and results in degradation of their mechanical properties. This has been well established and observed in experiments [1]. In low stacking-fault metals, such as Cu, the prevalent irradiation-induced defect is the vacancy-type stacking-fault tetrahedron (SFT) [2]. Depending on the fluence and energy of irradiated particles, the typical density of SFTs in irradiated fcc metals ranges between  $10^{21} - 10^{24} \text{ m}^{-3}$  [3]. The change in mechanical properties is manifest as an increase in the yield strength and a decrease in ductility. These changes are due to the fact that SFTs act as obstacles to the free glide of dislocation segments, causing them to be pinned at SFT sites. An increase in the applied stress is required to either break the dislocation free from the trapped configuration at the SFT site, or cut through the SFT and partially destroy it. A consequence of the physics of dislocation-SFT interaction is the onset of mechanical instabilities, such as plastic flow localization by forming defect free channels. This is attributed to dislocations absorbing SFTs, clearing paths for subsequent dislocations to glide freely, eventually creating defect-free dislocation deformation channels. Several numerical simulations showing the effect of SFT on the yield point and the interaction between dislocation segments and SFT have been reported in the literature, including atomistic simulations, discrete dislocation dynamics, and continuum dislocation dynamics. However, in these studies did not account for the effects of external surfaces on the onset of flow localization, nor did they consider the phenomenon in small-scale specimens, such as what is now commonly tested as micropillars.

---

<sup>1</sup> A manuscript with the same title has been submitted to Journal of Nuclear Materials in October 2013.

## RESULTS

Here, we model a Cu single crystal prismatic micropillar with a base of 250x250 nm and aspect ratio of 4:1. The pillar's bottom is fixed while its top surface is displaced with a fixed strain rate of 50 [1/s]. The lateral surfaces are free. The microstructure inside the pillar consists of dislocation segments and SFTs. The initial distribution of dislocations is generated randomly on all the 12 possible systems for fcc materials. The SFTs are randomly seeded inside the pillar following a uniform distribution. Image forces on the boundaries of the pillar are accounted for by coupling the DD method with elastic “correction” boundary value problem (bvp) and solved simultaneously. Due to the external and mutual stress, dislocations start to expand to form networks and interact forming junctions. During their motion, dislocation segments are randomly pinned at SFTs (Figure 1a). When enough local stress is accumulated, a dislocation can overcome the SFT obstacle. In the process, SFTs may be destroyed according to a cumulative probability (Figure 1c). Eventually a channel free of defects is formed (Figure 2). As a result, the glide of subsequent dislocations requires a lower applied stress.

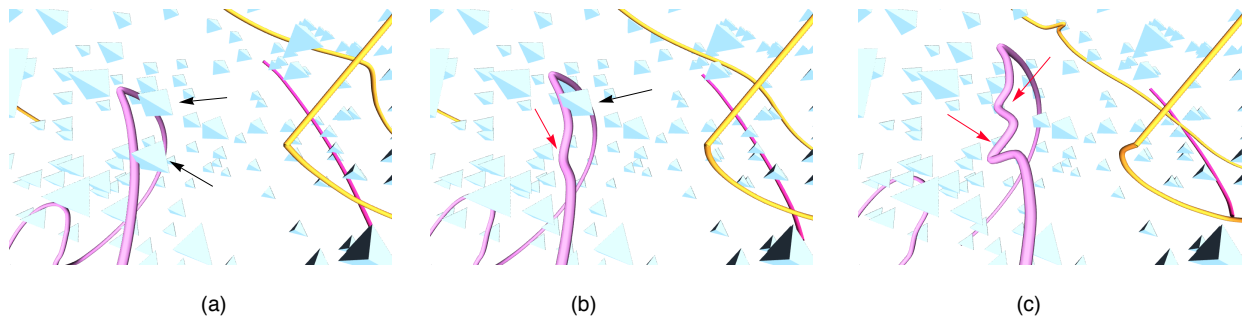


Fig. 1. Interaction between a dislocation segment and two SFTs. The dislocation segment is initially pinned at their location. Eventually, the two SFTs are destroyed, and the segment is freed.

The model showed the formation of localized channels with low SFT defect density, high dislocation flux, and localized plastic distortion. As expected, the boundary plays an important role in breaking the symmetry of channel formation due to the mutual interaction between dislocation segments and the confined domain. This study can be furthered in the future by extending this framework to model polycrystalline materials with focus on crack initiation due to flow localization at grain boundaries. The study is also predictive, and awaits experimental validation, where neutron or ion irradiated copper micro-pillars can be fabricated and mechanically tested ex-situ.

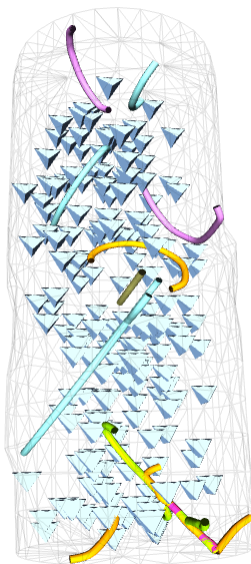


Fig. 2. Microstructure and channel formation.

## REFERENCES

- [1] M. Victoria, N. Baluc, C. Bailat, Y. Dai, M. I. Luppo, R. Schaublin, and B. N. Singh. "The microstructure and associated tensile properties of irradiated fcc and bcc metals," *J. Nucl. Mater.* **276**(1- 3): 114-122, 2000.
- [2] Y. Dai and M. Victoria, "Defect cluster structure and tensile properties of copper single crystals irradiated with 600 MeV pro- tons," MRS Proceedings, 439:319, February 1997.
- [3] B. N. Singh and S. J. Zinkle, "Defect accumulation in pure fcc metals in the transient regime: A review," *J. Nucl. Mater.* 1993.

**8.2 An Atomistic Assessment of Helium Behavior in Iron** — R. E. Stoller and Y. N. Osetskiy  
(Oak Ridge National Laboratory)

**EXTENDED ABSTRACT** - paper submitted to J. Nucl. Mater. after ICFRM-16

High helium generation rates in irradiated materials leads to the formation of small He-vacancy clusters that can evolve into larger bubbles and voids. In order understand and predict the behaviour of these He-vacancy defects, an accurate equation of state is required to reproduce their pressure- relationship. Previous research has employed equations of state of varying complexity, including the ideal gas, van der Waals, and hard sphere models. We recently used *ab initio* calculations to determine the energetics of helium-vacancy clusters and applied the results to develop a new three-body interatomic potential that describes the behaviour of helium in iron. This potential was employed in molecular dynamics simulations to determine the conditions for mechanical equilibrium between small helium-stabilized bubbles and an iron matrix, and to systematically map the pressure-temperature relationship for the bubbles. These atomistic results are compared to an existing equation of state and a modification is proposed for bubbles with high helium densities.

Our MD simulations with the iron interatomic potential by Ackland and co-workers [1] coupled with the ORNL three-body He-Fe potential [2] indicate that the helium-to-vacancy ratio for bubbles large enough to be visible in the transmission electron microscope is in the range of 0.3 to 1.0. Values greater than 1.0 are obtained only for bubbles with radii less than 1 nm. This result is consistent with a recent experimental measurements using electron energy loss spectroscopy to determine the helium-to-vacancy ratio for small helium bubbles in ferritic-martensitic steels. The helium density results of Wu et al. for a 1.3 nm bubble lead to a He/vacancy ratio ~0.6 [3], and earlier measurements by Frechard et al. for bubbles between 2 and 5 nm for which the He/vacancy ratio was in the range of 0.25 to 0.85 [4]. As shown in Figure 1, the helium pressure in equilibrium bubbles was in good agreement with estimates provided by the capillarity pressure of  $2\gamma/r$  where  $\gamma$  is the surface energy obtained from the iron potential and  $r$  is the bubble radius. The bubble compressibilities shown in Figure 2 were found to be consistent with a computationally tractable hard-sphere equation of state [5] with a minor adjustment in the effective hard-sphere diameter used to compute the helium density. Based on previous work in which we assessed the behavior of helium vacancy clusters using three different iron potentials in conjunction with our three-body He-Fe potential, it does not appear that the choice of a different iron potential would have any significant impact on our results. In recent work by Caro, *et al.* [6] which investigated the behavior of helium in iron at higher He/vacancy ratios and employed a different equation of state, they work suggests that the equilibrium He/vacancy ratio is about 1, which is higher than we observed in our simulations. The reasons for this discrepancy are not clear at this point and may be resolved by further research.

**REFERENCES**

- [1] G. J. Ackland, D. J. Bacon, A. F. Calder, T. Harry, *Philos. Mag. A* **75** (1997) 713-732.
- [2] R. E. Stoller, S. I. Golubov, P. J. Kamenski, T. Seletskaya, and Yu. N. Osetsky, *Philos. Mag.* **90** (2010) 923-934.

- [3] Y. Wu, G. R. Odette, T. Yamamoto, J. Ciston, and P. Hosemann, "An electron energy loss spectroscopy study of helium bubbles in nanostructured ferritic alloys," *Fusion Reactor Materials*, Semiannual Progress Report DOE/ER-0313/54, Oak Ridge National Laboratory (2013) pp. 173-179.
- [4] S. Fréchar, M. Walls, M. Kociak, J. P. Chevalier, J. Henry, and D. Gorse, *J. Nucl. Mater.* **393** (2009) 102.
- [5] I. R. Brearley and D. A. MacInnes, *J. Nucl. Mater.* **95** (1980) 239-252.
- [6] A. Caro, J. Hetherly, A. Stukowski, M. Caro, E. Martinez, S. Srivilliputhur, L. Zepeda-Ruiz, M. Nastasi, *J. Nucl. Mater.* **418** (2011) 261-268.

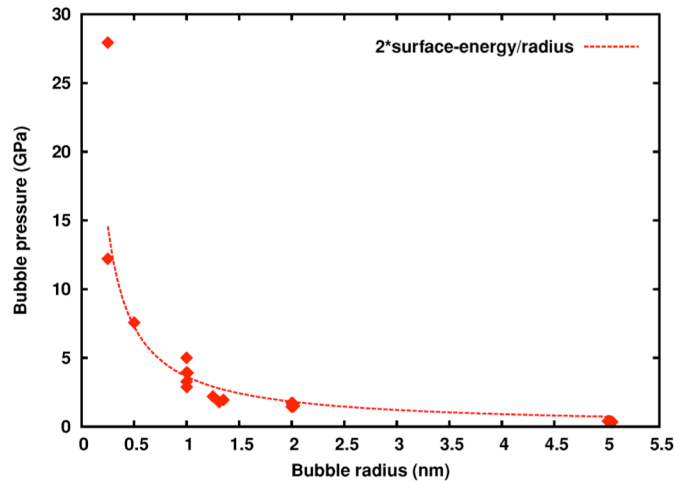


Figure 1. Bubble pressure obtained from MD simulations for bubbles in mechanical equilibrium with the iron lattice (red diamonds) compared with capillarity pressure using the surface energy obtained from MD.

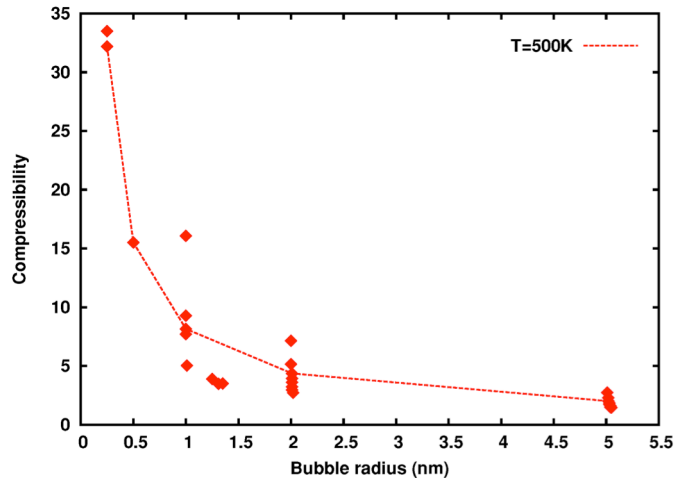


Figure 2. Compressibility of bubbles in mechanical equilibrium with the iron lattice as a function of bubble radius. Compressibility defined as ratio of pressure from MD simulations divided by ideal gas pressure.

### 8.3 Dynamics of Helium-Loaded Grain Boundaries under Shear Deformation in $\alpha$ -Fe — F. Gao, L. Yang, H. L. Heinisch and R. J. Kurtz (Pacific Northwest National Laboratory)

#### OBJECTIVE

To simulate the motion and behavior of helium-loaded grain boundaries (GBs) in bcc Fe under shear deformation using the molecular dynamics simulation method. Here, we report preliminary results on the effects of helium on coupled migration and relative translation of a S3 GB at 300 K.

#### SUMMARY

Helium produced in the fusion nuclear environment will interact with microstructural features in materials, such as GBs and dislocations. At elevated temperatures helium at GBs can significantly influence creep-rupture properties by enhancing cavity formation and lowering GB cohesive energy. Grain boundary sliding can lead to stress concentrations at GB triple junctions and hard precipitates in the GB plane that may be sufficient to nucleate cavities. Here we explore the effects of helium on coupled GB migration and sliding under an applied shear stress. The  $\Sigma 3$  symmetric tilt GB with a  $\langle 110 \rangle$  rotation axis in bcc iron was selected for study. The method for exploring helium effects on GB motion involved randomly inserting different concentrations of helium atoms around the GB plane and then applying a shear stress parallel to the GB plane at 300 K. We reported previously [1] that, in the absence of helium, the critical stress to induce coupled GB migration and sliding occurred at 300 K was 1.5 GPa. The current simulations show that when helium is present the critical stress for coupled GB motion, and the GB migration velocity are both reduced. When the GB helium concentration is low, most single helium atoms and small helium clusters migrate along with the GB. However, at high helium concentrations clusters easily form that remain behind in the bulk when the GB migrates away from its original position.

#### PROGRESS AND STATUS

##### Introduction

The behavior of He in Fe has been investigated widely [2-7], because in the fusion reactor environment high levels of insoluble He is generated in steels due to nuclear  $(n,\alpha)$  transmutation reactions. Experimental results and atomistic calculations demonstrate that grain boundaries (GBs) act as sinks to trap He atoms in  $\alpha$ -Fe. It is known that GBs play a significant role in the microstructure evolution and mechanical properties of materials. The nucleation of He bubbles at GBs in a ternary (Fe-15Cr-15Ni) austenitic steel after He implantation was investigated by Lane and Goodhew [2] using transmission electron microscopy (TEM), while Randle [3] investigated the interaction mechanisms of He bubbles with GBs in an austenitic steel using TEM. Dynamical interaction of He bubbles with GBs in Fe and Fe-9Cr was also studied by *in situ* electron microscopy and thermal desorption spectroscopy (TDS) [4]. In addition, the molecular dynamics (MD) method has been extensively employed to study the atomic-level processes of He behavior at GBs in bcc Fe. We have previously studied the diffusion mechanisms of He interstitials and di-He clusters at GBs in  $\alpha$ -Fe using MD simulations [5].

<sup>1</sup> PNNL is operated for the U.S. Department of Energy by Battelle Memorial Institute under Contract DE-AC06-76RLO 1830.

Of the four typical motions of GBs in response to shear stresses [7] it is the relative translation of the grains parallel to the GB plane (i.e., sliding) coupled with migration normal to the GB plane that we focus on in this study. The combination of GB sliding and migration is referred to as coupled GB motion in this report. In our previous work, the coupled motion of two tilt GBs ( $\Sigma 3$  and  $\Sigma 11$ ) in bcc iron with different concentrations of vacancy and self-interstitial point defects was investigated under a shear stress applied parallel to the GB plane and perpendicular to the tilt axis [1]. We also investigated the detailed mechanisms for a self-interstitial atom (SIA) loaded GB to annihilate with vacancies when the GB moves into a vacancy-rich region. We found that the SIA loading reduced the critical stress for coupled GB motion in a  $\Sigma 3$  GB [1]. The behavior of the point defect loaded GB depended on GB structure. The interstitials in the  $\Sigma 3$  GB easily formed  $\langle 111 \rangle$  clusters that remained behind in the bulk when the GB migrated. Vacancies in the  $\Sigma 3$  GB impeded coupled GB motion. In contrast, interstitials were found to move along with the  $\Sigma 11$  GB and recombine with nearby vacancies, leading to defect recovery and healing of radiation damage. It should be noted that this healing phenomenon was observed only in the  $\Sigma 11$  GB. In the present work, the effects of He on the motion of GBs under shear deformation in bcc Fe is studied at room temperature. The behavior of helium in the GB is further analyzed.

### Simulation Methods

Details of the simulation methods were reported previously [1]. Briefly, the simulation cell size for the  $\Sigma 3$  GB was  $84.20 \text{ \AA} \times 140.00 \text{ \AA} \times 80.84 \text{ \AA}$  with 80,240 Fe atoms. Periodic boundary conditions were imposed along the x and z directions, which were parallel to the GB plane. Fixed boundary conditions were applied along the y direction, which was normal to the GB plane. The x, y and z axes in the model correspond to the [1-11], [-112] and [-1-10] directions, respectively in crystal coordinates.

The NVT (constant number of atoms, volume and temperature) ensemble was used in the present simulations with a time step of 1 fs. To study the effects of He, different concentrations of interstitial He were inserted randomly within the GB plane. After the He atoms were inserted, the system was quenched to 0 K, followed by a temperature rescaling to 300 K for 50 ps. Then, applying a shear stress to selected atoms in the model drove the loaded GB. The orientation and identification of the specific regions of the simulation cell are shown in Reference 1. Helium concentrations of 5%, 10%, 20%, and 30% (the number He atoms were 34, 68, 136 and 204, respectively) were investigated. The percentage of He atoms was taken as a fraction of the Fe atoms on the GB plane.

### Results and Discussion

Coupled GB motion is observed when shear stress is applied along the x direction. Once the applied shear stress is increased to a critical value, the GB becomes mechanically unstable and migrates to a new position. Figure 1 shows several snapshots of the  $\Sigma 3$  GB with a 5% He concentration. It is of interest to note that some inserted interstitial He atoms accumulate to form small clusters after application of the shear stress. When the GB migrates in the  $-y$  direction, most single He atoms and small He clusters move along with the GB. This result is probably due to binding of He to the GB, even though that binding is relatively weak for this GB. However, in our previous work, we found that SIAs migrate easily along the  $\langle 111 \rangle$  direction and form  $\langle 111 \rangle$  clusters at 300 K [1]. When the GB migrates in the  $-y$  direction, the applied stress

enhances the motion of the SIA clusters along the x direction ( $\langle 111 \rangle$ ), but they seldom migrate with the GB. The present work suggests that He affects coupled GB motion. After applying a shear stress for 0.7 ns, the GB has migrated 7 atomic layers in the  $-y$  direction, which is smaller than the 9 atomic layers for the same system without He under the same simulation conditions.

Simulations of higher He concentrations (10%, 20%, 30%) were also performed. Figure 2 shows several snapshots of the  $\Sigma 3$  GB with 20% He. Initially, the He atoms are randomly distributed on the GB plane, as shown at 0.0 ns in Figure 2. After applying the shear stress, most He atoms have aggregated to form clusters near the GB plane within 0.2 ns. With increasing simulation time, we found that some large He clusters formed near the GB plane. For example, the largest He cluster consists of 17 He atoms at 0.7 ns. When the GB moves in the  $-y$  direction, only a few He clusters migrate along with it. Most He clusters remain behind in the bulk. This is shown in the snapshot at 0.7 ns in Figure 2, where the GB plane has migrated 6 atomic layers along the  $-y$  direction. From these results, along with those at the 5% He concentration, it is noted that the GB migration velocity is impeded by the He atoms and decreases with increasing He concentration. Similar to our previous observation [1], a large number of SIAs are emitted from these large He clusters. These SIAs distribute at the peripheries of the He-V clusters, and form interstitial loops.

The critical shear stress causing coupled GB motion is significantly reduced by the presence of He. The shear stress as a function of time for different helium concentrations at 300 K in the  $\Sigma 3$  GB is presented in Figure 3. It is of great interest that the critical stress decreases with increasing He concentration, and the GB migration velocity of the system with He atoms also decreases with increasing He concentration, as described above. For a system without He, the GB plane migrates three atomic layers but, for a system with He, the GB moves only one or two layers. This may be due to the dragging effect of the He clusters, reducing the ability for coupled motion of GBs.

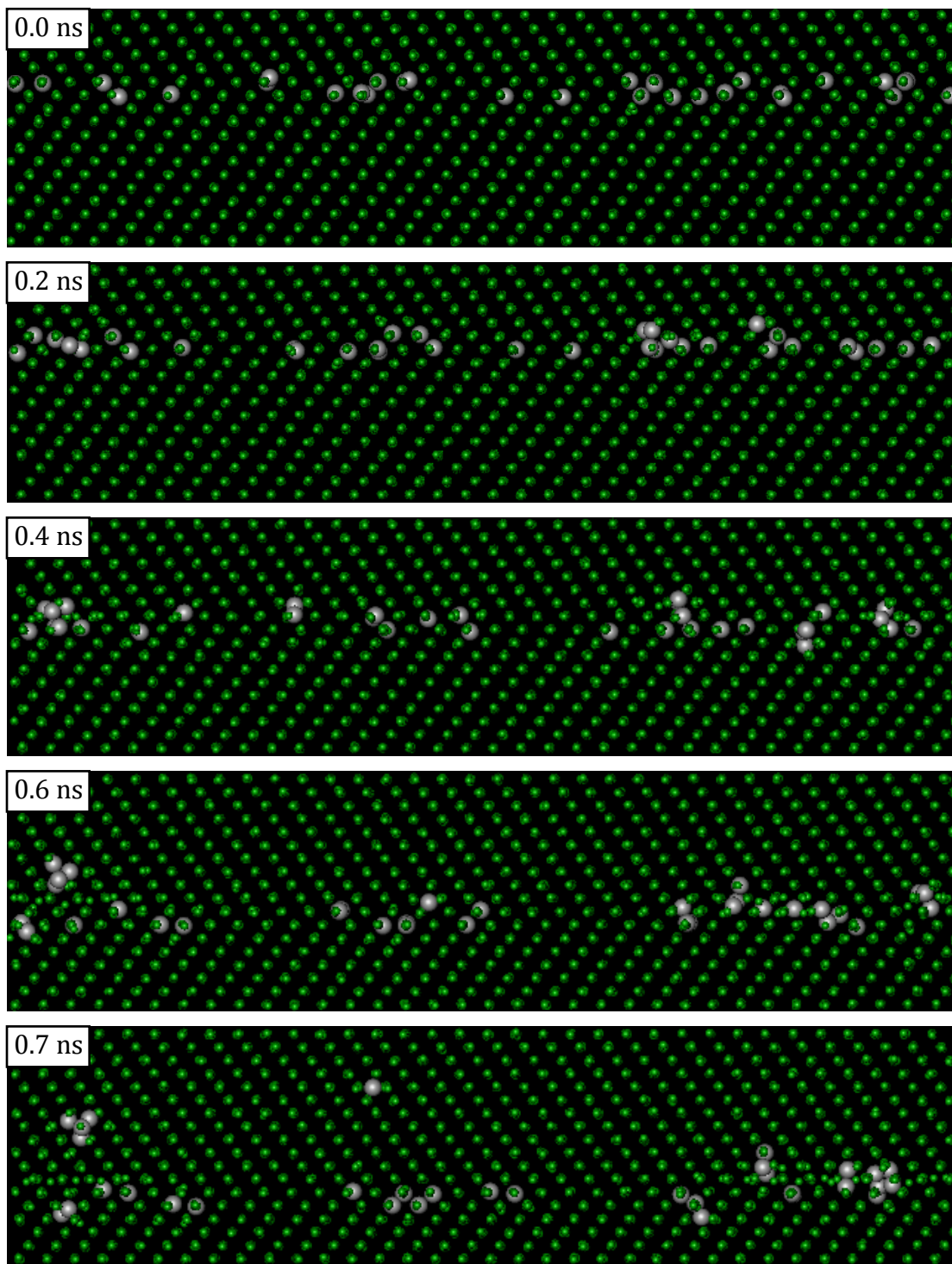


**Figure 1.** Several snapshots showing  $\Sigma 3$  GB migration at 300 K for a 5% He concentration.

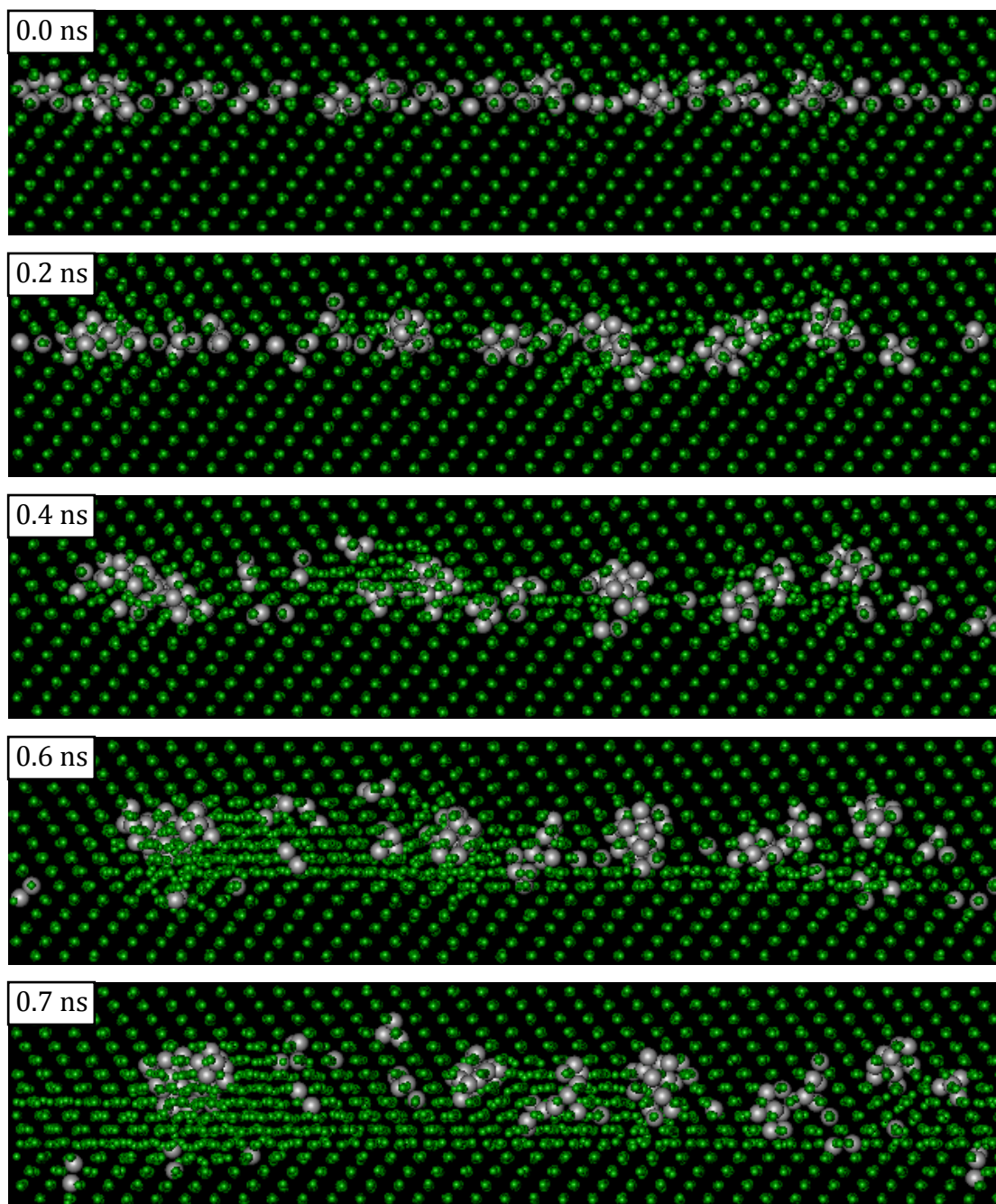


**Figure 2.** Several snapshots showing  $\Sigma 3$  GB migration at 300 K for a 20% He concentration.

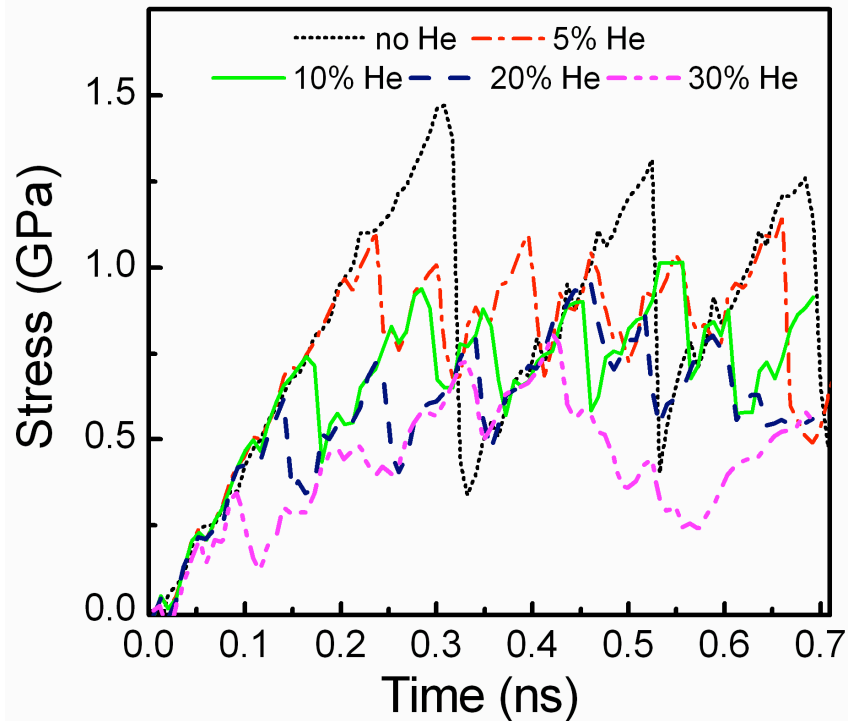


**Figure 3.** Shear stress as a function of simulation time for different He concentrations at 300 K in the  $\Sigma 3$  GB.

## SUMMARY

Helium atoms inserted randomly into a  $\Sigma 3$  GB were found to affect the coupled motion of that boundary. At a 5% He concentration, most single He atoms and small He clusters migrated along with the GB. However, at higher concentrations He atoms easily form clusters that spontaneously emit SIAs. These He-V clusters remain behind in the bulk when the GB migrates normal to the GB plane. Interstitial He reduced the critical stress for coupled motion of the  $\Sigma 3$  GB in Fe at 300 K.

## REFERENCES

- [1] L. Yang, F. Gao, H. L. Heinisch, and R. J. Kurtz, in DOE/ER-0313/54-Volume 54 semiannual Progress Report June 30, 2013.
- [2] P. L. Lane and P. J. Goodhew, *Philos. Mag. A* **48** (1983) 965.
- [3] V. Randle, *Acta Metall. Mater.* **39** (1991) 481.
- [4] K. Ono, M. Miyamoto, and K. Arakawa, *J. Nucl. Mater.* **367-370** (2007) 522.
- [5] H. Q. Deng, W. Y. Hu, F. Gao, H. L. Heinisch, S. Y. Hu, Y. L. Li, R. and J. Kurtz, *J. Nucl. Mater.* **442** (2013) S667.
- [5] G. Ackland, *Science* **327** (2010) 1587.

- [6] L. Yang, X. T. Zu, H. Y. Xiao, F. Gao, H. L. Heinisch, R. J. Kurtz, and K. Z. Liu, *Appl. Phys. Lett.* **88** (2006) 091915.
- [7] J. W. Cahn, Y. Mishin, and A. Suzuki, *Acta Mater.* **54** (2006) 4953.

**8.4 Radiation-Induced Obstacles in Iron and Ferritic Alloys: An Atomic-Scale View** —  
 Y. N. Osetskiy and R. E. Stoller (Oak Ridge National Laboratory)

**EXTENDED ABSTRACT** - paper submitted to J. Nucl. Mater. after ICFRM-16, with new results on the largest modeled 6nm obstacles added.

Radiation produces nanoscale defects which strongly affect mechanical properties. An extended study using atomic-scale modeling investigated strengthening mechanisms in irradiated iron and ferritic alloys, considering *inclusion-like* obstacles (precipitates, voids, bubbles). Both types have unique features, different strengthening mechanisms and demand different models for predicting hardening. The strengthening mechanism for dislocation loops depends on their size, interaction geometry and on impurity segregation to the loops and may vary from practically zero resistance to the maximum strength of an Orowan mechanism. Conditions which lead to the maximum strengthening resulting from different types of individual obstacles and a combination of multiple obstacles were investigated and the results are discussed in terms of existing experimental data.

**Model** To study dislocation dynamics at atomic scale we used a standard MD based model described earlier (Osetskiy&Bacon, MSMSE, 2000) and schematically depicted in the Figure 1. Within this model we studied screw and edge dislocations moving through a periodic array of obstacles under applied stress or stain and temperature. Typical system consists of 2-10 million mobile atoms interacting by EAM-type interatomic potentials and with a simulated dislocation density of  $\sim 10^{13}$ - $10^{14} \text{m}^{-2}$ . Applied strain rates of  $10^6$ - $10^8 \text{s}^{-1}$  provide dislocation velocity from 10 to 1000 m/s simulated over physical times 100 to 2000 ps. Typical output information include stress-strain dependence, crystal energy and visualization of a dislocation and obstacles.

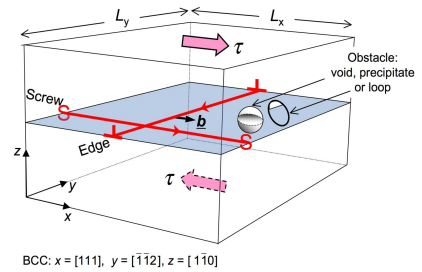


Figure 1. Atomic scale model for dislocation-obstacle interaction study.

**Voids, precipitates and bubbles.** Static modeling, i.e. 0K relaxation to the minimum energy state at a certain strain, allows a direct comparison with continuum models and dislocation dynamics modeling. The result is a set of equilibrium crystal states, which yields stress-strain and energy-strain dependences, Critical Resolved Shear Stress (CRSS) and dislocation-obstacle interaction mechanisms. Results for voids and Cu-precipitates are compared with continuum models in Figure 2. Here  $D$  is obstacle diameter and  $L$  is period along the dislocation line, all are in units of the edge dislocation Burgers vector  $b = \frac{1}{2}\langle 111 \rangle$ . Large enough obstacles are strong “Orowan-like” and their

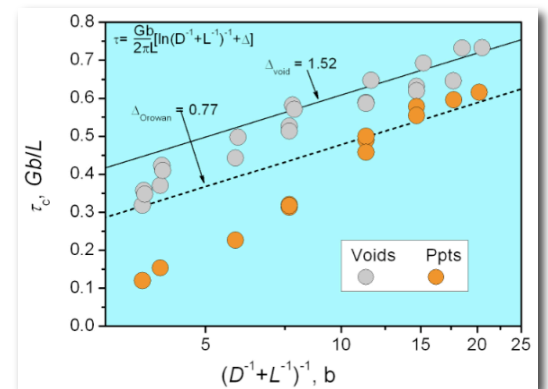


Figure 2. Comparison of atomistic and continuum results for void and precipitate hardening.

strengthening is well described by the continuum approach. However, small obstacles involve local atomic scale effects, which cannot be accounted for by continuum methods.

**Temperature effects in Cu-precipitate strengthening.**

The Fe-Cu system is relevant to the experimentally observed radiation-induced precipitate hardening in pressure vessel steels. Small precipitates are coherent with bcc-Fe matrix while large precipitates, >4-7nm, transform to fcc structure. Transformation and hardening depend on temperature and geometry of dislocation-precipitate interactions. An extensive study provided understand the basic mechanisms of Cu-precipitate hardening, phase transformation and their temperature dependence.

The results are presented in Figure 3: weak temperature dependence of CRSS for small precipitates is consistent with numerous data for neutron irradiated ferritic alloys where precipitates do not grow above 2nm while the stronger temperature dependence for large precipitates consistent with experiments in overaged alloys.

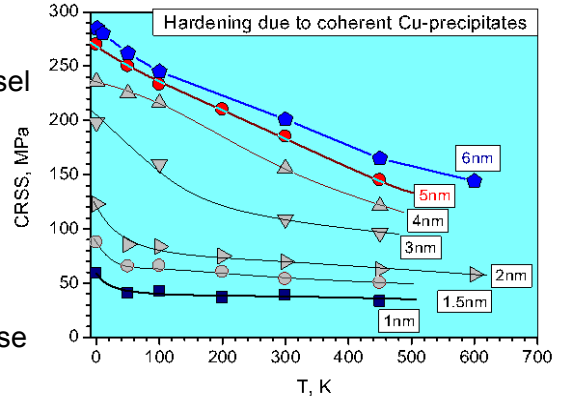


Figure 3. Temperature dependence of hardening due to Cu-precipitates of different size.

**Comparison of different inclusion-like obstacles.**

Other inclusion-like obstacles important in irradiated ferritic alloys include He bubbles and oxide nanoclusters as in ODS-alloys. The equilibrium state of He-bubbles and the effect of He-bubbles on moving dislocations have been studied. The bubble-dislocation interaction mechanisms are generally similar to that with voids. Near the equilibrium He-to-vacancy ratio (He/Vac) bubbles are stronger obstacles than voids, with their strength decreasing at higher He/Vac. Oxide particles we “simulated” as rigid inclusions coherent with bcc-Fe matrix. The inclusion had infinitely high elastic moduli while the whole inclusion interacted with the matrix atoms by the same Fe potential and can move inside matrix. Dislocation interaction with such an inclusion depends strongly on its size: small inclusions are weak obstacles and even an edge dislocation can overcome it whereas large ones, ≥4nm, are classical Orowan obstacles and Orowan loops are formed after the dislocation breaks away. A comparison of strength of all studied inclusion-like obstacles is presented in Figure 4.

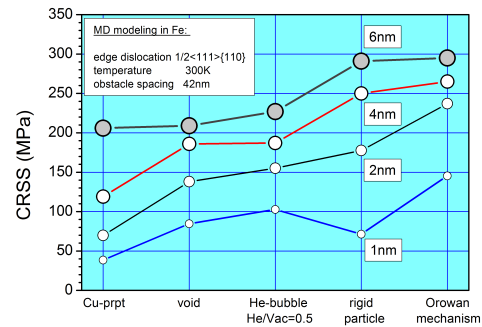


Figure 4. Comparison of strength of different types of obstacles of different size.

## 8.5 Modeling of Irradiation Hardening of Iron After Low Dose and Low Temperature Neutron Irradiation — X. Hu, D. Xu, B. D. Wirth (University of Tennessee, Knoxville), and T. S. Byun (Oak Ridge National Laboratory)

### OBJECTIVE

The objective of this work is to model the yield strength increase of iron after low dose and low temperature neutron irradiation and to provide insight into the underlying microstructure – property relationships.

### SUMMARY

Irradiation hardening is a prominent low temperature degradation phenomena in materials. In this paper, a reaction-diffusion cluster dynamics model is used to predict the distribution of vacancy and interstitial clusters in iron subject to low temperature ( $< 373\text{K}$ ) and low dose ( $< 0.1\text{ dpa}$ ) neutron irradiation. The predicted microstructure evolutions of high purity iron samples are compared to positron annihilation spectroscopy (PAS) and transmission electron microscopy (TEM) observations and show good agreement for neutron irradiation in this regime. The defect cluster distributions are then coupled to a dispersed barrier hardening model that assumes a strength factor,  $\alpha$ , which varies with cluster type and size to compute the yield strength increase, the results of which are compared to the values obtained from tensile tests. A reasonable agreement between modeling and experiments is achieved.

### PROGRESS AND STATUS

#### Introduction

Exposure of metallic structural materials to irradiation environments results in significant performance degradation, which limits the extended operation of current generation light water reactors and restricts the design of advanced fission and fusion reactors [1-4]. Irradiation hardening is the most prevailing degradation phenomena at low temperature ( $T_{irr} < 0.3 T_m$ ), routinely characterized by an increase of yield strength and decrease in uniform ductility in tension tests, and results from the accumulation of various irradiation-produced defects, e.g., defect clusters, impurity-defect cluster complexes, dislocation loops and lines, voids, bubbles and precipitates [5, 6]. The existence of these defects impedes dislocation glide during deformation, causing the increase of yield strength, which is almost always accompanied by degradation of other critical mechanical properties such as the loss of ductility resulting in embrittlement [7-11].

The problem of irradiation hardening has been investigated both experimentally and theoretically in considerable depth since the 1960s [9-27]. In experimental studies, the irradiation hardening behavior of body-centered cubic (BCC), face-centered cubic (FCC), and hexagonal close-packed (HCP) alloys and pure metals has been thoroughly investigated following neutron, spallation proton and ion irradiation at low temperatures by many researchers [12-19], which aimed to characterize the dose dependence of irradiation hardening and explain the results with respect to the plastic deformation and defect-cluster accumulation behaviors. For example, Byun and Farrell [18] examined the irradiation behavior of 19 polycrystalline metals after low temperature irradiation,

indicating the transition between the low-dose and high-dose regimes, and elucidated the relationship among irradiation hardening, plastic instability, deformation mechanism, and defect-cluster number density. Rice and Zinkle [19] correlated the TEM observed dislocation loop distributions to the yield stress increase of neutron irradiated vanadium alloys to study the barrier strength.

A great deal of effort has been made to reveal the mechanisms of irradiation hardening in metals due to the various irradiation-produced defects. The mechanical behavior of irradiated metals is routinely correlated to the observed microstructure by use of either a dispersed barrier-hardening model [20, 21, 22], a cascade-induced source hardening model [9,12], or a dislocation density-based constitutive model [23].

The dispersed barrier-hardening model is commonly used to correlate yield strength increases to the irradiation-produced defects. Although there are multiple hypotheses to correlate the change in yield strength with the number density and size of defects, the dose-dependence of the yield stress,  $\Delta\sigma_{YS}$ , has been frequently explored using an Orowan strength model associated with the assumption that dislocation bypass of impenetrable obstacles occurs by bowing around them. Based on Orowan's model, the most commonly used expression for the change in shear stress,  $\Delta\tau_s$ , induced in the dislocation glide plane by a regular array of defects is:

$$\Delta\tau_s = \alpha\mu b(Nd)^{1/2} \quad (1)$$

where  $\mu$  is the shear modulus of the matrix,  $b$  the magnitude of the dislocation Burgers vector,  $N$  the defect number density, and  $d$  is the defect diameter. In this formulation, the square-root factor represents the reciprocal of the average distance between obstacles. The  $\alpha$  factor is typically referred to as the 'barrier strength', and accounts for the fact that some obstacles may be partially cut or sheared by the dislocation as it bows out during the glide process, with a resistance less than an impenetrable Orowan obstacle ( $\alpha = 1$ ).

The cascade-induced source hardening model proposed by Singh [9] is based on the idea that the experimentally observed yield drop results from the unlocking of grown-in matrix dislocations decorated by self-interstitial dislocation loops. In order to initiate plastic deformation in materials, these dislocations act as Frank-Read dislocation sources. Consequently, the stress necessary to unlock the dislocations represents the upper yield stress, which has different expressions for two distinct cases: (i) the loops are clearly separated by distances similar to their size, and (ii) the loops are no longer well separated but form a network. The expressions of upper yield stress for these two cases are provided in Eq. (2) and (3), respectively.

$$\tau = 0.1\mu(b/l)(d/y)^2 \quad (2)$$

and

$$\tau = \mu b / 8\pi(1-\nu)y \quad (3)$$

where  $l$  is the average spacing of dislocation loops, and  $y$  is the distance between the straight row of sessile dislocation loops and the straight glide dislocation. However, this model does not adequately describe the dose dependence of hardening [24].

A dislocation density-based constitutive model successfully reproduced the post-yield deformation behavior of irradiated Cu tested in uniaxial tension at low to intermediate homologous temperature, based on information from molecular dynamic simulations of the interaction behavior between gliding dislocations and radiation-induced stacking fault tetrahedra [23]. This isotropic internal state variable plasticity model included mechanisms for dislocation density growth and multiplication, as well as for irradiation-induced defect density evolution as a result of dislocation interactions. The final coarse-grained model was implemented into a finite element framework and used to simulate the behavior of tensile specimens with varying levels of irradiation-induced material damage.

Despite extensive effort to investigate the irradiation hardening behavior through both experimental and modeling techniques, a self-consistent and complete model validated by experimental results is not yet available to bridge the irradiation-produced microstructure evolutions with the resulting hardening behavior. In this paper, neutron irradiation induced hardening of iron samples is taken as an example to demonstrate the quantitative influence of defect distribution on the increase of yield strength. Among the above-mentioned models, the dispersed barrier-hardening model is most commonly used to predict the yield strength increase, due to its explicit relationship with the irradiation-induced defect information. For the dispersed barrier model, it is noted that attempts to correlate irradiation-produced microstructural evolution with changes in mechanical properties rely on a well-established theory to compute the resolved shear stress required to move dislocations through a field of obstacles. Various modifications to the Orowan equation have been proposed [11, 25]. Similar to Equation (1), these efforts have focused on finding more accurate correlations between the resolved shear stress and the number density and size of the irradiation-produced defects. The comparisons of the yield strength increase computed using this model and the corresponding experimental measurements have been carried out for different structural materials, such as 304 and 316 stainless steels [26] and ferritic steels [27]. In these studies, a rough estimation of the defect cluster density was used such that the defect accumulation behavior was assumed linear at very low doses (less than 0.0001 dpa) and proportional to the square root of dose at higher doses. However, an accurate estimation of the yield strength increase requires a precise prediction of the defect distribution in the material under irradiation.

Cluster dynamics has proved to be a useful technique to simulate microstructure evolution under irradiation. For example, Xu et al., [28-30] developed a spatially dependent cluster dynamics model based on reaction-diffusion rate theory to study the nanoscale microstructural evolution of keV helium-implanted iron and 1 MeV krypton-irradiated-molybdenum. Hu et al., [31,32] also applied the same model to study the helium – point defect interactions in helium-implanted single crystalline iron. In addition, other researchers [33, 34] have made improvements to the computing efficiency of the cluster dynamics model and applied this method to various ion irradiation conditions. However, a limited number of papers exist in the literature [35] that utilizes the cluster dynamics model-to-model neutron irradiation experiments. The difficulty of neutron irradiation damage modeling arises from the need for an accurate estimation of the primary knock-on atoms induced by neutron scattering across a broad energy spectrum. A cluster dynamics model based on the reaction-diffusion rate theory is applied here to simulate the neutron irradiation induced microstructure evolution in BCC iron, which provides radiation-induced defect concentrations for the hardening model.

The objective of this study is, therefore, to introduce a coupled modeling and experimental study by applying the experimentally validated (i.e., PAS and TEM) cluster dynamics modeling results of the defect evolution in iron under neutron irradiation to a dispersed barrier irradiation-hardening model. The results presented here favorably compare to tensile test measurements of iron samples, and provide insights into the underlying microstructure-property relationships.

## Experiment

In the present study, microstructural and mechanical properties of two different high purity polycrystalline iron samples are investigated after neutron irradiation. The chemical compositions of the samples and their pre-irradiation heat treatments are shown in Table 1. Fast neutron irradiation experiments were conducted in the hydraulic tube facility of the High Flux Isotope Reactor (HFIR) at Oak Ridge National Laboratory. Eldrup *et al.* [36] examined the microstructures of the Fe-a samples after neutron irradiation using PAS and TEM. The positron lifetime measurements were performed to obtain information on vacancy cluster distribution while the interstitial cluster density was determined by TEM observation [36]. Tensile tests were performed for both the Fe-a and Fe-b specimens at room temperature in screw-driven machines at a nominal strain rate of about  $10^{-3} \text{ s}^{-1}$ . The neutron irradiation and testing conditions, and baseline tensile data of these two samples are listed in Table 1. The present paper will focus on modeling work to compare to the experiment observations presented in Section 4, and thus many of the specific details of the experiments are not described here; additional details are available in References [18, 36-39].

Table 1. Chemical compositions, heat treatment, irradiation conditions, testing conditions, and baseline tensile data of the two types of iron samples.

	Fe-a	Fe-b
Chemical composition (wt%)	99.995% purity	Fe-0.013C-0.018Mn-0.018Ni (99.94% purity)
Heat treatment in vacuum	Annealed at 873 K for 1 h	Annealed at 873 K for 1 h
Crystal structure	BCC	BCC
Tensile test temperature (K)	Room Temperature	Room Temperature
Yield stress (MPa at 0 dpa)	104	213
Uniform elongation (0 dpa)	0.26	0.29
Dose range (dpa)	0-0.79	0-1.07
Irradiation temperature (K)	333-373	333-373

## Modeling

### Cluster dynamics model based on reaction-diffusion rate theory

Free vacancies and self-interstitial atoms (SIAs), as well as spherical vacancy clusters and SIA clusters in the form of planar, prismatic dislocation loops are continuously formed and will evolve in pure body-centered cubic iron under neutron irradiation [40, 41, 42]. A cluster dynamics model based on the reaction-diffusion rate theory is used here to predict the evolution of the defect clusters, which is a modified version of the model developed by Xu and Wirth [28, 29, 30, 40] and only considers the intrinsic defects and their clusters. Furthermore, since the probability that SIA and vacancy co-exist in a single cluster is very low due to their strong tendency for recombination, no mixed I-V clusters were considered, and it is thus sufficient to define any cluster using just an integer, with its absolute value being the number of point defects contained in the complexes and its sign (‘-’ for SIA clusters, or ‘+’ for V-clusters) indicating the character of the cluster. Two numbers, NI and NV, are chosen as the number of interstitials in the largest SIA-cluster, and the number of vacancies in the largest V-cluster, respectively. Physically, these numbers prescribe the ‘phase space’ within which the clusters can interact with each other, and ensure the conservation of point defects. NI and NV should be chosen large enough so that the computational results are not impacted by a prescribed phase space that is too small (e.g., insufficient cluster size to allow growth to large defect cluster size). Note that a spatially dependent defect generation in metals occurs under ion implantations, and therefore was necessarily taken into account in the previous modeling effort [28-32, 40]. However, the nature of defect generation in metals induced by ions and neutrons is significantly different. Since the energy transfer cross section for ions is an atomic cross section ( $\sim 10^{-17}$  cm<sup>2</sup>) while that for neutrons is a nuclear cross section ( $\sim 10^{-24}$  cm<sup>2</sup>), neutrons have a much larger range when travelling in a material than an ion does. The damage production varies weakly along the depth direction for neutron irradiation and therefore, it is reasonable to treat the distribution of radiation damage production as homogeneous. Thus an explicit spatial dimension is no longer necessary in this model, different from the model introduced in Reference [40], at least for low neutron dose levels before a clear spatial correlation of the defect microstructure develops.

Since there is no spatial dependence, the concentration of each cluster is only a function of time, and ordinary differential equations are employed to describe the defect evolution. The binary reactions discussed in References. [28-32, 40-42] are still appropriate and become simpler, because there are only two types of defects (V- and SIA-clusters) considered during neutron irradiation. The generic form to describe the evolution of a cluster is:

$$\frac{dC_i}{dt} = \phi \times P_i + G\_T + G\_E - A\_T - A\_E, \quad (4)$$

where  $C_i$  refers to the volumetric concentration (in 1/m<sup>3</sup>) of the i-th cluster,  $\phi$  is neutron flux (in neutron/m<sup>2</sup>/sec),  $P_i$  is the production ‘probability’ of the i-th cluster by neutron irradiation,  $G$  refers to the collective generation rates,  $A$  indicates the collective annihilation rates,  $T$  refers to generation or annihilation by trapping events, and  $E$  refers

to generation or annihilation by emission events. The detailed construction of the

coupled system of ODEs is thus (for which  $\Lambda = [-NI, NV]$  is the prescribed phase space):

$$\frac{dC_i}{dt} = \phi \times P_i + \sum_{\substack{m+p=i \\ m,p \neq 0 \\ m,p \in \Lambda}} k_{m,p}^+ C_m C_p - \sum_{\substack{m \neq i \\ m \neq 0 \\ m,m+i \in \Lambda}} k_{m,i}^+ C_m C_i - k_i^- C_i \quad (5)$$

for  $i = NV$  or  $-NI$ , and

$$\frac{dC_i}{dt} = \phi \times P_i + \sum_{\substack{m+p=i \\ m,p \neq 0 \\ m,p \in \Lambda}} k_{m,p}^+ C_m C_p + k_{i+1}^- C_{i+1} - \sum_{\substack{m \neq i \\ m \neq 0 \\ m,m+i \in \Lambda}} k_{m,i}^+ C_m C_i - k_i^- C_i \quad (6)$$

for  $\frac{NV}{2} < i < NV$ , and

$$\frac{dC_i}{dt} = \phi \times P_i + \sum_{\substack{m+p=i \\ m,p \neq 0 \\ m,p \in \Lambda}} k_{m,p}^+ C_m C_p + k_{i+1}^- C_{i+1} - \sum_{\substack{m \neq i \\ m \neq 0 \\ m,m+i \in \Lambda}} k_{m,i}^+ C_m C_i - 2k_{i,i}^+ (C_i)^2 - k_i^- C_i \quad (7)$$

for  $2 \leq i \leq \frac{NV}{2}$ , and

$$\frac{dC_i}{dt} = \phi \times P_i + \sum_{\substack{m+p=i \\ m,p \neq 0 \\ m,p \in \Lambda}} k_{m,p}^+ C_m C_p + 2k_{-2}^- C_{-2} + \sum_{\substack{m > 2 \\ m \in \Lambda}} k_m^- C_m - \sum_{\substack{m \neq i \\ m \neq 0 \\ m,m+i \in \Lambda}} k_{m,i}^+ C_m C_i - 2k_{i,i}^+ (C_i)^2 \quad (8)$$

for  $i = 1$ , and

$$\frac{dC_i}{dt} = \phi \times P_i + \sum_{\substack{m+p=i \\ m,p \neq 0 \\ m,p \in \Lambda}} k_{m,p}^+ C_m C_p + 2k_{-2}^- C_{-2} + \sum_{\substack{m < -2 \\ m \in \Lambda}} k_m^- C_m - \sum_{\substack{m \neq i \\ m \neq 0 \\ m,m+i \in \Lambda}} k_{m,i}^+ C_m C_i - 2k_{i,i}^+ (C_i)^2 \quad (9)$$

for  $i = -1$ , and

$$\frac{dC_i}{dt} = \phi \times P_i + \sum_{\substack{m+p=i \\ m,p \neq 0 \\ m,p \in \Lambda}} k_{m,p}^+ C_m C_p + k_{i-1}^- C_{i-1} - \sum_{\substack{m \neq i \\ m \neq 0 \\ m,m+i \in \Lambda}} k_{m,i}^+ C_m C_i - 2k_{i,i}^+ (C_i)^2 - k_i^- C_i \quad (10)$$

for  $-\frac{NI}{2} \leq i \leq -2$ , and

$$\frac{dC_i}{dt} = \phi \times P_i + \sum_{\substack{m+p=i \\ m,p \neq 0 \\ m,p \in \Lambda}} k_{m,p}^+ C_m C_p + k_{i-1}^- C_{i-1} - \sum_{\substack{m \neq i \\ m \neq 0 \\ m, m+i \in \Lambda}} k_{m,i}^+ C_m C_i - k_i^- C_i \quad (11)$$

for  $-NI < i < -\frac{NI}{2}$ , where  $k^+$  is the forward reaction rate constant and  $k^-$  is the backward reaction rate constant, having the same expressions as the classic rate theory [41, 42], i.e.,

$$k_{m,p}^+ = 4\pi(r_m + r_p)(D_m + D_p), \quad (12)$$

$$k^- = k^+ C_0 \exp\left(-\frac{E_b}{k_B T}\right), \quad (13)$$

where  $r_m$  and  $r_p$  are the trapping radii of clusters  $m$  and  $p$ ,  $D$  is the diffusion coefficient of the reacting species,  $C_0$  is the atomic number density of the iron matrix,  $E_b$  is the binding energy of a single point defect to the cluster,  $k_B$  is Boltzmann's constant, and  $T$  is the temperature. Note that for emission ( $C \rightarrow A + B$ ), only those events in which at least one of the two products is a monomer (i.e., I or V) are considered since it is in general more energetically favorable for a cluster to emit a monomer than emit a dimer, trimer or multimer, which is consistent with previous models [28-30].

The external source of intrinsic point defects and the corresponding clusters is the neutron irradiation induced collision cascade occurring inside the iron samples exposed to the reactor environment. This generation term always exists during the neutron irradiation process and impacts the modeling results significantly, thus it is crucial to have an accurate predication of this damage production. In many previous cluster dynamic models [28, 29, 40, 41], the simple Frenkel pair point defect production mode has been applied without considering the generation of small defect clusters in displacement cascades. However, MD simulations [43-46] of cascades in BCC iron clearly show that energetic PKAs with kinetic energies greater than a few keV directly produce small interstitial and vacancy clusters rather than isolated Frenkel pairs. Xu et al. [40] discussed the applicability of Frenkel pair production versus intra-cascade cluster production in the modeling of 1 MeV krypton-ion irradiated molybdenum, concluding that the latter is the most applicable case. Therefore, here, intra-cascade cluster production is used to determine the defect production probability,  $P_i$ .

In our specific modeling of the neutron irradiation in HFIR, the PKA energy spectrum of neutron irradiation in iron was calculated by SPECTER [47, 48] (neutron damage calculations for materials under irradiations), the results of which are shown in Figure 1. The total displacements, created by the PKA were calculated using the Lindhard model [49], within which the kinetic energy,  $T$ , of a PKA is partitioned between electronic and nuclear stopping. The expression for the number of displacements is

$$v = \xi(T, Z) \left( \frac{T}{2E_d} \right), \quad (14)$$

where  $\xi(T, Z)$  is a function of  $T$  and  $Z$  (atomic number), and is used to describe the part of the PKA kinetic energy that is available to generate atomic displacements by elastic collisions.  $E_d$  is the displacement energy, taken as the reference value of 40 eV for iron [43]. This partitioning coefficient is computed by

$$\xi(T, Z) = \frac{1}{1 + 0.134Z^{2/3}A^{-1/2}(3.4\varepsilon^{1/6} + 0.4\varepsilon^{3/4} + \varepsilon)}, \quad (15)$$

$$\varepsilon = \frac{T}{2Z^2e^2/a}, \quad (16)$$

$$a = \frac{0.626a_{bohr}}{Z^{1/3}}, \quad (17)$$

where  $A$  is the atomic mass of the matrix element,  $a_{bohr}$  is Bohr radius, 0.529 Å, and  $e^2 = 14.4 \text{ eV}\cdot\text{Å}$ . Based on Equations (14) ~ (17), the total displacements (Frenkel pairs) can be calculated from the given PKA kinetic energy.

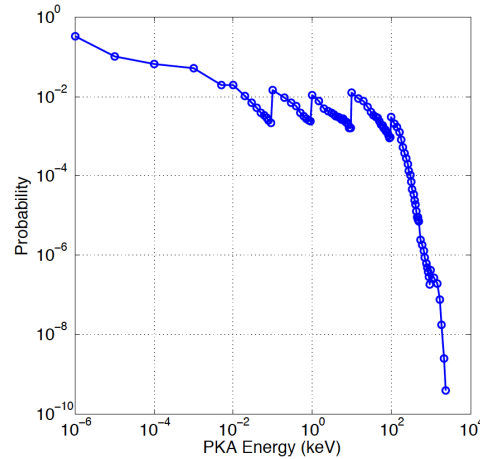


Figure 1. PKA spectrum in neutron irradiated iron in HFIR.

Xu et al., [40] summarized the fractions of total surviving point defects that are contained in small clusters  $I_1 \sim I_{20}$  and  $V_1 \sim V_9$  and the surviving efficiency of point defects for four cascade energy intervals starting from 1 keV, based on analysis of an MD cascade simulation database in BCC iron that was provided by Stoller et al. [43]. The survival efficiency,  $f$ , refers to the number of interstitials and vacancies that survive the rapid recovery stage of cascade evolution in MD simulations, as well as following the initial cascade aging when the remaining mobile interstitial and vacancy clusters diffuse through and away from the vacancy rich core of the cascade. In the MD stage of cascade healing/in-cascade recombination, Stoller et al., [43] reported that this survival efficiency varies from one at low PKA energy to about 1/3 for PKA energies greater than 10 keV. Wirth and co-workers [50, 51] used kinetic Monte Carlo simulations to evaluate the additional recombination during the initial interstitial diffusion stage

following a cascade and observed sufficient recombination occurring to reduce this value to about 0.4 for low energy PKAs and further to about 0.12 for PKA energies of 20 keV and above.

Consequently, the survival of point defects in the cascade,  $(\xi T / 2E_d) \times f$ , will be partitioned into small clusters according to the clustering fractions obtained from this combination of MD simulations [43, 44] with an initial stage of cascade aging [50, 51]. For those PKAs with  $\xi T < 1 \text{ keV}$ , only individual Frenkel pairs, i.e., isolated I and V, were added in the amount  $f \xi T / 2E_d$ . The numbers of clusters produced by all PKA energies are then multiplied by the corresponding probabilities. The resulting cluster production ‘probability’ in unit of  $1 / PKA$  listed in Table 2.

Now it is necessary to determine the cluster production rate with respect to a specific neutron flux. This requires the PKA production rate be specified. From SPECTER calculations, the displacement cross section of the neutron irradiation is also provided, which enables computation of the total displacement rate ( $R_d$ ) in iron, as defined in Equation (18),

$$R_d \left[ \frac{1}{\text{cm}^3 \cdot \text{s}} \right] = \phi \left[ \frac{1}{\text{cm}^2 \cdot \text{s}} \right] \sigma_d \left[ \text{cm}^2 \right] N \left[ \frac{1}{\text{cm}^3} \right], \quad (18)$$

where  $\phi = 3.5 \times 10^{15} [\text{neutron} / \text{cm}^2 / \text{s}]$ ,  $\sigma_d = 192 \text{ barn} = 1.92 \times 10^{-22} \text{ cm}^2$ , and  $N = 8 \times 10^{22} / \text{cm}^3$ . The displacement cross section for iron under neutron irradiation in HFIR has a low value due to the incorporation of thermal neutrons in the neutron flux energy spectrum, which in general do not cause direct displacements through elastic scattering.

Fortunately, there is another way to calculate the displacement rate, as defined in Equation (19),

$$R_d \left[ \frac{1}{\text{cm}^3 \cdot \text{s}} \right] = \lambda \left[ \frac{PKA}{\text{cm}^3 \cdot \text{s}} \right] P_d \left[ \frac{\text{displacements}}{PKA} \right], \quad (19)$$

where the displacements per PKA can be computed by the Lindhard model and the PKA spectrum as mentioned before.

Combining Equations (18) and (19) yields the PKA production rate,  $1.72 \times 10^{15} [PKA / \text{cm}^3 / \text{s}]$ . Thus, the intra-cascade cluster production probabilities can be obtained by multiplying the values in the third column of Table 2 with PKA production rate, and these values are noted in the last column of Table 2.

Table 2. Intra-cascade cluster production probabilities  $P_i$  in 1/PKA.

Type	Cluster Size	Production probability (1/PKA)	Production rate (1/cm <sup>3</sup> /s)
Interstitial Clusters	-20	0.0024	4.13×10 <sup>12</sup>
	-16	0.0048	8.26×10 <sup>12</sup>
	-12	0.0064	1.10×10 <sup>13</sup>
	-9	0.0144	2.48×10 <sup>13</sup>
	-8	0.0183	3.15×10 <sup>13</sup>
	-7	0.0413	7.10×10 <sup>13</sup>
	-6	0.0572	9.84 ×10 <sup>13</sup>
	-5	0.0838	1.44×10 <sup>14</sup>
	-4	0.1165	2.00×10 <sup>14</sup>
	-3	0.1794	3.08×10 <sup>14</sup>
	-2	0.3539	6.09×10 <sup>14</sup>
	-1	1.1215	1.93×10 <sup>15</sup>
Vacancy Clusters	1	1.8264	3.14×10 <sup>15</sup>
	2	0.5005	8.61×10 <sup>14</sup>
	3	0.1782	3.06×10 <sup>14</sup>
	4	0.1073	1.84×10 <sup>14</sup>
	5	0.0602	1.04×10 <sup>14</sup>
	9	0.0302	5.20×10 <sup>13</sup>

In the rate theory based reaction-diffusion cluster dynamics model, the mobile species determine the complication of the binary reactions, and correspondingly, the computational cost. In many previous reaction theory based models [28, 29, 41, 42], only V, SIA and di-SIA have been considered as mobile in order to simplify the model. However, experimental observations [52] have shown that interstitial loops containing a few to several hundreds of SIAs in BCC iron are mobile with nearly size-independent migration energies. These SIA clusters are predicted to be even more mobile in MD simulations [43, 50, 51, 53-56], in which the activation energies of the mobile SIA clusters are close to or even lower than the single SIA migration energy. Xu [40] et al., summarized the currently available expressions for the migration energies and the diffusivity pre-factors of interstitial clusters as a function of cluster size from MD

simulations, ab initio calculations and TEM experimental observations. Xu proposed a mobility parameter set for the prediction of microstructural evolution in krypton-ion irradiated molybdenum based on the simulations and experimental observation results available in the literature for BCC iron. In the present model of neutron irradiation of iron, all of the interstitial loops are considered mobile. Table 3 lists the set of mobility data chosen on an empirical basis by considering the various studies used for the modeling of Fe-a samples (high purity). The selected parameter set is quite similar to that chosen by Xu in a recent study [40].

Table 3. Mobility set for interstitial clusters/loops and single vacancy for the modeling of neutron irradiated Fe-a samples.

Cluster	V	I - I <sub>7</sub>	I <sub>8</sub>	I <sub>9</sub>	I <sub>10</sub>	I <sub>11</sub>	I <sub>12</sub>	I <sub>13</sub>	I <sub>14</sub>	I <sub>15</sub>	I <sub>n&gt;15</sub>
E <sub>m</sub> (eV)	0.75	0.34	0.45	0.50	0.55	0.65	0.75	0.80	0.9	0.95	1.1
D <sub>0</sub> (nm <sup>2</sup> /s)	1.37×10 <sup>11</sup>					1.37×10 <sup>11</sup> /n					1.37×10 <sup>11</sup> n <sup>-0.7</sup>

The energetics and expressions of V<sub>n</sub> and I<sub>n</sub> transitions (e.g., cluster dissolution) are consistent in almost all of the cluster dynamic models. The binding energies of SIA and single vacancy to the small clusters (up to 4) are obtained using ab initio calculations by Fu et al. [57]. For larger interstitial and vacancy clusters, an extrapolation method was used to calculate the required binding energies, based on the MD simulations of Soneda et al., [58], indicating that the formation energies of interstitial and vacancy clusters follow a 2/3 power law with increasing number of defects in the cluster.

#### Irradiation hardening model

As mentioned in the introduction, precise estimation of the increase of the yield strength induced by neutron irradiation relies on the establishment of a reliable relationship between the irradiation-induced defect density and the resolved shear stress required to move the dislocation through an obstacle field. The dispersed barrier-hardening model is used here to predict the increase of the yield strength. Equation (1) is the classical expression of the Orowan model and various corrections of this equation have been proposed, including (i) introducing the Kocks/Foreman and Martin statistical factor to convert the planar interparticle spacing to an effective interparticle spacing (i.e., 1.2 times the original value) and then allowing for finite particle size; (ii) using more refined estimates of the line tension; (iii) allowing for mutual interaction of the bowed-out segments of the dislocation on either side of the particle. Combing all these modifications for a set of particles of diameter *d*, Kelly [11] proposed the modified Orowan equation,

$$\Delta\tau_s = \alpha \frac{0.83\mu b}{\left[ (Nd)^{-0.5} - d \right]} \frac{\ln(d/r_0)}{2\pi(1-\nu)^{0.5}} \quad (20)$$

The  $\alpha$  factor has been included in Eq. (20) to indicate its correspondence with Equation (1). In Equation (20),  $\mu$  is the shear modulus, which is 82 GPa for BCC iron, and *b* is the magnitude of the  $a/2\langle 111 \rangle$  Burgers vector. *N* and *d* are the number density and

diameter of the defect clusters.  $r_0$  is the dislocation core radius, which is defined as the distance below which linear elasticity does not hold. The value of  $r_0$  is generally taken to be several times the Burgers vectors ( $b \sim 5b$ ).  $\nu$  is the Poisson ratio, which is approximately 1/3 for iron.

The obstacle strength is given by the factor  $\alpha$ . This value can vary between zero and one, and is strongly dependent on the types of defects. In pure iron under neutron irradiation, dislocation loops and nanovoids are the only two defect populations observed. All of the samples were fully annealed before being placed in the irradiation environment, therefore, it is reasonable to assume that the density of dislocations from the initial dislocation network is low compared to the density of prismatic loops created under neutron irradiation, and that its contribution to the radiation-induced yield stress change, or hardening, is negligible. In the present work, the increase of yield strength of the iron samples after neutron irradiation is exclusively ascribed to the existence of irradiation-produced vacancy cluster and interstitial loops, of which the  $\alpha$  values need to be identified.

The strength factor  $\alpha$  has been studied extensively using both experimental and modeling approaches for both voids and loops [19,59-63]. The hardening-contribution due to visible loops in vanadium alloys has been estimated by utilizing Equation (1) in combination with TEM measured loop density and size, giving  $\alpha$  values in the range from 0.40 to 0.50. Rice and Zinkle [19] also indicate that  $\alpha$  is a function of temperature. Similar experiments performed by Lambrecht and co-authors [59] show that  $\alpha$  values for dislocation loops can be as high as 0.7 in neutron irradiated pure iron but this value varies for different alloys. By combining PAS measurements with the tensile tests, they concluded that very small vacancy clusters contribute little to the hardening. Meanwhile, the strengthening effect of voids in iron has been investigated theoretically by many researchers [60-62], and these studies consistently indicate that voids are strong obstacles to dislocation motion. In the literature,  $\alpha$  is most often assumed to be a constant (e.g., 0.1 for loops and 0.16 for voids [63]) to describe the overall impeding resistance of the defects to the dislocation motion. However, it is reasonable to assume that the strengthening factor  $\alpha$  should be a function of the defect size, defect type, temperature, and possibly strain rate. Here, we assume that  $\alpha$  exclusively depends on the size of the defects since the tensile test conditions were the same. The exact functional form is unknown, but certain properties of the function are known. The strength of the defects should presumably monotonically increase with their size. It should reach a maximum value of unity for large defect clusters, and as the defect size approaches zero, it should reach a minimum value of zero. One such simple expression is thus

$$\alpha = 1 - \exp\left[-\left(\frac{d}{d_{ref}}\right)^n\right], \quad (21)$$

where  $d_{ref}$  is a reference defect size and  $n$  is the strength sensitivity to the defect size, which are further constrained such that  $\alpha$  is 0.1 for a loop size of 2 nm and 0.3 for a void size of 2 nm. The choice of these limits is based on the commonly used values of  $\alpha$  for loops and voids [63] and the comparison of the modeling results and experimental measurements. MD simulations [61, 62] reveal that voids are strong

obstacles when the size is larger than 2 nm. Moreover, loops act as slightly weaker obstacles compared to voids [63]. Consequently, 4 nm is assigned to  $d_{ref}$  and  $n$  is set equal to 1.5 and 3.3 for voids and loops, respectively. Figure 2 shows the calculated strength factor,  $\alpha$ , as a function of the diameter of interstitial and vacancy clusters, respectively, based on Equation (21).

Finally, we note that the increase of the critical shear stress cannot be directly compared to the experimental measurement. The Taylor factor (3.06 for non-textured BCC and FCC metals [64]) is routinely used to correlate the shear stress increase with the measured applied stress, which correspondingly has the form of

$$\Delta\sigma_y = M\Delta\tau_s, \quad (22)$$

where M is the Taylor factor.

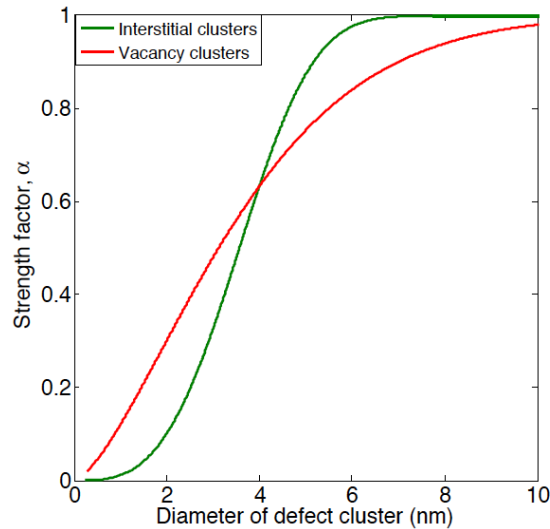


Figure 2. Strength factor,  $\alpha$ , as a function of the diameter of an interstitial (dislocation loop) or vacancy (cavity) cluster, respectively.

## RESULTS

### Predictions of vacancy and interstitial clusters produced in iron samples under neutron irradiation

Following the cluster dynamics model and parameters introduced in Section 3.1, the vacancy and interstitial cluster distributions have been simulated for the pure iron samples (Fe-a) under neutron irradiation. Note that the irradiation temperature during the irradiation of these samples was not constant due to placement variation within the hydraulic tube facility. A temperature gradient exists, for which the temperature varies from 333K to 373K, consistent with the experimental conditions described in Reference [18]. Therefore, the simulation results presented here have been performed at these two limiting temperatures. Figure 3 presents modeling results of the vacancy and interstitial cluster distributions as a function of irradiation dose. It can be seen that

interstitials undergo significant clustering at these doses and temperatures, while vacancies do not, which reflects that the interstitials are much more mobile than vacancies. By comparing Figure 3 (a) and (b), one can see that clustering of both interstitials and vacancies is larger at the slightly higher temperature at 373 K. As mentioned in the introduction, it is crucial to have precise predictions of interstitial and vacancy cluster distribution to determine the irradiation hardening. Thus the current cluster dynamics modeling results must be verified by experimental measurements before being used within the hardening model.

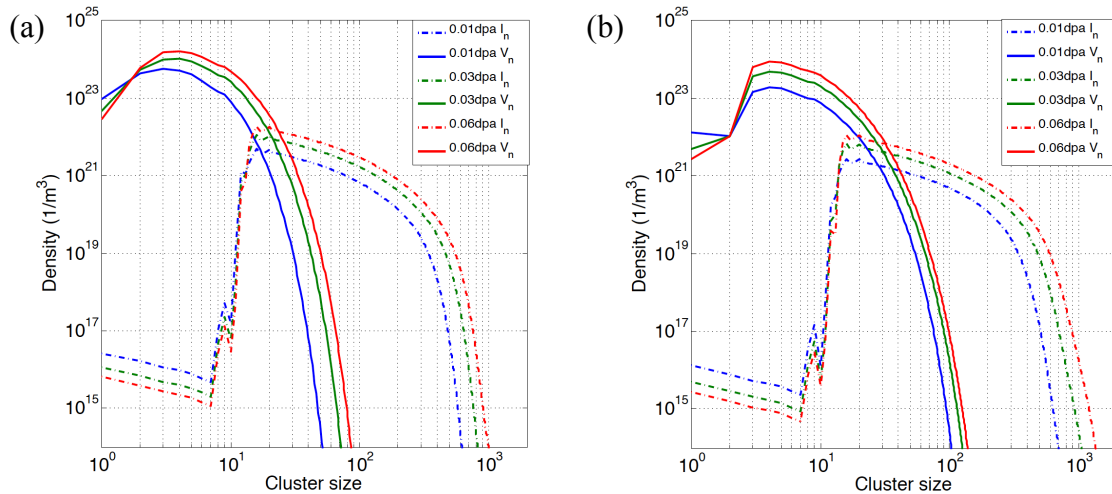


Figure 3. Model predicted volumetric density of interstitial and vacancy clusters plotted as a function of cluster size ( $n$ , # of point defects in the cluster) at (a) 333K and (b) 373K for Fe-a samples following selected radiation doses (0.01 dpa, 0.03 dpa, and 0.06 dpa).

Eldrup et al., [36] used PAS to obtain information on the vacancy cluster populations in pure iron (Fe-a) after these same neutron irradiation conditions. In the quantitative analysis, the measured lifetime spectra for the irradiated Fe-a samples were resolved into five lifetime components, four of which have fixed lifetimes: 200, 300, 400, and 500 ps, equivalent to three dimensional vacancy clusters with a size of about 0.35, 0.54, 0.73, and > 1.0 nm in diameter, respectively. The application of the trapping model to the measured positron lifetime spectra was used to obtain the density of different defect clusters, providing a rough size distribution of vacancy clusters for Fe-a under various irradiation conditions, shown in Figure 4. The total density of vacancy clusters for each irradiation dose level can thus be obtained by summing the concentrations of different defects, indicated in Figure 5. The output from the model predictions, similar to that shown in Figure 3 but at an appropriate dose level, can be easily analyzed to extract the quantities that are acquired in the experiments so that direct comparisons can be drawn between the modeling predictions and the PAS measurement. For example, the total volumetric density of vacancy clusters can be obtained by summing over different defects, and the size distribution can be obtained by binning the defects into various size intervals and summing the volumetric densities within each bin. In Figure 4, the modeling results of the vacancy cluster size distributions at 333K and 373K are plotted together with the PAS measurements for three different irradiation doses of 0.0001, 0.0009 and 0.009 dpa. Generally, the modeling results show a similar trend of

increasing density of increasing cluster sizes with increasing radiation dose, as the experimental measurements. For the neutron irradiation doses of 0.0001 dpa and 0.0009 dpa, the PAS experimental analysis indicates that most of the vacancy clusters have a size less than 3.5 nm and the densities decrease with increasing sizes. The models reproduce these features except the modeling predictions at 0.0009 dpa at 373K, for which the vacancy clusters of intermediate sizes have a slightly larger volumetric density. When the neutron dose increases to 0.009 dpa, the PAS results show that the vacancy clusters with diameters in a range of 0.35-0.54 nm are dominant in the measured positron lifetime spectra, which is also in good agreement with the model predictions. Figure 5 shows a comparison of the total density of vacancy clusters obtained from the PAS measurements with the modeling predictions at the two limiting temperatures. Overall, the modeling predictions at these two temperatures bracket the PAS measurements, and are in quite good agreement when considering the uncertainty within the experimental measurements.

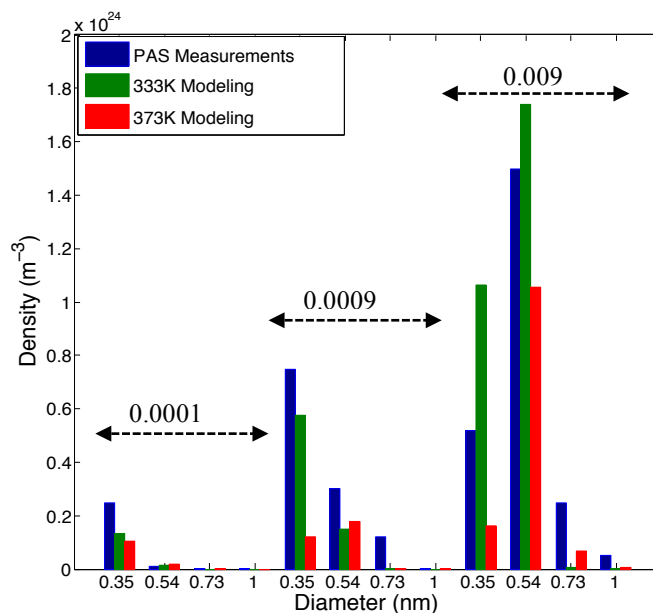


Figure 4. Comparison of modeling predictions and experimental measurements of size distribution of vacancy clusters in Fe-a at different irradiation dose levels of 0.0001, 0.0009 and 0.009 dpa.

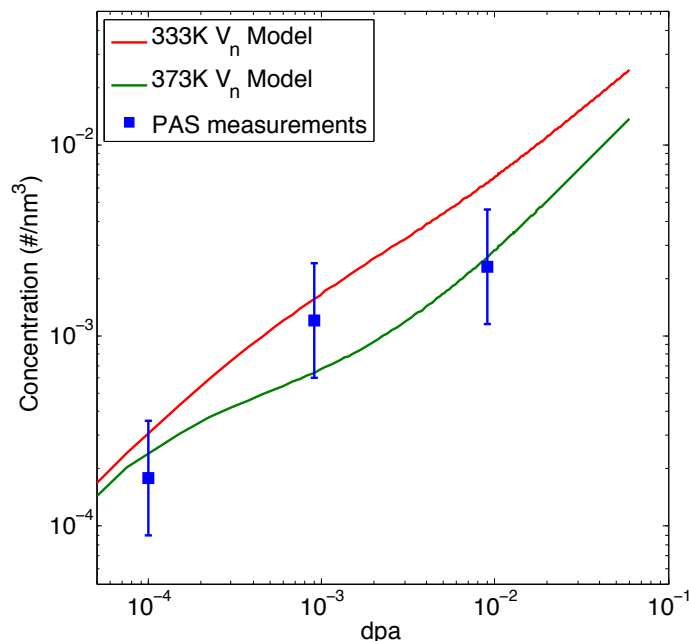


Figure 5. Comparison of modeling predictions and PAS measurements of the total density of vacancy clusters in Fe-a at different irradiation doses.

The PAS thus provide a comparison and verification of the vacancy cluster distribution predicted by the cluster dynamic model based on reaction-diffusion rate theory. As well, it is important to validate the modeling prediction of the interstitial cluster distribution. Reference [36] describes the results of a TEM investigation on the neutron irradiated Fe-a samples performed to characterize the density of the interstitial type dislocation loops. It is important to note that not all of the interstitial clusters, but only those with a diameter exceeding the TEM resolution limit, can be observed by TEM. Furthermore, not all dislocation loops will be resolvable in the TEM due to the **g·b** invisibility criteria [65]. The resolution limit in such TEM experiments varies slightly with material condition as well as TEM operating conditions, but is generally in the range of 1.0-1.6 nm. In BCC iron, a 1.4 nm diameter corresponds to a 32-member interstitial cluster ( $I_{32}$ ) of 2-D planar shape, and a 1.6 nm diameter corresponds to  $I_{42}$ . This implies that the comparison of the modeling results and the experimental observations will be sensitive to the choice of the TEM resolution limit. Given the overall interstitial cluster distributions shown in Figure 3, a straightforward calculation is performed to obtain the total density of the visible interstitial clusters by summing up the density of the defect clusters with sizes that exceed the TEM resolution limit. Figure 6 (a) lists the TEM observations and the modeling results at two different neutron irradiation temperatures for four different TEM resolution limits. Although there are some discrepancies between the modeling and TEM measurements, the order of the magnitude of the interstitial cluster densities are generally comparable, and within the experimental error [36]. It is

noted that the lower the TEM resolution limit (larger diameter for the smallest observable loop), the closer the experimental measurements and the modeling results are. Also, the modeling predictions at 373 K agree slightly better with the experimental observations. Another important parameter for the validation of the developed model is the average size of dislocation loop, which is obtained from weighted average of visible interstitial clusters. The comparison between modeling predictions and experimental observations [66] is shown in Figure 6 (b) and a quite good agreement is acquired.

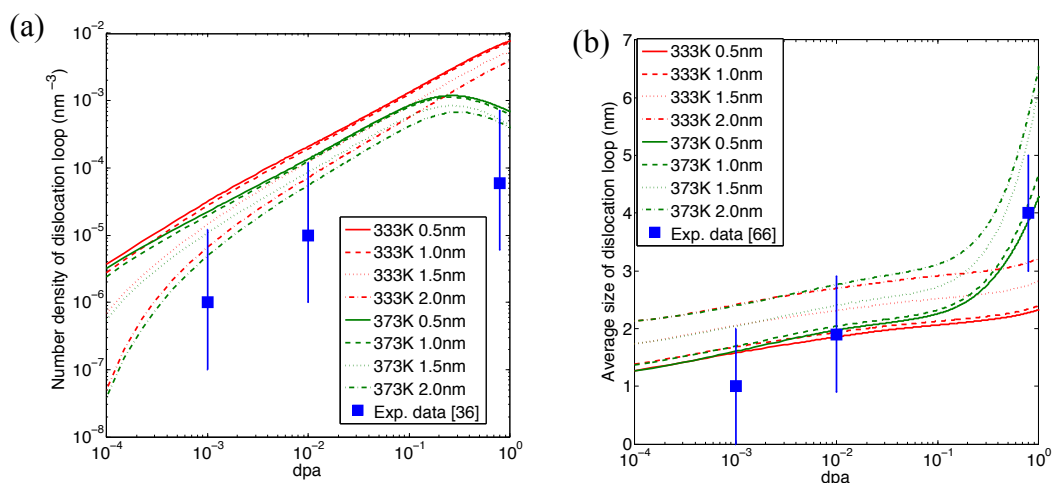


Figure 6. Cluster dynamics modeling predictions of (a) interstitial-type dislocation loop density and (b) average size of the visible dislocation loop for 4 different TEM resolution limits (0.5 nm, 1.0 nm, 1.5 nm, and 2.0 nm) at two different neutron irradiation temperatures for the Fe-a samples, as compared to the TEM observations of Reference [36, 66].

Based on these comparisons, we can conclude that our cluster dynamic model is providing acceptable predictions of the vacancy and interstitial clusters distributions produced in the Fe-a samples exposed to neutron irradiation in HFIR.

For the Fe-b samples, it is most likely inappropriate to directly use the modeling results obtained for the Fe-a samples due to differences in the impurity content of these two samples, as listed in Table 1. It is well known that the existence of impurities changes the kinetics and energetics of the defect clusters. In a recent study, Hu et al., [31] showed the influence of impurities on helium-point defect interactions by comparing the thermal desorption spectra of two different batches of single crystalline iron samples. Changes to the migration energies and binding energies of some important small clusters were observed. Note that the discrepancies between the two batches of samples are quite similar to the current Fe-a and Fe-b samples, therefore, it is reasonable to apply a similar change in the mobility parameter set in order to simulate the neutron irradiated defect microstructure of the sample Fe-b. Table 4 lists the optimized migration energies of interstitial clusters/loops and single vacancy used to predict the defect distribution of the Fe-b samples after neutron irradiation.

Table 4. Mobility set for interstitial clusters/loops and single vacancy for the modeling of neutron irradiated Fe-b samples.

Cluster	V	I	I <sub>2</sub>	I <sub>3</sub>	I <sub>4</sub>	I <sub>5</sub>	I <sub>6</sub>	I <sub>7</sub>	I <sub>n&gt;8</sub>
E <sub>m</sub> (eV)	0.85	0.38	0.45	0.50	0.55	0.65	0.75	0.85	1.2
D <sub>0</sub> (nm <sup>2</sup> /s)	1.37×10 <sup>11</sup>				1.37×10 <sup>11</sup> /n				1.37×10 <sup>11</sup> n <sup>-0.7</sup>

Unfortunately, detailed experimental characterization results of the neutron irradiated Fe-b samples are not available, which limits the ability to directly compare and validate the modeling results. Here, we show the modeling predictions of the interstitial and vacancy clusters as a function of irradiation dose levels at the two-irradiation temperatures of 333 and 373 K, which are subsequently used to compute the increase of yield stresses. However, as mentioned in the introduction, tensile test data does exist for the Fe-b samples, and will be compared to the model predictions. Figure 7 shows the model predictions of the vacancy and interstitial clusters using the mobility parameter set listed in Table 4. The results have similar features with those of the Fe-a samples shown in Figure 3. The most significant difference is that the predicted interstitial cluster population in Fe-b has a smaller size distribution due to the slightly lower assumed mobility of interstitials as a result of the higher impurity concentration in this sample.

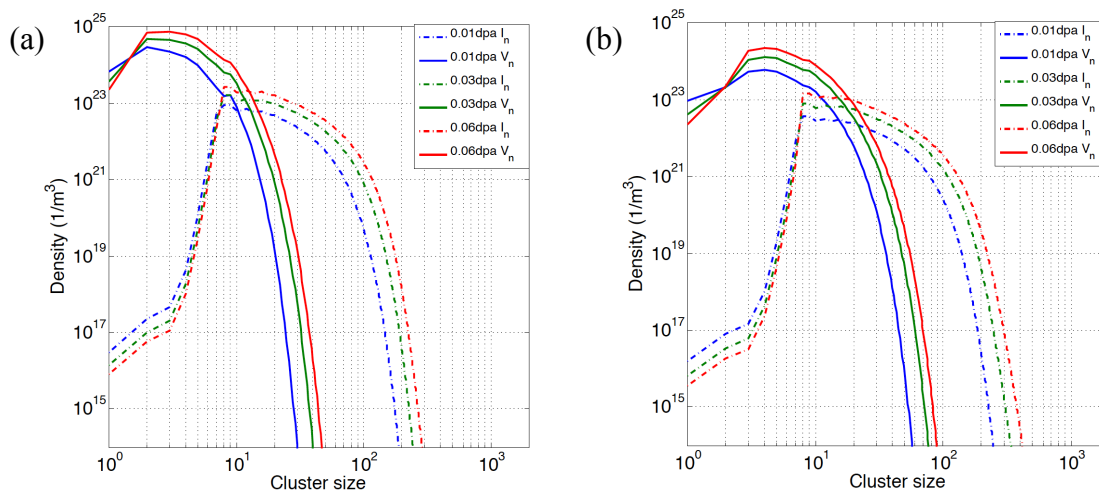


Figure 7. Model predicted volumetric density of interstitial and vacancy clusters as a function of cluster size at (a) 333K and (b) 373K for Fe-b samples following selected radiation doses (0.01 dpa, 0.03 dpa, and 0.06 dpa).

### Irradiation hardening prediction

As described in Section 3.2, the increase of yield strength is computed by Equation (20), for which all of the necessary parameters have been determined. Note that this equation is only valid for one specific defect cluster with a fixed diameter. However, as shown in Figure 3 and 7, the microstructure of the neutron-irradiated iron involves a continuous size distribution of both interstitial and vacancy clusters. In order to assess the hardening of a true irradiated microstructure, we must account for obstacles of different types, sizes and number densities. In most mechanistic models, the total yield strength increase under irradiation is obtained as the superposition of the different defects. This superposition can be performed using either a linear or a root-sum-square of the individual components. It is emphasized here that neither of these superposition laws is fully supported by any clear physical motivation. In the present work, interstitial loops and nanovoids are assumed to be the only two defect populations responsible for the radiation-induced hardening increment, and the total hardening increases will be given by the square root of the two contributions, as both loops and voids are assumed to be relatively strong obstacles, of similar strength, as suggested in Reference [27].

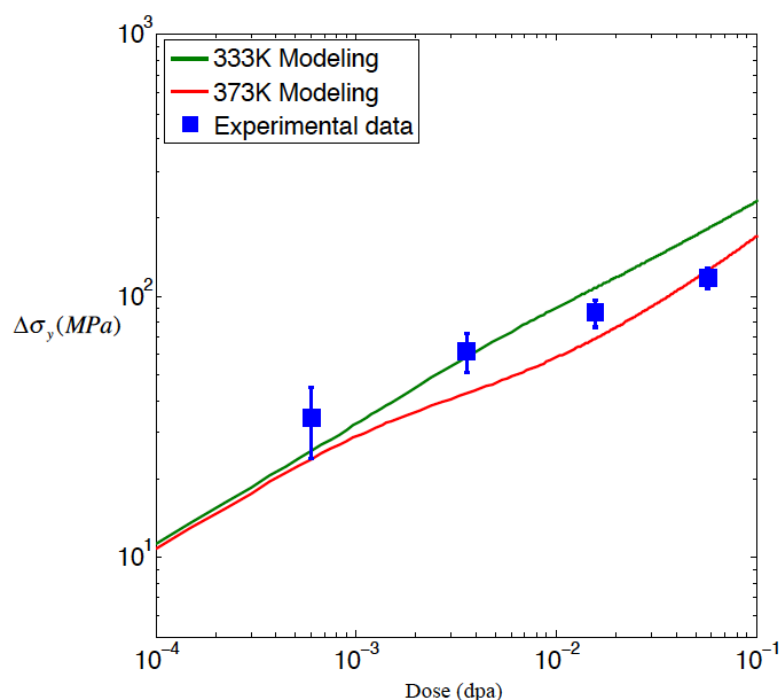


Figure 8. Hardening model predictions for the Fe-a sample at 333 and 373 K irradiation, as a function of dose (green and red lines, respectively) versus experimentally measured tensile data from Reference [18].

For the Fe-a high purity iron samples, the incorporation of the cluster dynamic modeling results, as shown in Figure 3, within Equations (20)-(22) leads to the prediction of yield strength increase. Figure 8 shows the irradiation hardening modeling results and the experimentally measured tensile data of yield strength increase for the Fe-a samples. The modeling results successfully bracket the measured yield strength increases at 0.0006 dpa, 0.0036 dpa, 0.0157 dpa, and 0.0574 dpa. The measured yield strength

increases are similar in the lower dose regime (less than  $10^{-3}$  dpa) as the modeling predictions at 333 K and 373 K. The 40 K difference in temperature does not impact the modeling prediction significantly until the neutron irradiation dose reaches slightly higher values, which is consistent with the loop and vacancy distributions predicted by the cluster dynamic model. In previous irradiation hardening studies, a simple power-law expression,  $\Delta\sigma_y = h\phi^n$ , where  $\phi$  is the radiation dose level, and  $h$  is a pre-factor, has been used to describe the hardening behavior in the low dose regime [12, 37]. At low doses below about 0.01 dpa, the exponent  $n$  has been measured to be about  $\frac{1}{2}$  for many metals [8, 20, 37, 67]. By applying this expression to the current model predictions, the exponent  $n$  can be determined to be 0.44, quite close to the previous values.

Table 5. Modeling results of the yield strength increase at two neutron irradiation temperatures and the tensile test measurements for two neutron irradiation conditions for Fe-b iron samples.

Dose (dpa)	0.0001	0.001
Tensile Tests (MPa)	13.2±5.5	27.5±5.5
333K (Model, MPa)	11.42	32.42
373K (Model, MPa)	10.94	29.06

The Fe-b samples contained higher level of impurities, which have been assumed to reduce the mobility of the mobile species and influence the predicted defect cluster distributions. The modeling predictions of the yield strength increase for the neutron irradiation doses of 0.1 and 1 mdpa are shown in Table 5 along with the experimental measurements. The model slightly underestimates the increase of the yield strength at 0.0001 dpa and slightly overestimates it at 0.001dpa. But, overall, the predicted yield strength increases at 333K and 373K is well matched with the measured tensile test results, and are certainly within the range of the estimated measurement error. The limited experimental data obtained on the Fe-b samples prevents further comparison with the model predictions.

It is emphasized that the current modeling results and experimental comparison are focused on the low dose and low irradiation temperature regime. Overall, the experimental measurements and the modeling predictions are in good agreement within the range of experimental uncertainty.

## DISCUSSION

Irradiation hardening is an extremely complicated problem resulting from the complex microstructures, which develop under neutron irradiation. In the present study, the dispersed barrier-hardening model provides some insights into the relationship between the yield strength increase and the primary microstructure evolution of two high purity iron samples under neutron irradiation. However, this simple model is not sufficient to

capture the contribution from every possible defect and to reveal all underlying mechanisms. As well, some uncertainties exist in the model, and it is necessary to evaluate these key factors, e.g., the dislocation core radius, the choice of the superposition law, the applicability of the model in the high dose regime, etc., which might significantly impact the results.

The value for the dislocation core radius,  $r_0$ , shown in Equation (20), of  $2b$  has been used in this work, and provides the best agreement between the experimental data and modeling predictions. However, the dislocation core radius has no recommended theoretical value, and is typically discussed with values from  $1b$  to  $5b$  [63], which makes it important to indicate the susceptibility of the predicted yield strength increase to  $r_0$ . Here, the modeling case of high purity iron under neutron irradiation at 333K is taken as an example to show how the model predictions of yield strength increase vary when using different  $r_0$ , as shown in Figure 9. When the radiation dose is lower than 7 mdpa, the predicted yield strength increase is almost independent of the dislocation core radius. The modeling results using  $r_0=2b$  are smaller than those using  $3b$  and  $4b$  when the radiation dose begins to exceed 7 mdpa. By 0.1 dpa, the predicted yield strength increase using a cut-off radius of  $2b$  is approximately 25% smaller than the value using either  $3b$  or  $4b$ . However, overall, the variation of dislocation cutoff radius,  $r_0$  does not significantly change the model predictions of the yield strength increase within the studied dose range.

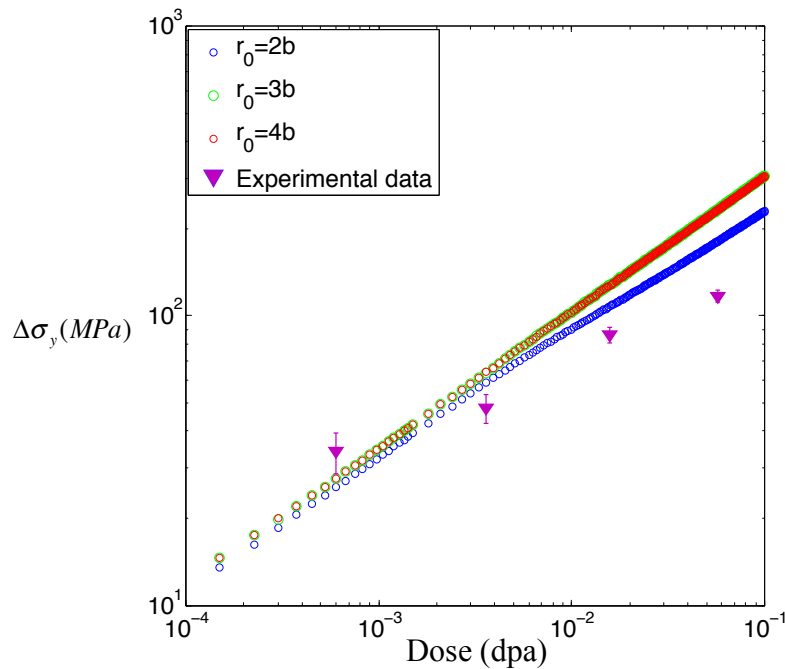


Figure 9. Model predictions of the yield strength increase of the Fe-a iron samples following neutron irradiation at 333 K, as a function of dislocation core radius sets as compared with the experimental measurements from Reference [18].

In Section 4.2, the root-sum-square superposition law was used to integrate the contributions from each interstitial cluster. Since the interstitials have long-range strain fields, the interactions between them are strong and it is possible to argue that a linear

superposition law might be more appropriate. Figure 10 shows a comparison of the model predictions resulting from these two different superposition laws for the neutron irradiated Fe-a iron sample at 333 K. It is obvious that the use of a linear superposition law overestimates the yield strength increase at irradiation doses above about 5 mdpa. Thus, given the good agreement between the predicted vacancy and interstitial cluster populations with the experimental PAS and TEM characterization discussed in Section 4.1, we conclude that the root-sum-square superposition law is most appropriate to predict the yield strength increases in the present study, which is consistent with the analysis by Lambrecht [59].

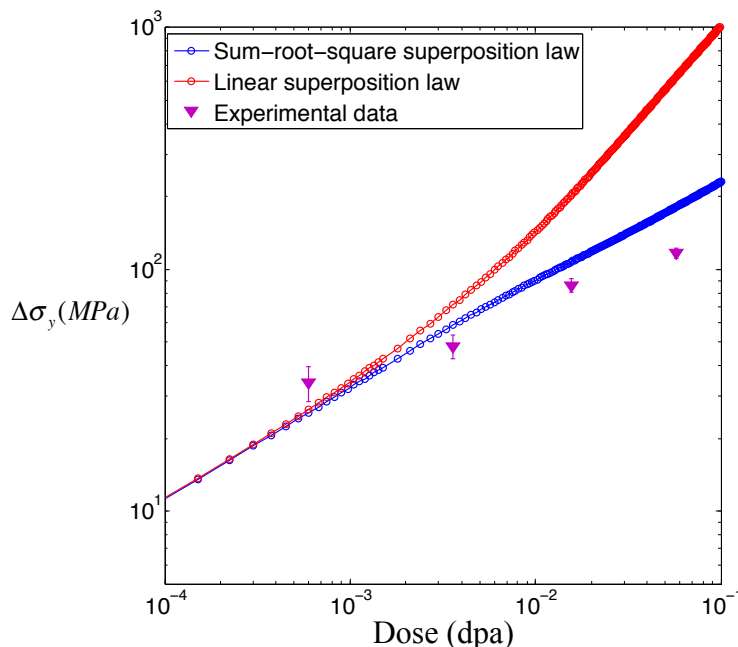


Figure 10. Model predictions of the yield strength increase for root sum square versus linear superposition laws applied to simulations of the neutron irradiated Fe-a iron sample at 333 K as compared with the experimental measurements from Reference [18].

As mentioned in Section 4.2, the present model is focused on the low irradiation dose regime, and thus it is not entirely clear the extent to which the current model is applicable to predicting higher radiation dose microstructure evolution and yield strength changes. Neutron irradiation continuously introduces point defects and defect clusters, which undergo diffusion-driven evolution dictated by the evolving radiation-damaged microstructure. As shown in Figures 3, 4 and 7, the model predicts that the vacancy and interstitial cluster size distribution continues to grow to larger size with increasing irradiation dose. Consequently, the average size and concentration of the vacancy and interstitial clusters are both increasing. However, this process will not continue forever. Equilibrium will be achieved at some point, when the collective generation and annihilation rates of vacancy and interstitial clusters equilibrate. Therefore, a saturation of the average size and concentration of the defect clusters can be expected to occur. Experimentally, a tendency towards saturation is observed when considering the mechanical property changes, such as yield strength increases [7, 18,

68], but not observed for dimensional stability such as swelling [69, 70]. However, the experimental data at high neutron exposure conditions is quite limited and there does not currently exist a consensus with respect to the tendency to saturate the radiation-defect microstructure or the resulting property changes.

However, given that the increase of yield strength is ascribed to the radiation-produced defect clusters, and the previous paragraph argues for a saturation of the defect cluster evolution; the saturation in radiation-induced defect clusters will also produce a saturation of the yield strength increase. Here, the modeling example of the low purity, Fe-b sample irradiated at 333K is taken as an example to show the model predictions of higher dose behavior, as shown in Figure 11. The model predicts that  $\Delta\sigma_y$  begins to saturate at a dose of about 2 dpa, with complete saturation by about 20 dpa. However, tensile tests indicate that the irradiation dose for this transition is around 0.05 dpa [18], much less than the model prediction. Moreover, the saturation value of  $\Delta\sigma_y$  predicted by the cluster dynamics model is around  $10^4$  MPa, which is almost two orders of magnitude larger than the strength increase experimentally measured in Reference [18].

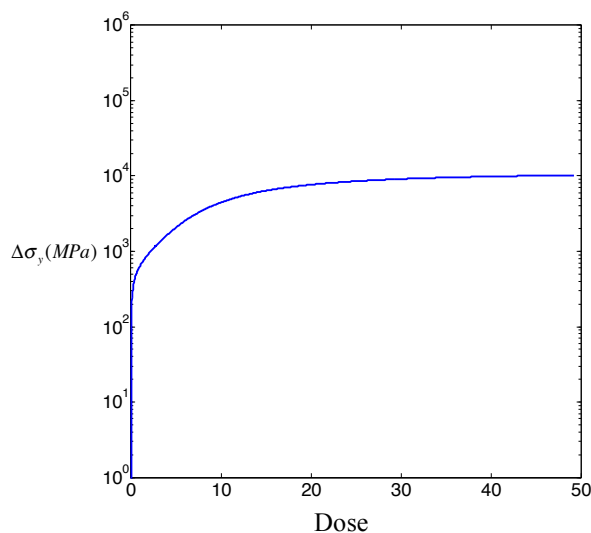


Figure 11. Model prediction of the yield strength increase as a function of irradiation dose for the Fe-b sample irradiated at 333 K.

We presume that this significant over-prediction of the model in the high dose regime is due to the complexity of the radiation-damaged microstructure and the corresponding irradiation hardening combined with the simplifying assumptions used in the model. For instance, plastic instability at yield and dislocation channel deformation can influence the transition from the low to high dose regime [18, 71, 72], and are not explicitly included in the dispersed barrier-hardening model. Additionally, it is clear that a spatially uniform defect cluster distribution, as predicted by a mean-field reaction-diffusion cluster dynamics model will not be reliable at high doses. Numerous experiments have shown the formation of spatially correlated dislocation loop microstructures in the form of rafts [36, 66], which begin to be observed at dose levels on the order of 1 dpa. Likewise, MD simulations [73, 74] indicate that as defect cluster volume fraction increases (and the inter-defect spacing decreases) at high radiation

doses, it is more likely that the defects in a newly produced displacement cascade will react with the existing clusters at the expense of new clusters, essentially promoting recombination or clustering reactions that marks a steady-state behavior and limits nucleation of new defect clusters. These effects are not included in the current model, and thus it is easy to see how the cluster dynamics model could over-estimate the defect cluster populations at high dose. Consequently, the predicted yield strength increase is over-estimated. Therefore, it is emphasized here that the current model is only applicable in the low dose regime prior to the occurrence of significant spatial correlation effects on the radiation-induced defect cluster microstructure including cascade overlap. Future efforts must be dedicated to better defining the spatial distribution of radiation-induced microstructure required to parameterize and fit spatially-dependent models of neutron-induced damage evolution and property changes.

## CONCLUSION

The neutron irradiation hardening behavior of two different, high purity polycrystalline iron samples at low dose and low irradiation temperature was modeled by applying a cluster dynamics model based on reaction-diffusion rate theory and the dispersed barrier hardening model. The evolution of the microstructure in terms of interstitial cluster type dislocation loops and nanovoids was simulated by the cluster dynamics model, of which the predictions of vacancy clusters and interstitial loops were validated by available PAS and TEM data, respectively. The dispersed barrier hardening model was used to correlate the defects with the increase of the yield strength by applying a continuous strength factor  $\alpha$  as a function of defect size. Overall, the modeling results compare quite well to the experimental observations in the low dose regime, and provide insight into the underlying microstructure – property relationships. Furthermore, we have assessed the impact of the dislocation core radius and the model for superposition of the individual strengthening contributions within the dispersed barrier-hardening model, and find that a core radius of  $2b$  and a root sum square superposition law are most appropriate for the current iron data at dose levels below 0.1 dpa. In considering the applicability of the model to predict radiation damage in the high dose regime, it is clear that spatially dependent modeling is required to accurately predict the saturation behavior of yield strength changes observed experimentally at higher dose levels. In the future, more experimental data, including the spatial distribution of defect clusters, are necessary to further verify the prediction of the defect cluster distributions obtained from the cluster dynamics model and to correctly model high dose phenomena.

## ACKNOWLEDGE

The aid and technical insight of Kurt A. Terrani and Yutai Katoh at ORNL is gratefully acknowledged, as is financial support from the U.S. Department of Energy, Office of Fusion Energy Sciences under grant DE-FG02-04GR54750 and the U.S. Department of Energy, Office of Nuclear Energy's Nuclear Energy University Programs (NEUP).

## REFERENCES

- [1] E. E. Bloom, *J. Nucl. Mater.* **258-263** (1998) 7.
- [2] K. L. Murty, *JOM* **53**(7) (2001) 8.
- [3] G. R. Odette and G. E. Lucas, *JOM* **53**(7) (2001) 18.
- [4] S. J. Zinkle and N. M. Ghoniem, *Fusion Eng. Des.* **51-52** (2000) 55.

- [5] C. E. Ells and C. D. Williams, *Trans. JIM* **9** (1968) 214.
- [6] R. P. Tucker and M. S. Wechsler, *Radiat. Eff.* **3** (1970) 73.
- [7] M. J. Makin and F. J. Minter, *Acta Metall.* **8** (1960) 691.
- [8] K. L. Murty and D. J. Oh, *Scr. Metall.* **17** (1983) 317.
- [9] B. N. Singh, A. J. E. Foreman, and H. Trinkaus, *J. Nucl. Mater.* **249** (1997) 103.
- [10] A. H. Cottrell and R. J. Stokes, *Proc. R. Soc. A* **233** (1955) 17.
- [11] P. M. Kelly, *Int. Metal. Rev.* **18** (1973) 31.
- [12] T. H. Blewitt, et al., *J. Nucl. Mater.* **2** (1960) 277.
- [13] J. V. Sharp, *Phil. Mag.* **4** (1967) 77.
- [14] J. V. Sharp, *Acta Metall.* **22** (1974) 449.
- [15] Y. Dai, et al., *J. Nucl. Mater.* **212-215** (1994) 393.
- [16] B. N. Singh, et al., *J. Nucl. Mater.* **299** (2001) 205.
- [17] M. Victoria, et al., *J. Nucl. Mater.* **276** (2000) 114.
- [18] T. S. Byun and K. Farrell, *J. Nucl. Mater.* **326** (2004) 86.
- [19] P. M. Rice and S. J. Zinkle, *J. Nucl. Mater.* **258-263** (1998) 1414.
- [20] A. Seeger, in: Proc. 2<sup>nd</sup> UN Int. Conf. on Peaceful Uses of Atomic Energy, Geneva, Sept. 1958, Vol. 6, p. 250.
- [21] E. Orowan, *Nature* **149** (1942) 643.
- [22] E. Orowan, Dislocations in Metals (AIME, New York, 1954) p. 131.
- [23] A. Arsenlis, et al., *Phil. Mag.* **84** (2004) 3617.
- [24] J. S. Robach, et al., *Phil. Mag.* **83** (2003) 955.
- [25] U. F. Kocks, *Mater. Sci. Eng.* **27** (1977) 291.
- [26] C. Pokor, et al., *J. Nucl. Mater.* **326** (2004) 30.
- [27] C. Deo, et al., *J. Nucl. Mater.* **377** (2008) 136.
- [28] D. H. Xu and B. D. Wirth, *Fusion Sci. Technol.* **56** (2009) 1064.
- [29] D. H. Xu and B. D. Wirth, *J. Nucl. Mater.* **403** (2010) 184.
- [30] D. Xu, X. Hu, and B. D. Wirth, *Appl. Phys. Lett.* **102** (2013) 011904.
- [31] X. Hu, D. Xu, and B. D. Wirth, *J. Nucl. Mater.* **442** (2013) S649.
- [32] X. Hu, Gas Diffusion in Metals: Fundamental Study of Helium-Point Defect Interactions in Iron and Kinetics of Hydrogen Desorption from Zirconium Hydride, Ph.D. Thesis, University of California, Berkeley, 2013
- [33] T. Jourdan, et al., *J. Nucl. Mater.* **444** (2014) 298.
- [34] S.J. Golubov, et al., *Philos. Mag. A* **81** (2001) 643.
- [35] A. Gokhman and F. Bergner, *Radiat. Eff. Defects Solids* **165** (2010) 216.
- [36] M. Eldrup, et al., *J. Nucl. Mater.* **307-311** (2002) 912.
- [37] K. Farrell and T. S. Byun, *J. Nucl. Mater.* **318** (2003) 274.
- [38] K. Farrell and T. S. Byun, Tensile properties of candidate SNS materials after irradiation in two neutron areas in the LANSCE accelerator, SNS/TR-211, Oak Ridge National Lab., January 2001.
- [39] T. S. Byun, et al., *J. Nucl. Mater.* **303** (2002) 34.
- [40] D. H. Xu, B. D. Wirth, M. M. Li, and M. A. Kirk, *Acta Mater.* **60** (2012) 4286.
- [41] C. J. Ortiz, M. J. Caturla, C. C. Fu, and F. Willaime, *Phys. Rev. B* **75** (2007) 100102.
- [42] C. J. Ortiz et al., *J. Appl. Phys.* **96** (2004) 4866.
- [43] R. E. Stoller, et al., *J. Nucl. Mater.* **251** (1997) 49.
- [44] R. E. Stoller, *J. Nucl. Mater.* **276** (2000) 22.
- [45] W. K. Phythian, R. E. Stoller, et al., *J. Nucl. Mater.* **223** (1995) 245.
- [46] R. E. Stoller, *J. Nucl. Mater.* **233-237** (1996) 999.
- [47] L. R. Greenwood, R. K. Smither, SPECTER: Neutron Damage Calculations for Materials Irradiations, ANL/FPP-TM-197 Report, Argonne NL, January 1985;
- [48] L. R. Greenwood, *J. Nucl. Mater.* **216** (1994) 29.

- [49] M. T. Robinson. BNES nuclear fusion reactors. London: British Nuclear Energy Society; 1970.
- [50] B. D. Wirth, G.R. Odette, R.E. Stoller, *MRS Soc. Symp. Proc.* **677** (2001) AA5.2.
- [51] P. R. Monasterio, B. D. Wirth, and G. R. Odette, *J. Nucl. Mater.* **361** (2007) 127.
- [52] K. Arakawa, et al., *Science* **318** (2007) 956.
- [53] Yu.N. Osetsky, et al., *Phil. Mag.* **83** (2003) 61.
- [54] C. C. Fu, et al., *Phys. Rev. Lett.* **92** (2004) 175503.
- [55] B. D. Wirth, G. R. Odette, D. Maroudas, and G. E. Lucas, *J. Nucl. Mater.* **244** (1997) 185.
- [56] J. Marian, et al., *Phys. Rev. B* **65** (2002) 144102.
- [57] C. C. Fu and F. Willaime, *Phys. Rev. B* **72** (2005) 064117.
- [58] N. Soneda, and T. Diaz de la Rubia. *Phil. Mag. A* **78** (1998) 995-1019.
- [59] M. Lambrecht, et al., *J. Nucl. Mater.* **406** (2010) 84.
- [60] R. O. Scattergood and D. J. Bacon, *Acta Mater.* **30** (1982) 1665.
- [61] Yu.N. Osetsky and D. J. Bacon, *J. Nucl. Mater.* **323** (2003) 268.
- [62] Yu.N. Osetsky and D. J. Bacon, *Phil. Mag.* **90** (2010) 945.
- [63] G. S. Was. Fundamentals of Radiation Materials Science: Metals and Alloys, New York: Springer; 2007.
- [64] R. E. Stoller and S. J. Zinkle, *J. Nucl. Mater.* **283-287** (2000) 349.
- [65] M. Li, et al., *Phil. Mag.* **92** (2012) 2048.
- [66] S. J. Zinkle and B. N. Singh, *J. Nucl. Mater.* **351** (2006) 269.
- [67] A. Okada, et al., *J. Nucl. Mater.* **141-143** (1986) 907.
- [68] J. E. Pawel, et al., *J. Nucl. Mater.* **239** (1996) 126.
- [69] F. A. Garner, M. B. Toloczko, and B. H. Sencer, *J. Nucl. Mater.* **276** (2000) 123.
- [70] S. J. Zinkle and G. S. Was, *Acta Mater.* **61** (2013) 735.
- [71] S. J. Zinkle, *J. Nucl. Mater.* **150** (1987) 140.
- [72] S. J. Zinkle, *Radiat. Eff. Defects Solids* **148** (1999) 447.
- [73] H. L. Heinisch and B. N. Singh, *J. Nucl. Mater.* **271-272** (1999) 46.
- [74] Y. Satoh, I. Ishida, T. Yoshiie, and M. Kiritani, *J. Nucl. Mater.* **155-157** (1988) 443.

## 8.6 Molecular Dynamics Modeling of Atomic Displacement Cascades in 3C-SiC — G. D. Samolyuk, Y. N. Osetskiy and R. E. Stoller (Oak Ridge National Laboratory)

**EXTENDED ABSTRACT** - paper submitted to J. Nucl. Mater. after ICFRM-16.

Designing silicon carbide components for fusion reactor blankets requires a basic understanding of defect formation and evolution, and the associated property changes. Molecular dynamics irradiation cascade simulations were carried out in SiC at energies of 10 and 50 keV and a range of temperatures with the widely used Tersoff interatomic potential [1]. The radiation-induced point defects in SiC consist of interstitials (I) and vacancies (V) of both carbon and silicon, as well as antisite defects of C on a Si site and Si on a C site. The results indicated that in-cascade recombination was much lower than in metals. For example, the ratio of defects at the peak time to the number of stable defects at ~10 picoseconds is about 2 in SiC and more than 100 in metals such as iron. About half of the carbon V-I pairs are apparently separated by a distance less than a lattice parameter, and would normally be expected to recombine. In order to understand this lack of recombination, the energy landscape in the region of a carbon interstitial was analyzed using the interatomic potential employed in these MD simulations and compared with first principles calculations using density functional theory (DFT). Both the Tersoff potential and an alternate modified embedded atom method potential reveal a barrier to recombination which is much higher than the DFT results (Figure 1). The barrier obtained with the newer Gao and Weber (GW) potential [2] is closer to the DFT result but the overall energy landscape is significantly different.

In order to demonstrate the sensitivity of cascade recombination to the value of barrier recombination additional cascade simulations have been done with the Gao-Weber potential. Point defects in SiC consist of interstitials (I) and vacancies (V) of both carbon and silicon, as well as antisite defects of C on an Si site ( $C_{Si}$ ) and Si on a C site ( $Si_C$ ). The carbon defects predominate. In a contrast to Tersoff potential, the GW potential produces almost twice as many C vacancies and interstitials at the time of maximum disorder (~0.2 ps) but only about 25% more stable defects at the end of the simulation (Figure 2). The ratio of peak-to-stable defects is much higher for the GW potential. Only about 20% of the carbon defects produced with the Tersoff potential recombine during the in-cascade annealing phase, while about 50% recombine with the GW potential. Such a significant difference is caused by the fact that the energy barrier for carbon V-I recombination with the GW potential is much smaller than with the Tersoff potential barrier.

The number of defects at the end of cascade evolution is weakly temperature dependent for Tersoff potential but reduces with temperature for the GW potential. The difference is due to unphysically large migration barriers for Tersoff potential.

To conclude, GW gives a much more realistic description of cascade dynamics in SiC.

## REFERENCES

1. J. Tersoff, *Phys. Rev. B* **39** (1989) 5566–5568 .
2. F. Gao and W. J. Weber, *Nucl. Instr. Methods Phys. Res. B* **191** (2002) 504-508.

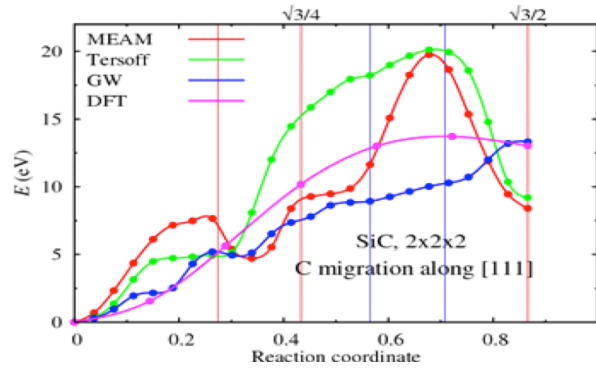


Figure 1. Energy of a carbon atom moved in the [111] direction.

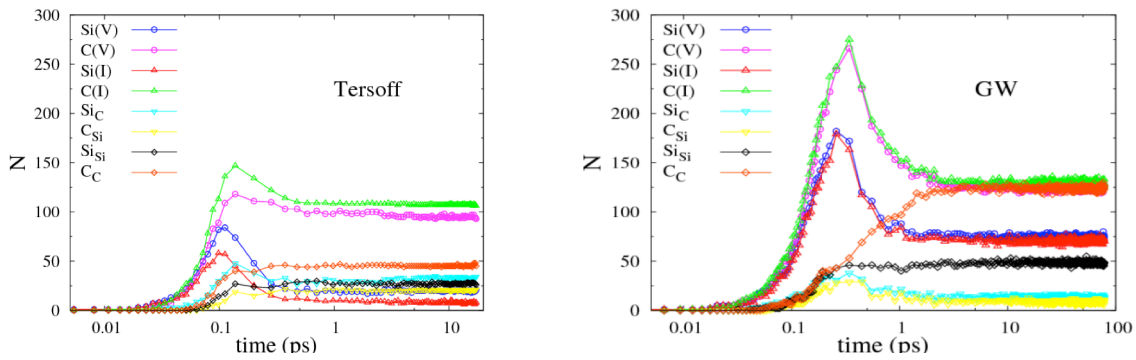


Figure 2. Time dependence of the number of point defects observed in MD displacement cascades.

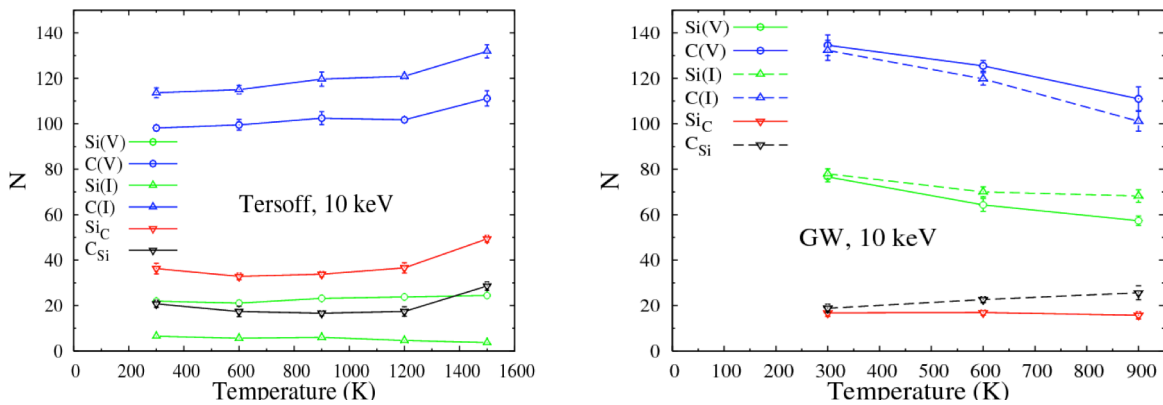


Figure 3. The number of defects at the end of cascade evolution.

## 8.7 First-Principles Calculations of Charge States and Formation Energies of Mg Transmutant in 3C-SiC — S. Y. Hu, W. Setyawan, W. Jiang, C. H. Henager, Jr. and R. J. Kurtz (Pacific Northwest National Laboratory)

### OBJECTIVE

To investigate the thermodynamic and kinetic properties of various transmutants in 3C-SiC using density functional theory.

### SUMMARY

We employed density functional theory to study the effect of electron potentials on charge states and the formation energies of Mg transmutant at different lattice sites in 3C-SiC. We found that  $Mg_C$ ,  $Mg_{TC}$  and  $Mg_{TSi}$  most likely have charge state +2 while  $Mg_{Si}$  prefers charge state -2. The results also show that the substitutional  $Mg_{Si}^{-2}$  has much smaller formation energy than that of  $Mg_C^{+2}$ , and interstitial  $Mg_{TC}^{+2}$  has lower formation energy than that of  $Mg_{TSi}^{+2}$ . These results imply that  $Mg_{Si}^{-2}$  is the most stable substitutional defect while  $Mg_{TC}^{+2}$  is the most stable interstitial defect in 3C-SiC. Since the quadrupole correction due to the spurious interactions between images of charged defects in periodic simulation cells was not taken into account, the calculated formation energies were overestimated. In future work we will examine the effect of quadrupole correction on the formation energies of defects. Additional studies on Al and Be transmutants in 3C-SiC are currently underway.

### PROGRESS AND STATUS

#### Introduction

Theoretical calculations by Sawan, *et al.*, [1] have predicted that at a fast neutron dose of ~100 dpa, there are ~0.5 at% Mg, ~0.15 at% Al, and ~0.2 at% Be generated in SiC through nuclear transmutation. These transmutants in SiC are expected to have potentially significant effects on phase stability, oxidation, transport properties (electrical and thermal conductivity), and elevated temperature mechanical properties. In our recent work [2], we calculated the formation and binding energies of neutral defects (intrinsic defects, Mg-related defects, and clusters) in 3C-SiC by density functional theory (DFT). The minimum energy paths and activation energies during point defect migration and small cluster evolution are studied using a generalized solid-state nudged elastic band (G-SSNEB) method with DFT energy calculations. Stable defect structures and possible defect migration mechanisms are identified. The evolution of binding energies during  $Mg_2Si$  formation demonstrates that the formation of  $Mg_2Si$  needs to overcome a critical nucleus size and nucleation barrier. It is also found that C vacancies promote the formation of the  $Mg_2Si$  nucleus. As we know, defects in semiconductor materials such as SiC might have different charge states, which depend on the local electron potentials. In order to determine thermodynamic and kinetic properties of defects in SiC, it is necessary to identify the charge states of defects and evaluate their effect on defect properties. This progress report presents possible charge states and formation energies of Mg transmutants in 3C-SiC, calculated from DFT. Further studies of Al and Be transmutants in 3C-SiC are currently underway.

<sup>1</sup> PNNL is operated for the U.S. Department of Energy by Battelle Memorial Institute under Contract DE-AC06-76RLO 1830.

## Simulation Method

The formation energy of a charged defect can be calculated using [3,4]

$$E^f(q) = E(q) - E_0(\text{SiC}) - \sum_{i=1}^m n_i \mu_i + q[E_{VBM} + (E^{core}(q) - E_0^{core}) + \mu_F] + E_{MP}(q), \quad (1)$$

where  $E(q)$  is the total energy of the defected crystal,  $q$  is the defect's charge,  $E_0$  is the total energy of the perfect crystal,  $\mu_i$  is the chemical potential of element  $i$ ,  $n_i$  is the difference of the number of element  $i$  ( $i = \text{Si, C, Mg, Be, Al, ...}$ ) in the defected crystal with respect to that in the perfect SiC, and  $E_{VBM}$  is the energy of the valence band maximum in the perfect crystal. The term  $(E^{core}(q) - E_0^{core})$  is an electronic potential shift, where  $E^{core}(q)$  and  $E_0^{core}$  represent the corelike electronic levels in the defected and perfect crystals, respectively, and  $\mu_F$  is the Fermi level measured from the valence band maximum  $E_{VBM}$ . The last term  $E_{MP} = -\frac{q^2 \alpha}{2\epsilon L} - \frac{2\pi q Q}{3\epsilon L^3}$  is the correction proposed by Makov and Payner [5] to correct the spurious interactions between images of charged defects in periodic simulation cells, where  $\alpha$  is the Madelung constant,  $\epsilon$  the static dielectric constant,  $Q$  its quadrupole moment, and  $L$  the size of the simulation cell.

The charge state of defects is given by the number of electrons (or holes) associated with the defect in addition to those obtained in a neutral DFT calculation of the defected cell. These additional electrons (or holes) are associated with states in the band gap. Possible charged states of a defect can be determined by adding electrons (or holes) into the defected cell until the added charges relax into the conduction (or valence) bands, i.e., the additional charges are no longer associated with the defect. The cases where the electrons (or holes) do not relax to the conduction (or valence) band lead to charged defects. The most stable charge state for a given defect is the one that has the lowest energy for a given electron potential  $\mu_e$  which is also called Fermi level  $\mu_F$ . The ionization level  $\mu_e^{q/q'}$  of a defect, which is the position of electron potential where the most stable charge state changes from  $q$  to  $q'$ , can be used to determine the possible charge states of a defect. If the ionization level  $\mu_e^{q/q'}$  falls in the band gap ( $0 < \mu_e^{q/q'} < E_{band}$ ), the charge states ( $q$  and  $q'$ ) are possible charge states of the defect. Ionization levels can be obtained by solving the following chemical potential equilibrium equation for the value of the electron chemical potential:

$$\begin{aligned} E(q) - E_0(\text{SiC}) - \sum_{i=1}^m n_i \mu_i + q[E_{VBM} + (E^{core}(q) - E_0^{core}) + \mu_e] + E_{MP}(q) \\ = E(q') - E_0(\text{SiC}) - \sum_{i=1}^m n_i \mu_i + q'[E_{VBM} + (E^{core}(q') - E_0^{core}) + \mu_e] + E_{MP}(q') \end{aligned} \quad (2)$$

We used the Vienna Ab-initio Simulation Package (VASP) [6] with accurate projector-augmented-wave (PAW) pseudopotentials [7] and the generalized gradient approximation (GGA) of PBE96 [8] to calculate the total energy, band gap  $E_{band}$ , and electron potential shift

$(E^{core}(q) - E_0^{core})$  of a charged defect in 3C-SiC. Initial convergence tests guided the choice of 500 eV for the energy cutoff,  $E_{cut}$ . For point defects in 3C-SiC crystals, a supercell  $2a_0 \times 2a_0 \times 2a_0$  (about 64 atoms) is used, with a  $4 \times 4 \times 4$  Monkhorst-Pack k-point mesh [9] for Brillouin-zone sampling. All structures are relaxed with energy convergence of 1 meV and 10 meV for the electronic and ionic relaxations, respectively. Full relaxation of lattice vectors and internal atom coordinates is performed in several runs. The relaxation runs are stopped when the energy difference between runs is less than 100 meV. After the relaxation runs, a static run (one self-consistent loop) is performed to eliminate numerical error associated with the plane-wave basis set incompleteness due to the change of the lattice vectors during the relaxations. For consistency with the majority of the reference literature, we calculate defect formation energies in SiC using the Si-rich limit, with the reference states (3C-SiC,  $Mg_2Si$ , Si(diamond)). So the chemical potentials  $\mu_i$  of C, Si and Mg can be calculated as

$$\begin{aligned}
 \mu_{Si} &= E_0(Si) \\
 \mu_C &= E_0(SiC) - \mu_{Si} \\
 \mu_{Mg} &= (E_0(Mg_2Si) - \mu_{Si}) / 2
 \end{aligned} \tag{3}$$

For the static dielectric constant  $\epsilon$  of 3C-SiC, we take the experimental value ( $\epsilon = 9.72$ ). The Madelung constant used here is 3.52, which was estimated for the  $2a_0 \times 2a_0 \times 2a_0$  supercell [10] [10]. In the calculations we only consider the dipole correction. The quadrupole correction usually is about one third of the dipole correction [11] which rapidly decreases with the increase of simulation cell size ( $L^{-3}$ ).

### Preliminary Results

The defect energies of Mg transmutant with different charges ( $q = -2, -1, 0, +1, +2$ ) at different lattice sites [Si, C, the tetrahedral center of Carbon atoms (TC), and the tetrahedral center of Si atoms (TSi)] in 3C-SiC have been calculated. The formation energy of a defect described by equation (1) is a linear function of electron potential  $\mu_F$  for a given charge state  $q$ . Figure 1 plots the formation energy  $E^f(q)$  of Mg with different charge states at different lattice sites as a function of electron potential  $\mu_F$ . Based on equation (2), the ionization level ( $q/q \pm 1$ ) can be determined by the intersection between two linear formation energy curves with charge  $q$  and  $q + 1$  (or  $q - 1$ ), respectively. The vertical dashed lines in Figure 1 shows the ionization levels for different defects. The segments defined by the intersections at ionization levels show the formation energy of the most stable charged defect for a given electron potential. We can see in Figure 1a that the substitutional Mg at C lattice ( $Mg_C$ ) prefers a charge state of +2 when  $\mu_F < 1.5eV$ . It prefers a charge state of -2 when  $\mu_F > 2.2eV$ . Figure 1b shows that the substitutional Mg at Si lattice prefers a charge state of -2 for the full range of electron potential  $0 < \mu_F < 2.4eV$ . The charge states of interstitial Mg at TC and TSi are similar to that of  $Mg_C$ . It is found that  $Mg_C$ ,  $Mg_{TC}$  and  $Mg_{TSi}$  most likely have charge state +2 while  $Mg_{Si}$  prefers charge state -2. We notice the size difference of covalent radii of Mg, Si and C (covalent radii are 1.41Å (Mg), 1.11Å (Si) and 0.68Å (C), respectively). Mg is a little larger than Si and

much larger than C, which is consistent with the fact that C and interstitial sites (Tc and TSi) that have small space prefer positive charge states, and Si sites that have larger space prefer negative charge states. The results in Figure 1 also show that the substitutional  $Mg_{Si}^{-2}$  has much smaller formation energy than that of  $Mg_C^{+2}$ , and interstitial  $Mg_{TC}^{+2}$  has lower formation energy than that of  $Mg_{TSi}^{+2}$ . Therefore,  $Mg_{Si}^{-2}$  should be the most stable substitutional defect while  $Mg_{TC}^{+2}$  should be the most stable interstitial defect in 3C-SiC.

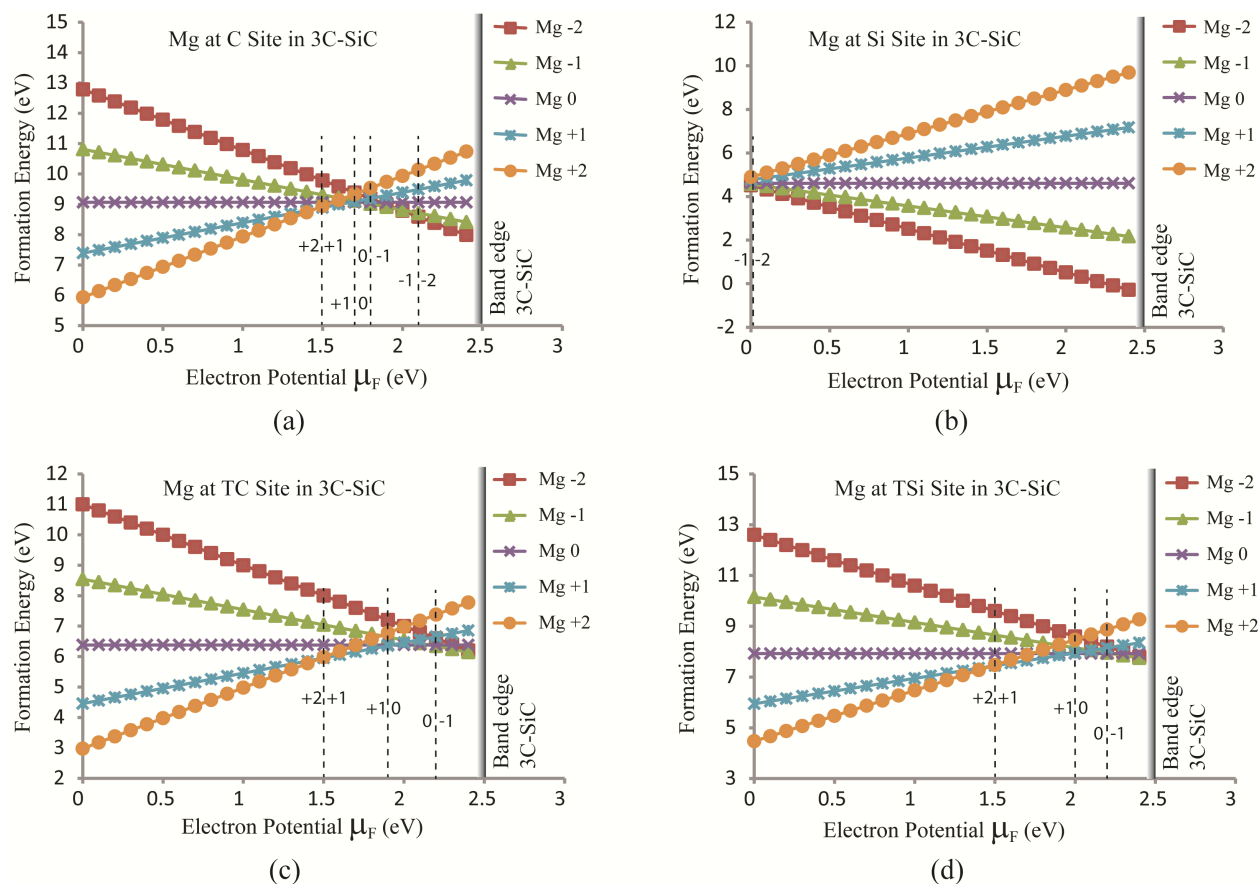


**Figure 1.** Formation energy of charged Mg at different lattice sites under different electron potential. The band gap value is taken as  $E_{band} = 2.39\text{eV}$ , determined from experiment [12].

## FUTURE WORK

In this report we present a part of our preliminary results that were calculated in a simulation cell  $2a_0 \times 2a_0 \times 2a_0$ . The results provide the thermodynamic properties including the formation energies of charged defects, possible charge states, and the most stable charged states. Since in the calculations we have not included the quadrupole correction due to the spurious

interactions between periodic images of charged defects in periodic simulation cells, the calculated formation energies are overestimated. More accurate calculations can be achieved by increasing the size of the simulation cell. In the future work, we will examine the size effect on the formation energies of charged defects, complete the formation energy calculations of other transmutants (Be and Al), and study the effect of charge states on migration mechanisms and migration energies of defects.

## ACKNOWLEDGEMENTS

This work was performed by Pacific Northwest National Laboratory, which is operated by Battelle for the United States Department of Energy under Contract DE-AC05-76RL01830. This study was supported by the U.S. Department of Energy, Office of Fusion Energy Sciences.

## REFERENCES

- [1] M. E. Sawan, Y. Katoh, and L. L. Snead, *J. Nucl. Mater.* **442** (2013) 5370.
- [2] S. Y. Hu, W. Setyawan, R. M. Van Ginhoven, W. Jiang, C. H. Henager, Jr. and R. J. Kurtz, *J. Nucl. Mater.* in press, 2014.
- [3] A. F. Kohan, G. Ceder, D. Morgan, and C. G. Van de Walle, *Phys. Rev. B* **61**(2000)15019.
- [4] J. Li, S. H. Wei, S. S. Li, and J. B. Xia, *Phys. Rev. B* **74** (2006) 081201.
- [5] G. Makov and M. C. Payne, *Phys. Rev. B* **51**(1995) 4014.
- [6] G. Kresse and J. Hafner, *Phys. Rev. B* **47**(1993) 558.
- [7] P. E. Blochl, *Phys. Rev. B* **50** (1994) 17953.
- [8] J. P. Perdew, K. Burke, and M. Ernzerhof, *Phys. Rev. Lett.* **77** (1996) 3865.
- [9] H. J. Monkhorst and J. D. Pack, *Phys. Rev. B* **13** (1976) 5188.
- [10] A. Mattausch, "Ab initio-Theory of Point Defects and Defect Complexes in SiC," Friedrich-Alexander Universität Erlangen-Nürnberg, Ph.D. Thesis, 2005.
- [11] J. Lento, M. Pesola, J. L. Mozos, and R. M. Nieminen, *Appl. Phys. Lett.* **77** (2000) 232.
- [12] W. J. Choyke, D. R. Hamilton, and L. Patrick, *Phys. Rev.* **133** (1964) A1163.

## 8.8 Analytical Model of Homogeneous Helium Trap-Mutation Evolution in Tungsten — W. Setyawan, G. Nandipati, K. J. Roche, H. L. Heinisch, R. J. Kurtz (Pacific Northwest National Laboratory) and B. D. Wirth (University of Tennessee, Knoxville)

### OBJECTIVE

The objective of this research is to support the prediction of irradiation damage properties of bulk tungsten-based materials using computational methods.

### SUMMARY

Homogeneous trap-mutation events in which helium (He) clusters above a minimum size displace tungsten (W) atoms from their lattice sites are simulated with molecular dynamics. Using a He concentration of up to 4600 appm and temperature up to 2050 K (half the absolute melting temperature), analytical models are formulated to describe the evolution of the number of trap-mutation nucleation sites ( $N_C$ ) and the number of created self-interstitial atoms ( $N_I$ ) as a function of He concentration and temperature. Consistent time scaling with respect to concentration (linear scaling) and temperature (Arrhenius scaling) is observed in the case of  $N_C$  curves. Therefore, a single analytical model can be obtained. On the other hand, while the linear time scaling still applies among the  $N_I$  curves, the Arrhenius time scaling holds only during early stages of the evolution due to the temperature-dependence of the saturation value (larger at higher temperatures). Hence, for  $N_I$ , a specific model is formulated for each temperature.

### PROGRESS AND STATUS

#### Introduction

Fusion devices employing the deuterium+tritium reaction will produce helium (He) and neutrons with characteristic kinetic energies of 3.5 and 14.1 MeV, respectively. These neutrons will cause two major challenges in the design of plasma-facing materials and first-wall materials by enabling solid and gaseous transmutation reactions as well as by inducing atomic displacement damage. Transmutation produced helium enhances displacement damage by forming bubbles that potentially facilitates void formation in the materials. On the grain boundaries, helium atoms cause significant interface decohesion. Another detrimental effect of helium is the formation of dendritic structures known as “fuzz” of the tungsten (W) surface [1]. When helium is formed, it is initially at interstitial sites. Subsequently, clustering occurs and large enough clusters (typically of size 7 at 1000 K) start to displace W atoms from their lattice sites, a process known as trap-mutation. The purpose of the current work is to develop an analytical curve to describe the time-evolution of the number of nucleation sites and the number of created W self-interstitial atoms (SIAs) due to a homogeneous trap-mutation process as a function of He concentration and temperature.

#### Simulation details

The molecular dynamics (MD) technique was employed to simulate trap-mutation. For the W-W interaction, the Finnis-Sinclair type potential developed by Ackland and Thetford [2] was taken, in which the short-range part was then modified to harden the repulsion [3]. Modification was also done at distances relevant to self-interstitial configurations to improve defect formation energies. The simulations were performed using LAMMPS software [4]. The simulations were

<sup>1</sup> PNNL is operated for the U.S. Department of Energy by Battelle Memorial Institute under Contract DE-AC06-76RLO 1830.

performed in the *NPT* ensemble at zero pressure and with a Nosé-Hoover thermostat. Periodic boundary conditions were applied in all axis coordinates. The simulation cell contains 524,288 W atoms. Helium atoms were introduced randomly at interstitial sites with no initial clustering, i.e. all He atoms were isolated interstitial atoms from each other.

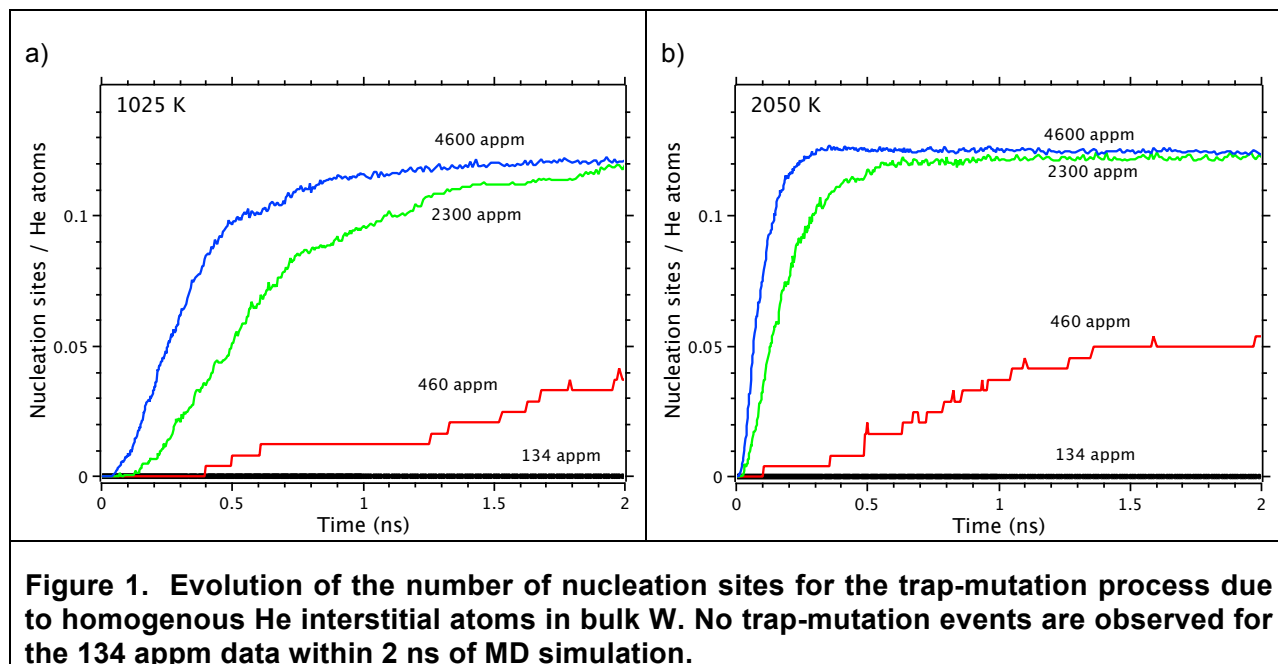
## RESULTS

Four different He concentrations at three different temperatures were simulated mostly up to 2 ns. The exact conditions are summarized in Table 1. At 300 K, no trap-mutation events occurred within 2 ns, therefore the data at this temperature will not be analyzed further. We first investigate the number of nucleation sites of a trap-mutation event. As time goes on, a nucleation site may contain more than one vacancy; however it will still be counted as one site. The number of nucleation sites and He atoms is denoted by  $N_C$  and  $N_{He}$  respectively. Figure 1a. and 1b show the evolution of  $N_C/N_{He}$ . Within 2 ns, saturation is reached for the 2050 K curves particularly the 2300 and 4600 appm data, meanwhile for the 1025 K curve only the 4600 appm data reaches saturation. From the 2300 and 4600 appm data,  $N_C/N_{He}$  saturates at approximately 0.12 regardless of temperature. A more accurate reading is 0.123 for the 2300 and 4600 appm data at 2050 K.

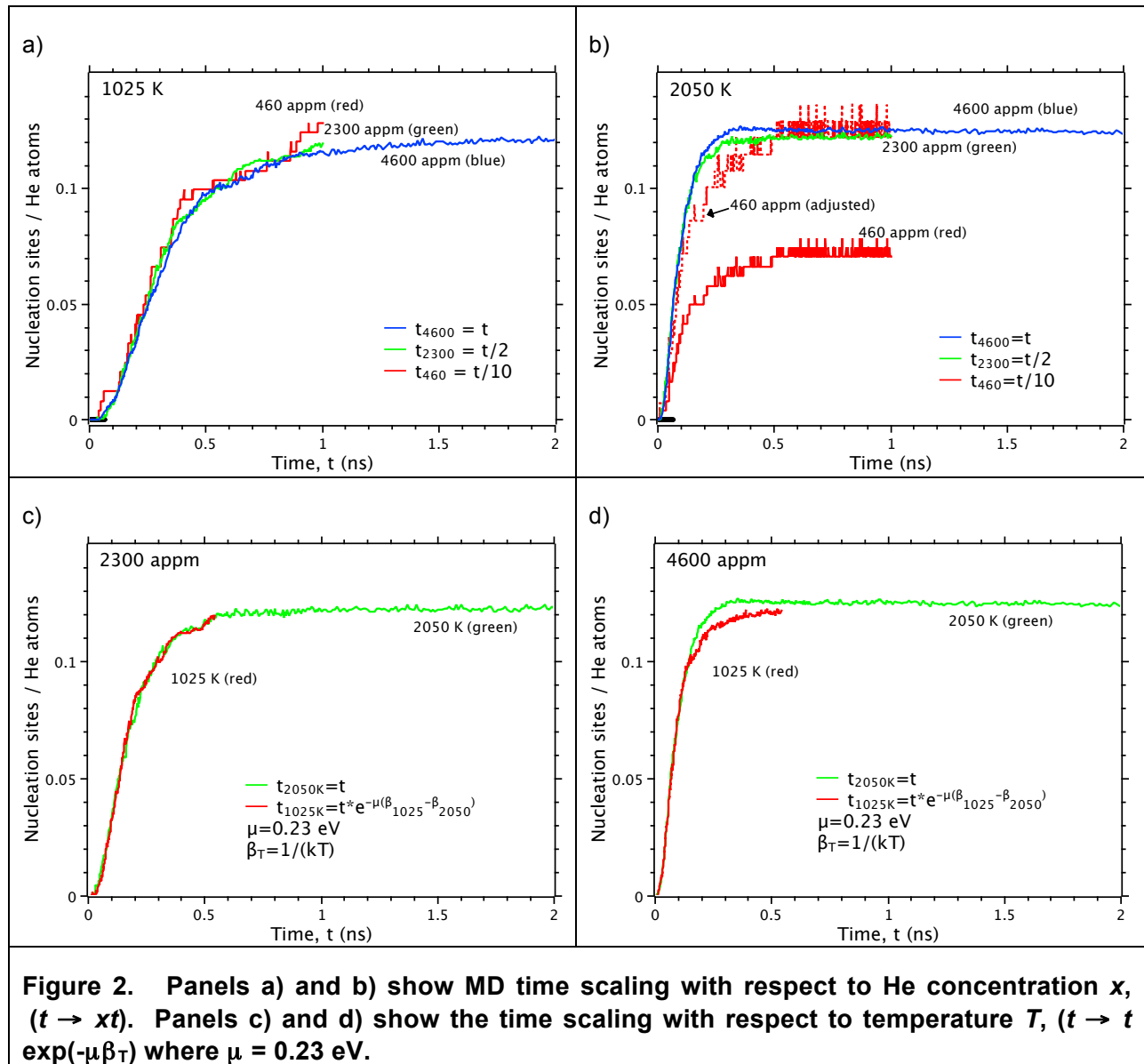
**Table 1. Time and conditions for helium trap-mutation simulations in tungsten. The 1025 K represents 0.25 of the melting temperature ( $T_m$ ) from the interatomic potential. The simulation cell contains 524,288 tungsten atoms.**

	300 K	1025 K (0.25 $T_m$ )	2050 K
134 appm (70 atoms)	2 ns	2 ns	2 ns
460 appm (241 atoms)	2 ns	10 ns	10 ns
2300 appm (1205 atoms)	2 ns	2 ns	2 ns
4600 appm (2410 atoms)	2 ns	2 ns	2 ns

Scaling of time,  $t$ , with respect to He concentration,  $x$ , is shown in Figure 2a. at 1025 K. In this figure, the proper time corresponds to that of the 4600 appm curve. It appears that the 2300 and 460 appm curves superimpose the 4600 appm curves if their respective timetag is scaled by a factor of 1/2 and 1/10. This indicates that time scales linearly with concentration, i.e., data with twice concentration saturates twice faster ( $t \rightarrow xt$ ). This simple scaling is well reproduced between the 4600 and 2300 appm data at 2050 K as shown in Figure 2b. We note that the 460 appm data at 2050 K does not follow this scaling that well, this particular curve saturates at 0.07 instead of 0.12. If this curve is multiplied by a factor of 0.12/0.07 (denoted as red dashed line and labeled as “460 appm adjusted” in Figure 2b), it appears to follow the scaling as well.



Scaling of time with respect to temperature,  $T$ , is shown in Figure 2c for the 2300 appm data. In this figure, the time of the 2050 K data is taken as the proper time. From Figure 2c, it is evident that Arrhenius scaling with effective migration energy of 0.23 eV fits the 1025 K curve to the 2050 K curve remarkably well ( $t \rightarrow t \exp(-\mu\beta_T)$ , where  $\mu = 0.23$  eV and  $\beta_T = 1/(kT)$ ). This scale is also reproduced between the 4600 appm data at 1025 K and 2050 K as shown in Figure 2d. The value of  $\mu = 0.23$  eV is slightly larger than the migration energy barrier (at 0 K) of a single He (0.21 eV) from the interatomic potential [3]. In a recent work of Reference [5], it was shown that the migration energy of small He clusters increases with temperature (non-Arrhenius diffusion at high temperatures) due to the increased number of super-basins. For example, the effective migration energy of He<sub>2</sub> cluster is 0.26, 0.41 and 0.69 eV at 0, 1025 and 2050 K respectively. Therefore, the value of  $\mu = 0.23$  eV suggests that the trap-mutation nucleation kinetics is governed predominantly by the migration of single He atoms.



The time scaling analyses suggest that a single empirical curve exists to model the evolution of the number of trap-mutation nucleation sites as a function of He concentration and temperature. In particular, the following model applies well in the vicinity of 4600 appm and 1025 K conditions. Motivated by the saturation behavior at  $t \rightarrow \infty$  and that the curves increase superlinearly at  $t \rightarrow 0$ , the curves are fitted to the following functional:

$$a[1 - \exp(-bt^n)] \quad (1)$$

Where the saturation value is taken to be  $a = 0.12$ . Figure 3 shows the curve fitting result for the 4600 appm and 1025 K data, i.e.  $b = 4.69$  and  $n = 1.60$ . Using this data, the empirical model for estimating the number of nucleation sites  $N_C$  can be written as

$$\frac{N_C}{N_{He}} = 0.12[1 - \exp(-4.69\tau^{1.60})] \quad (2)$$

$$\tau = \frac{x}{4600} t e^{-0.23\left(\frac{1}{T} - \frac{1}{1025}\right)\left(\frac{300}{0.0258}\right)} \quad (3)$$

where the He concentration  $x$  is in appm, temperature  $T$  is in K and time  $t$  is in ns. The performance of Equations 2 and 3 in approximating  $N_C/N_{He}$  curves for 2300 and 4600 appm at 1025 and 2050 K is demonstrated in Figure 3b. For conditions near 1025 K, Equations 2 and 3 can be used as is. For conditions near 2050 K, a better prediction is obtained by using the above Equations with a saturation value of  $a = 0.123$  instead of 0.12.

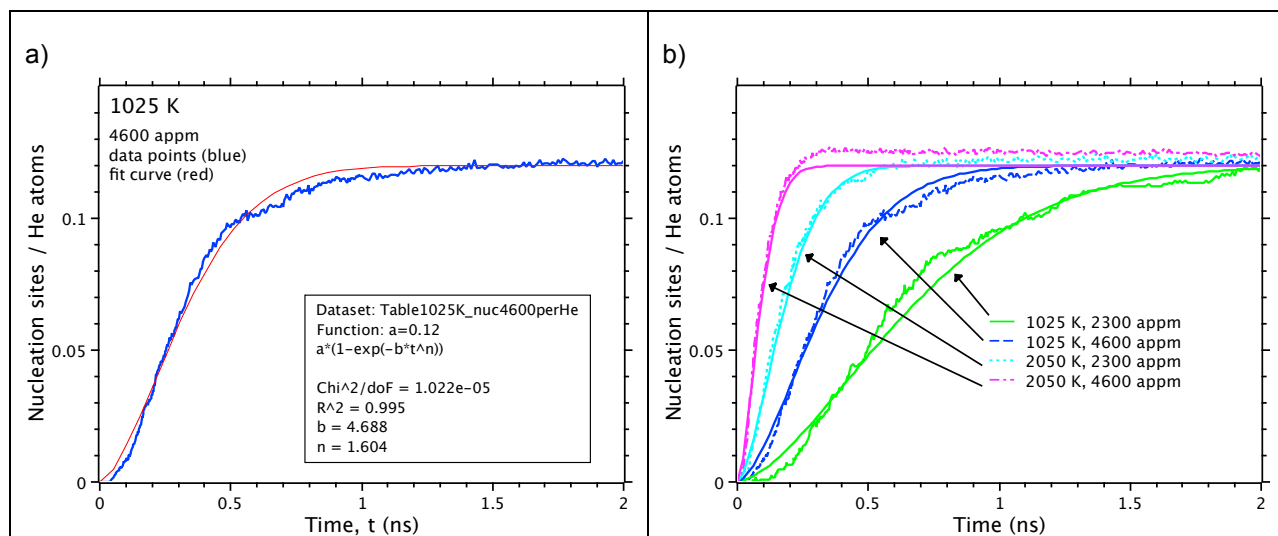
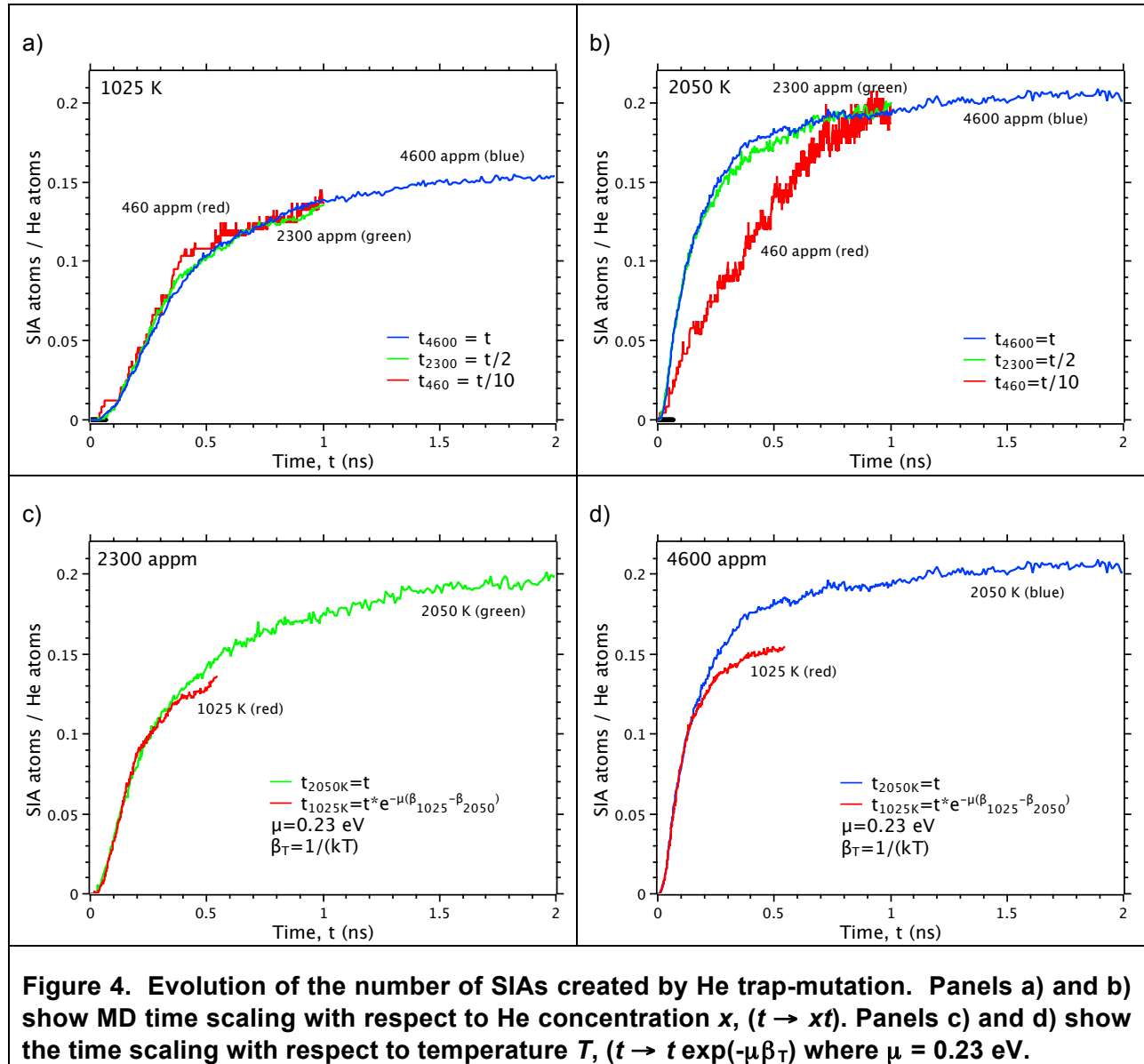


**Figure 3. a) Curve fitting of the 4600 appm and 1025 K data. b) The fit curve from a) is used to estimate the curves for other conditions simply by using a time scaling as given in Equation 3 (see text).**

Next we discuss the evolution of the number of SIAs,  $N_I$ . Similar to the case of nucleation sites, the curves of  $N_I/N_{He}$  also exhibit the same time scaling with respect to He concentration as shown in Figures 4a and 4b. Excellent scaling is observed for the 1025 K data. At 2050 K, the 2300 and 4600 appm data also scales well, however the 460 appm data at this temperature shows anomalous behavior as in the case of the nucleation sites curve. At 2050 K, the  $N_I/N_{He}$  curve of the 460 appm rises more slowly than predicted by the time scaling. Nevertheless, it appears to saturate to the same value as the other curves. The scaling with respect to temperature is displayed in Figures 4c and 4d using the same effective migration energy  $\mu = 0.23$  eV. The scaling works well to describe the early part of the curves (up to ~50% saturation). However, a perfect fit cannot be obtained due to  $t$  apparent differences in the saturation value, which are considerably larger at higher temperatures. At 1025 K, the saturation value is about 0.15, while at 2050 K it is 0.20. One could probably introduce another scaling parameter related to the saturation value as a function of temperature. However, the exact dependence cannot be determined with only two temperatures as it is clearly nonlinear.

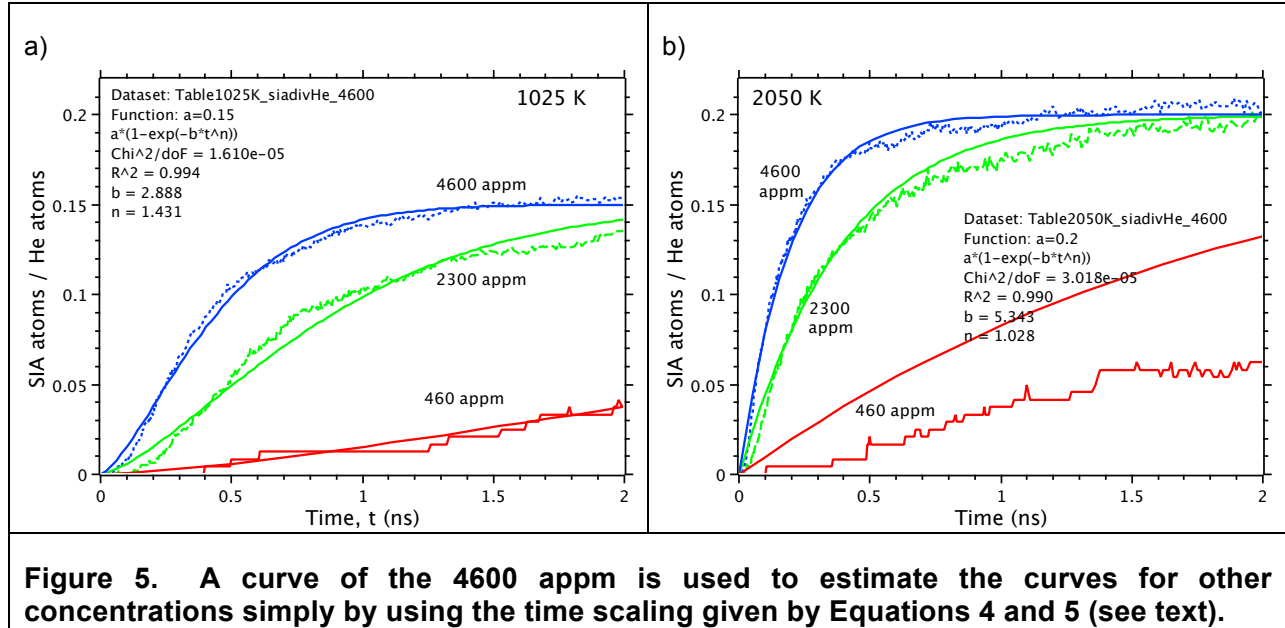


Consequently, two separate curve fits were calculated for the 1025 and 2050 K results. For both temperatures, the 4600 appm data was used for the fitting. The resulting empirical models as a function of He concentration for 1025 and 2050 K conditions are respectively:

$$\frac{N_I}{N_{He}} = 0.15[1 - \exp(-2.89\tau^{1.43})], \quad \tau = \frac{x}{4600} t \quad (\text{for 1025 K}) \quad (4)$$

$$\frac{N_I}{N_{He}} = 0.20[1 - \exp(-5.34\tau^{1.03})], \quad \tau = \frac{x}{4600} t \quad (\text{for 2050 K}) \quad (5)$$

Where time  $t$  is in ns and He concentration  $x$  is in appm. The performance of the models for describing other He concentrations is depicted in Figure 5. The 1025 K model describes the evolution well even for the 460 appm. While the 2050 K model sufficiently fits the 2300 and 4600 appm conditions.



## ACKNOWLEDGEMENT

Computations were performed on Olympus supercomputer at the Pacific Northwest National Laboratory.

## REFERENCES

- [1] S. Takamura, N. Ohno, D. Nishijima and S. Kajita, *Plasma Fusion Res.* **1** (2006) 051.
- [2] G. J. Ackland and T. Thetford, *Phil. Mag. A* **56** (1987) 15.
- [3] N. Juslin and B. D. Wirth, *J. Nucl. Mat.* **432** (2013) 61.
- [4] S. Plimpton, *J. Comp. Phys.* **117** (1995) 1.
- [5] B. P. Uberuaga and D. Perez, unpublished presentation given at the APS-DPP conference, Denver, CO, November 12-15 (2013).

**8.9 Object Kinetic Monte Carlo Simulations of Cascade Annealing in Tungsten —**  
G. Nandipati, W. Setyawan, H. L. Heinisch, K. J. Roche, R. J. Kurtz (Pacific Northwest National Laboratory) and B. D. Wirth (University of Tennessee)

**OBJECTIVE**

The objective of this work is to study the annealing of primary cascade damage created by primary knock-on atoms (PKAs) of various energies, at various temperatures in bulk tungsten using the object kinetic Monte Carlo (OKMC) method.

**SUMMARY**

We used our recently developed lattice based object kinetic Monte Carlo code; KSOME [1] to carry out simulations of annealing of individual displacement cascades in bulk tungsten that were generated using molecular dynamics (MD) simulations, at temperatures of 300, 1025 and 2050 K and PKA energies up to 100 keV. We find that at smaller PKA energies the fraction of surviving self-interstitial atoms (SIAs) and vacancies decreases with temperature, whereas at higher PKA energies the fraction of surviving defects at first decreases and then increases with temperature.

**PROGRESS AND STATUS**

**Introduction**

Tungsten is considered as the primary material choice for divertor components in future fusion reactors due to its high melting point, low sputtering coefficient, high thermal conductivity, low transmutation probability, low tritium retention and good mechanical strength. Bulk tungsten will be exposed to energetic neutrons escaping the plasma. The deuterium-tritium fusion reaction produces neutrons with a characteristic kinetic energy of 14.1 MeV. Collisions of 14.1 MeV neutrons with tungsten atoms produce tungsten primary-knock-on atoms with various recoil velocities. PKA atoms then lose the acquired energy to a large extent by displacing other atoms, in a sequence known as a displacement cascade. The whole process lasts for up to tens of picoseconds, and the debris left behind consists of point defects and clusters concentrated in a small volume, called primary damage.

MD has been used extensively to study the primary damage in materials. However, due to the requirement of femtosecond time steps in MD, long-term defect evolution is beyond its scope. Therefore the OKMC code, kSOME was used to carry out annealing simulations of primary damage. These simulations were intended to be an extension of MD simulations in time-scale. Accordingly, the OKMC method is used to carry out annealing simulations at exactly the same temperature at which the cascades were generated with MD, using a big simulation box. The purpose of the current work is to use the OKMC method to carry out annealing simulations of primary damage in pure tungsten produced by PKAs up to 100 keV at temperatures of 300, 1025 and 2050 K.

<sup>1</sup> PNNL is operated for the U.S. Department of Energy by Battelle Memorial Institute under Contract DE-AC06-76RLO 1830.

## Simulation Details

Simulations were performed on a cubic block of tungsten atoms having a side length of 512 lattice units or 162 nm, with each axis parallel to a  $\langle 100 \rangle$  direction of the crystal. In tungsten, cascades are compact, and the volume of the simulation box chosen is large enough that we expect the results to be insensitive to the box size. Each atom is allowed to hop to one of eight body-centered cubic nearest neighbor lattice sites at  $a/2 \langle 111 \rangle$ , where  $a$  is the lattice constant. Initial defect distributions of SIA and vacancy defects obtained from MD cascade damage simulations were placed in the center of the box. Absorbing boundary conditions were adopted in all three directions i.e., when a defect diffuses out of the box it is no longer tracked and is removed from the simulation. Such defects are counted as escaped defects and contribute to long-range defect diffusion. These defects will interact with the rest of the microstructural features leading to microstructural changes and damage accumulation.

The values of migration energies and pre-factors for diffusion and binding energies of defects used in our annealing simulations are taken from the *ab initio* calculations of Becquart *et al.* [3]. In the present model SIA clusters larger than size five were constrained to diffuse in 1-D along one of four  $\langle 111 \rangle$  directions. While SIA clusters up to size five were allowed to change their direction of 1D motion via rotation and thereby perform mixed 1D/3D motion. Activation barrier for changing the direction of their 1D motion from one  $\langle 111 \rangle$  direction to another is 0.38 eV. Since MD does not provide information on the orientation of SIA diffusion, the direction of 1D motion was assigned randomly to the SIAs at the start of a simulation. Also there is no information available on infrequently occurring immobile SIA clusters in these cascades therefore we assumed that all interstitial clusters are glissile (mobile). Their migration/diffusion rates decrease with increasing cluster size ( $n$ ) according to  $n_0 n^{-a}$  ( $n_0 = 6 \times 10^{12} \text{ s}^{-1}$ ,  $a = 0.5$ ).

For a single vacancy, the activation barrier for diffusion is taken as 1.66 eV, and vacancy clusters larger than five are assumed to be inactive i.e., they neither diffuse nor emit, although they interact with other defects if they are within the range of interaction. All vacancies migrate in 3D, and their diffusion rates decrease with cluster size ( $n$ ) according to  $n_0 (q^{-1})^{n-1}$  ( $n_0 = 6 \times 10^{12} \text{ s}^{-1}$ ,  $q = 1000$ ). The vacancy (SIA) dissociation rate is given by  $G_d = n_d \exp(-(E_m + E_d)/k_B T)$ , where  $E_d$  is the binding energy of a vacancy (SIA) to a vacancy (SIA) cluster, and  $E_m$  is the migration energy of a single vacancy (SIA). We have assumed that defect clusters of all sizes are spherical objects and their capture radii were also obtained from Reference [3].

**Table 1. Average number of surviving Frenkel Pairs in tungsten from MD simulations as a function of PKA energy and temperature [2].**

PKA Energy (keV)	TEMPERATURE (K)		
	300	1025	2050
10	12	9.3	9.3
20	22.1	18	15
30	29.6	22.4	21.7
40	34.7	31.7	32.3
50	50	43	38.1
60	60.8	52.7	50.7
75	81.3	80.5	72.9
100	116.3	110.5	100.3

## RESULTS

A database of 15-20 cascades at PKA energies ranging from 10 keV to 100 keV was created using MD simulations. With each MD cascade, i.e. the same PKA energy, the same location and the same direction, we carried out 20 runs with different random seeds. Results presented here were averaged over both different cascades and random seeds. Thus each data point in the plots shown in this report was averaged over 300-400 runs. Simulations were carried out at temperatures of 300, 1025 and 2050 K for up to 10 ns. Note that 1025 K and 2050 K correspond to 0.25 and 0.5 of the melting temperature of tungsten respectively (from the interatomic potential). We have also carried out simulations longer than 10 ns, but due to fast interstitial diffusion rates we found that almost all of the recombination and coalescence events happen in the very first few nanoseconds (ns) of the simulation, therefore we only show results up to 10 ns for all temperatures and PKA energies. Beyond 10 ns we find the most frequent events are interstitial clusters escaping the simulation box. To understand the annealing of single cascades in tungsten we have also collected runtime information like number densities of defects, reaction events (recombination, coalescence, emission, transformation), average cluster sizes and their size distributions, and number densities of defects escaping the box for all the types (in our case they are only SIAs and vacancies) as a function of time. Information about the details of MD simulations carried out to generate the database of cascades and other additional details about the cascades can be found in Reference [2]. Table 1 shows the average number of Frenkel pairs for 300, 1025 and 2050 K at various PKA energies. The number of Frenkel pairs increases with PKA energy and decreases very slightly with temperature. To compare annealing of cascades across different PKA energies and temperatures, the number of surviving defects was normalized by the average number of defects at the start of the simulation.

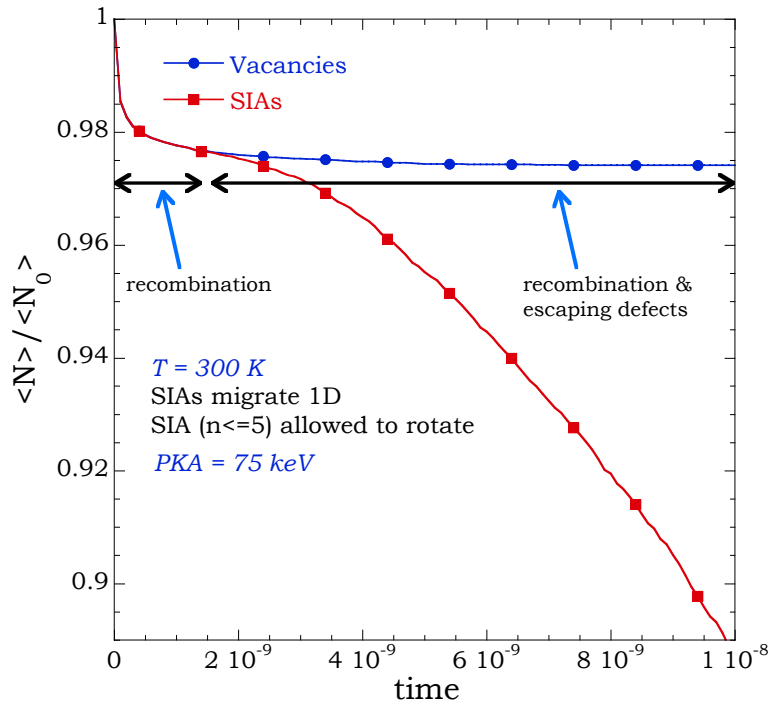


**Figure 1. Normalized surviving fraction of SIAs and vacancies as a function of time for a PK of 75 keV and at 300 K.**

Figure 1 shows a plot of the surviving fractions ( $n_d = \sum n S_d$ ,  $n$  = number of defect clusters of size  $S_d$ ) of all SIAs and vacancies as a function of time for a PKA energy of 75 keV at 300 K. This plot shows all the features of defect evolution common to all PKA energies and temperatures. One can see from Figure 1 that the initial decrease in surviving defects is due to recombination only (the surviving fraction of SIAs and vacancies are equal), and this occurs in the very first few ns. As the highly mobile SIAs diffuse beyond the boundary of the simulation box, the total number of interstitial defects is no longer equal to the number of vacancy type defects, which results in a drop in the fraction of surviving SIAs (see Figure 1). At 300 K, interstitials migrate very fast, and they very quickly diffuse away from the primary damage region, while the migration rate vacancy clusters is so low that they are immobile for the time-scale of the simulation and can be considered immobile for the time scales of the simulations up to 2050 K. It can be seen from Figure 1 that the surviving fraction of vacancies remains nearly constant after early recombination events. Therefore, for convenience we will show only the surviving fractions of SIAs in all the plots hereafter. As mentioned in the previous section, the emission rate is determined by the sum of binding and migration energies and this sum is large for both SIA and vacancy clusters. Therefore, for the very short time-scale of the simulation, emission is an infrequent event even at 2050 K. In our test runs to analyze different aspects of annealing we have observed that, within the simulation time of 10 ns, rotation of small SIA clusters is not very active and does not significantly affect the annealing of primary damage below 500 K. We do have results that show how cascades generated at different PKA energies anneal, but in this report we present only the temperature effects, which are much greater and even somewhat counterintuitive.

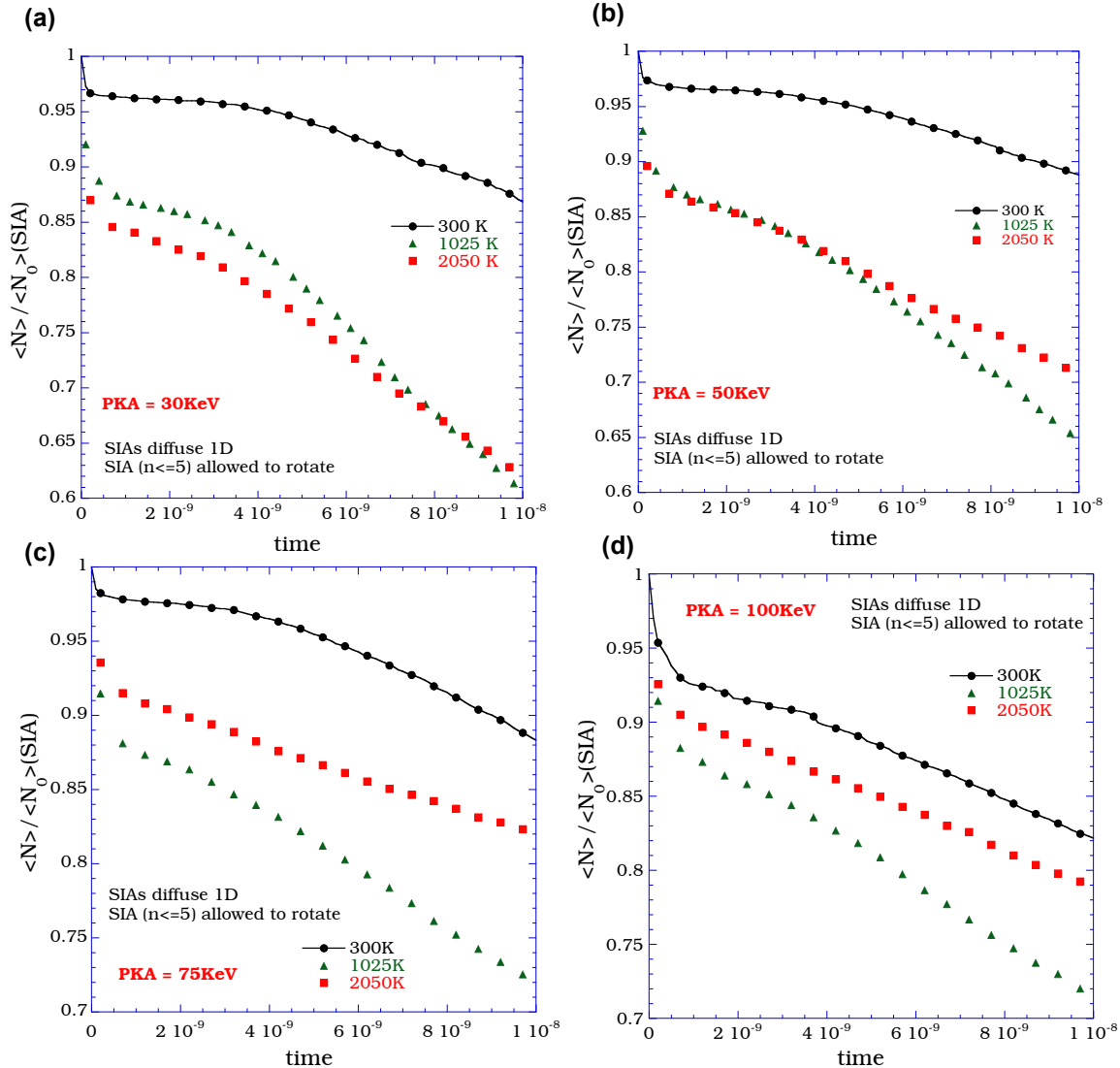


**Figure 2. Effect of temperature on the normalized surviving fractions of SIAs as a function of time for cascades at PKA energies of (a) 30 keV (b) 50 keV (c) 75 keV (d) 100 keV.**

Figure 2 shows the surviving fractions of SIAs in cascades as a function of time at temperatures of 300, 1025 and 2050 K for PKA energies of 30, 50, 75 and 100 keV. The results vary with increasing cascade energy. For 30 keV cascades the fractions of SIAs lost due to recombination increase with temperature (see Figure 2(a)). For cascades at 75 and 100 keV the fractions of SIAs lost to recombination increase with temperature from 300 K to 1025 K. Counterintuitively, it appears to decrease with temperature (see Figures 2(c) & (d)) and for 50 keV cascades the fraction of defects lost to recombination is almost the same at 1025 and 2050K (see Figure 2(b)). Note that the dotted line of filled red squares in Figure 2 represents the fraction of surviving SIAs at 2050 K which is in the middle of 300 K and 1025 K lines for 75

and 100 keV cascades. Another observation that can be made is that at 2050 K, for 30 and 50 keV cascades, SIAs escape the simulation box at a much slower rate than at 1025 K. We think that the reduced recombination observed at 2050 K for 75 and 100 keV cascades is due to a combination of factors like the spatial and size distributions of SIA and vacancy clusters (i.e., cascade morphology), the fast SIA diffusion rate, rotation/non-rotation of SIA clusters and, the cluster size distribution of SIA and vacancy clusters in the initial cascades.

## **FUTURE WORK**

We intend to carry out further tests to find out what causes the reduced recombination at 2050 K during annealing of high PKA energy cascades. In addition, we intend to carry out additional simulations to test the effect of rotation/non-rotation of SIA clusters, and migration barrier of both SIA and vacancy clusters on the annealing of primary damage. In addition, we plan to perform simulations of irradiation using the same set of MD cascades at the same temperature at which they were generated and at various dose rates.

## **ACKNOWLEDGEMENT**

All computations were performed on CARVER at National Energy Research Scientific Computing Center (NERSC).

## **REFERENCES**

- [1] G. Nandipati, *et al.*, Semiannual Progress Report DOE/ER-0313/54, June 2013, 179-183.
- [2] W. Setyawan, *et al.*, Semiannual Progress Report DOE/ER-0313/54, June 2013, 200-204.
- [3] C. S. Becquart, *et al.*, *J. Nucl. Mater.* **403** (2010) 75.

## **9.1 Fusion Material Irradiation Test Station (FMITS) at SNS — Mark Wendel and Phil Ferguson (Oak Ridge National Laboratory)**

### **OBJECTIVE**

The Fusion Materials Irradiation Test Station (FMITS) is a planned irradiation facility at the Spallation Neutron Source (SNS). The objective of the current effort is a Concept Design (30% level) to quantify the risk to normal operations and safety at the SNS. The deliverables are a Concept Design Report, Concept Design Review, and a Safety Assessment. The original study of FY2012 estimated a total project cost of \$10M over a 3-year schedule. This estimate is being refined as part of the current effort.

### **SUMMARY**

Highlights of the FMITS Concept Design include safety round-table findings, advances in the mechanical design of the harness and vent-line shield block (through which FMITS utilities pass), improved remote handling procedures and tooling, and refinements of the user science envelope. Samples would be welded inside the FMITS target harness in two horizontal tubes, which project out in front of the mercury target. For these specimen locations, the back-scattering neutron flux spectra should be close to the ITER fusion spectrum. The PKA spectra at the FMITS samples were also compared to those for ITER, and the results show good agreement. Radiation damage rates would be 1.6–5.5 dpa/y for steel, with the range of helium-to-dpa production ratios starting close to those expected in D-T fusion, and increasing toward beam center locations.

### **PROGRESS AND STATUS**

#### **Introduction**

Significant progress has been made this year to define a workable concept for design of the FMITS with well-understood impacts on the SNS operations and SNS safety case. Monthly meetings are conducted involving all aspects of the effort, and individual technical meetings for areas such as user science, instrumentation, mechanical design, remote handling, and safety are conducted as needed.

#### **Safety**

A safety round-table was held to comprehensively list and discuss any potential impacts on SNS safety due to the installation and operation of FMITS. Attendees included all safety experts, systems engineers, analysts, and design engineers. The minutes consisted of an overview of FMITS hardware and operations, explanation by the SNS Safety Officer of the scope and format of the meeting, and then an open floor discussion about potential impacts to SNS systems and safety concerns. The single issue identified during the discussion involved an indirect threat to the hydrogen moderator vessel or mercury target from a projectile emanating from a sudden burst of the FMITS (water-filled) tube annulus following a double total-flow blockage of the water. Impact to the moderator vessel was of particular concern due to the direct view of the moderator to some tube locations. Other secondary issues that needed to be addressed in the Safety Assessment were agreed as easily mitigated by standard design practices.

The safety officer proposes mitigation of projectile scenario by design, i.e. ensuring that any rupture of the FMITS tubes would occur in a direction away from the moderator vessels and target. To this end, a design of the FMITS tubes with weak spots machined into the outer surface has been proposed. Discussions are underway with Fike Inc., a company specializing in pressure relief that was contracted for a similar safety issue at the High Flux Isotope Reactor. The plan for FMITS would be to have Fike Inc. provide a design and test program for certification of the pressure relief component that is similar to the HFIR subcontract.

**User Program**

The purpose of FMITS is to provide a testing venue for experiments leading to advances in the fusion materials program, and the limitations on potential FMITS experiments must strike a balance between SNS operational reliability concerns with user scientific goals. Therefore, extensive investigations and discussions have led to revisions in the design parameters (Table 1) that were set in the FY2012 Design Study, and discussions are ongoing.

The 650°C irradiation limit should provide adequate range for testing of candidate steels while still in the higher reliability range for Type K thermocouples. Thermal analysis has been completed that assures the 250°C post-irradiation temperature. The limit on O<sub>2</sub> exposure allows for a simplified design. The lower sub-temperature dpa limit was made possible by the completion of a more comprehensive operating history study that took into account SNS beam trips and restarts.

**Table 1. Important parameters on specimen irradiation conditions at planned FMITS.**

Operational Parameter	FY2012 Design Study	2014 Concept Design	Future Capabilities
Maximum Irradiation Temperature	600°C	650°C	1300°C
Maximum Post-Irradiation Temperature	< Irradiation Temperature	250°C	<250°C
Maximum Temperature for O <sub>2</sub> Exposure	Only after removal from FMITS	250°C	<250°C
Percentage of dpa within 50°C of Target Irradiation Temperature	< 5%	< 3%	< 1%

The FMITS tubes will be water-cooled, and the loss of cooling could damage SNS equipment. TCATS (a combination of thermocouples fabricated into a common mineral insulated sheath) will be used for specimen temperature monitoring at FMITS. The temperature readings will also be important in an SNS machine protection strategy. The machine protection system is an important issue to the FMITS user science since certain failures in instrumentation could lead to premature termination of an experiment. Progress has been made in ensuring thermocouple reliability for the planned FMITS harness and in the design of an FMITS flow sensor that will

assure adequate cooling exists despite potential thermocouple failures. The thermocouple reliability case consists of:

- (1) Demonstrated (100%) reliability from SNS proton beam window halo thermocouples that are exposed to similar conditions as planned FMITS thermocouples.
- (2) High reliability of TCAT assemblies in experiments at the HFIR.
- (3) Published thermocouple reliability numbers from nuclear reactor applications.
- (4) Discussions with TCAT vendor (Delta-M) regarding their experience in nuclear applications.

A radiation-tolerant flow switch has been identified that appears to be adequate for reliable use in the FMITS water supply. The use of the flow switch with the thermocouple data should provide a means of ensuring the continued operation of FMITS despite limited thermocouple failures commensurate with previous thermocouple failure rates.

### **Mechanical Design**

Progress in the Concept Design for the primary hardware components is presented. Three components comprise the FMITS in-cell system: the target module itself, the replaceable FMITS harness containing the material samples, and the permanent Vent Line Shield Block (VLSB) which conducts the FMITS utilities along the SNS target carriage. Although other secondary FMITS components and tooling have been improved, the progress presented is for these main components.

Modifications must be made to the target module design for FMITS implementation. Since the FY2012 Design Study was performed, SNS has adopted a new target design, referred to as the Jet-Flow Target (JFT). These new targets will be in use before the FMITS facility is incorporated, and it is expected that they will continue to be used afterwards, so modifications to the new JFT design due to FMITS have been proposed to accommodate the FMITS harness assembly.

The all-welded FMITS harness (Figure 1) provides two independent material sample sections, located above and below the SNS proton beam centerline. The distance from the centerline for each sample section can vary for each experiment. The following changes have been incorporated:

- (1) The FMITS *harness flange* must provide the core vessel inflatable seal interface. The mechanical issue was the axial space required for the addition of the FMITS flange without challenging normal SNS operating functionality or remote handling maneuvers. The FMITS Concept Design now successfully integrates to the SNS JFT.
- (2) Moving the mixing location for the FMITS temperature-control gases upstream into the permanent shield block on the target carriage greatly simplifies the harness. New analysis of SNS operating data shows that moving the mixing location upstream is inconsequential to the temperature control of FMITS. This change eliminated the innermost concentric tube in the harness, reducing the number of umbilical hoses.
- (3) The gas-isolation valves were removed from the design, which opened up access space for remote handling. This change was made possible by the relaxation of the inert cover gas temperature (Table 1).

The VLSB (Fig. 2) is a 17-ft fabrication of solid stainless steel with internal passageways for the target and FMITS gas and electric connections. Simplifying changes to the FMITS VLSB design have reduced the number and changed the type of connectors used for FMITS gas supply. Since the gas mixing location was moved from the FMITS harness to the VLSB, the number of harness jumpers required was decreased by three (two supply jumpers and one exhaust jumper). Also, although threaded compression fittings are in the current FMITS design, quick-release connectors are more conducive to remote-handling (potential to reduce operational impacts), and technical discussions with the Staubli company are underway to make this change a reality.

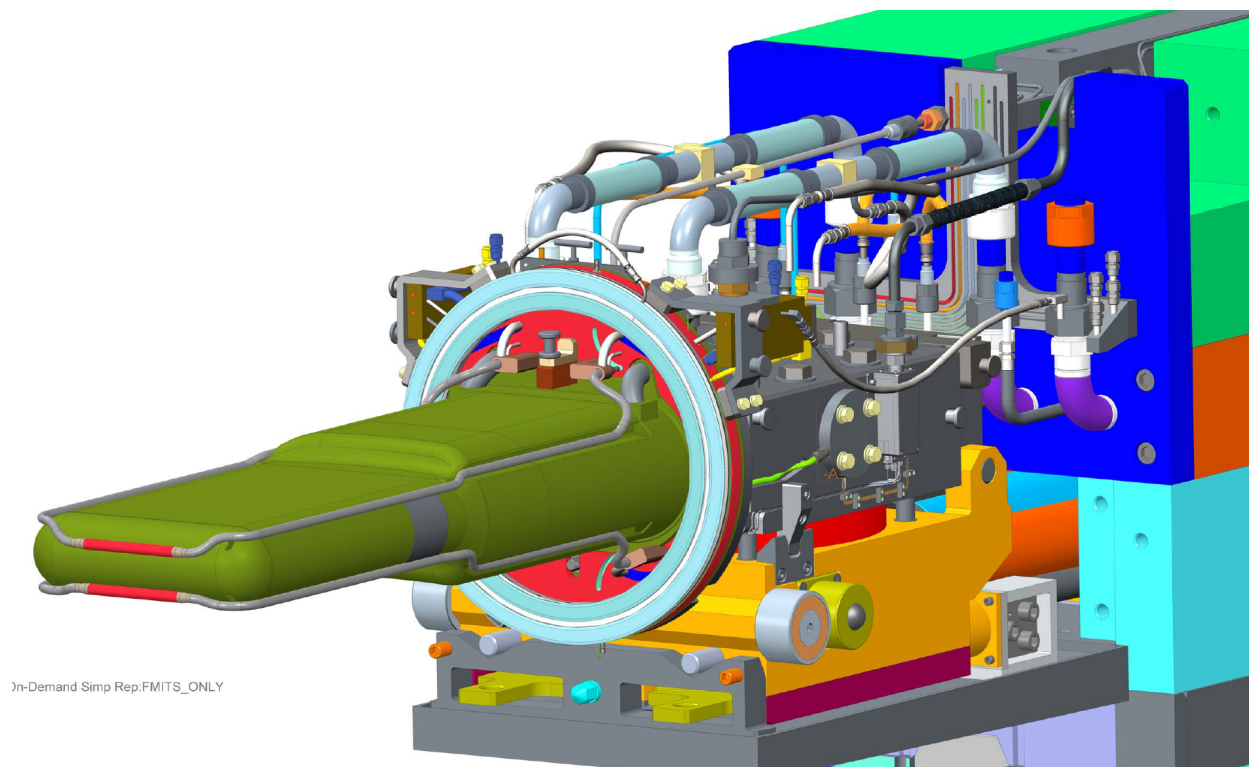


**Figure 1. Current concept for FMITS harness design with sample tubes out front of the target shown in red.**



**Figure 2. Current concept for FMITS VLSB design, which conducts the FMITS gas and electrical supplies alongside the pre-existing mercury, target vent-line and leak detection cabling.**

Other mechanical design progress is helping to reduce operational risk at SNS. Fabrication techniques to construct the concentrically welded FMITS tubes are being developed with experienced vendors for higher reliability and decreased cost.

### **Remote Handling**

Integration of FMITS into the existing SNS operational structure requires significant remote handling and extensive operations within the SNS Service Bay. The Service Bay is the shielded space where all target systems service operations are performed by remote handling including replacement of the target. The previous FY2012 Design Study effort provided notional concepts for operational steps in addition to the identification of new tooling and equipment required to accommodate FMITS. Continued successful SNS operation demands preservation of nominal Service Bay operational and maintenance activities. Successful integration of FMITS into nominal Service Bay operations necessitates minimal impact to existing capabilities. The goal is to re-visit these original notional solutions to ensure that a Concept Design meets all operational and technical requirements.

The present Concept Design began with a re-evaluation of all of the operational scenarios required to support FMITS operations. The objective of the operational scenarios was to define all of the FMITS-specific activities required that could impact existing SNS Service Bay operations or that were required to support FMITS operation and user program requirements. The outcome of this thorough examination resulted in a more detailed understanding of the specific processes and the tooling required supporting the processes.

Each operational scenario was then scrutinized to review the original solution envisioned in the FY2012 Design Study to ensure that the solution was viable and met the technical requirements of FMITS and the operational requirements of SNS. Based on this review, FMITS remote handling required additional scrutiny in the areas of:

- VLSB Service Bay operations,
- Service Bay Gas Line Routing, and
- FMITS-to-Target Integration.

Installation of the large FMITS Vent Line Instrument Assembly necessitated a review of all access methods to the Service Bay. The trade study resulted in the recommendation to install the new VLSB by removing selected T-beams in the roof of the Service Bay. Current efforts surround conceptual development of tooling and procedures to support this option. The radiological implications have been approved as manageable. Figure 3 shows computer modeling of the Vent Line being lowered through a T-beam opening in the High Bay.

The Gold Amalgamation Room located in the target-building basement was the location for the FMITS gas control system in the FY2012 Design Study. This location proved to have more difficult access in routing the gas lines to the FMITS harness. An improved location has been identified for the gas system in the Manipulator Gallery which is much closer and has a usable penetration and clear routing path for gas lines to the FMITS connections.

### **Target Imaging System**

Modeling and simulation of the performance of the target imaging system (TIS) with and without the FMITS harness installed on the target was performed. The TIS system monitors the position, size and peak density of the beam relative to the target by imaging the in-beam fluorescence of a chromia coating on the nose of the target. Since the FMITS sample tubes would partially obscure the TIS view to the target nose, it is necessary to assess the impacts. The TIS does not initiate automated hardware response in the SNS control system, however, operations have become to rely upon the ability of TIS to indicate that the beam position, size and power peaking are acceptable.

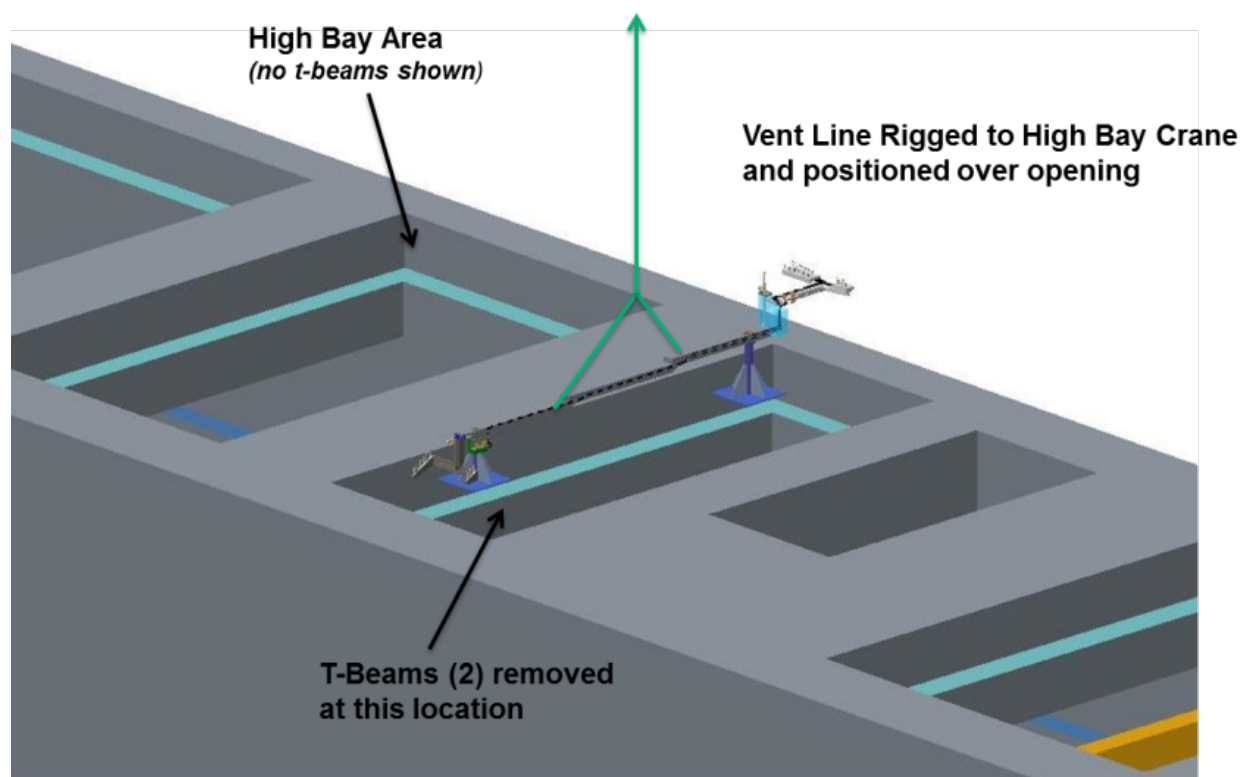


**Figure 3. VLSB will be installed T-Beam opening above the target Service Bay.**

An optical model of the TIS with FMITS tubes in front of the target was constructed, executed and evaluated based on historical data from October 15th, 2013 at 850 kW. The assumed positions for the tubes were 3-cm above and 5-cm below beam centerline. With this asymmetric arrangement, there was little impact (less than 1 mm in horizontal and less than 0.3 mm in vertical alignment) on the extrapolated beam alignment due to FMITS tubes according to the model, and with the centerline of the target being unobscured by FMITS, the peaking factor could accurately be determined in the model. Obscuring the centerline by positioning an FMITS tube on beam center would possibly be a problem, but the helium-to-dpa ratio is very high in the middle of the proton beam, a range of less interest to the fusion materials users.

Other considerations for potential FMITS impacts on the TIS were identified:

- Differences in luminescence and aging between the coating on the target and the coating on FMITS tubes will affect the measurement technique.
- FMITS tubes might reflect light and interfere with TIS signal, affecting resolution.
- The calibration procedure needs to change. The fiducial pattern on the target nose would have to be modified in order to be unobscured.

Additional TIS modeling will be completed before the Concept Design Review.

Some additional modeling could enhance the understanding of FMITS impacts. These include:

- Assess the effect of optical transfer (fiber pattern, blurring),
- Generate statistics by analyzing many images including those taken at the highest powers, and those collected further into the target lifetime,
- Assess near-symmetric tube distributions to quantify the degree to which symmetry affects the accuracy of the super-Gaussian fit,
- Determine the optimum fiducial pattern with FMITS tubes in place at various positions.

There is potential for mutual benefits for FMITS and SNS Operations due to the TIS which include:

- FMITS - The instantaneous dpa rate distribution would be available on the FMITS tubes, and therefore individual material specimens due to the TIS data.
- Operations - The FMITS tubes could be a testing site for optimization of luminescent coatings, thus, optimizing the performance of the TIS.
- FMITS and Operations - In the future it might be possible to use the TIS as a signal to temperature alarm since the coating luminosity has a precipitous drop-off at elevated temperatures. This signal could protect against a water shroud loss-of-flow event.

### **Resource-Loaded FMITS Schedule**

Part of the effort of the present Concept Design is to more accurately assess the cost of completing the FMITS facility. To that end, when possible, quotations from vendors are being solicited. For example: Airgas, Inc. based on the existing FMITS process and instrumentation diagram quoted a complete gas system. The quotation came in at \$200K for all of the gas system hardware. The floor footprint was acceptable for the planned installation and the cost data will be included in the revised cost estimate for the FMITS facility.

A project plan is begun in the Primavera cost planning system, and three meetings have been conducted to iterate on the structure of the project and requirements of the major phases of the FMITS build-out. Currently, manpower and materials estimates are being projected for Preliminary Design, Final Design, Procurement and Installation. Significant mock-up testing is planned mostly for the Preliminary Design phase. The FMITS-modified target module has a long lead time, so it would be separated out with an earlier design-completion date.

**9.2 HFIR Irradiation Experiments – December 31, 2013** — Y. Katoh (Oak Ridge National Laboratory)

**Summary of Recent, Current and Planned Fusion Materials Program Experiments**

Experiment Designation	Primary Materials	Specimen Types*	Irradiation Temperature (°C)	Max Exposure (dpa)	Number of Reactor Cycles	Irradiation Period (month/year)		
<i><b>Beryllium reflector (RB) irradiation positions</b></i>								
RB-15J	F82H	T, F, FT	300, 400	6	10	6/08	–	12/09
<i><b>Target zone full-length capsules</b></i>								
JP-25	F82H	T, FT	300, 500	20	10	2/99	–	1/01
JP-26	F82H	T, FT	300,400,500	9	5	12/03	–	11/04
JP-27	F82H	T, FT	300, 400	21	13	12/03	–	1/08
JP-28	F82H	T, FT	300,400,500	80	46	4/05	–	7/13
JP-29	F82H	T, FT	300,400,500	80	46	1/05	–	7/13
12-DCT	F82H	DCT	50	1.6	1	8/11	–	8/11
JP-30	F82H	T, FT	300,400,650	20	~10	11/11	–	8/13
JP-31	F82H	T, FT	300,400,650	20	~10	11/11	–	8/13
<i><b>Target zone rabbit capsules (DOE-JAEA)</b></i>								
F8A1	F82H	T, FT	300	50	29	2/09	–	7/13
F8A2	“	“	“	“	“	“	–	“
F8B1	“	“	“	“	“	“	–	“
F8B2	“	“	“	“	“	“	–	“
JCR-1	SiC/SiC	Bend bars	800	30	15	10/04	–	1/09
JCR-2	“	“	“	“	“	“	–	“
JCR-3	“	“	“	“	“	“	–	“
JCR-4	“	“	“	“	“	“	–	“
JCR-5	“	“	“	>50	>25	10/04	–	2/11
JCR-6	“	“	“	“	“	“	–	“
JCR-7	“	“	“	“	“	“	–	“
JCR-8	“	“	“	“	“	“	–	“
JCR-9	“	“	500	30	15	10/04	–	1/09
JCR-10	“	“	“	“	“	“	–	“
JCR-11	“	“	“	“	“	“	–	“
JCR-12	“	“	“	“	“	“	–	“
F11A3	F82H	T, FT	300	20	12	5/11	–	2/13
F11A4	“	“	“	“	“	“	–	“
F11B3	“	“	“	“	“	“	–	“
M4-TEN	F82H	DCT	50	1.6	1	8/11	–	8/11

JCR11-01	SiC/SiC	Bend bars	950	50	25	11/12	–	
JCR11-02	SiC/SiC	Bend bars	950	10	5	10/12	–	8/13
JCR11-03	SiC/SiC	Bend bars	950	30	15	5/13	–	
JCR11-04	SiC/SiC	Bend bars	950	30	15	5/13	–	
JCR11-05	SiC/SiC	Bend bars	950	50	25	10/12	–	
JCR11-06	SiC/SiC	Bend bars	950	10	5	10/12	–	7/13
JCR11-07	SiC/SiC	Bend bars	950	100	50	10/12	–	
JCR11-08	SiC/SiC	Bend bars	950	100	50	10/12	–	
JCR11-09	SiC/SiC	UDMC	950	4	2	6/13	–	11/13
JCR11-10	SiC/SiC	UDMC	950	10	5	6/13	–	
JCR11-11	SiC/SiC	UDMC	950	30	15	6/13	–	
JCR11-12	SiC/SiC	UDMC	950	100	50	6/13	–	
F13A5	F82H	T, FT	300	10	9	1/14	–	
F13A6	F82H	T, FT	300	20	18	1/14	–	
F13B4	F82H	T, FT	300	10	9	1/14	–	
F13B5	F82H	T, FT	300	20	18	1/14	–	
<b><i>Target zone rabbit capsules (TITAN)</i></b>								
T8A1	SiC	BSR	300	0.01	HT**	10/09	–	10/09
T8A2	SiC	BSR	300	0.1	HT	10/09	–	10/09
T8B1	SiC	BSR	500	0.01	HT	10/09	–	10/09
T8B2	SiC	BSR	500	0.1	HT	10/09	–	10/09
T8C1	SiC	BSR	500	~1	1	5/09	–	6/09
T8D1	SiC	BSR	800	0.1	HT	3/11	–	10/09
T8E1	SiC	BSR	800	~1	1	8/09	–	8/09
T8F1	SiC	BSR	1200	~1	1	8/09	–	8/09
T9A1	W, Ni	Discs	90	0.1	HT	1/09	–	10/09
T9A2	W, Ni	Discs	90	1.2	1	1/09	–	1/09
T9C1	Steels	T, MC	500	5.5	3	11/09	–	2/10
T9C2	Steels	T, MC	500	9.6	5	11/09	–	6/10
T9G1	Steels	T, MC	300	1.2	1	6/09	–	8/09
T9G2	Steels	T, MC	300	9.6	8	6/09	–	8/11
MTTN01	Steels	T, MC	300	4.8	4	1/12	–	8/11
300-LD-1	Steels	SSJ, MC	300	2	1	5/12	–	6/12
300-HD-1	Steels	SSJ, MC	300	12	6	5/12	–	2/13
500-LD-1	Steels	SSJ, MC	500	2	1	5/12	–	6/12
500-HD-1	Steels	SSJ, MC	500	12	6	5/12	–	2/13
500-HD-2	Steels	SSJ, MC	500	12	6	5/12	–	2/13
500-HD-3	Steels	SSJ, MC	500	12	6	5/12	–	2/13
650-LD-1	Steels	SSJ, MC	650	2	1	5/12	–	6/12
650-LD-2	Steels	SSJ, MC	650	2	1	5/12	–	6/12
650-HD-1	Steels	SSJ, MC	650	12	6	5/12	–	2/13
650-HD-2	Steels	SSJ, MC	650	12	6	5/12	–	2/13
300-LD-2	Steels, W	SSJ, MC	300	2	2	7/12	–	8/12
300-MD-1	Steels, W	SSJ, MC	300	7	4	7/12	–	2/13
500-LD-2	Steels, W	SSJ, MC	500	2	2	1/13	–	7/13

300-LD-3	Steels, W	SSJ, MC	300	2	2	7/12	–	11/12
300-HD-2	Steels, W	SSJ, MC	300	12	8	7/12	–	2/14
500-LD-3	Steels, W	SSJ, MC	500	2	1	7/12	–	8/12
500-HD-4	Steels, W	SSJ, MC	500	12	6	7/12	–	7/13
650-LD-3	Steels, W	SSJ, MC	650	2	2	10/12	–	7/13
650-HD-3	Steels, W	SSJ, MC	650	12	8	7/12	–	11/13
PC1	Various	SSJ, MC	80/100	0.02	HT	6/12	–	6/12
PC1A	Various	SSJ, MC	80/100	0.02	HT	6/12	–	6/12
PC2	Various	SSJ, MC	80/100	0.1	HT	6/12	–	6/12
PC2A	Various	SSJ, MC	80/100	0.1	HT	6/12	–	6/12
PC3	Various	SSJ, MC	80/100	0.5	HT	6/12	–	7/12
PC3A	Various	SSJ, MC	80/100	0.5	HT	6/12	–	7/12
PC4	Various	SSJ, MC	80/100	2	1	6/12	–	7/12
PC4A	Various	SSJ, MC	80/100	2	1	6/12	–	7/12
PC5	Various	SSJ, MC	80/100	20	9	6/12	–	11/13
TB-300-1	Steels, W	SSJ, MC	300	0.02	HT	8/12	–	8/12
TB-300-2	Steels, W	SSJ, MC	300	0.1	HT	8/12	–	8/12
TB-300-3	Steels, W	SSJ, MC	300	0.5	HT	8/12	–	8/12
TB-300-4	Steels, W	SSJ, MC	300	7	5	7/12	–	6/13
TB-500-1	Steels, W	SSJ, MC	500	0.1	HT	8/12	–	8/12
TB-500-2	Steels, W	SSJ, MC	500	0.5	HT	8/12	–	8/12
TB-500-3	Steels, W	SSJ, MC	500	7	4	7/12	–	2/13
TB-650-1	Steels, W	SSJ, MC	650	0.1	HT	8/12	–	8/12
TB-650-2	Steels, W	SSJ, MC	650	0.5	HT	8/12	–	8/12
TB-650-3	Steels, W	SSJ, MC	650	7	5	7/12	–	6/13
TB-650-4	Steels, W	SSJ, MC	650	20	11	7/12	–	
TTN09	SiC	Joint	500	3.4	2	8/11	–	11/11
TTN10	SiC	Joint	500	4.1	2	8/11	–	11/11
TTN11	SiC	Joint	800	4	2	3/12	–	5/12
TTN01	SiC	BSR	300	1	1	2/11	–	3/11
TTN02	SiC	BSR	300	10	6	2/11	–	12/11
TTN03	SiC	BSR	300	20	11	2/11	–	8/13
TTN04	SiC	BSR	500	10	6	5/11	–	4/12
TTN05	SiC	BSR	500	20	11	5/11	–	8/13
TTN06	SiC	BSR	800	10	6	5/11	–	4/12
TTN07	SiC	BSR	800	20	11	5/11	–	8/13
TTN08	SiC	BSR	1200	10	6	5/11	–	8/12
TTN16	SiC	Fiber BSR	500	1	1	11/11	–	12/11
TTN17	SiC	Fiber BSR	500	10	6	8/11	–	6/12
TTN18	SiC	Fiber BSR	500	20	11	8/11	–	8/13
TTN19	SiC	Fiber BSR	1200	1	1	3/12	–	4/12
TTN20	SiC	Fiber BSR	1200	10	6	3/12	–	11/12
<b>Target zone rabbit capsules (US-TITAN-JAEA)</b>								
T11-01J	V-4Cr-4Ti	BTC	425	2	1	11/12	–	12/12
T11-02J	V-4Cr-4Ti	BTC	425	6	3	1/13	–	7/13

T11-03J	V-4Cr-4Ti	BTC	425	2	1	11/12	–	12/12
T11-04J	V-4Cr-4Ti	BTC	425	6	3	1/13	–	7/13
T11-05J	SiC	BTC	600	2	1	11/12	–	12/12
T11-06J	SiC	BTC	600	6	3	1/13	–	7/13
T11-08J	SiC	BTC	600	6	3	1/13	–	7/13
T11-09J	SiC	BTC	600	2	1	11/12	–	12/12
T11-11J	SiC	BTC	600	2	1	11/12	–	12/12
T11-13J	Graphite	BTC	600	2	1	11/12	–	12/12
T11-14J	Graphite	BTC	600	6	3	1/13	–	7/13
J12-01	F82H	BTC	300	1.5	1	1/13	–	2/13
J12-02	F82H	BTC	300	6	3	5/13	–	7/13
J12-03	F82H	BTC	300	1.5	1	5/13	–	2/13
J12-04	F82H	BTC	300	6	3	1/13	–	6/13
J12-05	F82H	BTC	300	1.5	1	1/13	–	2/13
J12-06	F82H	BTC	300	6	3	5/13	–	6/13
<i>Target zone rabbit capsules (US-IMR)</i>								
MX-1	Ceramics	Various	400	2	1	7/13	–	8/13
MX-2	Ceramics	Various	400	TBD	TBD	7/13	–	
MX-3	Ceramics	Various	400	10	6	7/13	–	
MX-4	Ceramics	Various	700	2	1	7/13	–	8/13
MX-5	Ceramics	Various	700	TBD	TBD	7/13	–	
MX-6	Ceramics	Various	700	10	5	7/13	–	
MX-7	Ceramics	Various	1000	2	1	7/13	–	8/13
MX-8	Ceramics	Various	1000	TBD	TBD	7/13	–	
MX-9	Ceramics	Various	1000	10	5	7/13	–	

\*T = Tensile, F = Fatigue, FT = Fracture Toughness, MC = Multipurpose Coupon, BSR = Bend Stress Relaxation Creep, DCT = Disc Compact Tension, BTC: Bellows-loaded Tensile Creep, UDMC: Uni-directional Mini-composite. Most experiments also contain TEM disks, other special purpose specimens, and monitors occupying small spaces.

\*\*Hydraulic tube – fractional cycle exposures.